SYNTHESIS AND CHARACTERIZATION OF POROUS METAL PHOSPHONATES

A Dissertation

by

TIFFANY L. KINNIBRUGH

Submitted to the Office of Graduate Studies of
Texas A&M University
in partial fulfillment of the requirements for the degree of

DOCTOR OF PHILOSOPHY

Chair of Committee,	Abraham Clearfield
Committee Members,	Hong-Cai Joe Zhou
	Michael B. Hall
	Tahir Cagin
Head of Department,	David H. Russell

August 2013

Major Subject: Chemistry

ABSTRACT

This dissertation focuses on the challenge of developing porous metal arylphosphonates with both high crystallinity and functional porosity by using different synthetic approaches. Metal phosphonates are an extensive class of materials based upon extended inorganic-organic architectures such as chains, layers and three-dimensional networks. Metal phosphonates generally favor extended inorganic architectures leading to pillared materials with no porosity. We found that the use of template molecules, type of ligand and choice of metal ions could be used to deviate from the pillared structure. Many of these structures had interesting properties that were explored. The results can be divided into three areas:

We developed non-pillared monovalent metal phosphonates by investigating both the role of water and template molecules in the solvothermal synthesis. The role of water in solvothermal reactions was found to have a profound influence on the structure of monovalent metal phosphonates and the structures could be tailored from zero/one-dimensional to two-dimensional. Non-pillared structures could be synthesized by using template molecules.

For a zinc phosphonate, we converted a layered structure into a three-dimensional framework by using small template molecules in the solvothermal reaction. The compound exhibited reversible dehydration behavior. The change in the framework structure and guest positions was monitored during this process.

Two different ligands were used in the development of porous aluminum phosphonates. One series exhibited reversible dehydration behavior, which had a dramatic influence on permanent porosity of the material. The stability of the dehydrated phase is a result of the geometry of the aluminum atom, which in some cases has coordinatively unsaturated metal sites. The second series was developed with ion exchange applications in mind therefore the pore environment was tailored to favor ion exchange processes. The most important aspect is that these compounds exhibit high selectivity for Th^{4+} ions.

In total 28 new compounds were prepared, and their utility and structures clarified.

DEDICATION

To Tasha, Cecil, and James

May you always reach for the stars

ACKNOWLEDGEMENTS

I would like to thank my committee chair, Dr. Clearfield, and my committee members, Dr. Cagin, Dr. Hall and Dr. Zhou, for their guidance and support throughout the course of this research.

I cannot describe how grateful I am to Dr. Clearfield for allowing me to have the freedom to explore the chemistry I find interesting. I greatly enjoyed the discussions about chemistry and life. It has been a pleasure to be a part of your group and your research.

I want to thank the members of Dr. Clearfield's group and many fellow graduate students. Without their help and support in both chemistry and life I would not have gotten this far.

I had the pleasure to work with three undergraduate students: Nancy Garcia, Kylee Stouder and Matthew Stouder. I hope that you learned as much from me, as I did from you.

I want to thank Dr. Bhuvanesh and Dr. Reibenspies with the fruitful discussions on crystallography. Dr. Bhuvanesh always was a great source of information on structure determination from powder X-ray diffraction.

Dr. Bakhmutov had a wealth of knowledge on NMR and was always willing to run one more sample. I sincerely appreciate his help with solid state NMR and without it many of these studies would be inconclusive.

I want to thank Dr. Ray Guillemette in the Department of Geology at Texas A&M University for help with all of the microprobe work. He and the use of the microprobe enriched the research presented here.

I want to thank Gregory Halder, Lynn Ribaud and Matthew Suchomel from Argonne National Laboratory for help with recording the *in situ* and high resolution powder X-ray diffraction data on 1-BM and 11-BM beam lines.

I am thankful for the encouragement and support from my family. They always had faith in me. Finally, I must thank my fellow scientist and husband Andrey. His support, love and encouragement helped me through the tough days. He was always there for me to brighten my day. Without our everyday discussions I would have also never accomplished this work.

NOMENCLATURE

BTP	1,3,5-benzene triphosphonic acid
BPDPA	4,4’-biphenylenediphosphonic acid
MPDPA	4,4’-phenylenediphosphonic acid
MOF	Metal Organic Framework
PXRD	Powder X-ray Diffraction
UMOF	Unconventional Metal Organic Framework
MOF	Metal Organic Framework
TGA	Thermal gravimetric analysis

TABLE OF CONTENTS

Page

LIST OF FIGURES

Page

LIST OF TABLES

CHAPTER I

INTRODUCTION AND LITERATURE REVIEW

The challenge

Both the development of new ligands and modern synthetic techniques are being used to synthesize hybrid inorganic-organic materials with both high crystallinity and functional porosity.[1-7] Hybrid inorganic-organic materials contain both inorganic and organic moieties that together build continuous networks in at least one direction. The materials concerned here, are porous metal phosphonates: unconventional metal organic frameworks[5,7] (UMOFs, Figure 1) and regular metal organic frameworks[5] (MOFs). The development of these materials started with the expansion of the field of metal phosphates by the inclusion of phosphonic acids in the synthesis.[8]

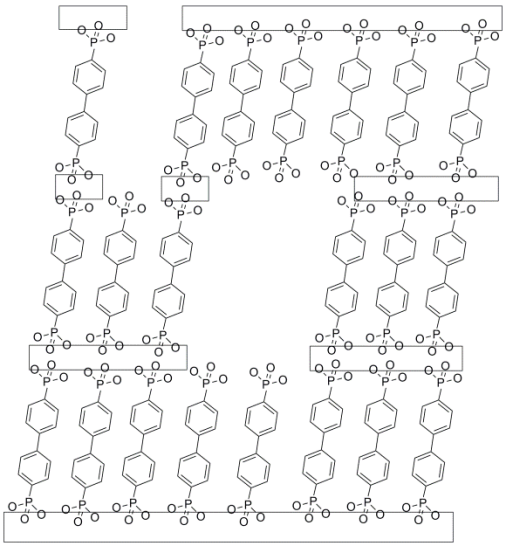

Figure 1. A scheme of a typical unconventional metal organic framework showing how micropores form by layer growth defects

Metal phosphonates are an extensive class of materials based upon extended inorganic-organic architectures such as chains, layers and three-dimensional networks.[5] Metal phosphonates generally favor extended inorganic architectures, instead of isolated metal clusters connected by organic moieties. This results in densely packed materials (pillared materials) with no porosity. However, layer growth defects[7,9,10] and "house of cards" arrangement of small global nano-size particles[11,12] can result in porous materials with a range of pore sizes (UMOFs, Figure 1 and 2)).

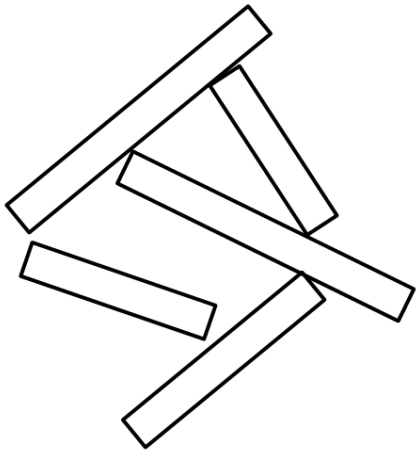

Figure 2. "House of cards" arrangement believed to be the cause of mesopores in metal hybrid materials[11,12]

Porous metal phosphonates with both high crystallinity and functional porosity, due to an ordered structure (which defines regular MOFs), are challenging to synthesize. The two major reasons are the favored pillared structure and poorly crystalline samples which hinders knowledge of the structure-property relationship. This chapter reviews

why the pillared structure is favored in metal phosphonates and strategies to obtain MOFs based on metal phosphonates. It highlights important factors that influence the resulting structures, such as reaction conditions, choice of metal ions and ligands.

Pillared architecture

In order to develop highly crystalline, functional porous materials, an understanding of why the pillared architecture is favored in metal phosphonates should be addressed. The pillared architecture is formed due to the tetrahedral geometry of the phosphonic acid groups and relative one dimensionality of the organic moieties. The phosphonate group has multiple bonding modes to metal atoms (Figure 3). It can bond to a metal atom either through one or two phosphonate oxygen atoms leaving the remaining oxygen atom/s free to bond to neighboring metal atoms. Further bonding modes are seen by chelation, where a phosphonate oxygen atom coordinated to a metal atom, donates a lone pair to a neighboring metal atom. The various bonding modes promote the formation of continuous inorganic structures such as chains and layers. Ligands with multiple phosphonic acids then link the chains or layers forming the pillared architectures.

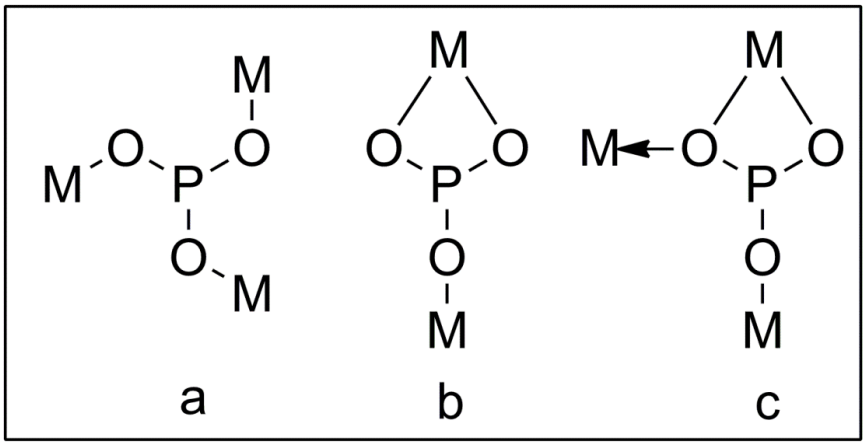

Figure 3. A scheme showing various metal bonding modes of phosphonates

Non-pillared architectures through use of secondary building units

To develop non-pillared architectures, secondary building units (SBUs) have been explored.[13-16] Generally two types of SBUs can be considered: (1) organic SBUs (the ligand) which can be tailored by ligand synthesis (2) inorganic SBUs built from metal ions or clusters. Development of the inorganic SBUs will be discussed in this section. In contrast to the pillared architectures in metal phosphonates, zeolites, phosphate molecular sieves and MOFs are built by linking SBUs to build porous frameworks.[1-3,17-19] Until recently, molecular phosphonates have been relatively rare, but they were proposed as SBUs to build open framework metal phosphonates.[13-16,20,21] Molecular phosphonates are isolated clusters formed from metal ions and phosphonic acids. Additionally, different types of ligands including alcohols, alkyl and amines coordinate to the metal ions. Similar types of SBUs found in zeolites and phosphate molecular sieves were successfully synthesized in metal phosphonate cages[16,22] and

include D4R (double-four ring)[14,17,20,23,24] , D6R (double single ring)[25] and S4R (single-four ring)[26]. These types of molecular phosphonates have been formed by five different synthetic methods: solvothermal/hydrothermal[27-29], alkane elimination[16,22], bulky phosphonic acids[24,30,31], ancillary ligand/co-ligand[32] and cluster expansion[33-35]. Only molecular phosphonates prepared by alkane elimination and cluster expansion will be discussed here, while others will be discussed in later sections.

Several molecular phosphonates with main group metals and metalloids were synthesized by alkane elimination reactions (Figure 4).[16] While the presence of hydrolyzable bonds suggests these materials would be ideal SBUs for open framework phosphonates, their stability towards O_2, H_2O, ROH, RNH_2, R_2NH, etc proved this to be more difficult.[16] However, cubic molecular phosphonates with either Al or Ga were sensitive to compounds containing acidic hydrogen atoms[22], thereby under the right synthetic conditions open framework metal phosphonates could be synthesized.

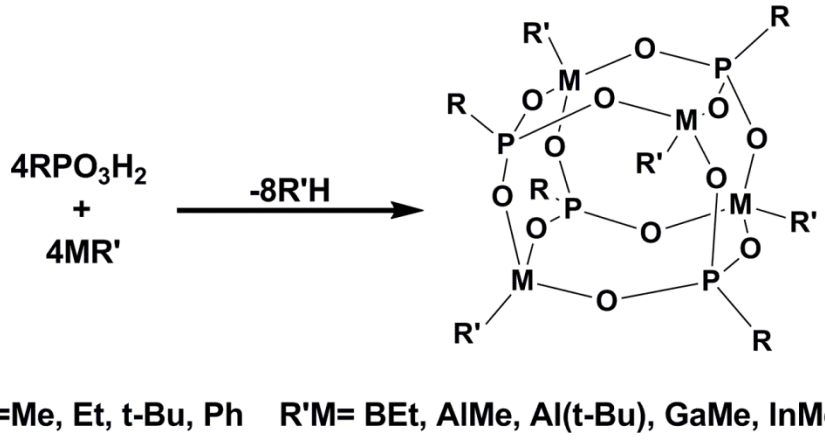

Figure 4. Formation of molecular phosphonate cages through alkane elimination reactions[15]

Cluster expansion is an alternative method to synthesize molecular phosphonates. This method involves the displacement of the bridging carboxylate in oxo-centered polymetallic cages with phosphonates (Figure 5).[34] The development in this area has resulted in many new complex molecular phosphonates and is described in a recent collection of reviews edited by Clearfield et al.[5]

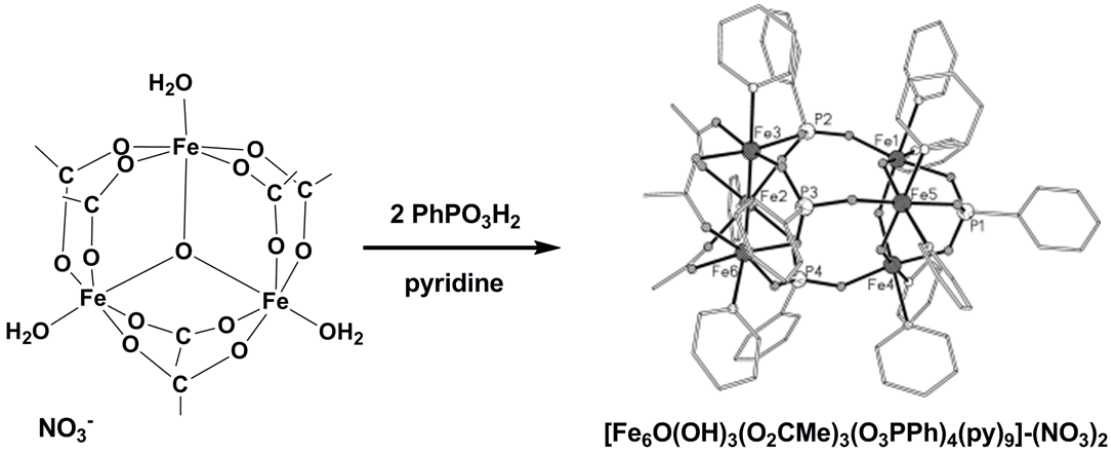

Figure 5. Formation of an iron molecular phosphonate through displacement of ligands in oxo-centered polymetallic cage[34*]

In both methods a two-step synthesis is required for the development of open framework metal phosphonates from SBUs. Either the ligand bound directly to the metal or the phosphonate must be displaced by a group which can link the molecular phosphonates into a three-dimensional framework. However, the displacement of the phosphonate may be difficult, so alternatively additional functional groups could possibly be incorporated on the phosphonate ligand in which a three-dimensional

*Figure 5 reprinted with permission from "Synthesis and Characterization of Iron(III) Phosphonate Cage Complexes" by Tolis, E. I.; Helliwell, M.; Langley, S.; Raftery, J.; Winpenny, R. E. P. Ang. Chem. Inter. Ed. **2003**, 42, 3804-3808, Copyright 2001 by John Wiley and Sons.

framework could form. A recent example of the expansion of a molecular phosphate with D4R units to a three-dimensional framework demonstrates the viability of this idea.[5,36] The ligand 4,4'-bipyridine and careful manipulation of the synthetic conditions resulted in the covalently bonded MOF with both micro-mesoporosity.

Influence of reaction conditions and types of metals on the structure of metal phosphonates

The concept to develop porous solids with high selectivity for required applications has driven the field of hybrid inorganic-organic frameworks to have enormous chemical and structural diversity.[3,4,37,38] This wealth of information has provided insight into how several factors play important roles in the resulting structure.[5,6,39] To obtain open-framework metal phosphonates a better understanding of the role of reaction conditions and the metal ion is important. The factors that affect metal phosphonates will be discussed here are temperature and pH of the reaction, and the metal ion kinetics, coordination, and geometry.

Temperature and pH

Some general trends of the influence of reaction pH and temperature on the resulting structures have been found.[39,40] The influence of temperature can be seen, where less hydrated and denser materials usually occur with an increase in reaction temperature. A study varying the reaction temperature from 90-190 ^{o}C highlights this trend, where a lower water content was found as the reaction temperature increased for a series of copper phosphonatoethanesulfonates.[40] Similarly, two forms of zinc 4-cyclohexene-cis-1,2-dicarboxylates were formed by varying the synthetic temperature: a

hydrate phase-below 100 ^{o}C and anhydrous phase at high temperature. Thermodynamic factors have been found to be more dominant than kinetic factors; however, time-dependent effects are seen in the rate of crystallization. [39,40]

The influence of pH has an effect on the M-O-M bonding where elimination of water molecules or hydroxyl groups by condensation reactions occurs at higher pH resulting in extended inorganic-organic networks.[39] In aqueous environments, the metal cations are solvated by water molecules. Depending on the pH, temperature of the solution, ionic radii and the charge of the metal various degrees of water deprotonation can occur.[41] The type of complex that will form in aqueous media for simple metal ions can be predicted based on the aqua-hydroxo-oxo equilibria (Figure 6).[42] Additionally, the ionic radius of a central atom can also influence the equilibria where a smaller radius shifts the acidity range to a lower value. An example is for Fe(III) and La(III) where the aqua region is below pH 2 for Fe(III) (ionic radius 55 pm) and 8 for La(III) (ionic radius 116 pm).[42] However, the hydrolysis behavior is more complicated close to neutrality for the usually hydroxide, where polynuclear species $M_a(OH)_b^{+(az-b)}$ can form.[42] The pH of a solution changes the metal species in solution and therefore influences the resulting metal phosphonate structure.

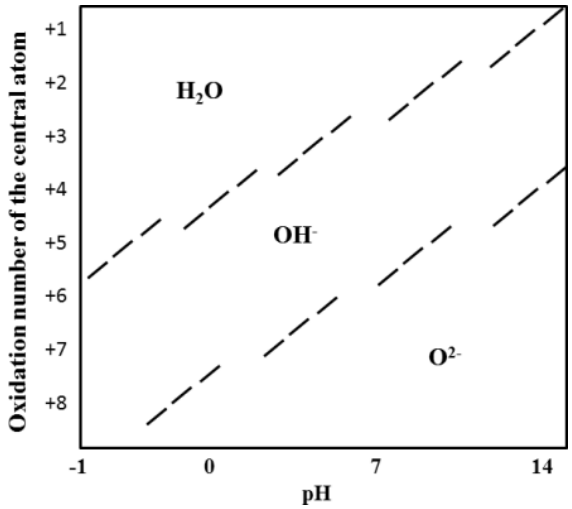

Figure 6. A graph showing the aqua-hydroxo-oxo equilibria for a central atom with different oxidation numbers at different pH values[42]

A unique example of the influence of pH on the structure of AlMepO, $Al_2(CH_3PO_3)_3$ H_2O, is apparent based on the work of Maeda and coworkers.[43-46] Three forms of the compounds were synthesized AlMepO-α, AlMepO-β, AlMepO-ζ. The structure changed from unidimensional channels found in AlMepO-α and AlMepO- β, to a layered material, AlMepO-ζ, by the addition of a basic component to the synthesis (Figure 7).[43-46] The coordination of the aluminum atoms changed from four and six-coordinate in AlMepO-α and AlMepO-β containing unidiminsional channels, to only a six-coordinate metal ion in the layered compound (AlMepO-ζ). Additionally, for another layered compound, AlMePO-2, two different types of aluminum coordination were obtained (octahedral and trigonal bipyramidal) where the initial solution was adjusted to pH 5.[47] Similar work using a carboxylic acid linker showed that slight changes in pH afforded different compounds.[4,48-51]

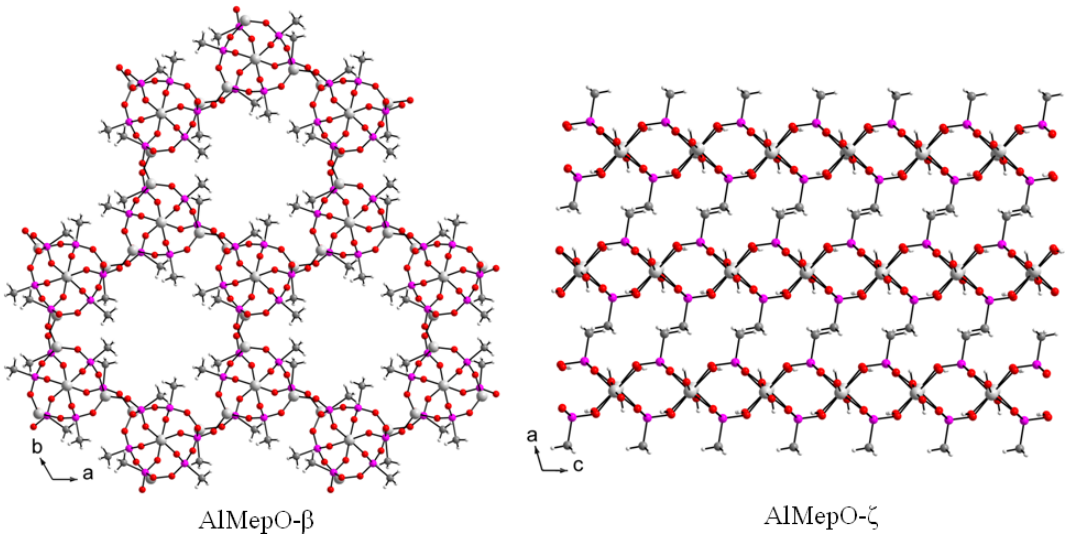

Figure 7. Two types of crystal structures of aluminum methylphosphonates obtained by varying the pH of the reaction[44-47]

Metal ion coordination

The metal ions used to form the metal phosphonate influences the structure formed by both the resulting metal coordination and geometry. For divalent and trivalent metal ions coordination geometries with specific ligands are well-known.[39] Versatility in both metal coordination and geometry can be seen with aluminum ions in AlMePO, where it can range from tetrahedral through penta-coordinate to octahedral.[43-47] Varying metal coordination and geometry makes the number of materials that can be synthesized very large.

Divalent metal phosphonates provide interesting examples on the type of metal vs. structure relationship. Isostructural layered materials were found to be formed in reactions of divalent metals (Mn, Zn, Co and Mg) phenyl and alkyl phosphonates. The metal ions were six-coordinate with formula $M(O_3PR)\cdot H_2O$ (R = phenyl or alkyl).[52-57]

However, the layered structure of the copper phosphonates, $Cu(O_3PR)\cdot H_2O$ (R = phenyl or methyl), differs from other divalent metal phosphonates with similar composition(Figure 8).[58] The copper atoms are five coordinate with a distorted tetragonal pyramidal geometry.[39]

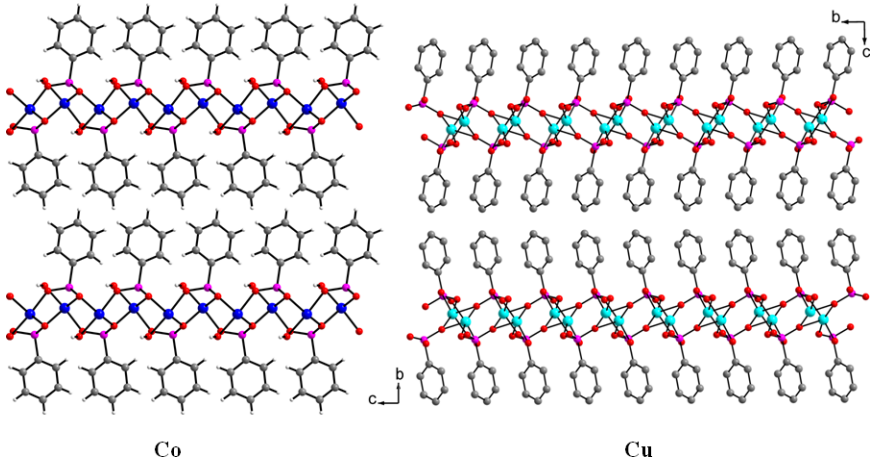

Figure 8. A structural comparison of $Cu(O_3PR)\cdot H_2O$ (right) with the general structure of other transition metal phosphonates, $M(O_3PR)\cdot H_2O$ (M = Co, Zn, Mg and Mn) (left)[58,59]

The crystal structures of tin(II) phosphonates also provide an interesting insight into the influences of metal atoms.[60,61] The lone pair on the tin atom influences the resulting structure of the compound. A different layered structure was found for a tin(II) phenylphosphonate, $Sn(O_3PC_6H_5)$, than other divalent metal phosphonates.[60] However, similar layers were found when the tin(II) phenylphosphonate was extended by using the phenylenediphosphonic acid (Figure 9). The crystal structure of $Sn_2(O_3PC_6H_4PO_3)$, is found to be a double layered structure.[61] Both $Sn(O_3PC_6H_5)$ and $Sn_2(O_3PC_6H_4PO_3)$ have

a three-coordinated metal ion. The tin (II) atom has a trigonal pyramidal geometry of SnO_3, where the lone-pair occupies the pyramidal position and is directed in intralayer.

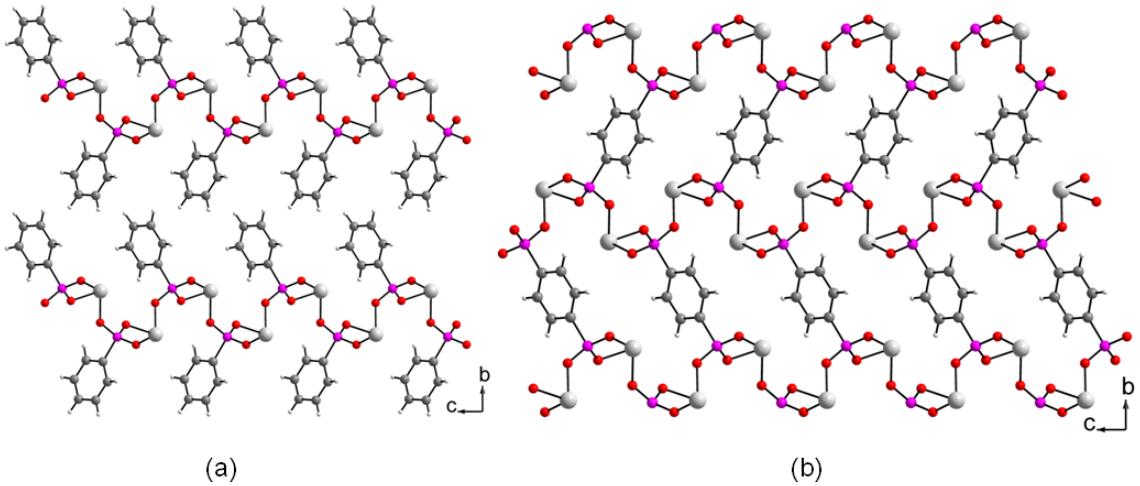

Figure 9. View of the crystal structure of $Sn(O_3PC_6H_5)$ (a) and $Sn_2(O_3PC_6H_4PO_3)$ (b)[66,61]

Analogous structural and physical properties may be expected for tetravalent metals as well, but mixed results have been found.[62-67] Similar synthesis of zirconium and tin phenylenediphosphonate\phosphate hybrids results in porous semi-crystalline materials.[64] These materials are being investigated as ion-exchangers. Two different types of adsorption isotherms were observed. The N_2 adsorption isotherms for the zirconium hybrid were generally characterized as a modified Type II isotherm with a small H4 hysteresis loop while for the tin(IV) hybrid the N_2 adsorption isotherm was characterized as a Type I isotherm with a small H4 hysteresis loop.[64] The differences in

pore structures are a reflection on the variation in structures of the materials due to the change in metal ion.

Metal ion size

The size of the metal ion also influences the resulting structure. Recently, Rao and Vidyasagar reported the structures of alkali metal ethylenediphosphonates (Figure 10).[68] It can be clearly seen, that the structure changes with increase in metal ion size. The pillared architecture is seen for both lithium and sodium ions, but with increase in the metal ion size more dense structures form. Decrease in amine intercalation was also observed with increase in metal ion size in these materials.[68] However, the pillared architecture is not formed for the crystal structure of $Na(HO_3PCH_2PO_3H_2)$.[69] The structure more closely resembles the densely packed larger alkali metal ethylenediphosphonates. Therefore not only is the size of the metal ion important in the resulting structure, but the characteristics of the ligand, also have a large influence.

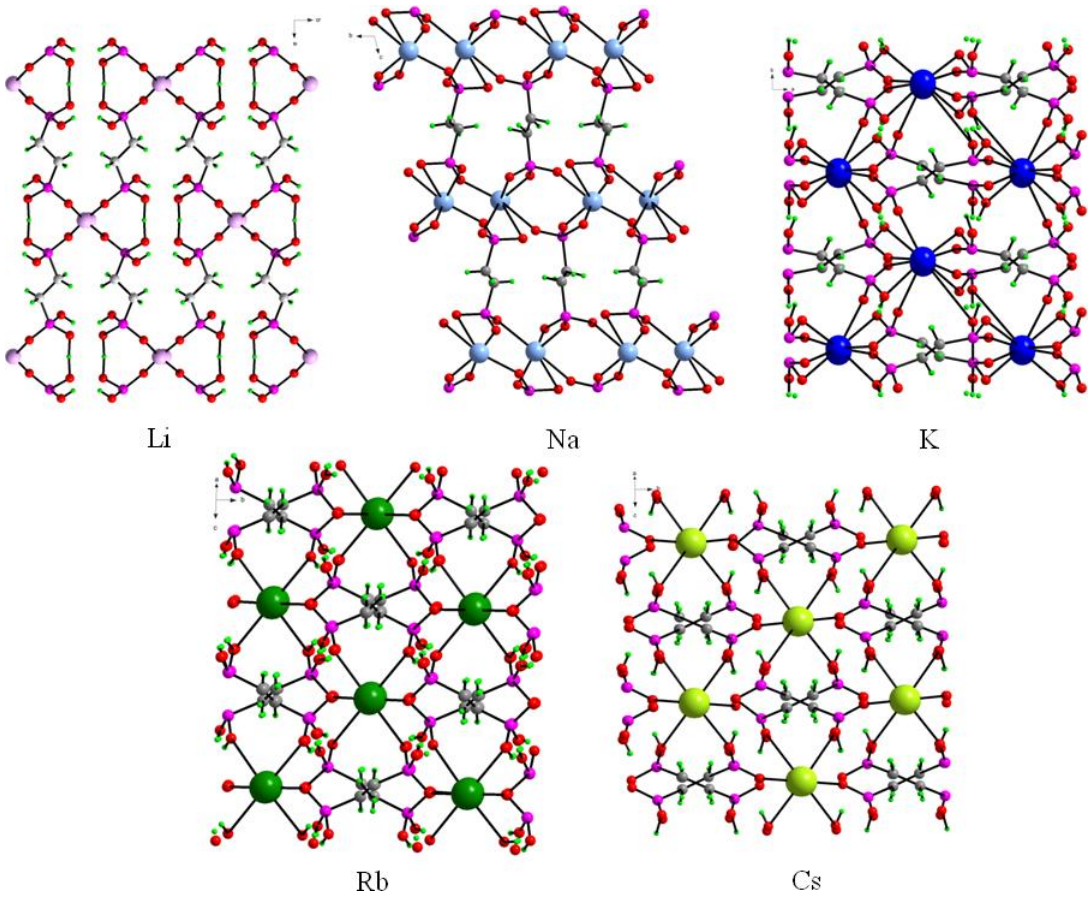

Figure 10. Crystal structures of alkali metal ethylenediphosphonates[68], $M(HO_3PC_2H_4PO_3H_2)$ M = Li^+, Na^+, K^+, Rb^+ and Cs^+.

Metal ion influence on crystallinity

The choice of metal ion is important due to the large influence on crystallinity of the synthesized metal phosphonantes and therefore the method and difficulty in their structure determination. The knowledge of the product structures is very important for better understanding of their properties and the improvement of the materials. In general it has been found that crystallinity decreases with increase metal ion charge. Monovalent metal phosphonates form single-crystalline compounds where the structures

can be determined from in house X-ray diffraction equipment. Divalent metal phosphonates form poorer quality single-crystalline compounds where data collection requires longer exposure times and brighter X-ray diffraction sources. Polycrystalline samples are general obtained for trivalent metal phosphonates; therefore powder X-ray diffraction methods are used for structure determination. The structures, of tetravalent metal phosphonates, are very difficult to determine due to the amorphous nature of the material.

Influence of ligands on the structure of metal phosphonates

The type of phosphonic acid has a large influence in the resulting architecture of metal phosphonates. Better knowledge of these properties can help in improved strategies to obtain highly crystalline open frameworks.

Number of phosphonic acid groups

The number of phosphonic acids on a ligand has an impact on the structure of the compound that results. Monophosphonic acids have resulted in structures with layers, unidiminsional channels and molecular phosphonates. The use of multiple phosphonic acids on a ligand generally result in pillared materials. The extension of layers to pillared structures is generally carried out by using the analogous diphosphonic acid. The interlayer distance is a reflection of the length of the pillar and increase in the length of the pillar increases the interlayer distance. An example is the extension of aluminum phenylenediphosphonic acid to biphenylenediphosphonic acid where the interlayer distance of the pillared materials increase from a d-spacing of ~9.7 Å to a d-spacing of

~13.0 Å, respectively. Pillared materials generally have low porosity due to the short distances between the pillars.

The ligand 1,3,5-benzene triphosphonic acid (BTP) has resulted in a nontraditional layered structure.[70-72] A three-dimensional framework was found for a CuBTP metal-organic framework (MOF, Figure 11).[72] The compound does not have a traditional inorganic layer; instead the layers consist of columns of dimers connected by Cu^{2+} ions. The Cu^{2+} ions have square pyramidal geometry and are coordinated to water molecules, which are directed into the channels. The three-dimensional framework is formed by a second Cu center bridging the layers together. Layered materials were found for LaBTP (LBP-II) and ZnBTP (PCMOF-3) to have the same non-traditional inorganic layer.[70,71] The geometry of the ligand seems to restrict the traditional pillared structure.

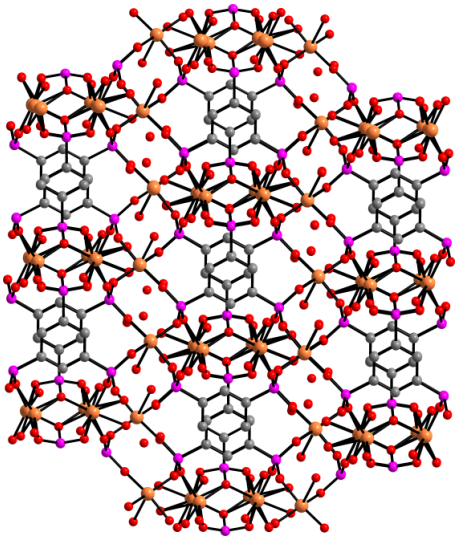

Figure 11. The 3D framework formed from Cu ions and the ligand BTP[72]

Ligand conformation

Influences on the structure can also be seen with changes in conformation of the ligand. The orientation of the phosphonic acids for odd and even numbered alkyldiphosphonic acids differ due to the conformation of the carbon chain (Figure 12). Two different structures were obtained for Zn alkyldiphosphonates when changing from odd to even numbered alkyl chains.[73] An anionic three-dimensional Zn MOF, $[(NH_4)_2Zn_3(O_3P(CH_2)_3PO_3)_2]$, with ammonium ions in the channels was synthesized using propylenediphosphonic acid; however, an anionic pillared layer was obtained from the synthesis with butylenediphosphonic acid[73]. The difference in the resulting structures is due to the conformation of the ligand, which affects the orientation of the phosphonic acid and thereby the M-O bonding scheme.

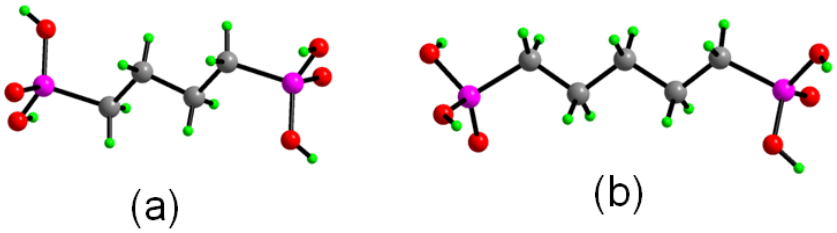

Figure 12. Different orientations of the phosphonic acids in alkyl chains can be seen in even (a) and odd (b) alkyl chains

Bulky ligands

Bulky ligands do not generally conform to the pillared architecture due to steric interactions. Bulky monophosphonic acids tend to prevent formation of continuous

inorganic structures (oligomerzation) by restricting the nuclearity of the cages.[5] For first row transition metals, this approach seems to favor tetrametallic cages.[5,24,30,31] Bulky ligands benzyl-, *t*-butyl- and 2,4,6-triisopropylphenyl-phosphonic acids have been used to form molecular phosphonates.[24,30,31]

Heterofunctional ligands

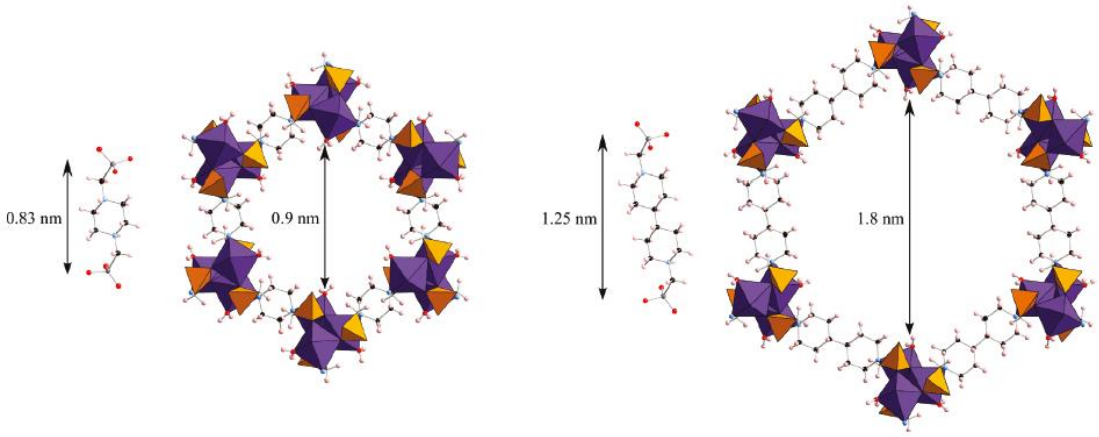

Figure 13. Expansion of the cobalt STA-12 framework to STA-16. Protonation of the amine and the geometry of the ligand results in an open framework[74*]

Heterofunctional ligands can add both functionality to the pore structure, but also influence the structure of the material. These ligands have multiply, different functional groups. Several interesting functional groups that have been incorporated in ligands containing phosphonic acids are amino groups[75-80], carboxylic acids[75,81,82], nitro[75] and

*Figure 13 reprinted with permission from "Extending the Pore Size of Crystalline Metal Phosphontes toward the Mesoporous Regiume by Isoreticular Synthesis" by Wharmby, M. T.; Mowat, J. P. S.; Thompson, S. P.; Wright, P. A. J. Amer. Chem. Soc. **2011**, 133, 1266-1451, Copyright 2011 by American Chemistry Society.

sulfonic acids[83], etc. The use of aminophosphonic acids have shown a wide range of structural arrangements with some resulting in open framework materials. This may be due to both the placement of the amino group in the ligand and its ability to be protonated. Recently, Paul Wright and coworkers published isoreticular frameworks (Figure 13) using N,N'-piperazinebis(methylenephosphonic acid) and N,N,N'-4,4'-bipiperidinebis(methylenephosphonic acid)).[74,84,85] The pore size increased from 0.9 nm to 1.8 nm by increasing the length of the ligand. To balance charges the amino groups are protonated. These materials have permanent porosity and coordinatively unsaturated metal sites upon loss of coordinated water, which is extremely important for gas adsorption applications.

The structures resulting from the use of carboxyphosphonic acids are interesting because the chelating ability of the different acids groups with respective to the metals is different.[75,81,82,86] It has been found that at low pH values the carboxylic group is protonated therefore not bonded to a metal atom. While at higher pH values, both groups are deprotonated and bond to metal atoms.[86] Additionally, the pKa values are lower for the two exchangeable protons on the phosphonic group than for the exchangeable proton on the carboxylic group. These differences result in multiply combinations of bonding modes for both acid groups and thereby an infinite number of possible structures.

Post-synthetic modifications

Post-synthetic modification can be used to functionalize the pore with additional chemical groups. Sulfonation of metal phosphonate hybrids resulted in strong Brönsted

acid materials.[10,83] Sulfonation of the phosphonate groups in zirconium and titanium hybrids resulted in conductivities as high as 1.3×10-1 $\Omega^{-1}cm^{-1}$ at 5 ^{o}C with 85 % RH.[83]

Synthetic "tricks" to favor the formation of non-pillared materials

This section highlights some useful "tricks" that may give non-pillared structures, while using the same ligands which traditionally have given pillared architectures. Additionally, it discusses templates/structure-directing agents, which have been highly successful in synthesis of porous materials.

Brönsted acids and esters

As previously mentioned, the pillared architecture is favored due to the tetrahedral geometry of the phosphonic acid and the multiply bonding modes which encourages continuous nucleation of the inorganic structure. However, by careful control of the synthetic conditions one of the exchangeable protons could remain, thus the nucleation could be stopped in that direction. These materials would be solid Brönsted acids and several examples are published in the literature.[68,69,87,88] Solid Brönsted acids from alkali metal phenyl phosphonates have the composition $M(HO_3PC_6H_5)(H_2O_3PC_6H_5)$ where three acidic protons remain.[88] The same concept could easily be applied to phosphonate esters when used as the starting material. Several porous structures have been published using phosphonate esters in the initial synthesis.[89,90]. These materials involve phenylenediphosphonate esters. The use of this ligand in the acid form has resulted in many pillared architectures.[61,91] However, by eliminating use of one phosphonate oxygen atom the ligand acts similar to a carboxylic

acid group used in MOFs and does not form the same pillared architecture (Figure 14).[89,90]

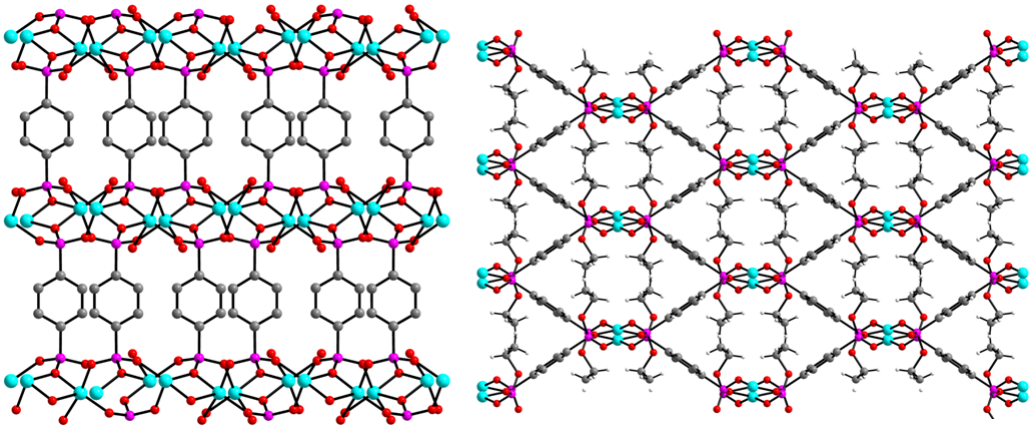

Figure 14. The difference in the resulting structures when the phenylenediphonate ester is used instead of the acid form. Synthesis with the acid resulted in the traditional pillared structure[91] (left) while synthesis with the ester resulted in the non-pillared structure[90] (right)

Mixed ligands

The continuous nucleation of the inorganic structure could also be prevented by a small ligand coordinating to the metal ion which does not have additional coordinating groups. These ligands could range from water molecules, fluoride ions, pyridines, to phosphites and phosphates. Incorporation of fluoride ions into metal phosphonates was carried out in zirconium phosphonates by using HF as a mineralizer[92]. Similarly, a water molecule can coordinate to one metal site restricting continuous growth in that direction. These materials exhibit reversible dehydration behavior. This process has been observed

for iron and aluminum phosphonates with coordinating water molecules.[93,94] Without rearrangement of the metal coordination upon loss of water molecules, unsaturated metal centers could occur which have potential as catalysts.

The mixed ligands system where amino groups have been used, have also been successful in developing molecular phosphonates.[32,34,95,96] Additionally, mixed ligand systems where both ligands have multiple coordinating groups can lead to non-pillared architectures. Kong and coworkers published several examples where addition of either 4,4′-bipyridine and 4,4′-trimethlyenedipyridine with BTP resulted in non-pillared structures.[97] Another recent example provides a one-step hydrothermal synthesis resulting in 2 three-dimensional Co(II)4-pyridyltetrazolate/phosphate systems.[98]

Template molecules

Addition of templates/structure-directing agents can also help form porous structures. This technique has been widely used in zeolites using organic templates which can be removed later by heating the sample to high temperatures.[18,19,99] Thereby different size pores could be developed by using different size structure-directing agents. This method has been successful in metal phosphonates; however, other procedures maybe required to remove organic compounds since heating to very high temperatures can often cause decomposition of the material. More recent examples involving iron, cobalt and zinc phosphonates have been published.[100-104] A series of hydrogen bonded networks made from chains of zinc 1-hydroxyethylidene diphosphonates were used to form channels filled with alkylamines (structure-directing agents)(Figure 15).[100] The study varied the chain length of the alkyl amine which changed the structure and size of

the channels. A layered structure was found for a Fe phosphonate with ethylenediamine in between the layers. Interestingly the phosphonate ligand used was a heterofunctional ligand with both an alcohol and carboxylic acid as additional functional groups.[101]

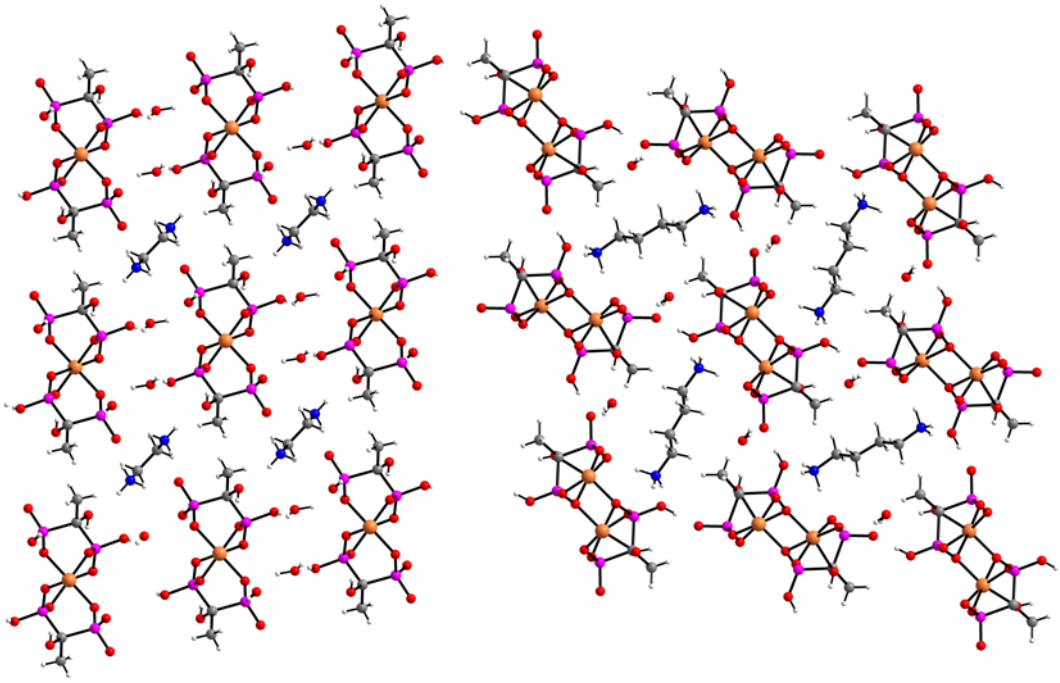

Figure 15. The crystal structures for Zn 1-hydroxyethylidenediphosphonates using ethylenediamine (left) and butylenediamine (right). The size of the channels and the structure change due to the use of different amines[100]

Conclusions

Metal phosphonates have a great future in modern chemistry due to the variety of possible applications.[5] These materials have found uses as catalysts[62,63,105,106], ion-exchangers[64,107,108] and continue to find uses in drug delivery[109], proton conductors[70,110] and in gas storage[111]. Phosphonic acids strongly coordinate to a wide range of metals and

show both chemical and high thermal stability which makes them advantageous over carboxylate analogues.

However, in the past the semi-crystalline nature hinders a complete understanding of the property-structure relationship, in contrast to metal-organic frameworks (MOFs) and zeolites with high crystalline properties. Different synthetic techniques and new ligand designs are providing new opportunities to develop highly crystalline, porous metal phosphonates with regular ordered pore structures (MOFs).

Additionally, the capability to determine the crystal structure from small, poorly diffracting crystals and semi-crystalline powders has improved due to brighter diffraction sources. This leads to a better understanding of the property-structure relationship and improved design of future materials. However, a delicate balance in functionality and crystallinity is needed for the UMOFs due to the pillared structure. More, highly crystalline pillared materials will have less growth defects and therefore less porosity. The pillared structure is dominate for many metal phosphonate materials thereby making the ability to obtain highly crystalline, functional, nonpillared porous materials very challenging.

Scope of study

Our goal is to investigate methods to develop highly crystalline, functional, nonpillared porous materials using rigid aryl phosphonic acids: 4,4-monopheneylenediphosphonic acid (MPDPA), 4,4-bipheneylenediphosponic acid (BPDPA), and 1,3,5-benzene triphosphonic acid (BTP). Both MPDPA and BPDPA generally result in pillared structures due to the linear geometry.[61,91,112,113] In order to

develop a porous structure for these ligands, the traditional inorganic layer can not be formed. The ligand BTP has the potential to develop many interesting MOFs. It has resulted in a three-dimensional Cu based MOF[72] and is analogous to the 1,3,5-benzene carboxylic acid which was used to synthesize many MOFs[114-117].

Chapter II and III presents the results from the investigation of monovalent metal phosphonates and their development to "non-traditional" structures. Chapter II details the development from layered to pillared structures, while Chapter III details the transition from pillared to "non-traditional" structures by the use of template molecules.

Chapter IV presents the hydrothermal synthesis of ZnBTP using two different amines as template molecules and the ligand BTP to prepare single crystals of an isostructural anionic MOF. It describes the reversible dehydration process exhibited by ZnBTP.

Chapter V presents the investigation of aluminum 4,4-monophenylenediphosphonates which resulted in three highly crystalline compounds $Al(H_2O)(O_3PC_6H_4PO_3H)$, $Al_4(H_2O)_2(O_3PC_6H_4PO_3)_3$ and $Al_4(O_3PC_6H_4PO_3)_{2.84}(OH)_{0.64}\cdot(H_2O)_4$. These materials exhibit reversible dehydration behavior which has a dramatic influence on permanent porosity of the material. The stability of the dehydrated phase is a result of the geometry of the aluminum atom, which in some cases has coordinatively unsaturated metal sites.

Chapter VI presents the investigation of aluminum 4,4-biphenylenediphosphonates which resulted in four different compounds $Al_4(O_3PC_{12}H_8PO_3)_3\cdot 8.75H_2O$, $Al(O_3PC_{12}H_8PO_3)_{0.5}(OH)\cdot 0.75H_2O$, $Al_4(O_3PC_{12}H_8PO_3)_{2.46}$

$(HPO_3)_{1.08}\cdot 7(H_2O)$, and $Al_4(O_3PC_{12}H_8PO_3)_{2.46}(HOPO_3)_{1.08}\cdot 7(H_2O)$ The materials were developed with the concept to be ion exchangers. Evaluation of metal ion affinities was carried out.

CHAPTER II

STRUCTURAL DIFFERENCES OF METAL BIPHENYLENEDIPHOSPHONATES WITH CHANGE IN THE ALKALI METAL*

Introduction

Metal phosphonate chemistry is an ever-expanding discipline which had its beginning in 1978 with the synthesis of a family of zirconium phosphonates.[118] Extensive work has now been reported on the broad sampling of divalent, trivalent, and tetravalent cations.[119-123] However, very little has been reported on phosphonates of monovalent ions.[68,69,88,124] Recently, Rao and Vidyasagar[88] reported on the series of group 1 phenyl phosphonates. The general formula for this group of compounds is $M(HO_3PC_6H_5)(H_2O_3PC_6H_5)$. All the compounds are layered except lithium which has the same composition but form one-dimensional chains. The intriguing aspect of these compounds is that one of the phosphonate ligands retains both the protons yet bonds to the metal ions by chelation. Another interesting aspect of these compounds is that they have three protons for every metal ion. This makes Brönsted acids that are able to intercalate amines.[88] No structures of the amine intercalates were reported. It should also be mentioned that there are three different structures among the five alkali metal

*Reprinted in full with permission from "Structural Differences of Metal Biphenylenediphosphonate with Change in the Alkali Metal" by Kinnibrugh, T. L.; Garcia, N.; Clearfield, A. *J. Solid State Chem.* **2012**, 187, 149-158, Copyright 2012 by Elsevier.

phenyl phosphonates. The principal driving force for the change in structure appears to be the increase in the size of the alkali metal ions.

Subsequently, the same authors prepared derivatives of the alkali metal ions with ethylene diphosphonate, $H_2O_3PC_2H_4PO_3H_3$ [68]. Interestingly, the products are three-dimensional of composition $M(HO_3PC_2H_4PO_3H_2)$, retaining three protons per alkali cation. The authors envision these compounds as strong Brönsted acids. Indeed, these phosphonates do intercalate and deintercalate ammonia. Of the seven such compounds prepared, thalium and ammonium along with the five alkali cations, four structure types were found. A different type of three-dimensional compound was formed from the monocarbondiphosphonic acid, $Na(HO_3PCH_2PO_2H_2)_n$.[69]

Our interest lies in whether these compounds can be prepared in porous form. If the pores were uniform, they would be lined with protons that could act as Brönsted acid catalysts, as ion exchangers and as base intercalation media. The unlikelihood of this porous form is attributed to the expected high solubility of such compounds due to the ionic nature of the cations. However, one may not have expected that the alkali metal ions would form supramolecular chains and layers rather than single molecular compounds with displacement of the protons by the metal ions forming strictly ionic species. One possible method of decreasing the solubility is to crosslink the layers into three-dimensional compounds with highly hydrophobic groups.

Experimental section

Materials

All commercially available reactants ($LiNO_3$ Aldrich, $Na_2CO_3 \cdot H_2O$ 99.5% Baker Analyzed, K_2CO_3 99% EMD, Rb_2CO_3 99% and Cs_2CO_3 99% Alfa Aesar were used as purchased without further purification unless specified. Toluene was dried on 3 Å molecular sieves. 4,4'-Biphenylenediphosphonic acid was synthesized according to previous methods.[10]

*Hydrothermal synthesis of $Li(HO_3PC_{12}H_8PO_3H_2)$, compound **1.2***

The hydrothermal reaction for lithium was carried out at 160 ^oC for 5 d with a 1:2 ratio of 4,4'-biphenylenediphosphonic acid (0.6 mmol, 0.1886 g) to lithium nitrate (0.6 mmol, 0.0828 g) in 5 mL of DI water. The reaction was carried out in a PTFE-lined pressure vessel of 12 mL capacity resulting in a white powder. The reaction resulted in a 74% yield based on the starting amount of ligand. Starting with the resulting powder (0.143 g), a further hydrothermal reaction was carried out at 180 ^oC in 4 mL water for 1 week to obtain single crystals. ICP-AES analysis gave a P/M ratio of 2.1.

*Hydrothermal synthesis of $M(HO_3PC_{12}H_8PO_3H_2)$, compounds **2.2-5.2***

The hydrothermal reactions for cations sodium through cesium were carried out at 145 ^oC for 7 d with 1:1 ratio of 4,4'-biphenylenediphosphonic acid (0.05mmol, 0.0158 g) to metal carbonate (0.05mmol) in 6 mL DI water. All reactions were carried out in a PTFE-lined pressure vessel of 12 mL capacity. The reactions resulted in single crystals for all cations. Larger reactions with the same cations (4,4'-biphenylenediphosphonic acid (0.6mmol, 0.1884 g)) were carried out at 180 ^oC for 3 d in 5 mL of DI water with an

expected 50% yield. The compounds were then washed with ethanol and dried in an oven at 65 ^{o}C overnight. [Yields based on the starting amount of ligand for compounds **2.2-5.2** respectively: 23.9%, 13.4%, 15.5%, 17.9%]. The yields were low due to solubility of the product. Slow evaporation of the products results in higher yields but is contaminated with reactants. Electron microprobe analysis gave P/M ratios of 1.8, 1.8, 1.9, and 2.1 for compounds **2.2-5.2** respectively.

*Microwave synthesis of $Na_2(HO_3PC_{12}H_8PO_3H)$, compound **6.2***

An CEM Explorer®12 Hybrid microwave was used for the microwave synthesis. Reactions with a 1:1 ratio of 4,4'-biphenylenediphosphonic acid (0.15mmol, 0.0458g) and sodium carbonate (0.15mmol, 0.0186 g) were heated at 145 ^{o}C in 1 mL of water for 7 h using microwave radiation (Average 18 W, max. 50 W). The product was washed with ethanol and dried in an oven at 65 ^{o}C overnight. A similar reaction was run for cesium biphenylenediphosphonate resulting in compound **6.2**. Single crystals were obtained only for the cations sodium (**6.2**) and cesium (**5.2**). [55% yield based on the starting amount of ligand] Electron microprobe analysis gave a P/M ratio of 0.9.

*Synthesis of $Na_2(O_3PC_{12}H_8PO_3H)(H_2NC_2H_6)(H_2O)_8$, compound **7.2***

The solvothermal reaction was carried out in 5 mL of dry toluene, 60 μL of DI water, 0.0106 g (0.086mmol) Na_2CO_3•H_2O, 0.0166 g (0.05 mmol) 4,4'-biphenylenediphosphonic acid hydrate, and 60 μL dimethylformamide and heated for 7 d at 120 ^{o}C. The reaction was carried out in a PTFE-lined pressure vessel of 12 mL capacity. A single crystal was selected from the mother liquid.

Characterization

PXRD patterns were recorded using a Bruker D8-Focus Bragg-Brentano X-ray powder diffractometer (Cu Kα radiation, λ = 1.54178 Å) operating at room temperature. Single crystal data were collected on a Bruker-AXS Apex II CCD X-ray diffractometer (Mo Kα radiation, λ = 0.71073 Å) operating at 110 K. The structures were solved by direct methods and refined by the full-matrix least-squares technique against F^2 with the anisotropic displacement parameters for all non-hydrogen atoms. Hydrogen atoms were added in idealized positions and refined using a riding model with $U_{iso} = nU_{eq}$ for carbon atoms connected to the relevant H-atom where n = 1.5 for methyl and n = 1.2 for other H-atoms except of compound **6.2**. Hydrogen atoms on water molecules and amine nitrogen were found using a difference map and refined using a riding model with $U_{iso} = nU_{eq}$ where n = 1.5 except for two water molecules in compound **7.2**. Anisotropic displacement parameters were established for all non-hydrogen atoms. The following programs were utilized: cell refinement and data reduction: SAINT[125]; semi-empirical method for absorption correction: SADABS[126]; structure solution: SHELXTL[127]; molecular graphics: ORTEPII[128], Mercury[129].

Thermogravimetric Analysis (TGA) was performed under airflow from room temperature to 1000 ^{o}C with a heating rate of 10 Kmin^{-1} on a TGA Q500 apparatus. An additional TGA for compound **1.2** was also performed under similar condition but instead under nitrogen gas flow. Surface area measurements were performed on an Autosorb-6 (Quantachrome) unit using nitrogen and hydrogen adsorption at liquid nitrogen temperature. Samples were pre-calcined at 150 ^{o}C overnight and then degassed

at 180 ^{o}C for 20 h. The data were analyzed using the software supplied by the Quantachrome Corporation and surface areas were calculated based on the Brunauer-Emmett-Teller (BET) model.

For elemental analysis of the compounds, both ICP and electron microprobe techniques were used. Quantitative compositional analyses for compounds **2.2**-**6.2** were carried out on a four spectrometer Cameca SX50 electron microprobe at an accelerating voltage of 15 kV at a beam current of 10 nA. All quantitative work employed wavelength-dispersive spectrometers (WDS). Analyses were carried out after standardization using well-characterized compounds or pure elements. Qualitative analyses (spectra) were obtained with an Imix Princeton Gamma Tech (PGT) energy dispersive system (EDS) using a thin-window detector. To prepare the samples for ICP-AES at Anderson Analytical, 0.0110g of compound **1.2** was dissolved in 20 μL of conc. HCl and 20 mL of DI water which then was shaken overnight.

Results

We have hydrothermally synthesized and structurally characterized five monovalent metal (M^+ = Li, Na, K, Rb, Cs) 4,4'-biphenylenediphosphonates, $M(HO_3PC_{12}H_8PO_3H_2)$, **1.2**-**5.2**, with three-dimensional structures. The resulting compounds have a 1:1 ratio of metal to ligand, but a 1:2 ratio of metal to phosphonic acid groups. In concert with the previous publications, the retention of three of the original four protons of the ligand imparts Brönsted acidity to these compounds.[68,88] Crystallographic data for the five compounds are presented in Tables 1 and 2. All of the compounds are three-dimensional including the lithium compound which formed linear

chains as the phenylphosphonate. In addition to these five compounds, a second sodium derivative (compound **6.2**) was prepared utilizing microwave radiation and a third potentially more porous version was prepared by addition of an amine as a reactant (compound **7.2**).

Crystal structure descriptions

Although the values of the triclinic unit cell parameters are similar for compounds **2.2** to **5.2,** several different structural types were found. Each centrosymmetric triclinic unit cell has two unit formulas per unit cell while the centrosymmetric monoclinc unit cells for compounds **1.2** and **6.2** have four unit formulas present. The monoclinic unit cell parameters found for compounds **1.2** and for $Li(HO_3PC_2H_4PO_3H_2)$[68] doubles the *a*-axis, thereby including two layers in the unit cell. The sodium phenylphosphonate compound synthesized by Rao and Vidasagar [88] has similar unit cell parameters to our compound **2.2**, except the *c*-axis is slightly longer. This is attributed to the van der Waals gap between the layers of sodium phenylphosphonates, whereas in compound **2.2** the phenyl groups are connected.

Table 1. Crystallographic data, details of data collection and refinement for compounds **1.2-5.2**

	1.2	**2.2**	**3.2**	**4.2**	**5.2**
Formula	$Li(HO_3PC_{12}H_8PO_3H_2)$	$Na(HO_3PC_{12}H_8PO_3H_2)$	$K(HO_3PC_{12}H_8PO_3H_2)$	$Rb(HO_3PC_{12}H_8PO_3H_2)$	$Cs(HO_3PC_{12}H_8PO_3H_2)$
M_r	320.09	336.14	352.25	398.62	446.06
Crystal color, habit	Colorless, plate	colorless, plate	colorless, plate	colorless, plate	colorless, plate
crystal size (mm^3)	0.20×0.09×0.02	0.25×0.20×0.03	0.22×0.15×0.03	0.36×0.24×0.04	0.21×0.05×0.03
T(K)	110	110	110	110	110
crystal system	Monoclinic	Triclinic	Triclinic	Triclinic	Triclinic
space group	C 2/c	P-1	P-1	P-1	P-1
a (Å)	27.368(3)	5.716(4)	5.879(5)	5.872(2)	6.1734(4)
b (Å)	8.6016(9)	7.905(6)	7.778(7)	7.680(3)	7.5322(5)
c (Å)	5.4046(6)	14.366(10)	15.134(13)	15.242(5)	15.3998(10)
α (^{o})	90.00	88.100(8)	79.077(12)	101.822(3)	102.2190(11)
β (^{o})	98.025(2)	84.499(8)	86.606(11)	91.516(4)	94.2830(10)
γ (^{o})	90.00	82.628(7)	85.822(12)	93.709(4)	94.3050(10)
V($Å^3$)	1259.8(2)	640.6(8)	676.9(10)	670.8(4)	694.86(8)
Z	4	2	2	2	2
ρ_{calc} (g cm^{-3})	1.688	1.743	1.728	1.974	2.132
2θmax(^{o})	58.2	52.8	54.7	52.0	58.4
μ (Mo Kα) (cm^{-1})	0.369	0.398	0.653	3.953	2.919
Min/max Trans factors	0.9312/0.9936	0.9059/0.9897	0.8697/0.9807	0.3342/0.8579	0.5793/0.9175
total reflections	9331	6252	7780	5184	14177
unique reflections	1607	2486	3065	2379	3333
observed reflections [I>2σ(I)]	1438	1313	2121	2590	3115
R_1/ ωR_2	0.0307/0.1183	0.0725/0.1513	0.0409/0.0922	0.0261/0.0645	0.0288/0.0763
no. of parameters	96	184	190	191	190
S	1.059	1.014	1.002	1.054	1.055
Diff. Density max/min	0.439/-0.406	0.846/-0.599	0.497/-0.423	0.454/-0.405	1.956/-1.874

Table 2. Crystallographic data, details of data collection and refinement for compounds **6.2** and **7.2**

	6.2	**7.2**
Formula	$Na_2(HO_3PC_{12}H_8PO_3H)$	$Na_2(H_2O)_7(O_3PC_{12}H_8PO_3)(H_2N(CH_3)_2)_2 \cdot H_2O$
M_r	358.12	547.33
Crystal color, habit	colorless, plate	colorless, plate
crystal size (mm^3)	0.20×0.16×0.02	0.25×0.20×0.03
T(K)	110	110
crystal system	Monoclinic	Triclinic
space group	C 2/c	P-1
a (Å)	28.28(2)	8.369(3)
b (Å)	7.547(6)	9.522(5)
c (Å)	6.390(6)	16.5383(15)
α (°)	90.00	78.33(4)
β (°)	101.26(2)	83.71(3)
γ (°)	90.00	72.19(4)
V($Å^3$)	1337.6(19)	1227.2(8)
Z	4	2
ρ_{calc} (g cm^{-3})	1.778	1.481
2θmax(°)	57.0	57.8
μ (Mo Kα) (cm^{-1})	0.416	0.278
Miniumum/maximum transmission factors	0.9196/0.9917	0.9329/0.9928
total reflections	9347	14440
unique reflections	1692	5802
observed reflections [I>2σ(I)]	1383	4747
R_1 / ωR_2	0.0337/0.0868	0.0442/0.1235
no. of parameters	121	373
S	1.035	1.094
Diff. Density max/min	0.468/-0.388	0.822/-0.547

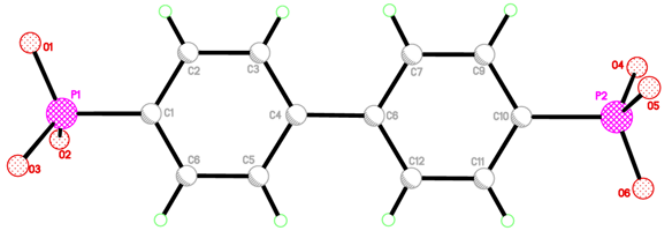

Figure 16. Labeling scheme for biphenylenediphosphonate

Structural similarities for compounds **2.2-5.2** have the M^+ ions approximately confined to the *ab* plane. The inorganic planes (MO_nP_m) are separated by hydrophobic regions of biphenylene groups and the oxygen atoms of phosphonates coordinate to the M^+ ions on both sides of the plane. Compounds **1.2** and **6.2** are similar except M^+ ions are approximately confined to the *bc*-plane instead of the *ab*-plane, because of the choice of their *a*-axes. The bond lengths (Table 3) are similar to those of reported structures in the literature.[68,69,88] The labeling scheme for the 4,4'-biphenylenediphosphonate utilized here is given in Figure 16.

Table 3. Bond distances for the five M(I) biphenylenediphosphonates, (Å)

Compounds					
	1.2	**2.2**	**3.2**	**4.2**	**5.2**
M-O	O1 1.932(2)	O1 2.437(5)	O1 2.756(3)	O1 2.865(2)	O1 3.220(2)
	O1A 1.963(2)	O2 2.485(5)	O2 2.704(3)	O2 2.861(2)	O2 3.067(2)
		O3 2.432(4)	O3 2.926(3)	O3 2.946(2)	O3 3.090(3)
		O4 2.478(5)	O4 2.699(3)	O4 2.980(2)	O3C 3.284(2)
		O5 2.287(5)	O5 2.710(3)	O5 2.819(2)	O4 3.065(3)
		O5D 2.340(5)	O6 2.812(3)	O6 3.178(2)	O4B 3.331(3)
				O6 3.220(2)	O5 3.340(3)
					O6 3.321(3)
M-O*			O3 3.322(3)	O2 3.396(2)	O2 3.430(3)
			O4 3.297(3)		O5 3.410(2)
P1-O1	1.494(1)	1.499(4)	1.556(2)	1.533(2)	1.558(2)
P1-O2	1.563(1)	1.541(4)	1.493(2)	1.496(2)	1.503(2)
P1-O3	1.542(1)	1.554(4)	1.554(2)	1.547(2)	1.527(2)
P2-O4		1.592(4)	1.523(2)	1.511(2)	1.505(3)
P2-O5		1.476(4)	1.562(2)	1.504(2)	1.529(3)
P2-O6		1.542(4)	1.510(2)	1.566(2)	1.563(3)

*long interactions

*Crystal structure of Li($HO_3PC_{12}H_8PO_3H_2$), compound **1.2***

The lithium atom in compound (**1.2**) has half-occupancy in the unit cell and is tetrahedrally bonded to oxygen atoms (O1 and O1A) of four phosphonate moieties as shown in Figure 17. Each tetrahedron (LiO_4), shares an edge with two other tetrahedra forming chains along the *c*-axis (Figure 17a). The metal oxygen bonds are given in Table 2 with the longer bonds represented by a dashed line in Figure 17a. The oxygen atoms O2 and O3 are not involved in metal oxygen bonding. The P-O bond lengths can indicate the degree of protonation of the oxygen atoms and are given in Table 3. The P-O bond lengths indicate that the nonbonded oxygen atoms bear the protons with atom O2 fully protonated and O3 partially protonated. The partial protontation of O3 is due to the half-occupancy of the lithium atom in the unit cell. The chains stack along the *b*-axis and terminate with O-H groups. Thus, hydrogen bonding within the chain (O3-H…O3) and across to neighboring chains (O2-H…O3) is observed (Table 4) forming a weak inorganic layer. The chains are linked together along the *a*-axis by diphosphonic acids forming a three-dimensional structure as seen in Figure 17b.

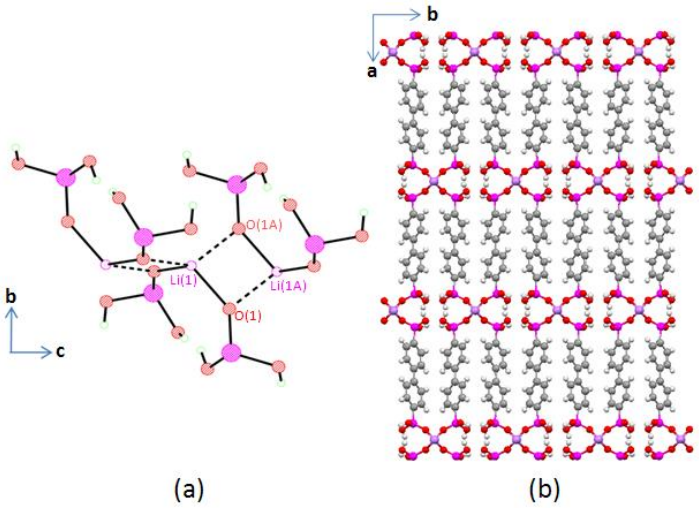

Figure 17. Metal oxygen chain showing the perpendicular 4-member rings (17a) and the crystal packing of compound **1.2** as viewed down the *c*-axis (17b)

Table 4. Hydrogen bond distances for several of the M(I) phosphonates

Compound	O-H…O	Bond Length, Å	symmetry
1.2	O2-H…O3	2.629 (1)	x, 2-y, -½+z
	O3-H…O3	2.434 (2)	-x, y, ½-z
2.2	O2-H…O6	2.561 (5)	1+x, -1+y, z
	O3-H…O6	2.509 (6)	x, -1+y, z
3.2	O1-H…O6	2.468 (3)	-x, 1-y, -z
	O5-H…O2	2.546 (4)	-1-x, 1-y, -z
4.2	O3-H…O5	2.471 (3)	-x, 1-y, 1-z
	O4-H…O1	2.414 (3)	1-x, 1-y,1-z
5.2	O3-H…O2	2.572(2)	x, 1-y, ½+z

*Crystal structure of Na($HO_3PC_{12}H_8PO_3H_2$), compound **2.2***

The sodium compound (**2.2**) has an edge-shared bioctahedral Na_2O_{10} motif, formed from 10 different phosphonate moieties (Figure 18). Each sodium atom in the Na_2O_{10} unit is six-coordinate and bonded to six different phosphonate moieties, thus no chelation is observed. The oxygen atom O6 does not bond to any metal atoms, instead it

forms hydrogen bonds to O2-H and O3-H (Table 4). Each octahedron shares one edge (O5 and O5D) resulting in the edge-shared bioctahedral, Na_2O_{10}, which is corner-connected to eight symmetry equivalent bioctahedra, together forming an inorganic layer in the *ab*-plane (Figure 18a). The layers stacked along the *c*-axis, have an interlayer distance of 14.94 Å. Each inorganic layer has alternating four and eight-membered rings along the *b*-axis. The diphosphonates, in compound **2.2**, cross-links the inorganic layer together forming a regular pillared structure (Figure 18c). Interestingly, neighboring pillars along the a*b*-diagonal are rotated 54^o from each other presumably to reduce strain caused by close contacts from other neighboring pillars (Figure 18b). Noteworthy, the potential C-H..π distances (shortest C-H..π 3.696 Å, 127 ^{o}C) are longer than the van der Waals radii.

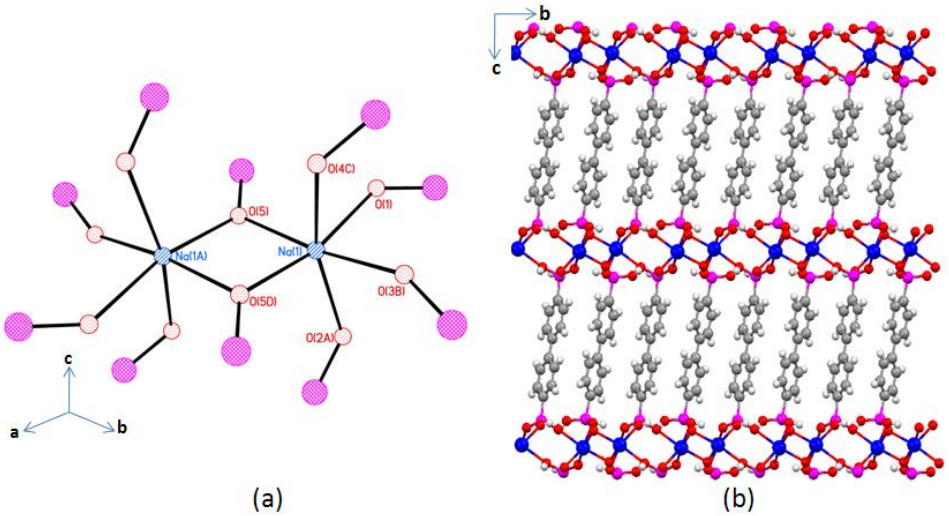

Figure 18. The Na_2O_{10} dimer (18a), neighboring pillars along the a*b*-diagonal (18b) and crystal packing (18c) of compound **2.2** as viewed down the *a*-axis

*Crystal structure of $K(HO_3PC_{12}H_8PO_3H_2)$, compound **3.2***

The potassium compound (**3.2**) consists of six-coordinate metal atoms with the K-O bond distances ranging from 2.699(3) Å to 2.926(3) Å (K1-O3) as shown in Figure 19a and Table 3. The average bond distance is 2.768 Å, which is in agreement with the sum of the ionic radii.[130] Six different phosphonate moieties are bonded to each octahedral potassium atom, three above and three below to form a trigonal prism arrangement. All three oxygen atoms of each phosphonate group are bonded to three different potassium atoms forming chains running long the *a*-axis as shown in Figure 19b. In the figure, the oxygen atoms are seen to bridge across potassium ions. The diphosphonates cross-link the chains as shown in Figure 19c. We note that in the *b* direction the chains terminate with O-H bonds where the shortest metal oxygen distance between neighboring chains is 3.753 Å. The inorganic layer is formed from hydrogen bonding between neighboring chains (Table 4). The biphenylene groups are rotated relative to each other by 54^o as shown in Figure 18b for the sodium structure.

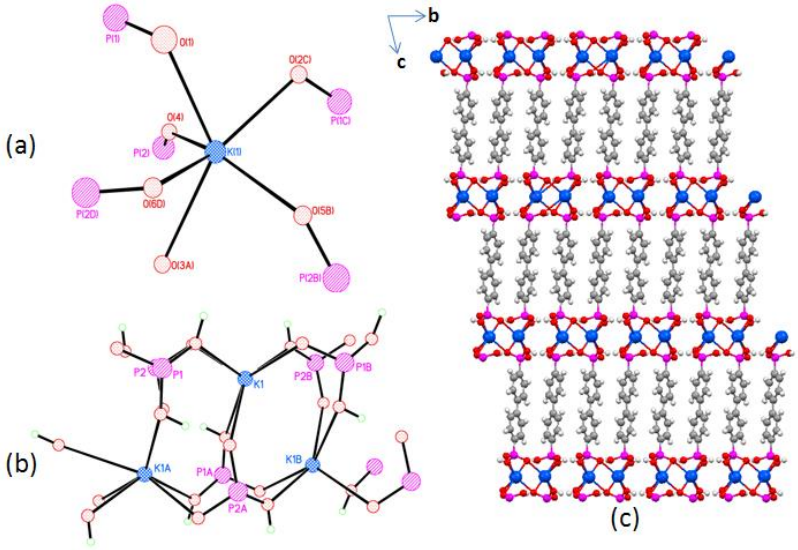

Figure 19. Numbering scheme (19a), top view of the chain made from corner connected octahedra (19b) and crystal packing (19c) for compound **3.2**

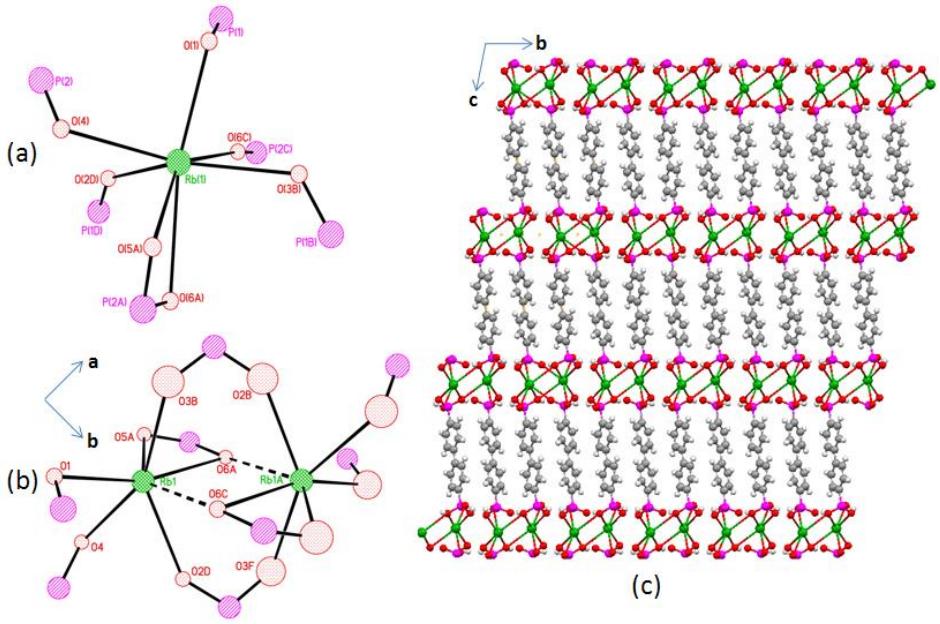

Figure 20. Numbering scheme (20a), dimer Rb_2O_{12} where the dashed lines indicate longer bonds (20b) and crystal packing (20c) for compound **4.2**

*Crystal structure of Rb($HO_3PC_{12}H_8PO_3H_2$), compound **4.1***

The rubidium atom is seven coordinate due to a chelating group (O5-P2-O6) and five additional bonds each from a different phosphonate group (Figure 20a). Two such Rb ions are bridged together by O3-P1-O2 phosphonate groups as shown in Figure 20b to form 8-membered rings. The Rb….Rb distance is 4.18 Å and this is close enough that O6c and O6a each donate an electron pair to an adjacent Rb atom to form a four-membered ring within the 8-membered ring. The P2-O bond distances to Rb in the chelate group are 2.819(2) Å for O5a and 3.178(2) Å for O6a. The donated bond P2-O6c is 3.220(2) Å. The motif shown in Figure 20b is an Rb_2O_{12} unit that then propagates by corner connections to form chains running along the *a* direction. The chains terminate along the *b*-axis with O-H groups where the shortest metal oxygen distance between neighboring chains is 3.518 Å. Hydrogen bonding occurs between chains building a weak inorganic layer, reducing the potential pore size in half (Table 4). As with the potassium compound, the Rb_2O_{12} units are cross-linked by the biphenylenediphosphonates (Figure 20c) in the *c* direction. Similar to both compounds **1.2** and **3.2**, the biphenylenediphosphonates cross-link the chains along the *c*-axis and neighboring pillars along the *ab*-diagonal are rotated 60^o from each other.

*Crystal structure of Cs($HO_3PC_{12}H_8PO_3H_2$), compound **5.2***

The cesium compound (**5.2**) has Cs^+ in an 8-coordinate distorted dodecahedral polyhedron, Figure 21a. The chelating atoms O4 and O5 have bond distances 3.065(3) Å and 3.340(3) Å, respectively. The O4 atom that chelates the Cs^+ ion, then donates to a neighboring Cs^+ ion forming a four-membered ring. In addition, another four-membered

ring is formed by O3 atoms from separate phosphonate groups (Figure 21b). The parallel Cs^+ ions bridged together by two different four-membered rings in the *a* direction, are then connected in the *b* direction by O2-P1-O1 and O2-P1-O3 forming a continuous layer with no gaps between rows (Figure 21c). Similar to compound **2.2**, the inorganic layers are cross-linked by diphosphonates forming a regular pillared structure where pillars are rotated 54^o from each other.

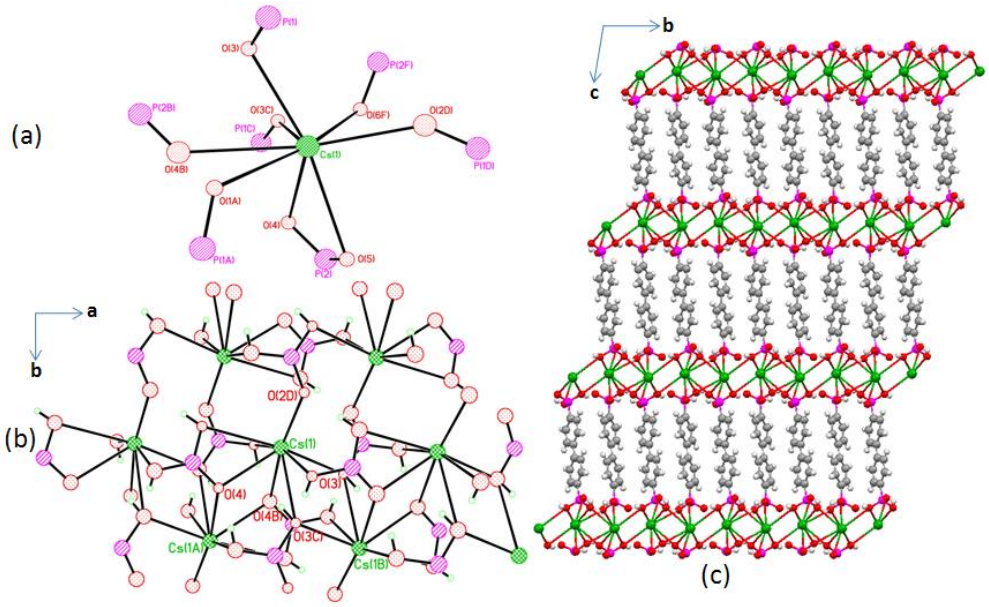

Figure 21. Numbering scheme (21a), top view of the metal layer built from chains of edge-shared dodecahedra linked together by O-P-O(2d) bridges (21b) and crystal packing of compound **5.2** as viewed down the *a*-axis (21c)

*Crystal structure of $Na_2(HO_3PC_{12}H_8PO_3H)$, compound **6.2***

The microwave synthesis resulted in a regular pillared structure formed when layers are cross-linked by the biphenylenediphosphonates for compound **6.2**, but the inorganic layers differ from that of compound **2.2**. There are two symmetry-independent sodium atoms (Na1 and Na2) each with half-occupancy in the unit cell. Each Na^+ ion is bonded to four different phosphonate moieties resulting in a tetrahedral geometry. The 4-coordinate metal is based on consideration of the ionic radii[130] and valence bond sum[131] (Table 4). Oxygen atom O3 is fully protonated and does not bond to any sodium atom. The symmetry independent sodium atoms form an edge-shared dimer, Na_2O_6, where oxygen atoms O1D and O1E form the edge. The dimers are corner connected together by O1-P1-O2 bridges forming alternating four and eight membered rings along the *b*-axis as shown in Figure 22a. Oxygen atom O3 is positioned above the 8-membered ring and hydrogen bonds to atom O2A (Table 5). Neighboring dimers in the *c*-direction share edges building the inorganic layer (Figure 22b). Diphosphonate groups cross-link the inorganic layers along the *a*-axis (Figure 23). As with previous structures, the neighboring biphenylene groups are rotated ~61^o to each other but in the *bc*-direction.

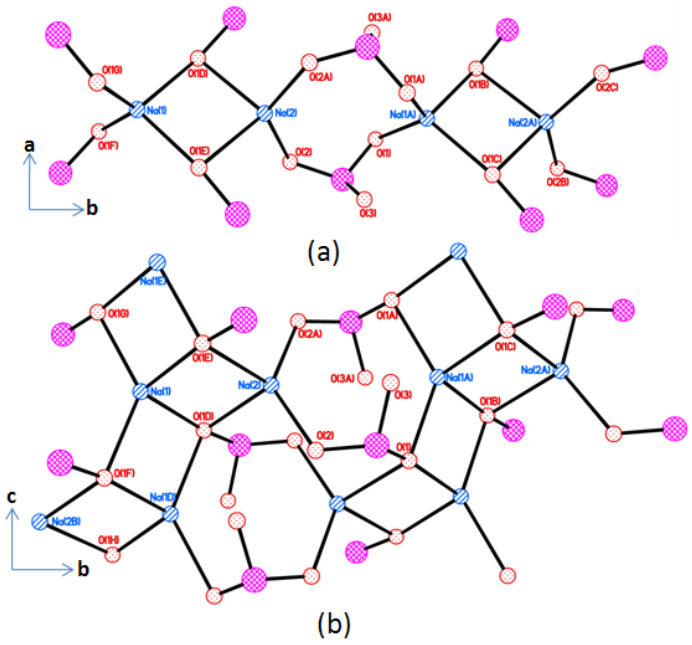

Figure 22. Four and eight-membered rings along the *b*-axis (22a) and a view of the inorganic layer in the *bc*-plane (22b) of compound **6.2**

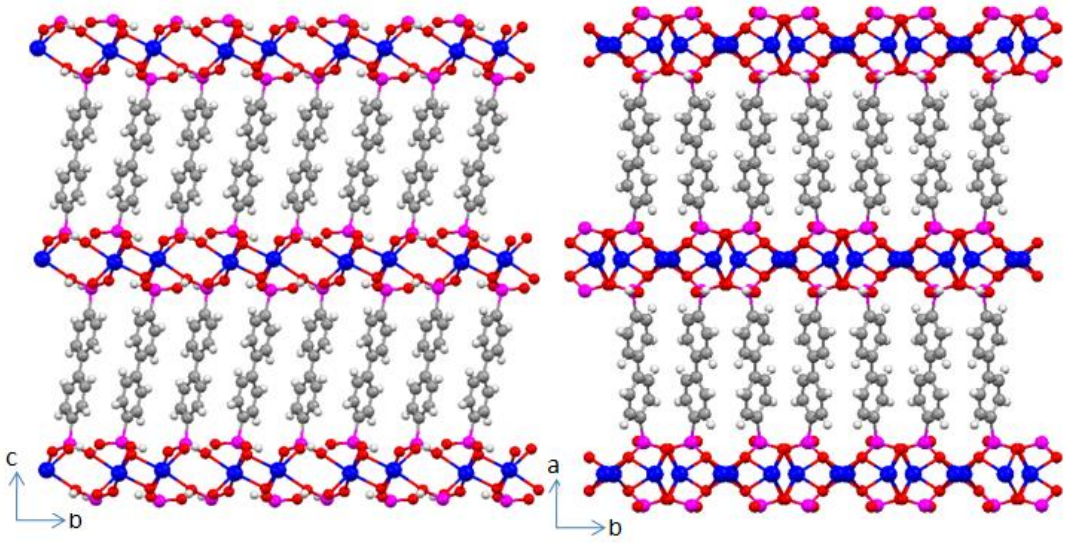

Figure 23. Comparison of the crystal packing for compounds **2.2** (left) and **6.2** (right)

Table 5. Bond distances for compound **6.2**, (Å)

Na1-O9	2.307(2)	Na2-O7A	2.356(2)	Na3-O13A	2.350(2)
Na1-O12	2.309(2)	Na2-O7B	2.356(2)	Na3-O13B	2.350(2)
Na1-O8	2.333(2)	Na2-O8A	2.405(2)	Na3-O10A	2.382(2)
Na1-O10	2.406(2)	Na2-O8B	2.405(2)	Na3-O10B	2.382(2)
Na1-O7	2.735(2)	Na2-O11A	2.454(2)	Na3-O9A	2.410(2)
		Na2-O11B	2.454(2)	Na3-O9B	2.410(2)
P1-O1	1.518(2)				
P1-O2	1.528(2)				
P1-O3	1.530(2)				
P2-O4	1.497(2)				
P2-O5	1.569(2)				
P2-O6	1.511(1)				

*Crystal structure of $Na_2(O_3PC_{12}H_8PO_3H)(H_2NC_2H_6)(H_2O)_8$, compound **7.2***

A three dimensional supramolecular structure was obtained from the addition of N,N-dimethyl formamide as a reactant (Figure 24c). The structure consists of chains built from sodium atoms and water molecules (Table 6). Three symmetry independent sodium atoms were determined where two metal atoms are six-coordinate with an octahedral geometry and the third is a five-coordinate trigonal bipyramidal atom. The six-coordinate sodium atoms have half-occupancy in the unit cell.

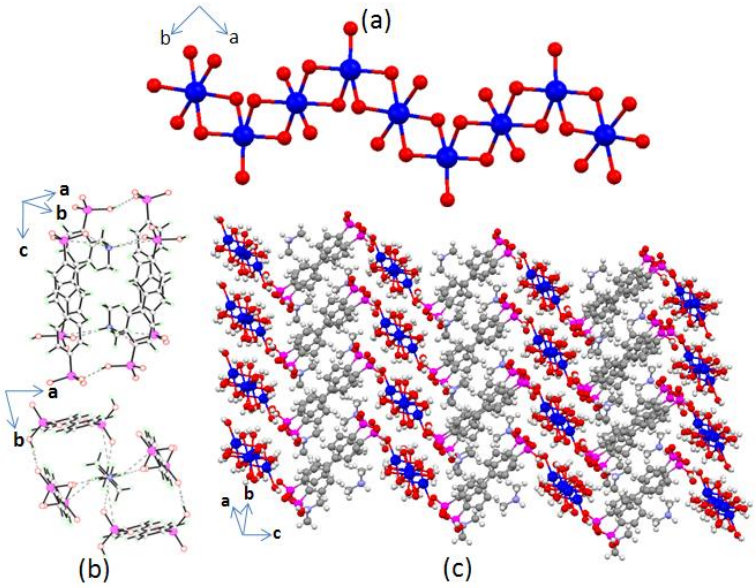

Figure 24. View of the inorganic zig-zag chain (24a) for compound **7.2**. Two perspectives of the cavity for compound **7.2** are presented, showing two dimethyl ammonium ions inside the cavity (24b). Crystal packing of the supramolecular structure (24c). Hydrogen bonding between the chains and the diphosphonic acids are not shown for clarity

The chains have a zig-zag form where the five-coordinate metal atom is on the corner. The six-coordinate sodium atoms connect the corners together by forming four-membered rings with each five-coordinate sodium atom thus forming the zig-zag chains (Figure 24a). The biphenylene diphosphonic acid molecules hydrogen bond (Table 7) to the chains (Figure 24c) and free water molecules, forming cavities with dimensions 8.52 Å × 7.57 Å × 11.78 Å. Each cavity is filled with two dimethyl ammonium ions from decomposed DMF (Figure 24b). Charge balance is achieved by a total negative three charge from the biphenylene diphosphonic acid molecule countered by two Na^+ ions and a dimethyl ammonium ion.

Table 6. Bond distances for compound **7.2**, (Å)

Na1-O9	2.307(2)	Na2-O7A	2.356(2)	Na3-O13A	2.350(2)
Na1-O12	2.309(2)	Na2-O7B	2.356(2)	Na3-O13B	2.350(2)
Na1-O8	2.333(2)	Na2-O8A	2.405(2)	Na3-O10A	2.382(2)
Na1-O10	2.406(2)	Na2-O8B	2.405(2)	Na3-O10B	2.382(2)
Na1-O7	2.735(2)	Na2-O11A	2.454(2)	Na3-O9A	2.410(2)
		Na2-O11B	2.454(2)	Na3-O9B	2.410(2)
P1-O1	1.518(2)				
P1-O2	1.528(2)				
P1-O3	1.530(2)				
P2-O4	1.497(2)				
P2-O5	1.569(2)				
P2-O6	1.511(1)				

Table 7. Hydrogen bond distances for compound **7.2**

O-H…O	Bond Length, Å	symmetry	O-H…O	Bond Length, Å	symmetry
O4…O1	2.561(2)	x, y, z	O11…O3	2.842(2)	x, y-1, z
O7…O6	2.738(2)	x, y, z	O12…O2	2.832(3)	x, y-1, z
O7…O13	2.791(3)	-x+1, -y+1, -z+1	O12…O6	2.744(2)	x-1, y, z
O8…O12	2.847(2)	-x+1, -y, -z+1	O13…O3	2.874(2)	-x+1, -y+1, -z+1
O8…O3	2.855(2)	x, y-1, z	O13…O14	2.710(2)	-x+1, -y+1, -z+1
O9…O1	2.749(2)	x, y, z	O14…O6	2.679(3)	-x+2, -y+1, -z+1
O9…O14	2.830(2)	-x+1, -y+1, -z+1	O14…O3	2.738(3)	-x+2, -y+1, -z+1
O10…O2	2.771(2)	-x+1, -y+1, -z+1	N1…O5	2.673(3)	x, y, z
O10…O11	2.866(2)	-x+2, -y, -z+1	N1…O2	2.721(3)	x+1, y-1, z
O11…O5	2.816(2)	x, y, z			

Discussion

An interesting result that arises from the structures of the five alkali metal ion biphenylenediphosphonates is the fact that the coordination number of the ions increase from four for Li^+ to eight for Cs^+, but the composition in each case is the same. This feat is accomplished by first producing linear chains with tetrahedral coordination of the lithium ions utilizing two of the six oxygen atoms available per Li^+ with four being non-

bonding. In the six-coordinate sodium structure, Na_2O_{10} dimers are formed by O5 and O5D bridging the two sodium ions with O6 being non-bonding. The motif is octahedral. The potassium structure also features a 6-coordinate metal with all the oxygen atoms bonding to the metal ions but the motif is trigonal prismatic. The rubidium structure attains a 7-coordinate polyhedron by chelation of one of the phosphonate groups with one of the oxygen atoms also donating to an adjacent metal ion. The coordination is a capped trigonal prism. An 8-coordinate Cs^+ is obtained by both chelation and donation from a neighboring O3 atom.

All compounds have three-dimensional supramolecular structures with similar orientation of the biphenylene groups where neighboring biphenylene groups are rotated ~54^o from each other presumably to reduce strain caused by close contacts from other neighboring pillars. Compounds **2.2** and **5.2** have regularly pillared structure types whereby a continuous inorganic layer is formed. Similar extended structure types were found for compounds **1.2**, **3.2**, and **4.2**, where hydrogen bonding between the neighboring chains builds the inorganic layers. Interestingly, the distance between the neighboring chains decreased along the *b*-axis as the atomic radii increased from compound **3.2** to **5.2**. This distance may be a reflection of the volume of the unit cell, where the volume decreases from compound **3.2** to **4.2**. The volume was expected to increase from compound **1.2** to **5.2**. In the cesium compound **5.2**, the distance between pillars is small enough for metal and oxygen atoms to bond, forming continuous inorganic layers.

The stability of the compounds may be thought to be low considering that these are monovalent metals surrounded by many oxygen atoms sharing the metal charge. On the contrary, TGA data showed that all compounds were stable up to approximately 300 ^{o}C (Figure A 1). This is approximately 50 ^{o}C more stable than the ligand alone.[132] This stability may be due to the 3D structures that were formed and the coordination of the phosphonates to the metal atoms. TGA ran under air resulted in a colorless glass residue with weight loss occurring in several steps. The initial weight loss beginning at approximately 300 ^{o}C for all compounds is attributed to loss of water due to condensation of the phosphonate. The TGA of compound **1.2**, run with nitrogen, initially had a similar TGA curve to those run in air, where the compound is stable to approximately 300 ^{o}C, but it began to deviate around 530 ^{o}C. It resulted in an amorphous black powder instead.

Noteworthy is that the metal to phosphonic acid ratio may be altered by choice of synthetic route. Using microwave radiation resulted in the sodium compound **5.2**, for which a 1:1 metal to phosphonic acid ratio was obtained. However, using a conventional heating method resulted in a 1:2 ratio for compound **2.2**. A similar result was reported for a barium phosphonate.[133] The structural differences may be due to a more uniform heat distribution when using microwave radiation. Even with the 1:1 ratio the materials are still a Brönsted acid with one acidic proton remaining per phosphonate group. A regular pillared structure is obtained for both compounds **2.2** and **6.2**, but they differ in both coordination number and inorganic layer types resulting in different pillaring effects as shown in Figure 23.

Previously, reported structures of alkali phosphonates used two types of phosphonic acid groups: ethylene and phenyl phosphonic acids. The alkali metals lithium and sodium are very similar to our compounds. Both compounds $Li(HO_3PC_6H_5)(H_2O_3PC_6H_5)$[88] and $Li(HO_3PC_2H_4PO_3H_2)$[68] are similar to compound **1.2**, where the lithium atom is tetrahedrally bonded to oxygen atoms forming chains. The structure of $Li(HO_3PC_6H_5)(H_2O_3PC_6H_5)$ is a one dimensional structure, conversely using a diphosphonic acid both compound **1.2** and $Li(HO_3PC_2H_4PO_3H_2)$ resulted in similar three dimensional structures.

The sodium compound **2.2** has similar metal coordination as $Na(HO_3PC_2H_4PO_3H_2)$[68] and $Na(HO_3PC_6H_5)(H_2O_3PC_6H_5)$[88] with edge-shared bioctahedra, Na_2O_{10}. In compound **2.2**, the layers stacked along the *c*-axis, have an interlayer distance of 14.94 Å which is shorter than 15.59 Å[88] for compound $Na(HO_3PC_6H_5)(H_2O_3PC_6H_5)$ where there is no interdigitation or π-π stacking of the phenyl rings thus forming a van der Waals gap. As with $Na(HO_3PC_2H_4PO_3H_2)$[68], the diphosphonic acid, in **2.2**, links the inorganic layer together forming a regular pillared structure.

Structural differences between our compounds and those previously reported were observed for alkali metals potassium to cesium. The reported structures for the potassium ion, range from 6- to 8-coordinate if the maximum bond distance 3.073 Å is considered.[68,88,124] Interestingly, a different structural type was found for compound $K(HO_3PC_2H_4PO_3H_2)$[68] than for our compound **3.2**, in that a traditional pillared structure is not formed. Rather, there is no distinct inorganic or organic layer. Similarly, both our

compounds **4.2** and **5.2** differ from the ethylene analogs ($Rb(HO_3PC_2H_4PO_3H_2)$ and $Cs(HO_3PC_2H_4PO_3H_2)$).[68] The differences in structural types may be due to flexibility and size of the ethylenediphosphonates.

Rao and Vidyasager stated that K, Rb and $Cs(HO_3PC_6H_5)(H_2O_3PC_6H_5)$ have similar layered structure types although in our study this differs slightly.[88] Compounds **1.2**, **3.2**, and **4.2** have similar extended structure types as lithium ethylene diphosphonate[68], where hydrogen bonding between chains build the inorganic layer. The cesium compound **5.2** differs from **3.2** and **4.2** where a continuous inorganic layer is formed.

The structure of the materials will influence the access to the acidic protons. Interestingly, the alkali phenylphosphonates, where the compounds form layers, intercalated both ammonium ions and amines. Here, an increase in d-spacing is observed with increase in amine size suggesting that the layers move apart to accommodate the amines. In the three-dimensional case, to accommodate the amine the framework must have some porosity. Intercalation/deintercalation of NH_4^+ into $Li(HO_3PC_2H_4PO_3H_2)$ was observed thus indicating flexibility of structure.[68] Less ammonium intercalation occurred for $Na(HO_3PC_2H_4PO_3H_2)$. [68] Still less intercalation of ammonia was observed for the potassium to cesium versions suggesting less porosity. Our compounds have similar structures to the lithium and sodium ethylenediphosphonates. In the case of **1.2**, **3.2**, and **4.2**, they are similar to $Li(HO_3PC_2H_4PO_3H_2)$ where the largest uptake of ammonia occurred. Additionally, the inorganic layer is built from chains hydrogen bonded together. One may suggest that

reducing hydrogen bonding between chains would result in porosity. Surface area measurements of compound **1.2** showed no internal porosity and very small surface area (Nitrogen 4.12 cc/g and Hydrogen 4.13 cc/g). For our compounds, due to their three dimensional structure and the more rigid ligand, intercalation of amines is not possible. Materials with larger pores would be needed.

In our study, *in situ* synthesis with DMF resulted in a new supramolecular structure with cavities containing dimethyl ammonium ions (compound **7.2**). This compound differs from the pillared structures found in compounds **2.2** and **6.2**, since the phosphonate groups are not coordinated to the metal atoms. A pillared structure still exists, where the inorganic and organic layers are separate. The organic pillars are arranged around the dimethyl ammonium ions to form cavities. With this arrangement and coordination of the phosphonate groups with the metal atoms would provide a more stable compound with potential porosity. This may suggest a different approach to obtain porosity for these materials is possible, where amines are used as templates. Several examples of amines as templates or structure directing agents for metal phosphonates and phosphates have been reported in the literature.[134-140] It could be envisioned that different amines would result in different three-dimensional structures with the amine incorporated in the structure. Removal of the amines would form pores where access to the protons is possible. This approach is being pursued.

Conclusions

Six monovalent metal biphenylenediphosphonates have been synthesized and their structures have been determined with retention of most of the original four protons

of the ligand imparting Brönsted acidity to these compounds. Unfortunately, access to these protons is blocked; therefore new methods to obtain Brönsted acid catalysts with pores so the protons can be accessed are needed. The i*n situ* synthesis with DMF led to a three-dimensional structure with cavities containing dimethyl ammonium ions, giving insight into alternative methods of obtaining porosity.

CHAPTER III

SYNTHESIS OF METAL PHOSPHONATES BY CAPITALIZING ON THE SENSITIVITY OF THE STRUCTURE TO SOLVOTHERMAL REACTION CONDITIONS

Introduction

The increase in development of porous inorganic-organic materials is due to the variety of applications such as gas storage[37,141-143], ion exchange[141,142], catalysis[144], sensors[3] and optical properties[145]. In particular, the growth in the field of metal organic-frameworks (MOFs) based on carboxylates or imidazolates has advanced owing to ease of their construction and modification of their structure.[1,146,147] Two characteristics are: large surface areas and the ability to grow single crystals.

MOFs based on phosphonates are at a disadvantage from their tendency to form densely packed structures and the polycrystalline nature of the products impeding structure determination. The tetrahedral geometry and the numerous bonding modes of the phosphonate group also results in less predictability of the structure. However, metal phosphonates are robust porous solids and despite the tendency to form densely packed structures open-coordination frameworks have been reported.[38,148,149] Recently, these porous metal phosphonates result from unique aspects of the ligands that are used[74,89], but some porous solids have been developed through the use of template molecules[46,100,104,137,140] .

The use of template molecules in metal phosphonates prevents the formation of the densely packed structures by forming pores occupied with the template molecules.[150-154] The shape and functionality of the template molecule has an important effect on the pore structure and properties.[18] It has also been found, that the solvent system has a profound influence on the products of metal phosphonates given any metal and ligand system.[155-157]

Recently, we reported how the change in synthetic approaches resulted in different sodium biphenylenediphosphonates.[158] One synthetic approach led to a hydrogen-bonded sodium biphenylenediphosphonate framework with dimethylammonium ions occupying the cavities, $Na_2(H_2O)_8(O_3PC_{12}H_8PO_3H)$-$(NH_2C_2H_6)$.[158] The phosphonate groups were not directly bonded to the metal ions in the structure. A hydrothermal synthetic approach resulted in pillared monovalent biphenylenediphosphonate frameworks with the phosphonate groups directly bonded to metal ions ($M(HO_3PC_{12}H_8PO_3H_2)$ M = Li^+ Na^+, K^+, Rb^+ and Cs^+).[158] The results of the different synthetic approaches intrigued us to probe how template molecules and solvent influence the structures of monovalent phosphonates. Importantly, structure determination can be carried out due to the ease of single crystals formation for these systems. This is advantageous for the investigation of how the structures change with the use of different template molecules and synthetic parameters.

The first step in our synthesis approach was to investigate the role water played in solvothermal reactions containing lithium carbonate and either *tert*-butylphosphonic acid (*t*-BuPA) or phenylphosphonic acid (PPA). In the second step, both the roles of

water and template molecules were investigated in solvothermal reactions of sodium carbonate and PPA. The third step in our synthesis approach was to investigate the role of metal to ligand ratio and template molecules in solvothermal reactions containing sodium carbonate and 4,4'-biphenylenediphosphonic acid (BPDPA).

Variation in these parameters was used to investigate four different metal/ligand systems: Li^+/t-BuPA, Li^+/PPA, Na^+/PPA and Na^+/BPDPA. The systems Li^+/t-BuPA and Li^+/PPA were used to probe how small amounts of water affects the products in the solvothermal synthesis. Template molecules, mole ratios and the amount of water present in the solvothermal synthesis were varied for the Na^+/PPA and Na^+/BPDPA systems. Thirteen different metal phosphonate products of these reactions were identified by single crystal X-ray diffraction.

Experimental section

Materials

All commercial reagents (Li_2CO_3 99.1% Fisher, $Na_2CO_3 \bullet H_2O$ 99.5% Baker Analyzed, *tert*-butyl phosphonic acid (t-BuPA) 98% Aldrich, phenylene phosphonic acid (PPA) Alfa Products, methyl amine (40% water) Mallinckrodt, butyl amine Aldrich, diethyl amine Baker, ethylene amine Fisher) were used as purchased without further purification. Toluene was dried on 3 Å sieves. 4,4-biphenylenediphosphonic acid (BPDPA) was prepared according to the adapted literature procedure.[159]

Solvent effects on systems Li^+/t-BuPA and Li^+/PPA

The effect of the amount water in the solvothermal synthesis was studied for the systems Li^+/*t*-BuPA and Li^+/PPA. The general solvothermal synthesis was carried out in

12 mL Telfon-lined autoclaves to afford lithium phosphonates: $Li_9(H_2O)_3(HO_3PC_4H_9)_5(O_3PC_4H_9)_2 \cdot 1.5(H_2O)$ (**1.3**), $Li_4(H_2O)(O_3PC_4H_9)_2$ (**2.3**), $Li(H_2O)_3(HO_3PC_4H_9) \cdot H_2O$ (**3.3**), $Li_2(O_3PC_6H_5)$ (**4.3**), $Li(HO_3PC_6H_5)(H_2O_3PC_6H_5)$ (**5.3**). The detailed experimental conditions used are given in Appendix B (Table B 1). The reactions were carried out for 3 d at 120 ^oC in 6 mL of toluene. The metal salt to ligand molar ratio is 0.96:1 for Li_2CO_3: *t*-BuPA and 1.1:1 for Li_2CO_3:PPA. The amount of water present in the synthesis was varied from 30 to 210 μL. Attempts to isolate products resulted in multi-phased materials containing both known and unknown phases. Results given are based on the known phases determined from single crystal experiments. Experimental conditions used and results obtained for the systems Li^+/t-BuPA and Li^+/PPA are given in Figure 25.

		Ligand	
		t-BuPA	PPA
H_2O, μl	30	1	4
	90	2	4
	210	3	5

Li_2CO_3 + *t*-BuPA → (6 mL toluene, 145 ^oC, 3 days)

Li_2CO_3 + PPA → (6 mL toluene, 145 ^oC, 3 days)

Figure 25. Metal phosphonates obtained from the systems Li^+/*t*-BuPA and Li^+/PPA by varying the amount of water in the reaction mixture. The temperature, mole ratio and amount of toluene remained constant

Effect of template size and solvent on the system Na^+/PPA

The effect of both, the amount of water and the type of amine used in the synthesis, were studied for the system Na^+/PPA. The general solvothermal synthesis was carried out in 12 mL Telfon-lined autoclaves to afford sodium phosphonates: $Na_2(H_2O)_8 \cdot 2(O_3PC_6H_5) \cdot 2(C_4H_9NH_3) \cdot 4(H_2O)$ (**6.3**), $Na_3(H_2O)_{13} \cdot 3(O_3PC_6H_5) \cdot 3(CH_3NH_3) \cdot 2(H_2O)$ (**7.3**), $Na_2(H_2O)_{10}(O_3PC_6H_5)_2 \cdot 2(CH_3NH_3)$ (**8.3**), $Na_4(H_2O)(O_3PC_6H_5)_2$-$(HO_3PC_6H_5)_2 \cdot 2(CH_3NH_3)$ (**9.3**). The detailed experimental conditions used are given in Appendix B (Table B 2). The reactions were carried out for 5 d at 120 ^oC in 4 mL of toluene. The metal salt to ligand ratio is 0.5:1 for $Na_2CO_3 \cdot H_2O$:PPA. Two different amine templates were used: $C_4H_9NH_2$ and CH_3NH_2 (40% water).The amount of water present in the synthesis was varied from 30 to 60 μL. Attempts to isolate products resulted in multi-phased materials containing both known and unknown phases. Results given are based on the known phases determined from single crystal experiments. Experimental conditions used and results obtained for the system Na^+/PPA are given in Figure 26.

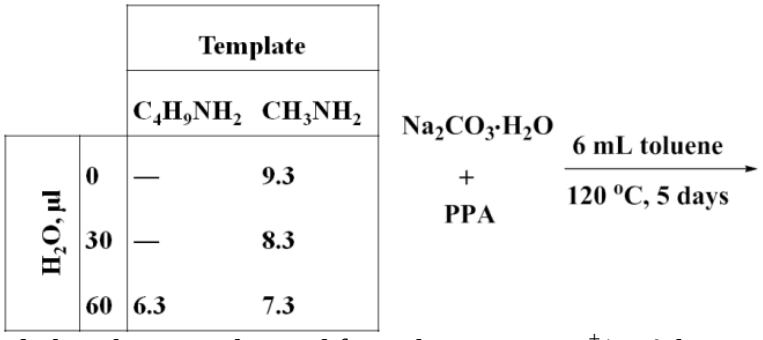

Figure 26. Metal phosphonates obtained from the system Na^+/PPA by varying the amount of water in the reaction mixture and using the template molecules $C_4H_9NH_2$ and CH_3NH_2. The temperature, mole ratio and amount of toluene remained constant. The symbol (—) means that the synthesis was not carried out

Effect of template molecules and change in metal to ligand ratio on the system Na^+/BPDPA

The effect the type of amine template and the metal salt to ligand ratio used in the synthesis were studied for the system Na^+/BPDPA. The general solvothermal synthesis was carried out in 12 mL Telfon-lined autoclaves to afford sodium phosphonates: $H_8NaO_4 \cdot 0.5(C_{12}H_8O_6P_2) \cdot C_6H_4O_3P \cdot 0.5(H_{16}Na_2O_8) \cdot 2(HH_9C_4NH_3)$ (**10.3**), $Na_4(H_2O)_{12}(O_3PC_{12}H_8PO_3H)(O_3PC_6H_4) \cdot ((C_2H_5)_2NH_2) \cdot H_2O$ (**11.3**) and $Na_3(H_2O)_3(O_3PC_{12}H_8PO_3) \cdot NH_2C_2H_4NH_3$ (**12.3**). The detailed experimental conditions used are given in Appendix B (Table B 2). The reactions were carried out for 7 d at 145 °C in 6 mL of toluene and 60 µL of water. Four different types of amine templates were used. Attempts to isolate products resulted in multi-phased materials containing both known and unknown phases. Results given are based on the known phases determined from single crystal experiments. Experimental conditions used and results obtained for the system Na^+/BPDPA are given in Figure 27.

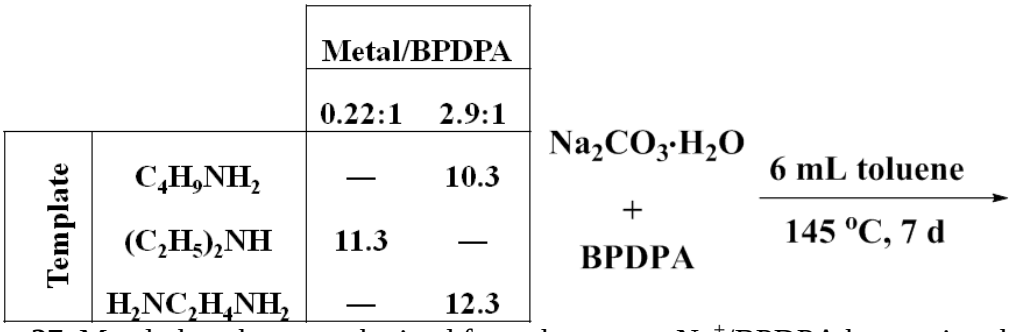

Figure 27. Metal phosphonates obtained from the system Na^+/BPDPA by varying the metal to ligand ratio and using different template molecules. The temperature and solvent ratio remained constant. The symbol (—) means that the synthesis was not carried out

X-ray characterization

Single crystal data were collected on a Bruker-AXS Apex II CCD X-ray diffractometer (Mo Kα radiation, λ = 0.71073 Å) operating at 110 K. A GADDS Bruker-AXS MWPC 3-circle X-ray diffractometer (Cu Kα radiation, λ = 1.54178 Å) was use to collect single crystal data for compound **11.3**. The structures were solved by direct methods and refined by the full-matrix least-squares technique against F^2 with the anisotropic displacement parameters for all non-hydrogen atoms. Hydrogen atoms were added in idealized positions and refined using a riding model with $U_{iso} = nU_{eq}$ for carbon atoms connected to the relevant H-atom where n = 1.5 for methyl and n = 1.2 for other H-atoms. Hydrogen atoms on water molecules and amine nitrogen were found using a difference map and refined using a riding model with $U_{iso} = nU_{eq}$ where n = 1.5, when possible. Anisotropic displacement parameters were established for all non-hydrogen atoms. Twinning occurred in compounds **1.3** and **9.3**. Additionally, the one *tert*-butyl group and the free water molecule were disordered in compound **1.3**. The N-C distance

for the amine of compound **13.3** was restrained. The following programs were utilized: cell refinement and data reduction: SAINT[125]; semi-empirical method for absorption correction: SADABS[126] and TWINABS[160]; structure solution: SHELXTL[127]; molecular graphics: Diamond[161], Mercury[129]. The experimental and refinement parameters for compounds **1.3-12.3** are given in Appendix B (Table B 3, B 4, and B 5).

Results and discussion

For monovalent metal biphenylenediphosphonates, the hydrothermal approach resulted in densely packed pillared structures with no porosity[158]; therefore alternative synthetic approaches are required to obtain porous monovalent metal phosphonates. However, the hydrothermal synthesis of monovalent metal phosphonates resulted in single crystals[68,69,88,158], unlike many metal phosphonates[162-164]; therefore it is advantageous to investigate structural changes that occur by systematically changing synthetic parameters for these compounds. The disadvantages for these materials are the high solubility (difficult to wash product) and comparatively low thermal stability. To determine how different synthetic factors affect the resulting structure, three different steps were taken.

Structural description

Due to the large number of structures, a detailed structural description of each compound (**1.3-13.3**) is provided in Appendix B. The trends observed in the three different synthetic approaches mentioned in the synthesis principle section are discussed below.

Solvent effects on systems Li^+/t-BuPA and Li^+/PPA

The solvent system has a profound influence on the products of metal phosphonates given any metal and ligand system.[155-157] Sensitivity of the structure to solvothermal conditions can be seen in the structures obtained from the systems Li^+/*t*-BuPA (compounds **1.3**-**3.3,** Figure 28) and Li^+/PPA (compounds **4.3** and **5.3**, Figure 29) where the amount of water added to the reaction varied from 30-210 µl. All other reaction variables remained constant.

Both a change in structure and metal to ligand ratio of the products were found for reactions **1.3**-**3.3** with the ligand *t*-BuPA (Figure 28). The metal to ligand ration changed from 1:1.3 (**1.3**), 2:1 (**2.3**) to 1:1 (**3.3**). Compound **1.3** was produced in the reaction with the least amount of water (30 µL). It formed a layered structure presented in Figure 28a. The metal phosphonate **2.3** resulted from the reaction with 90 µl of water (Figure 28b). A corrugated layered structure was formed. The layers are built from six member rings in both compounds **1.3** and **2.3,** but the lithium ion coordination differs. The layered structure in compound **1.3** is built by linking the corners of the triangular lithium phosphonate clusters. Water molecules fill the voids that are formed. Each lithium ion has a tetrahedral geometry. The corrugated layered structure in compound **2.3** is built with lithium ions having both tetrahedral and trigonal planar geometry. The bulky *tert*-butyl group hinders the coordination to a fourth oxygen atom from either axial position for the lithium ion with the trigonal planar geometry. The reaction containing 210 µl of water yielded a lithium phosphonate trihydrate moiety (compound **3.3**, Figure 28c). Each lithium ion has tetrahedral geometry. A hydrogen bonded layered structure is

formed from hydrogen bonds between the uncoordinated phosphonate oxygen atoms and the water molecules.

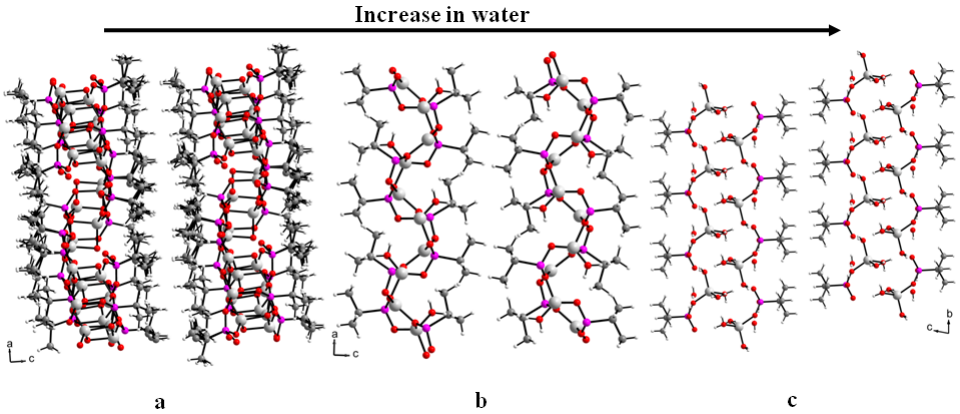

Figure 28. The changes in the products of Li^+/*t*-BuPA reactions with the change in solvothermal conditions (a) **1.3**, (b) **2.3** and (c) **3.3**

Similarly to the Li^+/*t*-BuPA series (**1.3**-**3.3**), both the metal to ligand ratio and the structure changed by differing the solvothermal reactions for Li^+/PPA (compounds **4.3** and **5.3**, Figure 29). The metal to ligand ratio changed from 2:1 (**4.3**) to 1:2 (**5.3**). With addition of more water in the solvothermal reactions, the two-dimensional layer changed to a one-dimensional chain. Reactions containing 30 µL of water resulted in a layered lithium phosphonate structure (**4.3**), while the reaction containing 210 µL of water formed a chain structure (**5.3**). Interestingly, compound **5.3** had previously resulted from a slow evaporation of water, with the bulk being a single phase material.[88]

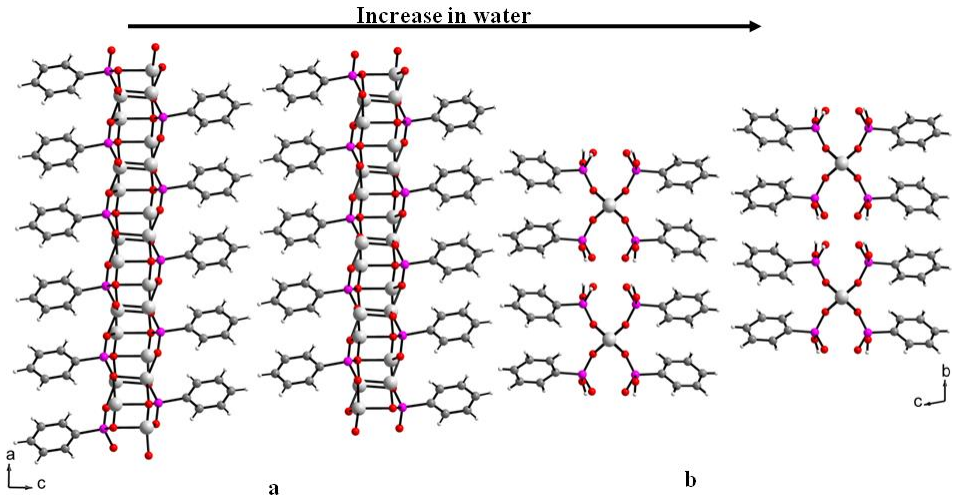

Figure 29. The changes in the products for Li^+/PPA reactions with the change in solvothermal conditions: (a) **4.3** and (b) **5.3**[88]

A decrease in structure dimensionality is observed with an increase in amount of water added to the solvothermal reactions for both the Li^+/*t*-BuPA and Li^+/PPA series. Overall, a decrease in metal to ligand ratio is observed with increase in the amount of water in the solvothermal reactions.

Effect of template size and solvent on the system Na^+/PPA

Alternatively, instead of changing the solvothermal reaction conditions to modify the structure, template molecules have been used. In particular, amines have often been used as template molecules for metal phosphonates.[29,100,101,104,137,139,140] Structure modification through the use of amines has been investigated for many types of materials with the idea that the amine could be removed later resulting in a porous material.[19,99,136,165] The geometry and charge of the amine would be reflected in the size, shape, and chemical properties of the pore. For layered materials, the same methodology can be used where template molecules would form pockets within the organic layer. In

contrast to the lithium phosphonates, a layered sodium phenyl phosphonate is formed under hydrothermal conditions and seemed most suitable to carry out these reactions.[88] The initial reactions did not form coordinated, layered structures instead hydrogen-bonded networks were obtained (compounds **6.3**-**7.3**, Figure 30). However, these reactions provided insight into how a coordinated layered structure could be synthesized. The solvothermal reactions formed hydrogen-bonded networks where either butyl (**6.3**) or methyl (**7.3**) ammonium ions alternate with phenylphosphonate along a pseudo inorganic structure to form a 2D layer (Figure 30b,c). Under these reaction conditions, planes of sodium-water moieties hydrogen bonded together to formed the pseudo inorganic backbone. This presents an additional challenge to the synthesis of templated layered structures, when too much water is incorporated into the structure, hydrogen-bonded networks forms instead.

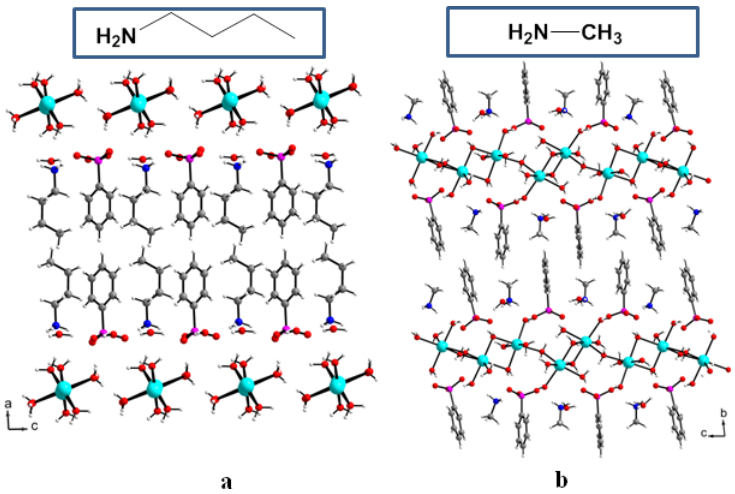

Figure 30. The changes in the products for the Na^{+}/PPA solvothermal reactions with the change in template molecule (a) **7.3** and (b) **6.3**

To circumvent this problem, successively less water was added to the solvothermal reactions (30 and 0 μL) containing CH_3NH_2 as the template molecule**.** The structures for compounds **8.3**-**9.3** are given in Figure 31. For compound **8.3**, a similar hydrogen-bonded network as compound **7.3** was obtained**,** with phosphonates and methyl ammonium ions alternating along the pseudo inorganic layer. The same metal to ligand ratio was found for the two compounds. However, the sodium-water moieties differ with a chain structure in compound **7.3** and edged-shared bioctahedral Na_2O_{10} motifs in compound **8.3** which results in different pseudo inorganic layers. A templated coordinated layered structure was obtained from reaction **9** where no water was added to the solvothermal reaction. The inorganic layer differs from the layered structure obtained from the product based on slow evaporation from water, $Na(HO_3PC_6H_5)(H_2O_3PC_6H_5)$.[88] A 1:1 metal to phosphonate ratio was found for compound **9.3** versus a 1:2 ratio in the evaporation product.[88] The difference is due to the methyl ammonium ion that helps counter balance the negative charge of the phosphonate groups. Pockets containing methyl ammonium ions are formed with phenylphosphonates acting as the walls. Compound **9.3** differs from other published templated layered structures where the protonated amines lay between the two adjacent layers.[29,101,139]

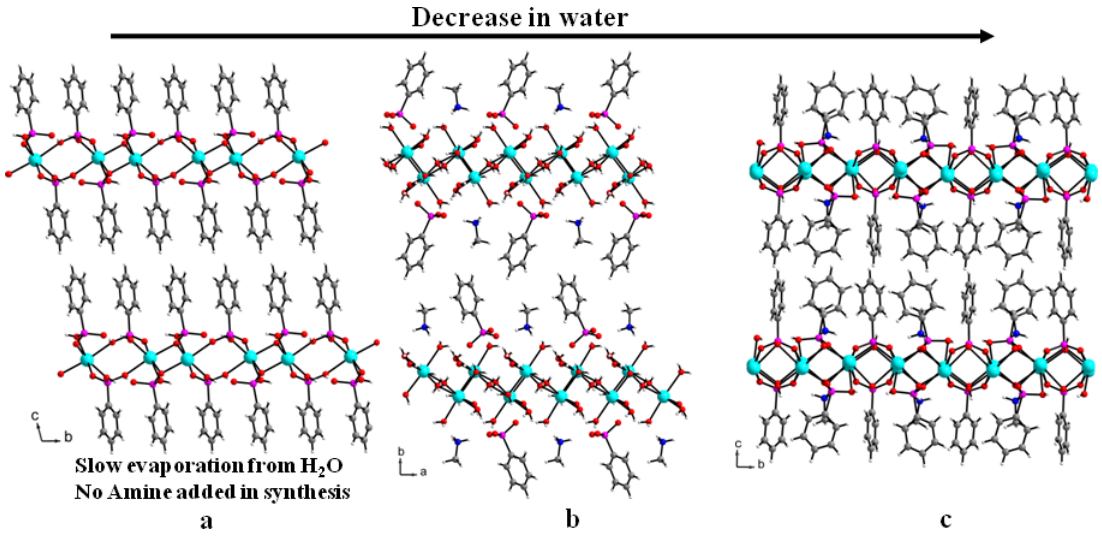

Figure 31. The changes in the products for Na^+/PPA solvothermal reactions with the change in amount of water: (a) slow evaporation[88], (b) 30 μL (**8.3**) and (c) 0 μL (**9.3**)

Effect of template molecules and change in metal to ligand ratio on the system Na^+/BPDPA

Generally for metal phosphonates, replacing a monophosphonic acid with a diphosphonic acid cross-links the adjacent inorganic layers.[7,112,166-168] The diphosphonates act as pillars and are spaced close together to form densely packed structures. The hydrothermal synthesis with sodium carbonate and BPDPA resulted in a densely pillared structure, $Na(HO_3PC_{12}H_8PO_3H_2)$.[158]

To obtain porous sodium biphenylenediphosphonates, amine templates were added to the solvothermal synthesis. Reported herein is the direct addition of amines as template molecules to the solvothermal synthesis of sodium biphenylenediphosphates (compounds **10.3-12.3**). Two different types of structures were obtained: (1) A three-dimensional hydrogen bonded network, where the phosphonate groups are not directly

bonded to the metal ions (compound **10.3**). (2)Three-dimensional coordinated structures with the phosphonate group directly bonded to the metal ions (compounds **11.3** and **12.3**).

Three-dimensional hydrogen-bonded network

A three-dimensional hydrogen-bonded network resulted from the solvothermal reaction containing butyl amine (**10.3**, Figure 32). The structure consists of a butyl ammonium ion, a biphenylenediphosphonate moiety, two water molecules, an edged-shared trigonal bipyramidal Na_2O_8 motif and edged-shared octahedral chain $(Na_2O_{10})_n$. The pseudo inorganic layer is built from hydrogen bonds between the water molecules, and the Na_2O_8 and $(Na_2O_{10})_n$ moieties. The biphenylenediphosphonate moiety and the butyl ammonium ion alternate along the pseudo inorganic layer. The biphenylenediphosphonate cross-links the pseudo inorganic layers. The structure (Figure 32) is similar to that of compound **6.3** (Figure 30). However, the pseudo inorganic layers differ. Hydrogen bonding between the edged-shared octahedral chains $(NaO_6)_n$ build the pseudo inorganic layer in compound **6.3**.

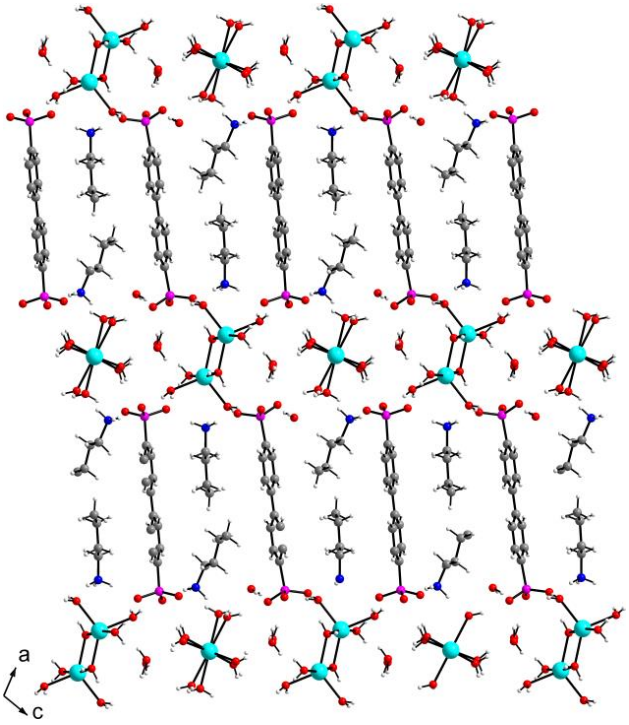

Figure 32. The crystal structure of sodium 4,4'-biphenylenediphosphonate (**10.3**) with butyl amine as the template molecule

Three-dimensional coordinated structures

The solvothermal reactions containing either diethylamine (**11.3**) or ethylenediamine (**12.3**) formed products with three-dimensional structures. Channels containing either protonated diethylamine or ethylene diamine were formed (Figure 33). The inorganic layer in compound **11.3** is built mainly through water-sodium coordination with only three metal-phosphonate oxygen bonds.

The product **12.3**, with a two-dimensional "non-traditional" layer, is formed by the reaction containing ethylenediamine where inorganic chains are cross-linked by the

diphosphonates to build the layer. The "non-traditional" layers are bridged by bioctahedra Na_2O_{10} motifs to form channels containing protonated ethylenediamines.

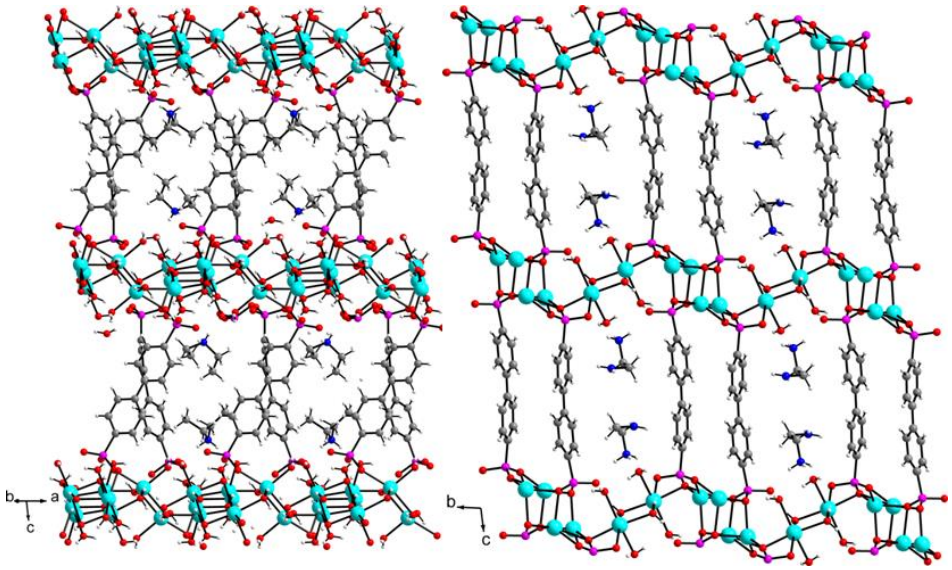

Figure 33. Crystal structures of compound **11.3** (left) and **12.3** (right) with both having channels containing protonated amines

Conclusions

Summarizing the results, we have explored the role that both template molecules and synthetic factors play in monovalent metal phosphonates. The role of water in the solvothermal synthesis was found to have a profound effect on the structure. The use of template molecules helped to form non-pillared structures.

Four different metal/ligand systems were used: Li^+/t-BuPA, Li^+/PPA, Na^+/PPA and Na^+/BPDPA. The metal to ligand ratio and the structure of the resulting products for the systems Li^+/t-BuPA (**1.3**-**3.3**) and Li^+/PPA (**4.3** and **5.3**) were found to change, with the

amount of water added to the reaction. Optimizing the amount of water in the Na^+/PPA/H_3CNH_2 system resulted in a different layered compound, $Na_4(H_2O)(O_3PC_6H_5)_2(HO_3PC_6H_5)_2 \cdot 2(CH_3NH_3)$ (**9.3**), than the compound obtained by slow evaporation, $Na(HO_3PC_6H_5)(H_2O_3PC_6H_5)$[88]. The change in mole ratio and amine resulted in three different products (**10.3**-**12.3**) for the Na^+/BPDPA system. Nonpillared structures were obtained for compounds **11.3** and **12.3**. In total, 12 different products were identified by single crystal X-ray diffraction.

CHAPTER IV

PROBING STRUCTURAL CHANGES IN A PHOSPHONATE-BASED MOF EXHIBITING REVERSIBLE DEHYDRATION*

Introduction

The immense research in metal-organic frameworks (MOFs) is due to the wide potential in applications owing to the diversity in topological architectures.[3,37,141,143-146] The differences in chemical and physical properties of their pores make MOFs selective for particular guest molecules. External stimuli can alter the structure of a material and thereby the physical properties.[169-174] This has an influence on the selectivity of guest molecules and the arrangement of guest molecules in MOFs. Both temperature and pressure are external stimuli that have an impact on the structures.[169,172-176] In particular, negative thermal expansion (NTE) is an isochemical process where, upon heating, the volume of the material decreases and has been observed in silicates, zirconium tungstate, zeolites and other materials.[177-180] MOFs have also been reported to exhibit negative thermal expansion.[181-183] The IRMOFs have been described as one of the most contracting materials known[181], and many studies are still being carried out investigating this phenomenon for MOF-5 and HKUST-1.[182-188] Studies showing negative expansion in porous materials have focused on the change in structure vs. temperature.[181,182,186]

*Reprinted in full with permission from "Probing Structural Changes in a Phosphonate-based MOF Exhibiting Reversible Dehydration" by Kinnibrugh, T. L.; Ayi A. A.; Bakhmutov, V. I.; Zon J.; Clearfield, A. *Cryst. Growth Des.* **2013**, accepted, Copyright 2013 by America Chemical Society.

However, little is known about how the guest molecules respond under these same conditions.

In MOFs that exhibit negative thermal expansion, the overall structure shrinks upon heating resulting in smaller pores.[181,186] For functional materials with proton or ion carriers occupying the pores, the loss in free volume could alter the positions of the guest molecules, thereby changing the conductive properties. The positions of the guest molecules in high temperature structures are important due to the challenge of developing MOFs with high conductivity at elevated temperatures (up to 120 ^{o}C) required for fuel-cell hydrogen conversion technology.[189]

Monitoring the changes in the guest molecules and framework can be carried out by *in situ* X-ray diffraction and solid state NMR. This allows mapping of the guest molecule positions throughout the negative thermal expansion process. The relative stability of the guest molecules in proton conducting MOFs over a range of temperatures allows for these types of studies to be carried out.[189-192]

Non-traditional inorganic-organic metal phosphonates synthesized using the ligand 1,3,5-benzenetriphosphonic acid (BTP) have been investigated for their proton conducting properties.[70] A layered material, PCMOF-3, with an extended microstructure of water molecules was formed using Zn(II) ions and BTP.[70] The material provided modest conductivity data due to constrained intergrain proton transfer.[70] An anionic form was also prepared using large cation ions.[193] A layered material (LBP-II) was also found for lanthanum ion and BTP.[71] However, the use of BTP with Cu(II) ions formed a three-dimensional framework where water molecules protrude into the pores, leading to

a promising proton conducting material.[72] To extend PCMOF-3 to a three-dimensional structure, a topotactic pillaring approach of anionic layers was used.[194,195] This resulted in four semi-crystalline versions of the extended-PCMOF-3.

Reported herein, are the crystal structures of two anionic three-dimensional frameworks with small amines as countercations, $Zn_{2.5}(H)_{0.4\text{-}0.5}(C_6H_3O_9P_3)(H_2O)_{1.9\text{-}2}(NH_4)_{0.5\text{-}0.6}$ (ZnBP-NH_4) and $Zn_{2.5}(H)_{0.75}(C_6H_3O_9P_3)(H_2O)_2(CH_3NH_3)_{0.25}$ (ZnBP-CH_3NH_3) resulting from the hydrothermal synthesis using Zn(II) cations and BTP. This approach differs from the topotactic pillaring approach however a similar structure was obtained.[194] Several types of protons are present within the pores (ammonium ions, acid protons and water molecules). The reversible dehydration process was investigated with solid state NMR and *in situ* X-ray diffraction. The experiments showed that the material shrinks upon heating, reducing the free volume of the pores and thus altering the positions of the solvent molecules. The negative expansion is a result of a phase change due to the loss in water molecules.

Experimental section[1]

Materials

Commercially available reactants were used without further purification. The ligand 1,3,5-benzenetriphosphonic acid was synthesized according to a previous procedure.[72.]

[1] The solid state NMR studies were carried out and written in full by Dr. Vladimir I. Bakhmutov. The BTP ligand was synthesized by Jerzy Zon and the ZnBP-NH_4 was synthesized by Ayi A. Ayi.

Synthesis of ZnBP-NH_4

The material $Zn_{2.5}(H)_{0.4\text{-}0.5}(C_6H_3O_9P_3)(H_2O)_{1.9\text{-}2}(NH_4)_{0.5\text{-}0.6}$ was hydrothermally synthesized (autogenous pressure for 6 d) at 160 ^oC from a mixture of zinc oxide (Aldrich, 98%), HCl (Fisher Scientific), ligand BTP, potassium acetate (Fisher Scientific), urea (EM Science) and H_2O/dioxane. In a typical synthesis of ZnBP-NH_4, ZnO (0.100 g, 1.2 mmol) was dispersed in 2 mL of water followed by the addition of 0.52 mL HCl and 1.68 mL 1,4-dioxane. To this mixture was added BTP (0.100 g, 0.31 mmol), urea (0.120 g, 2.0 mmol) and potassium acetate (0.180 g, 1.8 mmol). The resulting suspension with a pH of 1 was sealed in a Teflon-lined steel autoclave and heated at 160 ^oC for 6 d. The product, a crop of colorless plate-like crystals was filtered and washed with distilled water and dried at ambient temperature. Yield: 0.143 g (87.1% based on BTP). Elemental analysis (%) and ICP-AES: Calc (%) C 13.79, N 1.58, H 1.88 P/Zn ratio1.20 and Exp (%) C 13.97, N 1.57, H 1.51 P/Zn ratio 1.25

Synthesis of ZnBP-CH_3NH_3

The compound $Zn_{2.5}(H)_{0.75}(C_6H_3O_9\ P_3)(H_2O)_2(CH_3NH_3)_{0.25}$ was synthesized by a similar procedure as compound ZnBP-NH_4 except that urea was replaced with 1,3-dimethylurea. In a typical synthesis, ZnO (0.100 g, 1.2 mmol) was dispersed in 2 mL of water followed by the addition of 0.52 mL HCl and 1.68 mL 1,4-dioxane. To this mixture was added BTP (0.100 g, 0.31 mmol), 1,3-dimethylurea (0.174 g, 2.0 mmol) and potassium acetate (0.180 g, 1.8 mmol). The resulting suspension with a pH of 1 was sealed in a Teflon-lined steel autoclave and heated at 160 ^oC for 7 d. The product, a crop of colorless plate-like crystals was filtered and washed with distilled water and dried at

ambient temperature. Yield: 0.109 g (66.5 % based on BTP). Elemental analysis (%) and ICP-AES: Calc.(%) C14.4, N 0.67, H 1.79, P/Zn ratio 1.20 and Exp. (%) C 14.1, N 0.62, H 1.21, P/Zn ratio 1.23

Ion-exchange, ZnBP-Li

The material $Zn_{2.5}(C_6H_3O_9P_3)(H_2O)_2(Li)_{1.31}(OH)_{0.31}$ was obtained by dispersing ZnBP-NH_4 (0.239 g, 0.46 mmol) and $LiOH \cdot H_2O$ (0.049 g, 1.17 mmol) in 65 mL DI water and refluxing for 40 h. The solution was then filtered and washed with 250 mL of DI water. Yield 0.169 g Elemental analysis (%) and ICP-AES: Calc. (%) C 13.8, N 0.0, H 1.36, P/Zn ratio 1.20, P/Li ratio 3.00 and Exp. (%) C 13.6, N 0.0, H 1.23, P/Zn ratio 1.20, P/Li ratio 2.29

Materials characterization

Thermogravimetric analyses were carried out on a T.A. Instrument TGA Q-500. The samples were heated from 25 - 1000 °C using a heating rate of 5 °C/min with a 90/10 air /N_2 flow. Elemental analysis for carbon, nitrogen and hydrogen (C, N and H) was performed by Atlantic Microlab, Inc.. Compositional analysis for zinc, phosphorus and lithium was carried out at using ICP-AES Anderson Analytical. To prepare a typical sample, 0.033 g was dissolved in 40 μL of conc. HCl, 40 μL of conc. HNO_3, and 20 mL of DI water which then was shaken overnight. A Mettler Toledo polymer DSC equipped with a liquid nitrogen cooling system and 50 mL/min purge of dry nitrogen gas. Samples (~3 mg) were weighed into 40 μL aluminum pans and subjected to one heating cycle at 5 ^oC/min over the various ranges.

Solid state NMR dehydration-hydration study

The $^{31}P\{^{1}H\}$, CP $^{31}P\{^{1}H\}$, CP $^{13}C\{^{1}H\}$ and ^{1}H MAS NMR experiments were performed with a Bruker Avance-400 spectrometer (400 MHz for ^{1}H) using a standard 4-mm MAS probe head. Standard one pulse (direct nuclear excitation) and/or standard cross-polarization pulse sequences were applied in these experiments at relaxation delays necessary for a quantitative analysis of the spectra. The MAS NMR spectra have been recorded at variation in spinning rates between 5 and 14 kHz. The external standards used for calculations of chemical shifts of ^{13}C and ^{31}P nuclei were TMS and H_3PO_4 solution, respectively. The ^{1}H chemical shifts were determined by direct addition of CH_3OH into the sample and recalculated relatively TMS. The ^{1}H T_1 measurements were performed with a standard inversion-recovery pulse sequence where RF pulses were carefully calibrated. The ^{1}H relaxation data were treated with a standard program.

To study the dehydration process, a ZnBP-NH_4 sample was heated under vacuum to 300 ^{o}C for 24 h on a Quantachrome degasser. The sample was rehydrated by exposing it to the atmosphere overnight. Both ^{1}H and ^{31}P MAS NMR were recorded at each step of the experiment: initial, dehydration and rehydration. Elemental analysis for carbon, nitrogen, and hydrogen was acquired for the 1st step (%) C 13.97 N 1.57 H 1.51 and 3rd step (%) C13.93 N 1.41 H 1.36.

Structure determination from single crystals data

Single crystal data were collected on a Bruker-AXS Apex II CCD X-ray diffractometer (Mo Kα radiation, λ = 0.71073 Å) operating at 110 K. Crystallographic parameters and experimental details are given in Appendix C, Table C 1. The structures

were solved by direct methods and refined by the full-matrix least-squares technique against F^2 with the anisotropic displacement parameters for all non-hydrogen atoms. Hydrogen atoms were added in idealized positions and refined using a riding model with $U_{iso} = nU_{eq}$ for carbon atoms connected to the relevant H-atom where n = 1.2 for H-atoms. Hydrogen atoms on water molecules and ammonium nitrogen were found using a difference map and refined using a riding model with $U_{iso} = nU_{eq}$ where n = 1.5. Anisotropic displacement parameters were established for all non-hydrogen atoms. The following programs were utilized: cell refinement and data reduction: SAINT[125]; semi-empirical method for absorption correction: SADABS[126]; structure solution: SHELXTL[127]; molecular graphics: Diamond[161] and Mercury[196].

For compound ZnBP-CH_3NH_3, the carbon and nitrogen atoms in the methyl ammonium ion are positionally disordered.

In situ X-ray diffraction hydration study

All synchrotron powder diffraction data for the *in situ* X-ray diffraction hydration experiments were recorded on 1-BM-C at Advance Photon Source (APS), Argonne National Laboratory (Argonne, USA) with an average beamline wavelength of 0.6124 Å. Data collection was performed with a Perkin-Elmer flat panel area detector (XRD 1621 CN3-EHS) over the angular range 1-25° 2θ.

Samples were loaded in a kapton capillary (0.9 mm diameter), which was attached to the flow-cell setup for *in situ* synchrotron PXRD measurements.[197] The samples were heated at a heating rate of 3 $Kmin^{-1}$ with a He-gas flow to reach the target

temperature and then cooled down to 298 K. To rehydrate the materials at 298 K, the samples were exposed to water vapor with a He-gas flow.

Structure determination of phase II and III for ZnBP-NH_4

Two phases were identified during the *in situ* X-ray diffraction experiments and the structure for each phase was determined from a PXRD pattern at a specific temperature (phase II at 333 K and phase III at 423 K).

A set of approximately 20 Bragg peaks were used by the index procedure[198] in the TOPAS program[199]. Evaluation of the unit cell and all possible space groups were analyzed by the "profile matching mode" (Le Bail decomposition[200]) with the TOPAS[199] program. Analysis for systematic absences and best profile matching led to the correct space groups. The initial models were found by direct space methods in the FOX[201,202] program. The initial model was found using the following scattering units: two zinc atoms, one rigid BTP unit without free orientation and two water molecules and an ammonium molecule without hydrogen atoms with free orientation and position in the unit cell. The initial coordinates for all scattering units were taken from the single crystal data of ZnBP-NH_4. For phase III of ZnBP-NH_4, no water molecules were included in the initial model. The parallel tempering algorithm was used by the global optimization procedure.

The synchrotron PXRD data were used in the Le Bail decomposition to refine the unit cell and profile parameters in JANA2006[203]. The background was defined using 20 Chebyshev polynomials. The peak shape profiles were defined by a pseudo-Voigt function. The structure was refined by the Rietveld method. The crystallographic and

refinement parameters are given in Appendix C Table C 2. Hydrogen atoms were geometrically placed and fixed before the final refinement. Rietveld plots are given in Appendix C (Figure C 1-Figure C 4). The BTP unit was restricted to geometric correct values. For phase III, the Simpson correction was applied for asymmetry.

Results

Crystal structure of ZnBP-NH_4

The ZnBP-NH_4 MOF crystallized in the orthorhombic *I bam* space group. The asymmetric unit consists of two Zn(II) ions, a BTP molecule sited on a center of symmetry with one-half of the molecule as the asymmetric portion, a water molecule and an ammonium ion. The structure of ZnBP-NH_4 is a three dimensional framework built from layers linked by ZnO_4 tetrahedra (Figure 34). The structure is not a traditional pillared material where the inorganic layer is linked by organic groups. Instead the ZnO_4 centers act as pillars that link an inorganic-organic layer together. The layer is built from Zn(II) ions in tetrahedral coordination linking columns of BTP molecules. The columns are formed from roughly parallel π-stacked dimers of BTP molecules along the *a*-axis (d…d distance = 8.472 Å). In the π-stacked dimers, the BTP molecules are rotated 180 ^{o} to each other with π...π distance of 3.672 Å. For each BTP molecule, one phosphonate group (P2) lies parallel to the layer and the others (P1) are rotated 60 ^{o} into the interlayer. Within the intralayer, the phosphonate oxygen atoms from a BTP molecule, coordinate to eight ZnO_4 centers (Zn1-O = 1.905 –2.006 Å). The phosphorus oxygen atom, O2, does not coordinate the intralayer ZnO_4 centers. The ZnO_4 center, situated above the layer is coordinated only to oxygen atom, O2, from four symmetry equivalent

BTP groups (Zn2-O2 = 1.930(3) Å). The Zn2 sites act as pillars linking the inorganic-organic layers. The interlayer distance is 9.908 Å, corresponding to half of the *c*-axis.

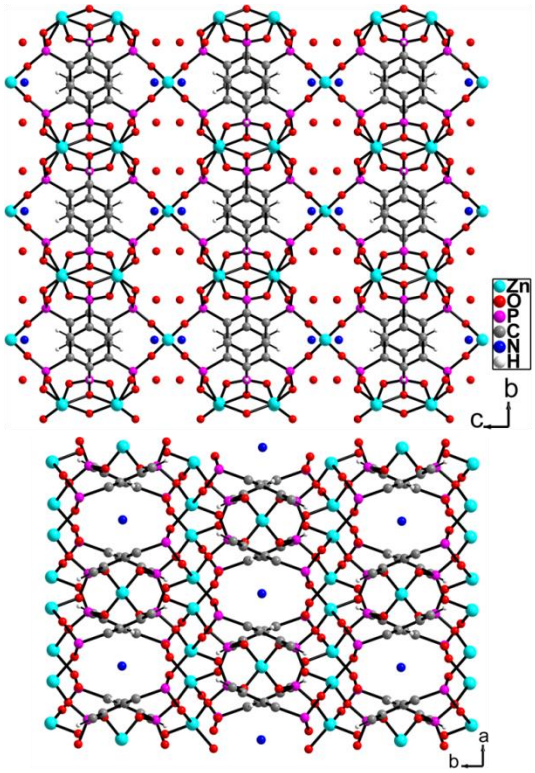

Figure 34. Views of the crystal structure along the *a*-axis (top) and *c*-axis (bottom) ZnBP-NH_4

The three dimensional framework forms two types of pores that interconnect (Figure 34 and 35). The pores are formed from the spaces between the ZnO_4 pillars. The larger pore runs along the [100] direction and the smaller pores run along the [110] direction and interconnect the larger pores. Both pores are filled with water and ammonium ions. The ammonium ions compensate the -1 charge on the ZnBP

framework. The formula determined from single crystal data, $Zn_{2.5}(H)_{0.4\text{-}0.5}(C_6H_3O_9P_3)(H_2O)_{1.9\text{-}2}(NH_4)_{0.5\text{-}0.6}$, is in good agreement with the formula derived from elemental analysis ($Zn_{2.5}(H)_{0.41}(C_6H_3O_9P_3)(H_2O)_2(NH_4)_{0.59}$). In both cases, the NH_4/ZnBP ratio is less than one therefore the framework must be partially protonated to have charge balance.

A topotactic pillaring approach resulted in the same compound, however, single crystals were not obtained.[194] Determination of the structure from powder diffraction data resulted in the space group *Iba*2; however, we find from single crystal data that the space group is *Ibam*. Determination between *Iba*2 and *Ibam* from powder diffraction data is difficult because these groups are indistinguishable by systematic absences. The determination of the position for the ammonium ion and water molecules is difficult. Previously from powder diffraction data, the ammonium ion positions were reported in the larger pores.[194] Reported herein, are two structures where the ammonium ion occupies a position first in the small pore (ZnBP-NH_4, Phase Ia) and then in the larger pore (ZnBP-NH_4, Phase Ib). The site occupancy of the ammonium ion is restricted to 0.25 for phase Ia which results in slightly less %N than determined by elemental analysis. The methyl ammonium ion also occupies the same position as ammonium ion in phase Ia and is described below. The refinement parameters for phase Ia are slightly better (Table C 1). However, it is believed that the ammonium ions can occupy either positions and therefore the solvent molecules are disordered.

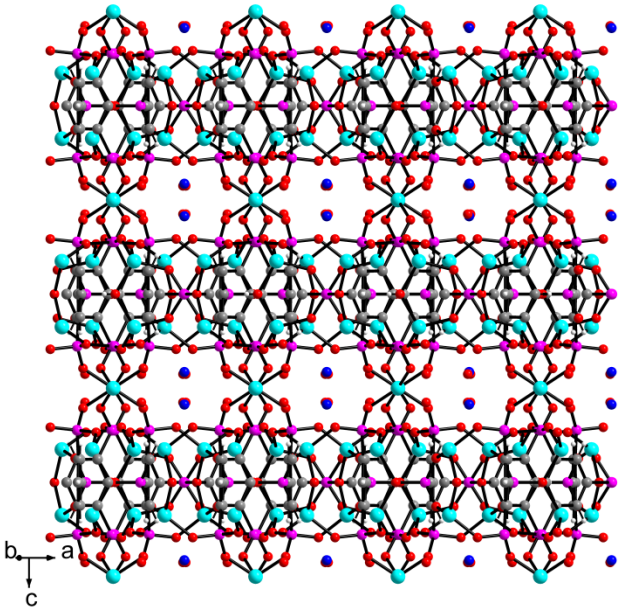

Figure 35. View of the smaller pores running along the [110] direction which interconnects the larger pores. The organic-inorganic layers and the ZnO_4 pillars can be clearly seen. The solvent molecules are disordered

Crystal structure of ZnBP-CH_3NH_3

The ZnBP-CH_3NH_3 MOF crystallized in the orthorhombic *Ibam* space group (Table C 1). The asymmetric unit consists of two Zn(II) ions, a BTP molecule sited on a center of symmetry with one-half of the molecule as the asymmetric portion, a water molecule and an methyl ammonium ion. The framework is isostructural to the ZnBTP framework (Figure 36). 1,3-dimethylurea decomposed into methyl ammonium ions. The carbon and nitrogen atoms in the methyl ammonium ion are positionally disordered and occupy two symmetry equivalent sites of the NH_4 ion in the ZnBP-NH_4 MOF. The formula was determined to be $Zn_{2.5}(H)_{0.75}(C_6H_3O_9P_3)(H_2O)_2(CH_3NH_3)_{0.25}$ indicating that the framework must be protonated to obtain charge balance.

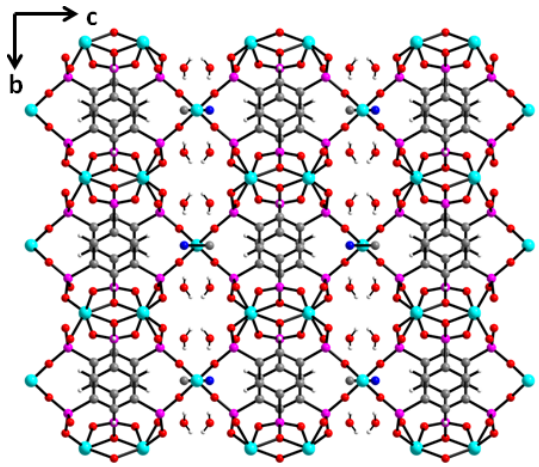

Figure 36. A view of the crystal structure along the *a*-axis for ZnBP-CH_3NH_3. The CH_3NH_3 molecules are disordered

Ion-exchange: ZnBP-Li

The replacement of NH_4^+ ions in the ZnBP-NH_4 materials was carried out by refluxing the material with $LiOH \cdot H_2O$. Refluxing helps drive the reaction by removing NH_3 from the solution. The material remained crystalline under the basic conditions (pH 10, Figure C 5). The TGA is similar to that of ZnBP-NH_4 where initially water loss occurs. However, there is no loss due to NH_3 owing to their replacement by Li^+ ions (Figure 37). For ZnBP-NH_4, weight loss due to NH_3 occurs between 320-460 ^oC. Both materials have high thermal stability (~600 ^oC). The difference wt% loss in the TGA from decomposition is consistent with the different compositions. Based on ICP the resulting material has the following formula $Zn_{2.5}(C_6H_3O_9P_3)(H_2O)_2(Li)_{1.31}(OH)_{0.31}$.

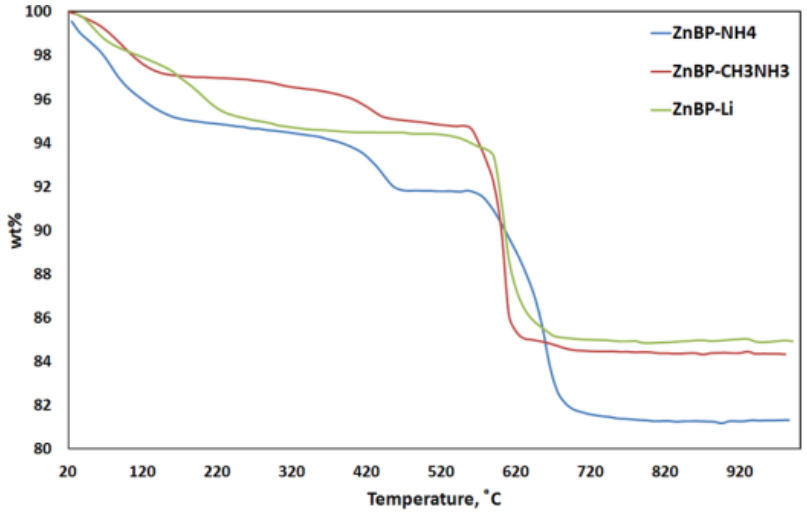

Figure 37. Thermogravimetric analysis of compounds ZnBP-NH_4, ZnBP-CH_3NH) and ZnBP-Li

Solid state NMR studies

The $^{31}P\{^{1}H\}$ MAS NMR experiment, performed with a single-pulse proton-decoupled sequence for freshly-prepared compound ZnBP-NH_4 spinning at 10 kHz shows two resonances at 19.3 and 13.2 ppm. In an excellent agreement with the X-ray structure their integral intensities are related as 1 to 2 (Figure 38). Both of the signals are symmetric and relatively sharp with line widths of 70 and 122 Hz, respectively, and accompanied by low intensity sidebands. The slightly larger broadening of the high-field resonance is obviously connected with a larger local disorder around the phosphorus atoms participating in the formation of cavities. The presence of NH_4^+ ions and H_2O molecules in the cavities could explain the slight increase in the relative intensity of the high-field resonance in the cross-polarization ^{31}P MAS NMR experiment.

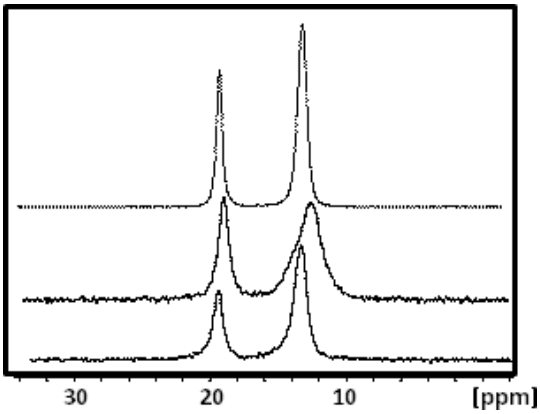

Figure 38. The $^{31}P\{^{1}H\}$ MAS NMR spectra recorded for ZnBP-NH_4 at a spinning rate of 10 kHz from top to bottom: a freshly-prepared ZnBP-NH_4, the thermally treated (~300 ^{o}C) ZnBP-NH_4 just after heating, the thermally treated ZnBP-NH_4 after 14 h

Finally non-equivalency of phosphorus atoms in the $^{31}P\{^{1}H\}$ MAS NMR spectra of ZnBP-NH_4 corresponds to appearance of numerous signals in the well-resolved $^{13}C\{^{1}H\}$ CP MAS NMR spectrum of ZnBP-NH_4 spinning at a rate of 10 kHz. The spectrum shows at least three ^{13}C-P doublet resonances at 130.9, 130.5 and 126.3 ppm with ^{1}J(C-P) constant of 184, 185 and 194 Hz, respectively. It is interesting that in the solid state these constants are larger than in solutions[72]. A group of ^{13}C lines, observed at 132.7-132.6 ppm, obviously illustrates the absence of fast rotation of the aromatic rings leading to the observation of two signals in solutions only[72].

The $^{31}P\{^{1}H\}$ MAS NMR spectrum recorded just after thermal treatment of ZnBP-NH_4 (Figure 38) reveals the following spectral changes: the low-field, still symmetric resonance broadens to 126 Hz shifting insignificantly to 19.0 ppm, while the high-field resonance becomes broad (262 Hz) and non-symmetrical showing shoulders and undergoes a high-field displacement to 12.4 ppm. Generally, such changes

correspond well to increasing amorphous character of the sample[204] where after heating a local disorder increases for the phosphorus atoms forming cavities. However after 14 h the $^{31}P\{^{1}H\}$ MAS NMR spectrum shows recovered structural regularity and the two initial phosphorus resonances are again observed at the same chemical shifts (Figure 38). The phase transition of ZnBP-NH_4 can be well traced by ^{1}H MAS NMR (Figure 39). The initial sample shows two broad ^{1}H resonances centered at of 7.3 and 3.6 ppm. Their integral intensity ratio is determined as 2.9 to 1. Just after the thermal treatment the high-field signal (3.6 ppm) completely disappears and the low-field broad line transforms to two resonances centered at 7.6 and 6.6 ppm (Figure 39) with intensities related to 2: 1. Then after 14 h, as in the case of ^{31}P MAS NMR, the ^{1}H MAS NMR spectrum again converts to the initial spectrum to show two resonances at 7.4 and 3.8 ppm (Figure 39).

To understand better the nature of these signals and thus to make ^{1}H signal assignments we have performed inversion-recovery (^{1}H T_1) experiments for ZnBP-NH_4 (before heating and after its structural recovery) spinning at 10 kHz. The experiments carried out for a fresh-prepared sample of ZnBP-NH_4 have shown that both of the ^{1}H resonances (7.4 and 3.6 ppm) relax very similarly and their spin-lattice relaxation is not exponential. The relaxation curves can successfully be treated with a stretched exponential[204,205], $I = I_0(1-2\exp(-(\tau/T_1)^{\beta}))$ (Figure 40), where the β parameter takes the values of 0.73 (δ = 7.4 ppm) and 0.68 (δ = 3.6 ppm) and T_1 times are calculated as 1.5 – 1.3 s for both lines. Note that such β parameters could be caused by a partial contribution of spin diffusion into spin-lattice relaxation[204].

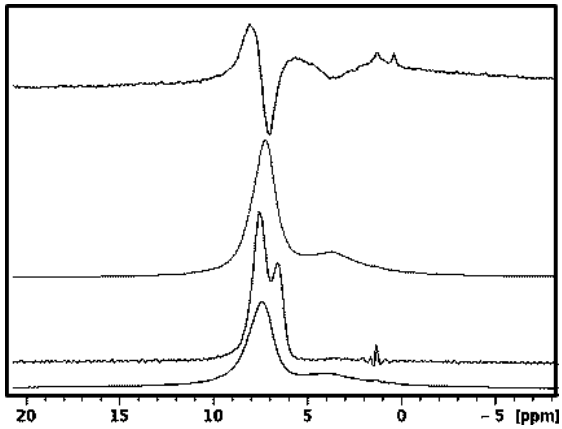

Figure 39. The ^{1}H MAS NMR spectra of ZnBP-NH_4 spinning at 10 kHz from top to bottom: the partially relaxed spectrum obtained for fresh-prepared ZnBP-NH_4 at delay time of 1 s; the single pulse spectrum obtained for fresh-prepared ZnBP-NH_4, the single pulse spectrum obtained for ZnBP-NH_4 in 30 min after heating the FID is treated with a Gauss function to increase resolution, the single pulse spectrum obtained for ZnBP-NH_4 in 14 h after heating.

It is interesting that after the structural recovery both of the ^{1}H resonances again relax similarly but the non-exponential character of relaxation increases. Now the relaxation curves are treated with a stretched exponential at the β parameter of 0.40 - 045 and T_1 times of 1.0 s for both lines (Figure 40). Generally speaking, such decrease in β could correspond to a more broad distribution of ^{1}H T_1 times[204] which, in turn, shows that an amorphous character of the thermally treated sample is still present even after 14h. It should be noted that the relaxation curves obtained for the sample after its structural recovery are better treated with a bi-exponential function (Figure 40) to give a short and long ^{1}H T_1 components of 0.010-0.013 and 2.0 s for the both resonances. Such short T_1 components could be attributed to very high proton mobility[206] or explained by

the presence of oxygen as paramagnetic centers. However we believe that even in these terms the smaller times are too short to be plausible.

In the frameworks of signal assignments, it is important to emphasized that according to careful inspection of the partially relaxed ^{1}H NMR spectra of ZnBP-NH_4 before and after heating, the line observed at 7.4 ppm is actually a superposition of three resonances at 8.0, 7.0 and 5.6 ppm (Figure 39). They can be assigned to protons of C_6H_3 rings[72], ions NH_4^+ [207,208] and H_2O molecules absorbed by the surface of ZnBP-NH_4. Thus the thermal treatment of the sample does not eliminate NH_4^+ in accordance with an elemental analysis of ZnBP-NH_4 performed before and after heating. We believe that the NH_4^+ line is directly seen as a resonance at 6.6 ppm in the ^{1}H MAS NMR spectrum recorded just after heating (Figure 38). Then the ^{1}H resonance observed for ZnBP-NH_4 before the thermal treatment at 3.6 ppm, which disappears just after heating and again appears in the spectrum after 14 h necessary for structural recovery of ZnBP-NH_4, can be attributed to H_2O molecules in cavities located close to ions NH_4^+ (Figure 34). Due to this assignment and on the basis of the solid state NMR data we can conclude that the structural regularity of ZnBP-NH_4 is strongly supported by P-O$\cdots$HN$^+$H$\cdots$OH$_2$ hydrogen bonded network in cavities and elimination of the H_2O elements from this network is the driving force of the phase transition observed for ZnBP-NH_4 during its heating.

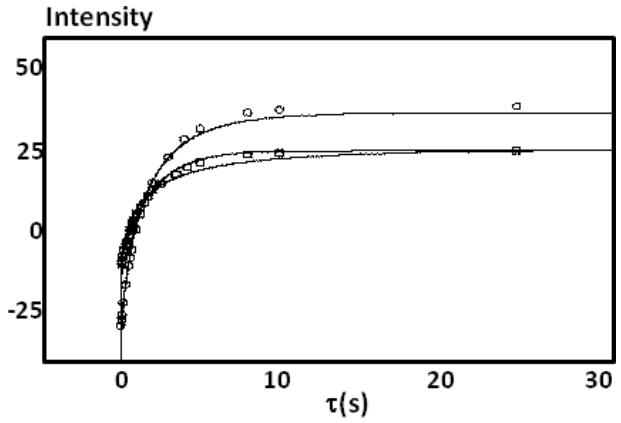

Figure 40. Relaxation curves in coordinates Intensity (arb. units) versus delay time τ (in sec) in the inversion-recovery experiments: O - the fresh-prepared ZnBP-NH_4 for signal at 7.1 ppm where solid line is the treatment with a stretched exponential; □ - ZnBP-NH_4 after 14 h after heating where solid lines the treatments with a stretched exponential and bi – exponential

Finally, as we have shown above, all of the ^1H resonances in the fresh-prepared ZnBP-NH_4 relax very similarly with a relatively short T_1 time of 1.3-1.5 s. It is well known that ions NH_4^+ and water molecules can undergo fast reorientations in such solids as ZnBP-NH_4 and even fast proton exchanges leading to proton conductivity[205,209]. These motions reasonably result in fast reorientations of their proton-proton dipolar vectors to cause the relatively fast ^1H spin-lattice dipole-dipole relaxation. It is obvious that these motions can remarkably reduce ^1H T_1 times for protons of the C_6H_3 rings which are located in a structurally rigid part of ZnBP-NH_4. Nevertheless it seems to be unlike that the C_6H_3 ^1H T_1 times can be equal to those for protons of NH_4^+ and H_2O. We assume that the effect is connected with spin diffusion when spin flips for NH_4^+ are accompanied by spin flips of aromatic rings[210].

In situ X-ray diffraction studies

The *in situ* X-ray diffraction experiment of ZnBP-NH_4 was carried out to study the reversible dehydration process. The X-ray diffractogram of the experiment shows a change in peak positions, with increase in temperature to 200 ^{o}C, and no change when cooled back to 25 ^{o}C (Figure 41). Upon exposure to water vapor, the peaks shift back quickly to their original positions suggesting structural changes accompanied rehydration of the framework. Additionally, heating the sample to 80 ^{o}C also caused a shift in peak positions, which was reversible upon cooling back to 25 ^{o}C (Figure 42). Complementary to this, is the DSC curve which indicates two endothermic phase transitions (Figure 43). From the *in situ* X-ray diffraction experiment, three phase changes occurred during the reversible dehydration process (Figure 44). The phase changes that occur: after heating to 45 ^{o}C a phase change occurs without loss of solvent (phase II), continued heating to 120 ^{o}C resulted in a phase change with loss of solvent (phase III), and then rehydration occurs upon exposure to water vapor 25 ^{o}C resulting in the initial compound (phase I).

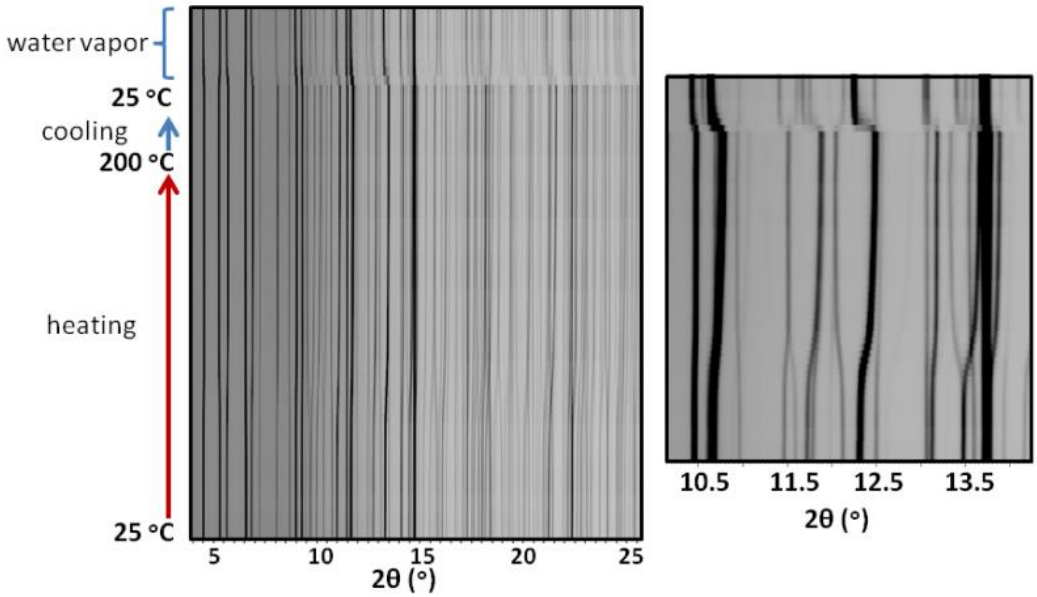

Figure 41. The diffractogram of the *in situ* hydration study (left) and a narrow 2θ region of the diffractogram giving a closer view of the change in the diffraction peaks for the reversible dehydration process (right)

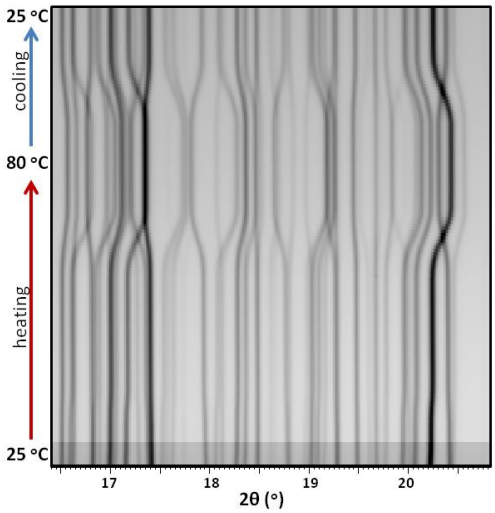

Figure 42. A diffractogram showing the reversible process upon heating to 80 ^{o}C and then cooling down to 25 ^{o}C

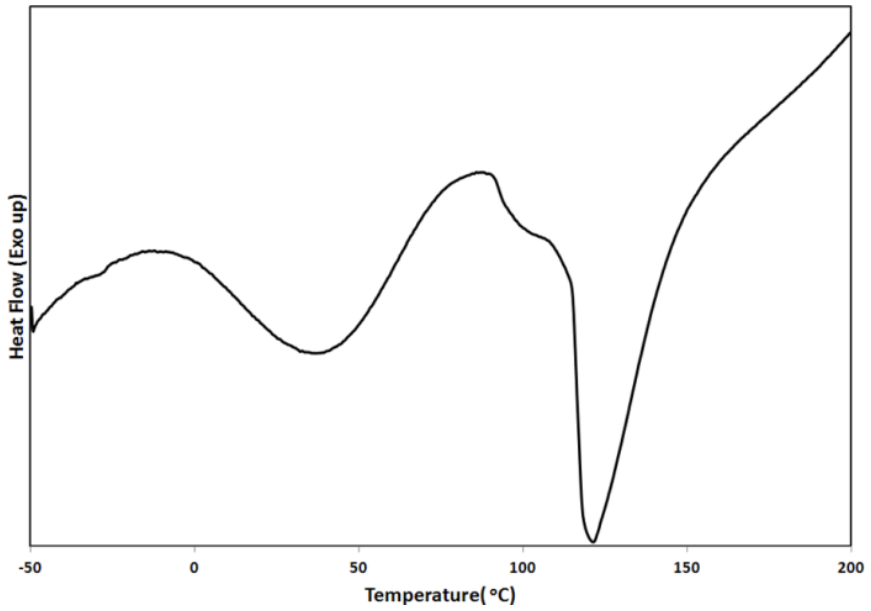

Figure 43. Differential scanning calorimetry analysis showing two endothermic phase changes

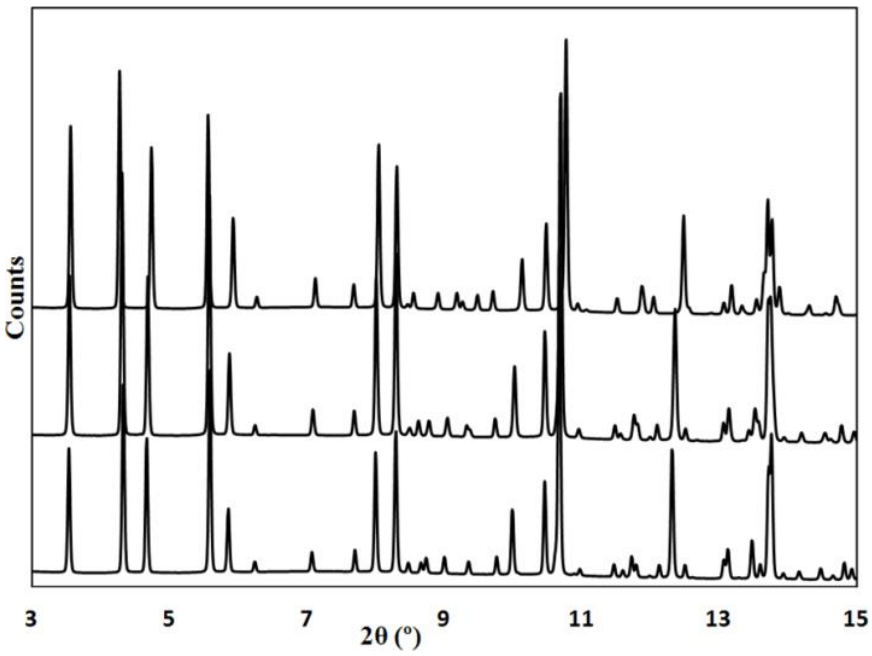

Figure 44. PXRD of the three different phases of ZnBP-NH_4: initial (bottom), 60 ^{o}C (middle) and 150 ^{o}C (top)

The structures for the different phases were determined from powder X-ray diffraction data showing that the framework stays intact upon heating to 200 ^{o}C (Figure 45 and 46). The crystallographic parameters are similar for the three phases. Each phase crystallized in the orthorhombic *Ibam* space group and the asymmetric unit consists of two Zn(II) ions, one BTP molecule sited on a center of symmetry with one-half of the molecule as the asymmetric portion, and solvent molecules. For phase II at 60 ^{o}C, no loss of solvent occurs. The reversible solid-solid transition between phase I and phase II leads to enantiotropic polymorphs. The second solid-solid transition occurs at ~120 ^{o}C which is approximately where water loss occurs on the TGA. The structure of the phase III was determined at 150 ^{o}C. Water loss had occurred on heating to this temperature; however, the ammonium ions were present in the larger pores.

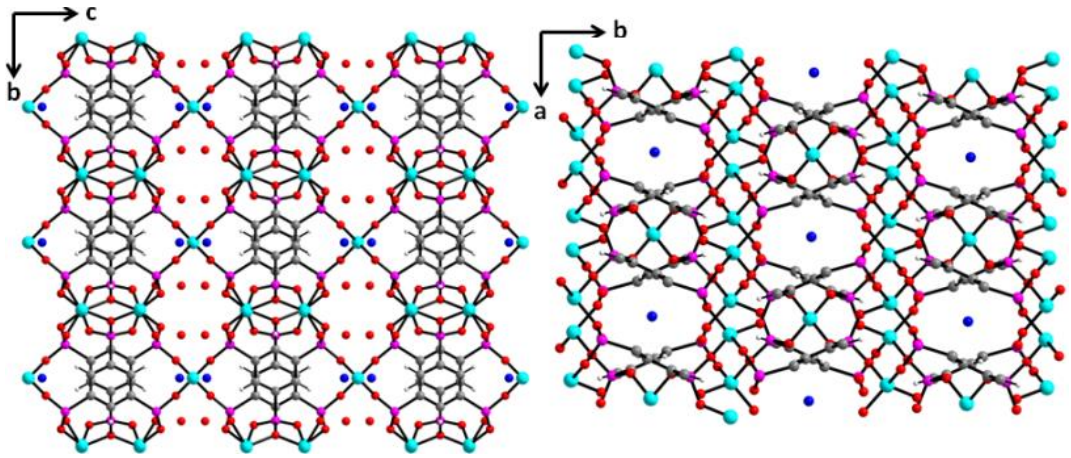

Figure 45. Views of the crystal structure along the *a*-axis (left) and *c*-axis (right) for compound ZnBP-NH_4-2 after heating to 60 ^{o}C (phase II). There solvent molecules are disordered

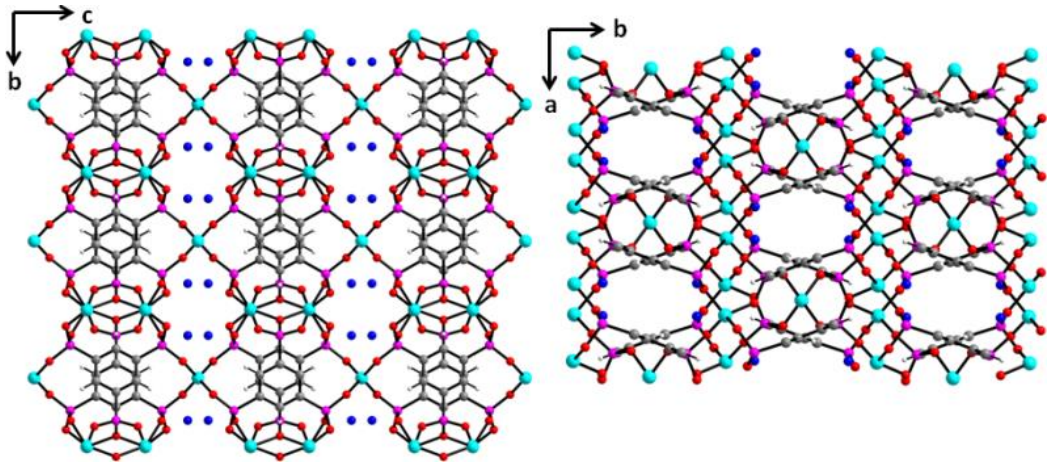

Figure 46. Views of the crystal structure along the *a*-axis (left) and *c*-axis (right) for compound ZnBP-NH_4-3 after heating to 150 ^oC (phase III)

The change in the free space of the crystal structure is reflected in the change of the unit cell parameters and volume. The plot of the normalized unit cell parameters and volume is given in Figure 47. A negative expansion is exhibited by the material as seen by a decrease in volume with an increase in temperature due dehydration. All cell parameters decrease with increase in temperature except for the *b*-axis. The *c*-axis has the smallest change with a slight decrease which shortens the distance between the layers, narrowing the larger pores. Axis *b* lies parallel to the layers and is lengthened upon heating, elongating the larger pores. The *a*-axis decreases the distance between the dimers which decreases the distance between pillars (d…d distance = 8.443, 8.296 Å, π… π = 3.720, 3.669 Å for phase II and III respectively). This reduces the size of the smaller pore and no solvent molecules occupy this position.

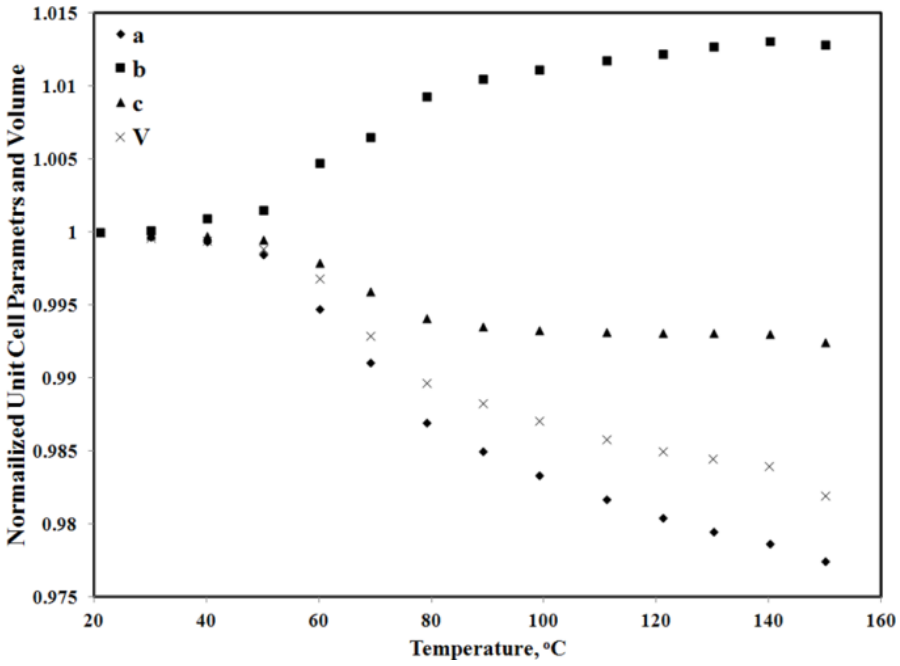

Figure 47. A plot showing the change in unit cell parameters and volume with increasing temperature. All data was normalized to unit cell determined at room temperature

Discussion

The extension of the non-classical organic-inorganic layered material[70], PCMOF-3, to a three-dimensional material was successful by a one-step hydrothermal synthesis. The layers are bridged by ZnO_4 centers to form an anionic framework. The bridged layers reduce the interlayer distance from 11.486 Å (PCMOF-3) to 9.908 Å. The decomposition of urea to ammonium provides the cations to help balance the -1 charge on the framework however some acidic protons are still present giving the formula $Zn_{2.5}(H)_{0.4\text{-}0.5}(C_6H_3O_9P_3)(H_2O)_{1.9\text{-}2}(NH_4)_{0.5\text{-}0.6}$. The material has high thermal stability (~600 ^oC based on TGA, Figure 37).

It is interesting that two synthetic approaches resulted in the same material. The topotactic pillaring approach of anionic layers provides the same anionic three-dimensional framework in a two-step process.[195] It is thought that the zinc ions are partially dissolved from the anionic layers to form the anionic three-dimensional framework.[195] This method provides a complete exchange of the acid protons in contrast to the one-step hydrothermal synthesis. However, the use of small amines in the hydrothermal synthesis in contrast to the large amines used in the topotactic pillaring approach, provides the three-dimensional framework directly rather than the anionic layers.

The anionic framework has similarities to a copper based MOF synthesized using the BTP ligand.[72] An organic-inorganic layer is formed with Cu centers bridging the layers together. The layers consist of columns of dimers connected by Cu(II) ions. The dimers are not parallel to the layer due to the geometry of the metal centers. The Cu(II) ions have square pyramidal geometry and are coordinated to water molecules which are directed into the pores. This leaves a small amount of free space in the pores in comparison to the ZnBP framework.

The ZnBP framework has two types of pores. The larger pores are interconnected by smaller pores in the [110] direction. The solvent molecules (water and ammonium ions) are disordered in ZnBP-NH_4; however, for ZnBP-CH_3NH_3 the $CH_3NH_3^+$ ion occupies the position in the smaller pore. Based on TGA, the NH_4^+ ions are not removed below 320 ^oC indicating strong interactions with the framework. Both the solid state

NMR and *in situ* X-ray diffraction experiments determined that NH_4^+ ions remained in the pores after dehydration.

A reversible dehydration process occurs with two phase transitions and reveals that the material exhibits negative expansion. The *in situ* X-ray diffraction study mapped both the changes in the framework and guest molecules positions as the negative expansion process occurred (phase change). The first phase transition forms an enatiotropic polymorph. A slight decrease in volume is seen but there is no large change in guest molecules positions. For the second phase transition, loss of water occurs and the NH_4^+ ions occupy the positions in the larger pore. These experiments suggest that the loss of hydrogen bonding due to water causes the contraction of the structure.

A less coordinating cation would allow for easier removal, therefore the compound was synthesized with methyl ammonium ion (decomposition byproduct of 1,3-dimethylurea). The synthesis of an isostructural framework with different templating agents was successful. However, 25% less of the templating agent was present due to the larger size of the cation.

Replacement of the NH_4^+ ions through ion-exchange is possible. Maeda and coworkers studied the cation exchange of ZnBP-NH_4 with alkali metal cations: Na^+, K^+, Rb^+ and Cs^+ ions.[194] A larger affinity for Rb^+ ions in aqueous alkali metal mixtures was determined due to cation size.[194] Maeda and coworkers did not investigate ion-exchange with Li^+ ions. Our preliminary study resulted in ion-exchange of the NH_4^+ with Li^+ ions. The ion-exchange reaction using $LiOH{\cdot}H_2O$, resulted in $Zn_{2.5}(C_6H_3O_9P_3)(H_2O)_2(Li)_{1.31}(OH)_{0.31}$ with all cation positions occupied with Li^+ ions.

Both PCMOF-3 and ZnBP have pores with water molecules which could be used as proton conductors. A difference in proton conductivity should occur due to differences in mobility, type of the charges and structural differences in the framework s. An increase in proton conductivity for ZnBP-NH_4, is possible because of the decrease in size of the pores, and thus an improved ion pathway.

Additionally, lithium ion conductivity could occur. In the dehydrated phase, free volume is loss and the Li^+ ions are believed to occupy the larger pores. This creates an improved ion pathway and therefore the potential for lithium ion conductivity should increase. Conductivity studies still need to be investigated.

This material highlights that the negative expansion exhibited in MOFs either by loss in some solvent molecules or temperature influences the positions of the guest molecules and thereby the possible applications due to the guest molecules.

Conclusions

The one-step hydrothermal synthesis resulted in isostructural materials with different cations: (ZnBP-NH_4 and ZnBP-CH_3NH_3). The cations can be exchanged for lithium ions. The reversible dehydration process was studied by both *in situ* X-ray diffraction and solid state NMR which revealed two additional phases. The structures for all phases were determined (phase II and phase III). The reversible dehydration process caused the ZnBP framework to exhibited negative expansion due to a phase change. The loss in free volume forces the lithium or ammonium ions to occupy the larger pores in the dehydrated phase. Maximum lithium conductivity should be found in the dehydrated

phase due to forced alignment of lithium ions in the pores. Studies pertaining to both proton and lithium conductivity for ZnBP are being pursued.

CHAPTER V

REVERSIBLE DEHYDRATION BEHAVIOR REVEALS COORDINATIVELY UNSATURATED METAL SITES IN MICROPOROUS CRYSTALLINE ALUMINUM PHOSPHONATES

Introduction

Metal organic frameworks (MOFs), built from ligands containing phosphonic acids rather than carboxylates have been suggested, however obtaining highly crystalline porous materials is challenging.[16,21,74,85,89,90,211] Phosphonic acids strongly coordinate to a wide range of metals and show both chemical and high thermal stability which makes them advantageous over carboxylate analogues. Highly crystalline, open-framework metal phosphonates have been recently reported.[74,76,85,89,211] These materials do not have the traditional pillar architecture that is generally found for metal phosphonates.[74,85,89,211] Unlike MOFs with isolated metal clusters or atoms, extended arrays are favored due to the tetrahedral geometry of the phosphonate group. The pillared architecture is formed by closely packed pillars which link the inorganic layers, resulting in nonporous materials.

The structures of the "non-traditional" metal phosphonates result from unique aspects of the ligands that are used. The heterofunctional ligands N,N'-piperazinebis-(methylenephosphonic acid) and N,N,N'-4,4'-bipiperidinebis(methylenephosphonic-acid)) were used to synthesize isorectucular structures where the pore size increased from 0.9 nm to 1.8 nm.[74,85,211] The protonated amino group balanced the overall charge.

The materials have permanent porosity and coordinatively unsaturated metal sites upon loss of coordinated water, which is extremely important for gas adsorption applications.[74,85,211]

Several porous structures have been published using phosphonate esters in the initial synthesis.[89,90] These materials involve phenylenediphosphonate esters. The use of this ligand in the acid form has resulted in many pillared architectures.[61,91] However, by eliminating use of one phosphonate oxygen atom by careful synthetic control, the ligand acts in a manner similar to a carboxylic acid group used in MOFs but does not form the same pillared architecture[89,90].

The continuous nucleation of the inorganic structure could also be prevented by a small ligand coordinating to the metal ion which does not have additional coordinating groups. These ligands could range from water molecules[212,213], fluoride ions[92], phosphates[7] to amines[72]. Reported herein are three highly crystalline aluminum phenylenediphosphonates $Al(H_2O)(O_3PC_6H_4PO_3H)$, $Al_4(H_2O)_2(O_3PC_6H_4PO_3)_3$ and $Al(O_3PC_6H_4PO_3)_{0.75}\cdot 2H_2O$ that exhibit reversible dehydration behavior which has a dramatic influence on permanent porosity of the material. The stability of the dehydrated phase is a result of the geometry of the aluminum atom which in some cases has coordinatively unsaturated metal sites.

Experimental section[2]

Materials

All reagents were used as purchased with no further purification. The ligands 4,4-phenylenediphosphonic acid (H_4MPDPA) was prepared by an adapted literature procedure.[159] The aluminum source, bayerite ($Al(OH)_3$), was also prepared according to the literature procedure.[214,215]

*Hydrothermal synthesis of $Al(H_2O)(O_3PC_6H_4PO_3H)$, (**1.5**)*

The hydrothermal reaction was carried out with 4 mL of ddi water and 2.5 mL of conc. HCl which was added to a 12 mL capacity PTFE-lined pressure vessel containing 0.111 g (1.42 mmol) of bayerite and 0.321 g (1.34 mmol) of H_4MPDPA. The sealed reaction vessel was then heated to 160 ^oC for 5 d. The resulting white powder was filtered, washed with ddi water and acetone and then air dried. Initial pH: -1.00, Yield: 0.262 g. Elemental analysis (%) and microprobe Al/P ratio Calc: C 25.73, H 2.52, P/Al ratio 2.00. Exp: C 25.6, H 2.5, P/Al ratio 1.99

*Synthesis of $Al(O_3PC_6H_4PO_3H)$, (**1d.5**)*

Dehydration of $Al(O_3PC_6H_4PO_3H)\bullet H_2O$ at 200 ^oC overnight results in $Al(O_3PC_6H_4PO_3H)$ quantitatively. Elemental analysis (%) and microprobe Al/P ratio Calc: C 27.50, H 1.92, P/Al ratio 2.00. Exp C 27.4, H 1.9, P/Al ratio 2.00.

[2] The solid state NMR studies were carried out in full by Dr. Vladimir I. Bakhmutov. The hydrogen adsorption experiment was conducted by Julian Sculley.

*Synthesis of $Al_4(H_2O)_2(O_3PC_6H_4PO_3)_3$, **(2.5)***

$AlCl_3$ (0.5684 g, 4.26 mmol) and H_4MPDPA (0.1681 g, 0.706 mmol) were placed in a 12 mL Telfon-lined autoclave and filled with ddi water (4 mL) and heated at 210 ^oC for 5 d. The white gel was washed with ~200 mL of water and dried in an oven at 70 ^oC giving a white powder. Initial pH: -0.124, Yield: 0.162 g. Elemental analysis (%) and microprobe Al/P ratio Calc: C 25.6, H 1.91 P/Al ratio 1.50 Exp: C 23.0, H 2.57 P/Al ratio 1.44 (Discrepancies between elemental analysis and formula may be due to surface water or water molecules not located in the channels of the crystal structure).

*Synthesis of $Al_4(O_3PC_6H_4PO_3)_{2.84}(OH)_{0.64}(H_2O)_4$, **(3.5)***

$AlCl_3$ (0.5684 g, 4.26 mmol) and H_4MPDPA (0.1682 g, 0.707 mmol) were placed in a 12 mL Telfon-lined autoclave and filled with ddi water (2.5 mL)/ acetone (1.5 mL) and heated at 210 ^oC for 5 d. The product was washed with ~200 mL of water/acetone mixture and dried in an oven at 70 ^oC giving a white powder. Initial pH: -0.789, Yield: 0.169 g. Elemental analysis (%) and microprobe Al/P ratio Calc: C 23.9, H 2.36 P/Al ratio 1.42, Exp: C 22.0, H 2.91 P/Al ratio 1.42

Characterization

Elemental analysis for carbon, nitrogen and hydrogen (C, N and H) was performed by Atlantic Microlab, Inc. The Al:P ratio were determined on a four spectrometer Caeca SX50 electron microprobe using a PGT energy-dispersive X-ray system at an accelerating voltage of 15 KV at a beam current of 20 nA. All quantitative work employed wavelength-dispersive spectrometers (WDS). Analyses were carried out after standardization using very well characterized compounds or pure elements.

Thermogravimetric analyses were carried out on a T.A. Instrument TGA Q-500. The samples were heated from 30-1000 °C using a heating rate of 10 °C/min with a 90/10 air /N_2 flow. A Bruker Advance 400 Solids NMR spectrometer equipped by a standard 7, MAS probe head was used to acquire solid state $^{27}Al\{^1H\}$ and $^{31}P\{^1H\}$ MAS NMR operating at a 5 kHz spinning rate for both $^{27}Al\{^1H\}$ and $^{31}P\{^1H\}$ with 0 ppm for $AlCl_3$ and H_3PO_4 as external chemical shift standards. N_2 sorption-desorption isotherms were obtained on a Quantachrome Autosorb-6 instrument at liquid nitrogen temperature. Compound 1 was dried in the oven for 12 h at 150 ^oC and then degassed under vacuum at 200 ^oC for 20 h on a Quantachrome degasser. All other compounds were dried in an oven over night at 150 ^oC and then degassed under vacuum at 180-210 ^oC for 20 h Quantachrome degasser. Surface areas were derived from the isotherms by the BET and *t*-plot methods. Some powder patterns were obtained on the Bruker D8-Focus Bragg-Brentano X-ray Powder Diffractometer operating with Cu radiation (1.54 Å).

In situ X-ray diffraction hydration study

All synchrotron powder diffraction data for the *in situ* X-ray diffraction hydration experiments were recorded on 1-BM-C at Advance Proton Source (APS), Argonne National Laboratory (Argonne, USA) with an average beamline wavelength of 0.6124 Å. Data collection was performed with a Perkin-Elmer flat panel area detector (XRD 1621 CN3-EHS) over the angular range 1-25° 2θ.

Samples were loaded in a kapton capillary (0.9 mm diameter), which was attached to the flow-cell setup for *in situ* synchrotron PXRD measurements. The samples were heated with a heating rate of 3 $Kmin^{-1}$ with a He-gas flow to reach the

target temperature and then cooled down to 298 K. To rehydrate the materials at 298 K, the samples are exposed to water vapor with a He-gas flow.

High resolution synchrotron PXRD

Samples were loaded in Kapton capillaries (0.9 mm diameter) and mounted on bases provided by the Advance Photon Source (APS), Argonne National Laboratory. The samples were mailed to APS for analysis. High resolution synchrotron powder diffraction data were collected using beamline 11-BM with an average wavelength of 0.41625 Å for all compounds. Two platinum-striped mirrors and a double-crystal Si(111) monochromator are used for the X-ray optics[216]. The data points were collected at room temperature with a step size of 0.001^{o} 2θ and scan speed of 0.01 ^{o}/s. Data are collected while continually scanning the diffractometer 2θ arm. High resolution and short collection time is obtained by using a unique 12-element Si (111) crystal analyzer/detector .[217] For quick and precise sample exchange, a Mitsubishi robotic arm is used to mount and dismount samples on the diffractometer.[218] Sample **1.5**, **1d.5** and **2.5** were collected at 295 K. Additional steps were taken for sample **2d**, the dehydrated phase of **2.5**. Sample **2d.5** was heated at 450 K for 1 h prior to data collection and then collected at 450 K.

Structure determination

A set of approximately 20 Bragg peaks were used by the index procedure[198] in the TOPAS program[199] to determine the unit cell. Evaluation of the unit cell and all possible space groups were analyzed by the "profile matching mode" (Le Bail decomposition[200]) with the TOPAS program. Analysis for systematic absences and best

profile matching led to the correct space groups. The initial models for compounds **1.5**, **1d.5** and **2.5** were found by the charge flipping method[219,220] in the TOPAS program. This method was unsuccessful for compound **2d.5** therefore the initial model was found by direct space methods in the FOX[201,202] program. The initial model was found using the following scattering unit, $Al_2(O_3PC_6PO_3)(O_3PC_3)$. The parallel tempering algorithm was used by the global optimization procedure. The structure and geometry of organic ligands in the initial models were corrected to reasonable values using the SHELXTL suite[127].

The high resolution synchrotron PXRD data were used in the Le Bail decomposition to refine the unit cell and profile parameters in JANA2006[203]. The background was defined using either 20 Legendre or Chebyshev polynomials. The background term 1/x was used for compound **1.5** and **2.5**. Additionally for compound **2.5**, an anisotropic strain broadening[221] term was applied. The peak shape profiles were defined by a pseudo-Voigt function. A Rietveld refinement was successful for compounds **1.5**-**2d.5**. The crystallographic and refinement parameters are given in Table 8. H atoms were geometrically placed and fixed before the final refinement. Rietveld fits are given in supplementary data (Appendix D, Figure D 1and D 8).

Table 8. Crystallographic and refinement parameters

Compound	**1.5**	**1d.5**	**2.5**	**2d.5**
Chemical formula	$C_6H_7AlO_7P_2$	$C_6H_5AlO_6P_2$	$C_9H_6Al_2O_{10}P_3$	$C_9H_6Al_2O_9P_3$
M_r	280	262	421	405
Crystal system, space group	Monoclinic $P2_1/c$	Monoclinic $P2_1/c$	Monoclinic $C2/m$	Triclinic $P\bar{1}$
Temperature (K)	295	295	295	453
a, *b*, *c* (Å)	10.05306 (4) 9.22355 (4) 10.09498 (4)	9.8780 (1) 8.7643 (1) 10.1088 (1)	38.186 (1) 5.0041 (1) 8.3810 (2)	8.5943 (3) 4.9707 (1) 19.5499 (6)
β (°)	104.7759 (3)	105.5357 (1)	102.535 (3)	98.870 (4) 105.933 (2) 89.598 (3)
V (Å^3)	905.10 (1)	843.19 (2)	1563.34 (7)	792.91 (4)
Z	4	4	4	2
Radiation type	Synchrotron λ=0.41398Å	Synchrotron λ=0.41241Å	Synchrotron λ=0.42463 Å	Synchrotron λ=0.41397Å
Diffractometer at	APS 11-BM-B	APS 11-BM-B	APS 11-BM-B	APS 11-BM-B
Scan method	Continuous	Continuous	Continuous	Continuous
2θ values (°)	$2\theta_{min}$=0.501 $2\theta_{max}$=38 2 θ_{step}=0.001	$2\theta_{min}$=2.001 $2\theta_{max}$=37.999 $2\theta_{step}$=0.001	$2\theta_{min}$=1.001 $2\theta_{max}$=33.999 $2\theta_{step}$=0.001	$2\theta_{min}$=1.101 $2\theta_{max}$=24.999 $2\theta_{step}$=0.001
R factors and	R_p=0.076 R_{wp}=0.098 R_{exp}=0.065 $R(F)$ =4.19 χ^2= 2.250	R_p=0.080 R_{wp}=0.097 R_{exp}=0.077 $R(F)$ =3.86 χ^2= 1.850	R_p=0.138 R_{wp}=0.176 R_{exp}=0.102 $R(F)$ =10.74 χ^2= 3.028	R_p=0.089 R_{wp}=0.114 R_{exp}=0.075 $R(F)$ =3.28 χ^2= 2.310
No. of data points	37501	37500	49497	49496
No. of parameters	94	87	75	104
No. of restraints	3	7	49	38

Results and discussion

*Compound **1.5** and **1d.5***

The structure of compound **1.5** was determined from PXRD data (Figure 48). Compound **1.5**, $Al(O_3PC_6H_4PO_3H)\cdot H_2O$, crystallized in the monoclinic $P2_1/c$ space group and the asymmetric unit consists of one Al(III) ion, one water molecule and one HMPDPA molecule. The inorganic layer in the (*b*,*c*)plane, is built from AlO_6 octahedra bridged together by O-P-O bridges to form 8- and 16-member rings (Figure 48, right). Oxygen atoms from five distinct phosphonate moieties and one water molecule form the

AlO_6 octahedron. The free space in the 16-member ring is occupied by two symmetry dependent water molecules that protrude into the ring. The 2D layer described so far is interlinked by the HMPDPA molecule along the [100] direction to form a 3D framework (Figure 48, left). One proton remains on the phosphonate group for charge balance. The compound could be described as an I^2O^1 framework using the notation I^mO^n where m and n stand for the dimensionality of the inorganic and organic connectivity, respectively[39]. Interestingly, the inorganic layer is similar to metal ethylenediphosphonates with the formula M(III) $(H_2O)(O_3P(CH_2)_2PO_3H)$ (M = Fe, Ga, Al).[213] The pendent protonated oxygen found in both of these systems is relatively rare with iron/aluminuim/gallium structures.[213]

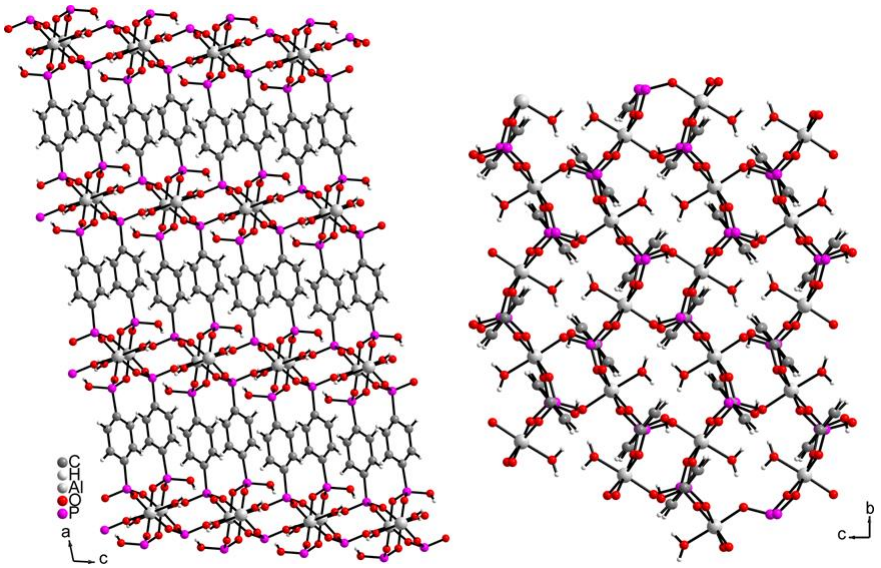

Figure 48. Two views of compound **1.5** showing the view of how the pillars link the inorganic layer together (left) and the connectivity of the inorganic layers (right)

Upon dehydration of compound **1.5**, the material retained the I^2O^1 framework and converted to $AlO_3PC_6H_4PO_3H$ (**1d.5**) (Figure 49**).** In compound **1.5**, the aluminium atom has octahedral geometry but with loss of a water molecule the geometry of the aluminum atom would then be square pyramidal without rearrangement of the inorganic framework. The geometry of the aluminum atom was determined to be trigonal bipyrmidal therefore rearrangement of the inorganic framework occurred and can be clearly seen in Figure 50**.** The monoclinic space group $P2_1/c$ was determined for compound **1d.5**, however changes in the structure caused by dehydration can be described by a comparison of the crystallographic data for compound **1.5** and **1d.5**. The *a*-axis is slightly shortened upon dehydration (Table 8), but this does not significantly affect the inorganic interlayer distance (7.266 and 7.296 Å for **1.5** and **1d.5** respectively). Viewed down the *b*-axis the crystal structures for **1.5** and **1d.5** have similar pillared structures where phenylenediphosphonate bridges the inorganic layers. The *b*-axis is shortened and has an effect on the inorganic layer, lying in the (*b*,*c*) plane. As the geometry transforms from octahedral to trigonal pyramidal (Figure 51), the *b*-axis is shortened and the free space in the 8 and 16-member ring decreases: (a,b = 4.5,8.2 Å and 3.5, 8.2 Å for compound **1.5** and **1d.5**, respectively, Figure 51). Thus dehydration causes a change in the aluminum geometry, which results in a decrease in both *a*- and *b*-axis and a decrease in volume of the unit cell (loss of 62 $Å^3$).

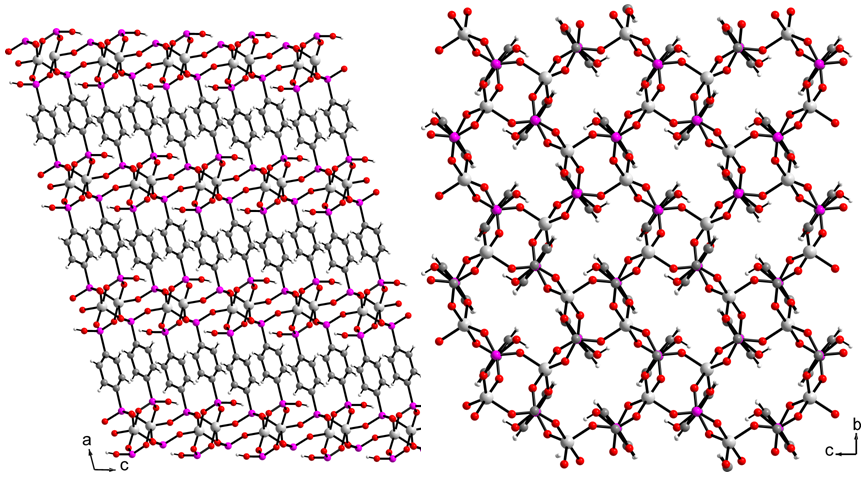

Figure 49. Crystal structure of compound **1d.5** showing a view down *b*-axis (left) and *a*-axis (right) showing the inorganic layer

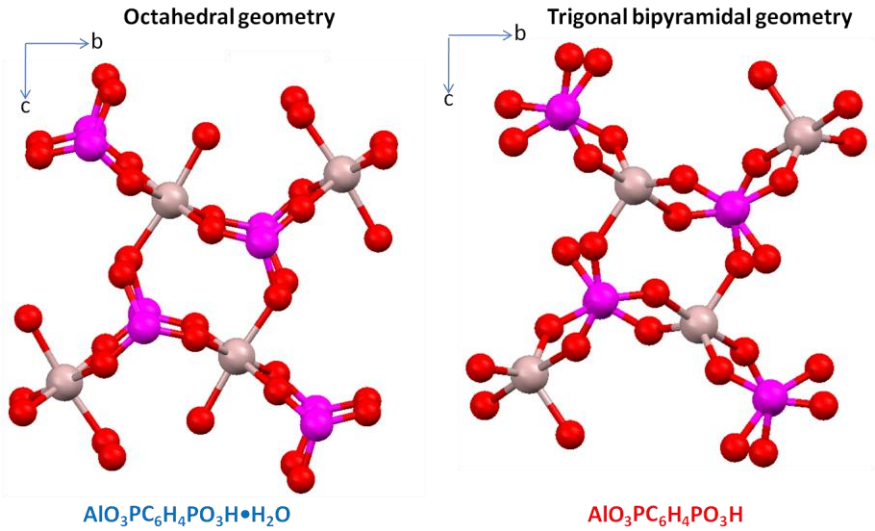

Figure 50. A view showing a comparison of the coordination and geometry around the aluminum atoms and the rotation in the phosphonate groups after dehydration (compounds **1.5** (left) and **1d.5** (right))

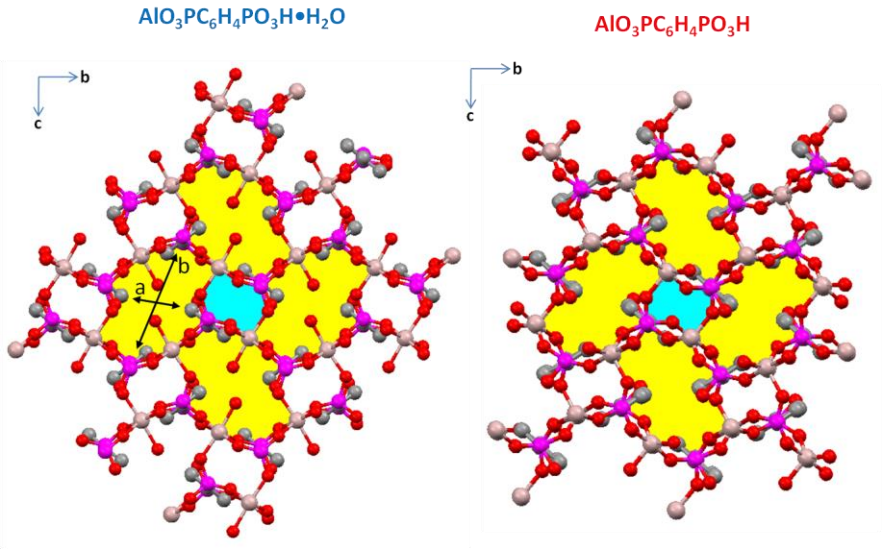

Figure 51. A comparison of the several distances in the inorganic layers for compound **1.5** (left) and **1d.5** (right) showing a decrease in free space in the 16-member rings

*Compound **2.5** and **2d.5***

The structure of compound **2.5** has been determined from PXRD data (Figure 52). Compound **2.5**, crystallized in the monoclinic *C*2*m* space group and the asymmetric unit consists of two Al(III) ions, one and a half MPDPA molecules and one water molecule. The aluminum species, AlO_4 and AlO_6, are coordinated to four or five distinct oxygen phosponate atoms, respectively, with the AlO_6 group bonding to an additional water molecule. The inorganic layer in the (*b*,*c*)plane, is built from double metal chains bridged in the [001] direction forming 12-member rings (Figure 52, right). The double metal chain is built from columns of AlO_6 octrahedra and AlO_4 tetrahedra running in the [010] direction. The inorganic layers are bridged by two distinct alternating pillared layers in the [100] direction. The first pillared layer is a traditional layer where the

pillars are spaced close together to form a densely packed structure. The second pillared layer is a "non-traditional" layer, where the pillars are spaced apart such that channels are formed. The water molecule coordinated to the AlO_6 can be clearly seen to protrude into the interlayer spacing of these channels. Based on elemental analysis and TGA (10.4 wt% water) additional water may be present within the pores but could not be determined from the PXRD data. The formula $Al_4(H_2O)_2(O_3PC_6H_4PO_3)_3(H_2O)_4$ better represents both the elemental and TGA data. The structure could be described as a I^2O^1 framework.[39]

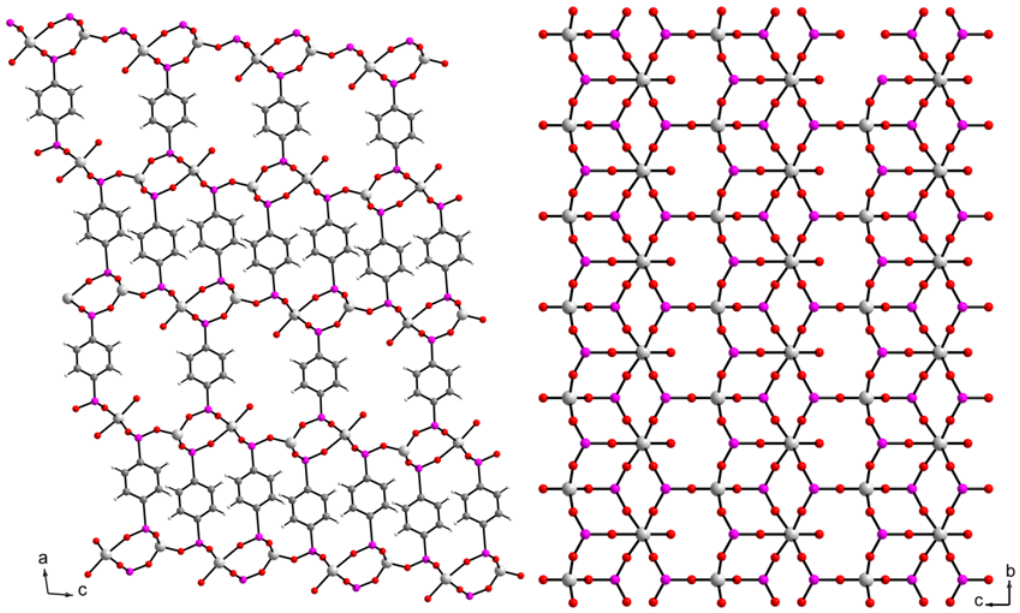

Figure 52. Crystal structure of compound **2.5** viewed down the *b*-axis (left) and the *a*-axis (right) showing the inorganic layer

Upon dehydration of compound **2.5**, the compound was converted to $Al_4(O_3PC_6H_4PO_3)_3$ (**2d.5**) with the octahedral aluminum atom losing one coordinated water molecule (Figure 53). The loss of water did not change the I^2O^1 framework[39] but differences in the structures were found. The triclinic $P\bar{1}$ space group was determined with the asymmetric unit consisting of one MPDPA molecule, half a MPDPA molecule, a tetrahedral aluminum atom (AlO_4) and a five-coordinate aluminum atom (AlO_5). The geometry of the AlO_5 was determined to be a distorted square pyramidal. To accommodate the new metal geometry, the phosphonate groups rotate from the original positions altering the inorganic layer (Figure 54). The distance between the double metal chains which build the inorganic layer increased from 8.381 to 8.594 Å upon loss of water. This increases the width of the channels. However, along the [010] direction there is no significant change in the structure (Al….Al distance: 5.004 and 4.971 Å for **2.5** and **2d.5**).

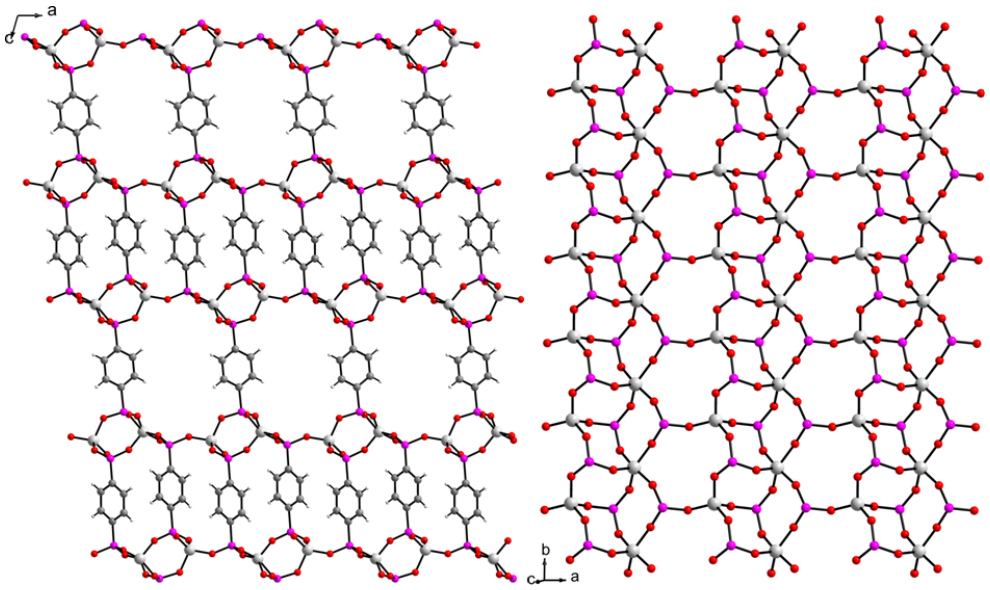

Figure 53. Crystal structure viewed down two different axis of the dehydrated phase (**2d.5**) of compound **2.5**

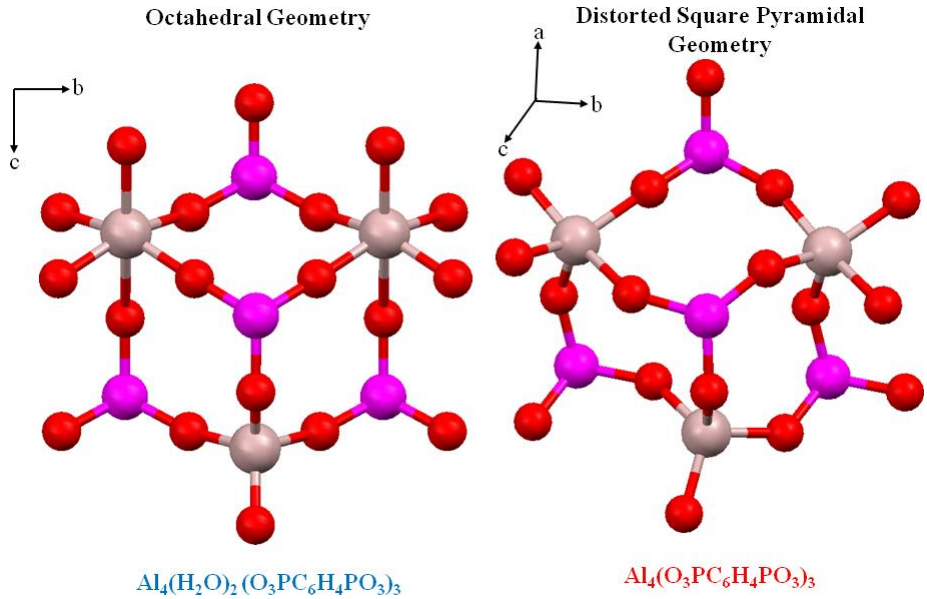

Figure 54. A view showing a comparison of the coordination and geometry around the aluminum atoms and the rotation in the phosphonate groups after dehydration (compounds **2.5** (left) and **2d.5** (right))

*Compound **3.5***

Although in reactions **2.5** and **3.5** the same ligand, H_4MPDPA, was used again as with compound **1.5**, three different PXRD patterns were recorded (Figure 55). A decrease in crystallinity is observed in changing the source of aluminum from bayerite to aluminium chloride; however, other factors may play a role as well, such as solubility. Similar d-spacings were found when the solvent was changed from water for **2.5**, to a mixture of water/acetone for **3.5**. However, other differences are seen in the PXRD patterns of compound **2.5** and **3.5** indicating different structures were formed from the two different solvent systems. The crystal structure for **3.5** could not be obtained due to the poor powder crystallinity, however continuing efforts are being made to determine the structure. Differences can be seen in the PXRD patterns for **3.5** and its dehydrated phase (**3d.5**) (Figure D 9).

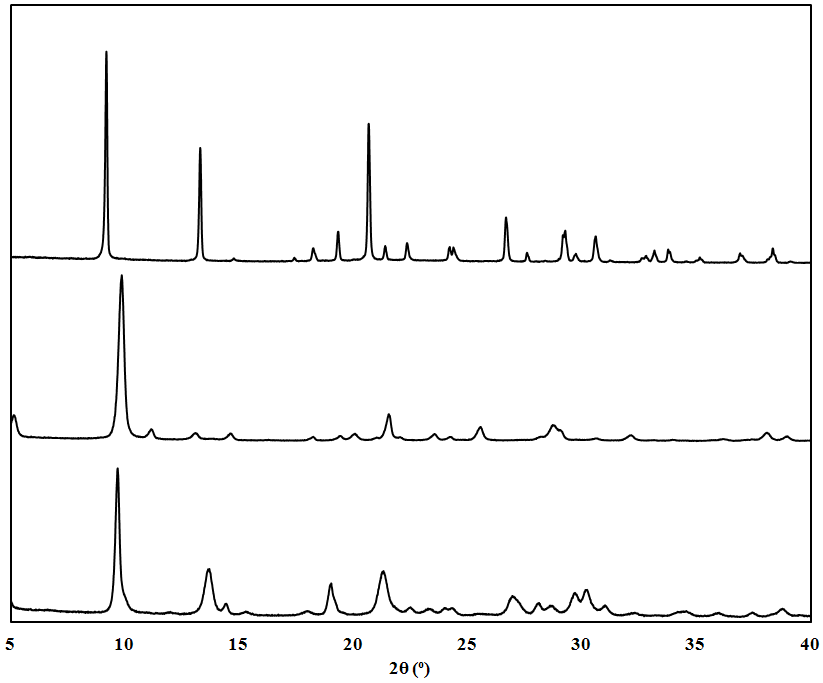

Figure 55. X-ray diffraction powder patterns of the different aluminum compounds: compounds **1.5** (top), **2.5** (middle) and **3.5** (bottom). (Powder pattern was obtained on the Bruker D8-Focus Bragg-Brentano X-ray Powder Diffractometer, Cu (λ = 1.542 Å) radiation)

Thermal effects

For reactions **1.5** and **2.5**, a change in the reaction temperature resulted in phase changes in the compounds (Figure 56 and D 10). For both reactions two phases were obtained: one at low temperature and one at high temperature. The low temperature phase for reaction **1.5** was not isolated. Interestingly, the low temperature phase for reaction **2.5** resulted in compound **1.5** except it is less crystalline (Figure D 11and D 12). It is interesting that different reaction conditions resulted in the same material. Similar behavior would be expected for compounds **2.5** and **3.5** which differ only in the solvent

systems. However, for reaction **3.5** no phase change occurred with change in reaction temperature; rather increase in reaction temperature lead to an increase in crystallinity (Figure D 13) and solid state NMR also suggest similar structures (Figure D 13).

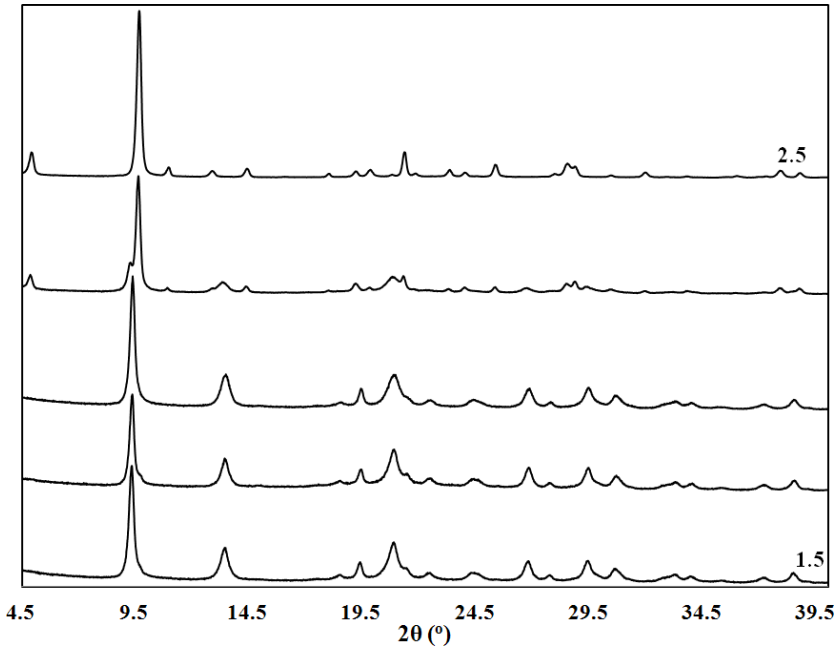

Figure 56. A series of X-ray diffraction powder patterns where the reaction temperature was varied from 120 ^{o}C (bottom, compound **1.5**) to 210 ^{o}C (top, compound **2.5**), showing a phase change with increase in temperature. (Reaction temperatures from bottom to top: 120, 140, 160, 180, 210 ^{o}C) (Powder pattern was obtained on the Bruker D8-Focus Bragg-Brentano X-ray Powder Diffractometer, Cu (λ = 1.542 Å) radiation)

Solid state NMR

Solid state ^{27}Al{^{1}H} and ^{31}P{^{1}H} NMR reveal differences in the structures for compounds **1.5-3.5** (Figure 57). The ^{27}Al{^{1}H} NMR spectra show relatively broad peaks for compounds **1.5-3.5** (-24.3 to -29.6 ppm, respectively) which are characteristic for

aluminum sites with octahedral oxygen environments.[45,46,93] The line shapes are characteristic for quadrupolar splitting interaction.[222] Additionally, less broad peaks in the region 38-39 ppm are observed for compounds **2.5** and **3.5** which are characteristic for aluminum sites with tetrahedral oxygen environments.[46,222] The $^{31}P\{^{1}H\}$ NMR spectra show multiple peaks in the range of 4.5 to –10 ppm which are characteristic of phosphonates.[46] Peaks in the region –7 to -10 ppm region for compound **2.5** do not appear in the $^{31}P\{^{1}H\}$ NMR spectra for **3.5** although both have four and six-coordinate aluminum atoms. Considering this and the PXRD data three different compounds have been synthesized using the ligand H_4MPDPA.

The dehydration of compound **1.5** and **2.5** resulted in changes in the aluminum coordination. In the $^{27}Al\{^{1}H\}$ NMR for compound **1d.5**, the chemical peak shifts from the six-coordinate atom range to a five-coordinate atom range upon dehydration (Figure D 15).[93,222] A similar chemical shift would be expected for compound **2d.5**.

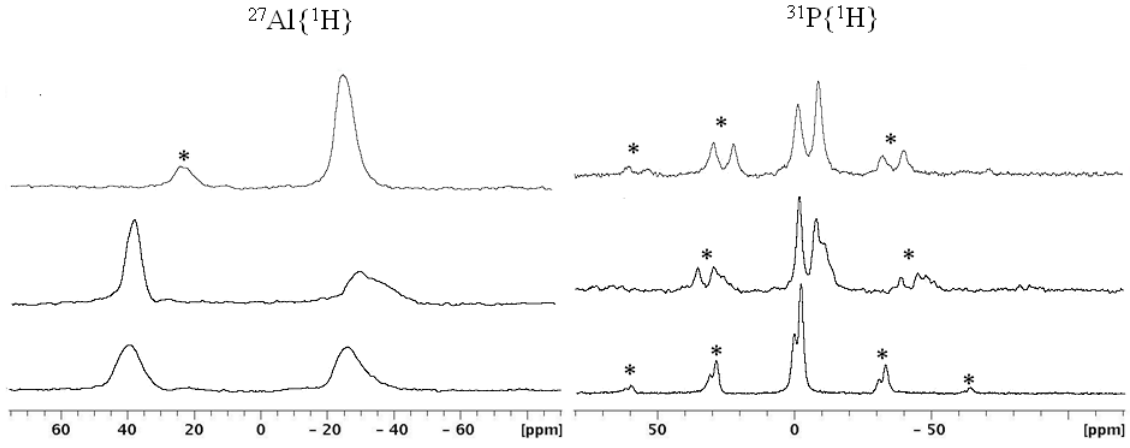

Figure 57. ^{31}Al and ^{31}P NMR spectra for the aluminum phosphonates: compounds **1.5** (bottom), **2.5** (middle) and **3.5** (top). The symbol * represent side bands

Thermal gravimetric analysis

The thermal gravimetric analysis data differs for compounds **1.5**-**3.5** (Figure 58). Compound **1.5** has a three step weight loss. The first weight loss occurs at ~180 ^{o}C and is attributed to coordinated water molecules. The structure of the dehydrated phase was determined (**1d.5**), and is stable up to ~440 ^{o}C, where a small weight loss occurs, after which decomposition of the material occurs at 740 ^{o}C. The second weight loss may involve the loss of the acidic proton. Compound **2.5** has one weight loss step before decomposition (515 ^{o}C) and occurs below 100 ^{o}C. It is attributed to loss of water molecules and the resultant structure was determined (**2d.5**). Compound **3.5** has two weight losses before decomposition (515 ^{o}C). The first is below 100 ^{o}C and the second occurs at ~120 ^{o}C. Both are attributed to water molecules in slightly different environments. Interestingly, full decomposition did not occur for all compounds under these conditions, indicating high thermal stability. The dehydrated phases for compound **2.5** and **3.5** are stable to ~515 ^{o}C.

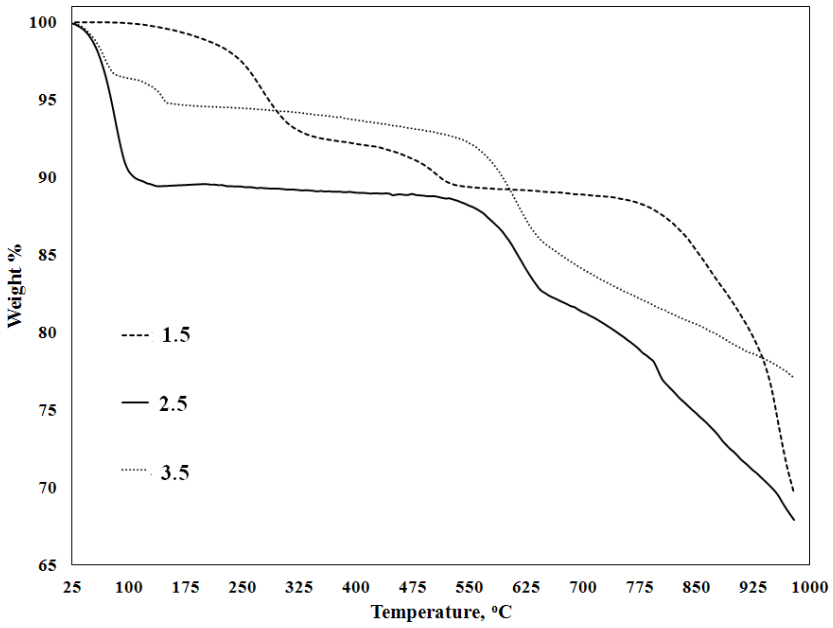

Figure 58. Thermogravimetric analysis of the three different aluminium phosphonates

Textural properties

The textural properties of the materials have provided interesting insight into the structures (Figure 59). The N_2 adsorption isotherms indicate that compounds **2.5** and **3.5** have a type I isotherm suggesting uniform microporosity. Compound **2.5** was found to have the largest surface area (Table 8) which is in contrast to general trends; increase in reaction temperature generally decreases porosity.[39,40] The high temperature phase, **2.5**, was found to have a larger surface area than the low temperature phase. The change in reaction solution from water for **2.5**, to a water/acetone mixture for **3.5** resulted in a decrease in surface area; however, both were greater than 80% microporous. At 10^{-3} P/P_o the volume is already at 75 and 46 cc/g respectively for compounds **1.5** and **2.5**, after which there is a very shallow slope to ~0.80 P/P_o. This indicates that the pores were

mostly full at very low P/P_o and the pore size must be less than 10 Å. The thermal gravimetric analysis shows a one-step weight loss for compound **2.5** and a two-step weight loss for compound **3.5** below 250 ^oC, associated with loss of water. These data suggest that the pore structures are different for compounds **2.5** and **3.5**.

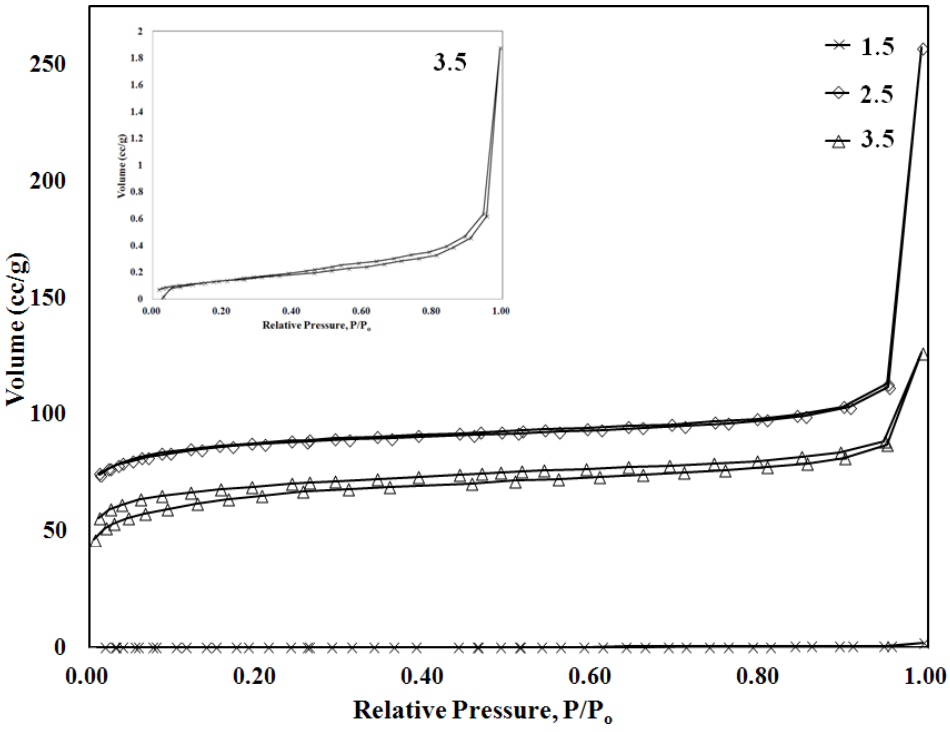

Figure 59. Nitrogen adsorption isotherms for compounds **1.5**-**3.5**

Table 9. Textural parameters calculated for compound **2.5** and **3.5**

Sample	S_{BET} (m^2/g)	Microporosity (%)
2.5	312.1	88
3.5	217.1	81

Additionally, based on thermal gravimetric analysis (Figure 58), all compounds lose water, a telling sign for porosity. However, a type III isotherm indicating a nonporous material was found for compound **1.5**. The inorganic layer for **1.5** differs most from **2.5** and **3.5**, where only a six-coordinate aluminum atom is present. The difference in surface area can be explained by the reversible dehydration behavior exhibited by both compounds **1.5** and **2.5**.

In situ X-ray diffraction

Reversible dehydration behavior was found for all compounds, with only compound **1.5** having a stable dehydrated phase (**1d.5**). $^{27}Al\{^{1}H\}$ and $^{31}P\{^{1}H\}$ NMR studies were performed on the initial phase and the dehydrated phase for compound **1.5**. *In situ* PXRD was used to study the dehydration process for compounds **2.5** and **3.5** where rehydration occurs rapidly upon exposure to air (Figure 60). *In situ* PXRD diffractograms show a change in diffraction peak positions upon heating and a rapid conversion to the hydrated phase upon exposure to water for compounds **2.5** and **3.5**. Upon loss of water for compound **2.5**, a more dramatic shift in the diffraction peak positions is observed in the PXRD diffractogram, indicating a larger change in the structure.

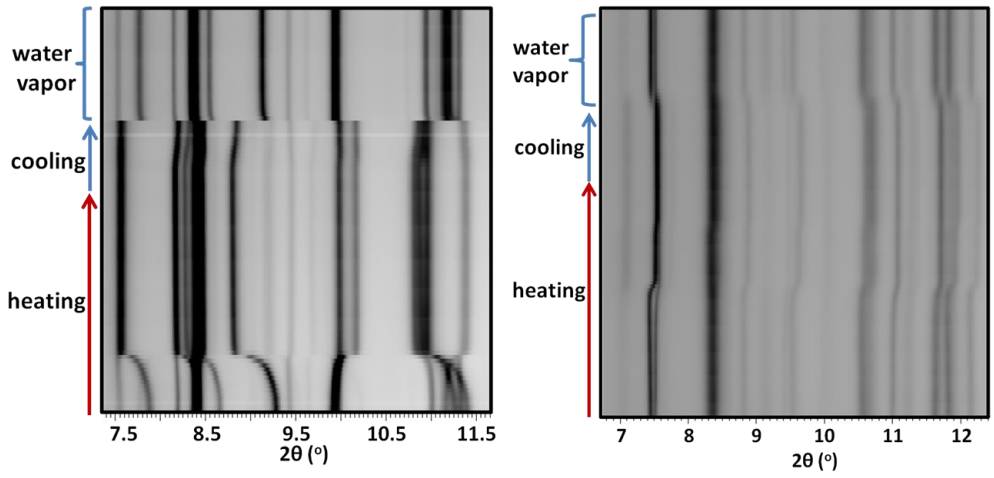

Figure 60. X-ray diffractograms of the *in situ* dehydration-rehydration studies for compound **2.5** (left) and compound **3.5** (right). In both cases reversible processes were observed

For compound **1.5**, the original structure can be regenerated from the dehydrated phase either by rehydration of water through exposure to the atmosphere for several months or refluxing in water overnight. Rehydration of water is rapid for compound **2.5** suggesting a less stable dehydrated phase than for compound **1.5**. The dehydration behavior of these materials can be described by the parent structures. In both compounds, the aluminum atom has an octahedral geometry with one oxygen atom from a water molecule. A five-coordinate metal would be expected from the loss of water. The geometry of the aluminum atom would then be square pyramidal without rearrangement of the inorganic framework. The geometry of the aluminum atom was determined to be trigonal bipyramidal for compound **1d.5** therefore rearrangement of the inorganic framework occurred, reducing free volume (Figure 50 and 51). However, for compound **2d.5** the aluminum atom has a distorted square pyramidal geometry (Figure

54). The slight change in geometry resulted in a wider channel which leads to having porosity.

A similar dehydration behavior to compound **2.5** was determined for $Al_2(OH)_2(H_2O)_2(O_3PCH_2CH_2PO_3)$ where the compound rehydrates upon exposure to air within five minutes.[212] The inorganic layer differs from the structures reported here; however, a distorted square pyramidal geometry was determined for the dehydrated phase.[212] The preference to adopt the trigonal bipyramidal geometry is restricted in both compound **2.5** and $Al_2(OH)_2(H_2O)_2(O_3PCH_2CH_2PO_3)$ by the rigid lattice. The distorted square pyramidal geometry results in an uncoordinated metal site which rapidly reabsorbs water. The activity of the uncoordinated metal site increases due to the preference to obtain an octahedral geometry. Coordinately unsaturated metal sites are important in gas adsorption properties and catalysts. Lewis acidity has been shown in microporous solids with accessible metal sites, so compound **2.5** is expected to show catalytic activity.

Conclusions

Three new aluminum phenylenediphosphonates ($Al(H_2O)(O_3PC_6H_4PO_3H)$ (**1.5**), $Al_4(H_2O)_2(O_3PC_6H_4PO_3)_3$ (**2.5**) and $Al(O_3PC_6H_4PO_3)_{0.75}\cdot 2H_2O$ (**3.5**)) were prepared under hydrothermal conditions using the same ligand and have strikingly different properties. All compounds exhibit reversible dehydration behavior. Compound **2.5** and **3.5** rapidly reabsorb water, while readsorption was much slower for compound **1.5**.The crystal structures of the hydrated and dehydrated phases were determined using PXRD data for compounds **1.5** and **2.5**. The aluminum coordination changed from octahedral to

distorted trigonal bipyramidal for compound **1.5** and to the less stable distorted square pyramidal geometry for compound **2.5** upon dehydration. The change in geometry of the aluminum ions helps to understand the difference in rehydration rates. Compounds **2.5** and **3.5** were microporous while compound **1.5** was found to be nonporous.

CHAPTER VI

DEVELOPMENT OF ALUMINUM HYBRIDS AS ION EXCHANGERS

Introduction

Metal diphosphonates are well known layered materials where the structure consists of an inorganic layer built from coordinating phosphonate groups to the metal ions.[9,61,91,112,158,212,213] The layers are cross-linked by an organic moiety forming a pillared structure. The pillars are regularly spaced forming densely packed materials. The interlayer distance is dependent on the length of the organic pillar that links the adjacent layers. Despite the formation of densely packed structures, synthesis of porous materials with microporosity as high as 416 m^2/g have been shown with mircopore distribution centered between 7-20 Å.[7,9] These materials are poorly crystalline, where the generation of pores is believed to be caused by two mechanisms: layer growth defects, where two adjoining layers are not cross-linked to create a large size distribution of micropores[7,9,10] and interparticle mesopores formed by stable aggregates of platelet particles, "house of cards arrangement"[11] (Figure 61). Increase in porosity due to layer growth defects was reported, with addition of a second ligand in the synthesis, resulting in hybrid metal phosphonates. More importantly, this allows for functionalization of the pore by using ligands with different R-groups. Hybrid metal phosphonates are of interest due to the ease at which pores can be functionalized and the tuneability of the pore density and dimensions.

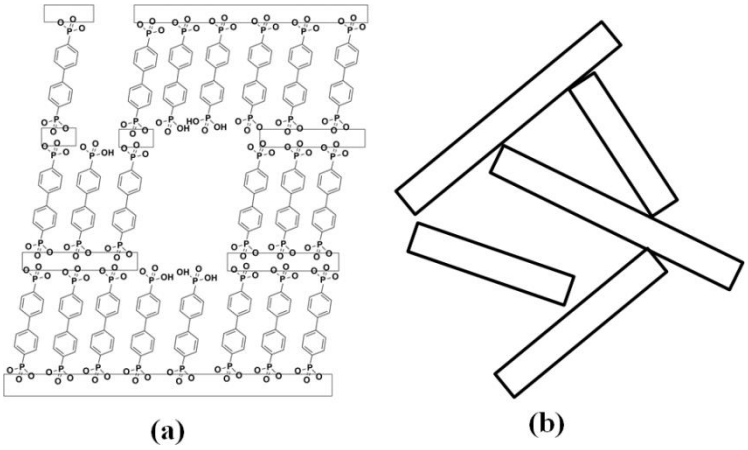

Figure 61. Proposed mechanisms for the formation of the two types of pores that occur in metal phosphonates: (a) layer growth defects and (b) aggregation of small platelets "house of cards arrangement"

Metal phosphonates have promise as ion exchangers by the ease at which new materials can be developed with different metal ion selectivity.[223] Burns and coworkers reported the separation of oxidized americium from curium with pillared M(IV) phosphonates as the ion-exchanger.[107] This separation is very important for developing technologies for treating spent nuclear fuel.[224] Ground and surface water are often polluted by radioactive uranium and thorium ions from mining causing serious environmental hazards.[225,226] Patel and coworkers reported a M(IV) phosphonate with high affinity towards thorium ions.[227] The affinity for different metal ions was further tailored by using different phosphonic acids and metals.[64,228-232]

The synthetic procedure has a profound impact on the properties of metal phosphonates.[11] Variation in pH, mole ratio of reactants, temperature, time and mixing rate can significantly change the environment of the ion exchange group and ultimately

ion exchange capacity. Changes in these parameters yield materials with different total porosity, pore structure, and particle size. This area of study provides continuously new materials with different ion exchange capacities.

In the present case of Al(III), variation in the synthetic conditions resulted in nine different aluminum(III) biphenylenediphosphonates with surface areas as high as 400 m^2/g.[111,123] Both mesopores and micropores are present in the materials. Functionalization of the pores occurred by incorporation of the secondary ligands phenyl phosphonate and phosphite.[111,123] The ease in which pore size and properties can be modified in hybrid aluminum biphenylenediphosphonates and the possibility of different ion affinities obtained with M(IV) phosphonates makes them attractive as ion exchangers. In the present study, temperature variation of the synthesis for aluminum biphenylenediphosphonate was investigated to determine the conditions best suited to develop ion exchange materials. Functionalization of the pore was carried out by addition of secondary ligands to determine if selectivity could be altered. Four different aluminum materials $Al_4(O_3PC_{12}H_8PO_3)_3 \cdot 8.75H_2O$, $Al(O_3PC_{12}H_8PO_3)_{0.5}(OH) \cdot 0.75H_2O$, $Al_4(O_3PC_{12}H_8PO_3)_{2.46}(HPO_3)_{1.08}(H_2O)_7$, and $Al_4(O_3PC_{12}H_8PO_3)_{2.46}(HOPO_3)_{1.08}(H_2O)_7$ were synthesized. The materials were studied to evaluate metal ion affinities.

Experimental section

Materials

Commercially available reactants ($AlCl_3 \cdot 6H_2O$, 99%, Baker Analyzed; phosphorous acid 99%, Aldrich; $Na_2S_2O_8$ 98%, Alfa Aesar) were used without further purification. The ligand 4,4'-biphenylenediphosphonic acid (BPDPA) was synthesized

according to a previous procedure.[11] All product yields were calculated based on aluminum content. No single crystal products were obtained.

Characterization

Powder X-ray data were collected on a BRUKER D8-Focus Bragg-Brentano X-ray Powder Diffractometer using Cu-Kα radiation (λ = 1.54178 Å). The powder patterns were recorded between 5^o and 40^o (in 2θ). Thermogravimetric analyses were carried out on a T.A. Instrument TGA Q-500. The samples were heated from 25 - 1000 °C using a heating rate of 10 °C/min with a 90/10 air /N_2 flow. A Bruker Avance 400 Solids NMR spectrometer was used to acquire solid state $^{27}Al\{^1H\}$ and $^{31}P\{^1H\}$ MAS NMR operating at 5-6 kHz for both ^{27}Al and ^{31}P with $AlCl_3 \cdot 6H_2O$ and H_3PO_4 as external chemical shift standards (0 ppm). IR spectra were recorded on a Thermo Scientific Nicolet 6700 FTIR spectrometer with a dry N_2 environment. Samples were mounted on KBr pellets with approximately 1% sample material. The Al:P:Cl: ratios were determine on a four spectrometer Caeca SX50 electron microprobe using a PGT energy-dispersive X-ray system at an accelerating voltage of 15 KV at a beam current of 10 or 20 nA .All quantitative work employed wavelength-dispersive spectrometers (WDS). Analyses were carried out after standardization using very well characterized compounds or pure elements. Elemental analysis for carbon, nitrogen and hydrogen (C, N and H) was performed by Atlantic Microlab, Inc. N_2 sorption-desorption isotherms were obtained on a Quantachrome Autosorb-6 instrument at liquid nitrogen temperature. The samples were dried in the oven at 80 ^{o}C for 12 h and then degassed under vacuum at 100 ^{o}C for

24 h on a Quantachrome degasser. Surface areas were derived from the isotherms by the BET and *t*-plot methods.

*Synthesis temperature for Al-materials **I** and **II***

In a typical synthesis, a 8:3 mmol ratio of $AlCl_3 \cdot 6H_2O$ (0.386 g, 1.60 mmol) and BPDPA (0.1894 g 0.603 mmol) were added to a 12 mL Teflon liner followed by a 3:1 solution of ethanol to ddi water (4 mL). The reaction vessels were sealed and placed in ovens 120, 140, 160, 180° C for 5 d. For the synthesis carried out in an oven at 210 ^oC the reaction time was 10 d. The products were centrifuged and washed with ~150 mL 3:1 solution of ethanol to ddi water. The white powders were dried overnight in a 60-80° C oven. Compound **I** (120 ^oC): $Al_4(O_3PC_{12}H_8PO_3)_3 \cdot 8.75H_2O$ Yield (based on Al): 0.218 g (45%) Elemental analysis (%) and microprobe Al/P ratio Calc: C 36.15, H 3.49, P/Al ratio 1.5. Exp C 36.31, H 3.31, P/Al ratio 1.48. Compound **II** (210 ^oC): $Al_6(O_3PC_{12}H_8PO_3)_3(OH)_6 \cdot 4.5H_2O$ Yield: 0.231g (68%) Elemental analysis (%) and microprobe Al/P ratio Calc: C 33.90, H 3.08, P/Al ratio 1.0 Exp C 33.70, H 2.56, P/Al ratio 0.95.

*Synthesis of bulk Al-hybrid materials **III,** $Al_4(O_3PC_{12}H_8PO_3)_{2.46}(HPO_3)_{1.08}(H_2O)_7$*

The synthetic procedure for the Al-hybrid with phosphite as the spacer was to have a 8:1.5:1.5 mmol ratio of $AlCl_3 \cdot 6H_2O$ (5.825 g, 24.1 mmol), BPDPA (1.420 g, 4.46 mmol) and phosphorous acid (0.371 g 4.63 mmol) added to a 82 mL Teflon liner followed by a 3:1 solution of ethanol to ddi water (60 mL).). The liner was sealed in a steel reaction vessel and heated at 120° C for 5 d. The product was centrifuged and washed with 150 mL 3:1 solution of ethanol to ddi water. The white powder was dried

overnight in a 60-80° C oven. Yield 1.76 g Elemental analysis (%) and microprobe Al/P ratio Calc: C 32.7, H 3.23, P/Al ratio 1.5. Exp C 32.65, H 3.57, P/Al ratio 1.44.

*Oxidation of phosphite to phosphate **III-ox**, $Al_4(O_3PC_{12}H_8PO_3)_{2.46}(HOPO_3)_{1.08}(H_2O)_7$*

In the typical synthesis to oxidize phosphite to phosphate, 1.00 g (0.923 mmol) of compound **2** was dispersed in 50 mL of ddi water containing 0.460 g (1.93 mmol) of $Na_2S_2O_8$ in a 100 mL round bottom flask. The solution was heated at 80 ^oC for 20 mins and then cooled to room temperature. The product was filtered, washed with ~200 mL ddi and air dried. Elemental analysis (%) and microprobe Al/P ratio Calc: C 32.2, H 3.18, P/Al ratio 1.5. Exp C 33.53, H 3.50, P/Al ratio 1.54.

Ion affinity determination

The general procedure for the uptake studies was to mix ~100 mg of sample in contacted with a 5 mL mixed solution containing either monovalent (Na^+ and Cs^+), divalent (Ca^{2+}, Sr^{2+}, Co^{2+} and Zn^{2+}), or tri/tetravalent (Yb^{3+}, Sm^{3+}, Nd^{3+}, Th^{4+}) metals on a vial carousel for 24 h at ~ 4 rpm. A typical mixed solution had 50 ppm each of the respective metal ions. The supernatant was removed and passed through a syringe filter (0.045μm). The initial concentration C_i and the final concentration C_f after contact with the Al-materials were measured using ICP-AES and Flame-AA (Cs ions) at Anderson Analytical. The values were used to calculate the distribution coefficients (K_d) with the following formula

$$K_d(\text{mL g}^{-1}) = \frac{(C_i - C_f)}{C_f} \times \frac{\text{Vsolution(mL)}}{m_{\text{solid(g)}}}$$

Results and discussion

Al-materials: Effect of reaction temperature

The role of reaction temperature on the formation and structure of the Al-biphenylenediphosphonates was studied by a series of reactions varying the temperature from 120 to 210 ^{o}C. The PXRD patterns reveal the semi-crystalline nature of the Al-materials with broad, weak reflections in the range from 5-40^{o} 2θ (Figure 62). The PXRD patterns change with the increase in temperature indicating a phase change. The first low angle reflection occurs at 6.79^{o} 2θ for the low temperature phase (**I**). A slight increase in crystallinity is observed with the increase in reaction temperature from 120 to 160 ^{o}C. A new low angle reflection (6.02^{o} 2θ) is observed with the reaction temperature at 180 ^{o}C, however, a very weak reflection still is present at 6.79^{o} 2θ. A further increase in reaction temperature to 210 ^{o}C causes a complete loss of the reflection at 6.79^{o} 2θ. The phase change occurs between 160-210 ^{o}C.

Generally, these materials have layered structures where the adjacent inorganic layers built from coordination of the phosphonate and metal ions are linked by organic pillars (Figure 61). The first low angle reflection is believed to be the interlayer spacing; the distance between the inorganic layers held apart by the phosphonate pillars. The interlayer distance for the high temperature phase (**II**, d = 14.68 Å) is larger than for the low temperature phase (**I**, d = 12.99 Å).

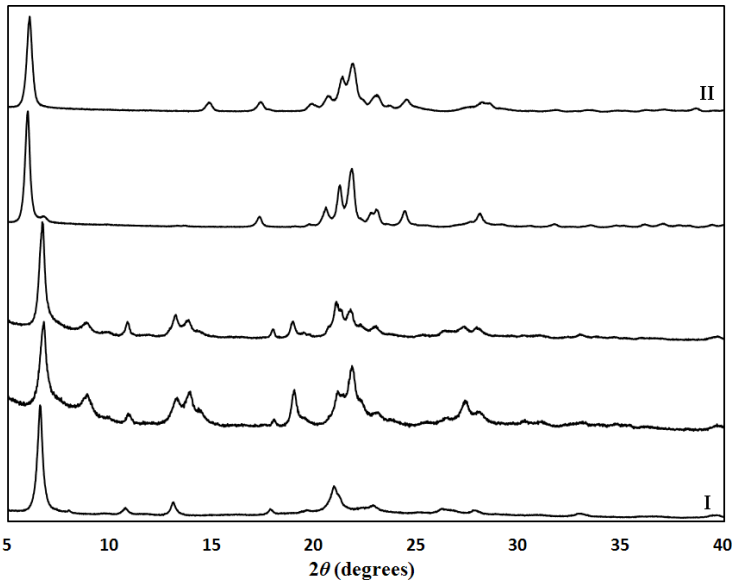

Figure 62. PXRD patterns for Al-materials synthesized from 120 ^{o}C (**I**) and 210 ^{o}C (**II**)

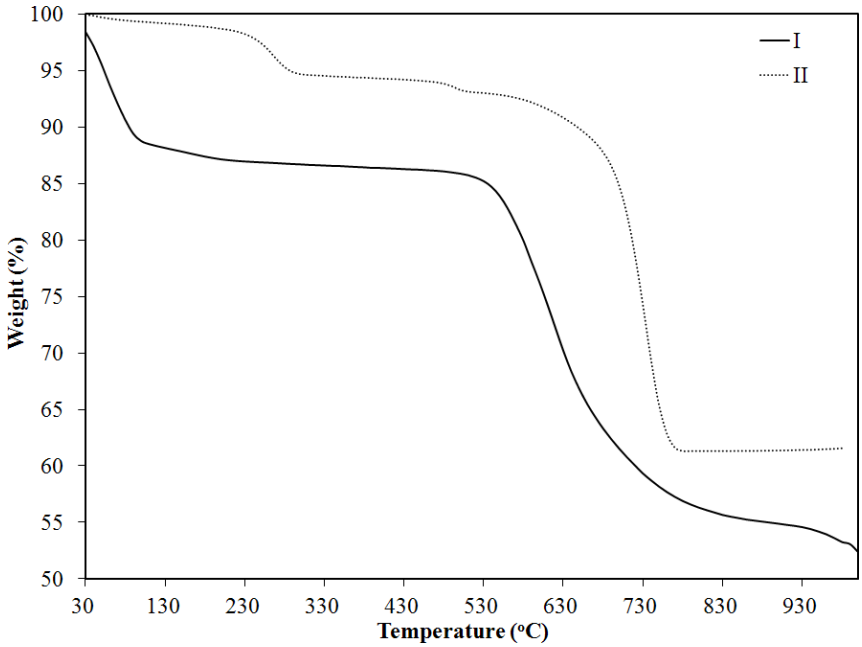

Figure 63. Thermal decomposition of the Al-materials **I** and **II**

However, the same phosphonate pillar is used; thus difference in the interlayer distance is believed to be caused by changes in the architecture of the inorganic layer. The remaining reflections are believed to correspond to the intralayer spacing. The shortest distances between the organic pillars reported for an aluminum 4,4'-phenylenediphosphonate was 4.16 Å, which resulted in a nonporous material (Chapter V).

The general thermal decomposition for the two phases is shown in Figure 63. There are three weight losses observed for both phases. For the low temperature phase (**I**), the first loss below 200 ^{o}C is attributed to loosely bound water molecules and is ~12%. The second, slow loss between 200-500 ^{o}C is believed to be associated with trapped water molecules in the pores. The third loss is attributed to the decomposition of the organic groups. The total weight loss is ~48 %. The thermal decomposition differs for the high temperature phase (**II**) with a total weight loss of 38.4 %. There are three distinct weight losses. The first occurs below 250 ^{o}C (30-250 ^{o}C, 5.33 %). This may be due to loss of coordinated water molecules which generally occurs around 200 ^{o}C. The second loss occurs below 550 ^{o}C. It is not a gradual loss as in the low temperature phase therefore it is not believed to be due to trapped water molecule in the pores. It may be due to condensation of the OH groups. The third loss associated with the decomposition of the organic group occurs above 550 ^{o}C. The TGA residue for compound I contained both $AlPO_4$ and $AlPO_3$ while for compound II it was only $AlPO_4$ (Figure E 1).

Comparing the TGA results with elemental analysis, the derived molecular formulas for compound **I**, $Al_4(O_3PC_{12}H_8PO_3)_3 \cdot 8.75H_2O$, and **II**,

$Al_6(O_3PC_{12}H_8PO_3)_3(OH)_6 \cdot 4.5H_2O$, are consistent within experimental error. The molecular formulas found for the two phases have different Al to ligand ratios even with the same initial synthesis ratio (8:3 ratio of $AlCl_3 \cdot 6H_2O$ to BPDPA). The molar ratio for the low temperature phase (**I**) was found to be 4:3, while the high temperature phase (**II**) was 2:1. These reactions are carried out with an excess of aluminum ions. Compound **I** requires only half of the aluminum present in the synthesis and compound **II** requires ¾ of the aluminum present in the synthesis. The reaction yields reflect the difference in amount of aluminum consumed in the reactions; the yields based on Al are 45% for **I** and 68% for **II**. Yields based on BPDPA reflect that the ligand is almost completely consumed for both reaction conditions: **I** (91%) and **II** (90%). This data suggests that the reaction changes with temperature resulting in two different compounds.

Solid state NMR of Al-materials

The solid-state $^{27}Al\{^1H\}$ and $^{31}P\{^1H\}$ NMR spectra of compounds **I** and **II** are given in Figure 64. The low temperature phase (**I**) has two chemical shifts (-27.6 and 38 ppm) and are attributed to aluminum sites with octahedral and tetrahedral oxygen environments respectively.[45,46,212,222] [212,222]The $^{31}P\{^1H\}$ NMR spectra for compound **I** shows multiple peaks in the range of -2 to -16 ppm. Resonance of -1 to -10 ppm were observed for an aluminum 4,4'-phenylenediphonsphonate with similar metal coordinate (Chapter V). The NMR spectra for compound **II** is more difficult to interpret. The aluminum resonance could be attributed to a five coordinate aluminum atom where chemical shifts have been reported between -0.4 (Chapter V) and 20 ppm[212,222]. However, the phosphorus resonances for these five coordinate aluminum atoms are

observed between 3 to 13 ppm (Chapter V).[212,222] The phosphorus resonances for compound **II** are most closely resemble compound **I** with both tetrahedral and octahedral aluminum geometry. Therefore it is unclear if the aluminum atom is five or six coordinate.

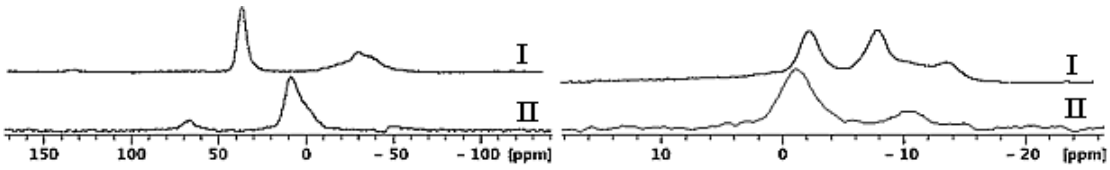

Figure 64. Solid-state $^{27}Al\{^{1}H\}$ (left) and $^{31}P\{^{1}H\}$ (right) NMR spectra for the high and low temperature reaction phases

Textural properties of Al-materials

The N_2 isotherms for the two materials are given in Figure 65. The low temperature phase (**I**) is generally characterized as a modified Type II isotherm with a small H4 hysteresis loop. This indicates a major combination of slit-like micropores to the total surface area. Mesopores are the other contribution of porosity and are attributed to interparticle mesopores formed by stable aggregates of platelet particles, "house of cards arrangement".[11] The high temperature phase (**II**) is generally characterized as a Type III isotherm with only external surface area. The calculated values of both the total surface area (BET) and the percent microporosity based on the *t*-plot method are given in Table 10.

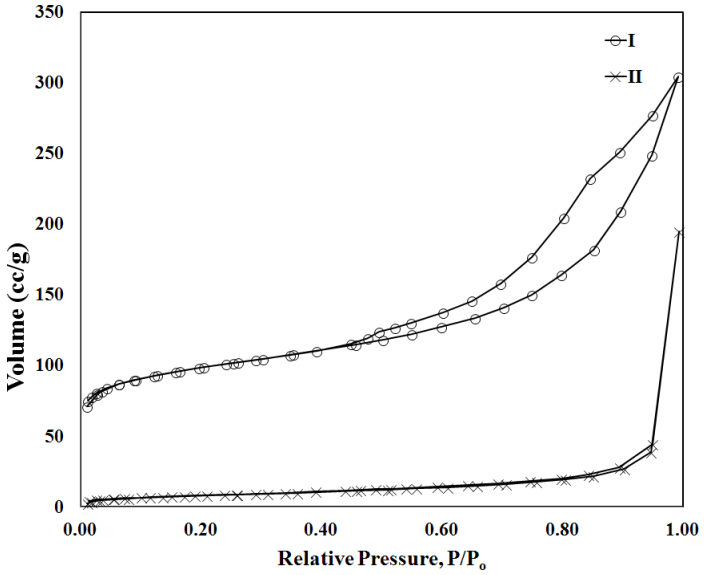

Figure 65. N_2 isotherms for Al-material synthesized at 120 and 210 ^oC

Table 10. The calculated surface area (BET) and percent microporosity (*t*-plot) for Al-materials synthesized at 120 and 210 ^oC

Compound	Reaction Temperature (^oC)	Total Surface Area (m^2/g)	Microporous (%)
I	120	344	46
II	210	29	0

Varying the reaction temperature resulted in two materials with different properties believed to be due to the change in structural architectures. The high temperature phase conformed to similar trends observed in metal phosphonates where less hydrated and denser materials occur with increase in reaction temperature.[39,40] The low temperature phase provides the ideal conditions to generate materials best suited for our purpose in synthesizing Al-hybrid materials.

Compound **I** was found to have similar properties as a compound published by Brunett and coworkers ($Al_4(O_3PC_{12}H_8PO_3)_3$ $5.4H_2O$).[111] The synthesis differs by using anhydrous $AlCl_3$ in an acetone/water mixture at 180 ^oC.[111] However, increasing the reaction temperature (210 ^oC) for $Al_4(O_3PC_{12}H_8PO_3)_3$ $5.4H_2O$ did not result in a change in phase as with compound **I** (Figure E 2). It is interesting that the two different synthetic routes resulted in similar compounds, but with increase in reaction temperature compound **II** was not formed in the previously published work.

Al-hybrid materials

The strategy was to incorporate additional ion-exchange activity into the Al-materials by addition of a spacer group. The low temperature Al-material (**I**) seemed the most promising for incorporation of a spacer group. The process to develop Al-hybrids can be imagined as replacing some of the phosphorus sites from the diphosphonates with small spacer groups. Importantly, the PXRD patterns of the Al-material and the Al-hybrid material should not differ greatly. The addition of a spacer group into a pillared material should not disturb the reflections due to the interlayer distance because this is highly dependent on the length of the pillar. The reflections due to intralayer distances which are associated with the inorganic layer also should not be disturbed due to the same intralayer connectivity. The spacer group acts like an impurity which does not change the overall architecture of the material. However, the ion-exchange capability will be improved with the increase in the amount of spacer groups incorporated into the Al-hybrid materials, but lower crystallinity may occur due to loss in some long range order (↑ spacer = ↑ ion-exchange sites = ↓ crystallinity).

Phosphoric acid was initially tried as a spacer because of the high ion selectivity obtained by the zirconium hybrid materials.[64,107] However, it was unsuccessful which is believed to be due to the solubility of aluminum phosphate in acid media. To incorporate the -POH functionality, phosphorous acid was used as a spacer with the intention to oxidize phosphite to phosphate. A radical oxidation process ($Na_2S_2O_8$) was use to oxidize phosphite (compound **III**) to phosphate (compound **III-ox**). The PXRD patterns were found to be similar (Figure 66) and the materials were relatively homogeneous (Figure E 3).

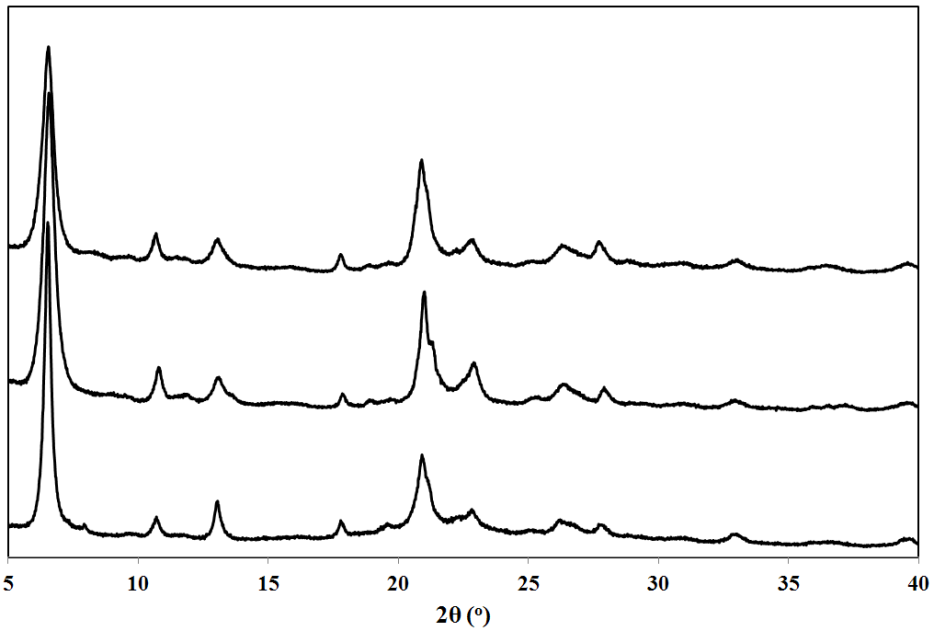

Figure 66. PXRD patterns for Al-hybrid materials **I** (bottom), **III** (middle) and **III-ox** (top)

The general thermal decomposition for compounds **III** and **III-ox** are shown in Figure 67. The thermal decompositions of **III** and **III-ox** have a similar trend as for compound **I**. In all materials, there are three weight losses observed and weight loss percentages are given in Table 11. The first loss below 200 ^{o}C is attributed to loosely bound water molecules and is in the range between 9-13 %. The second loss occurs at ~400 ^{o}C and is believed to be due to tightly bound water molecules trapped in the material. The last weight loss at ~500 ^{o}C is attributed to the decomposition of the organic groups.

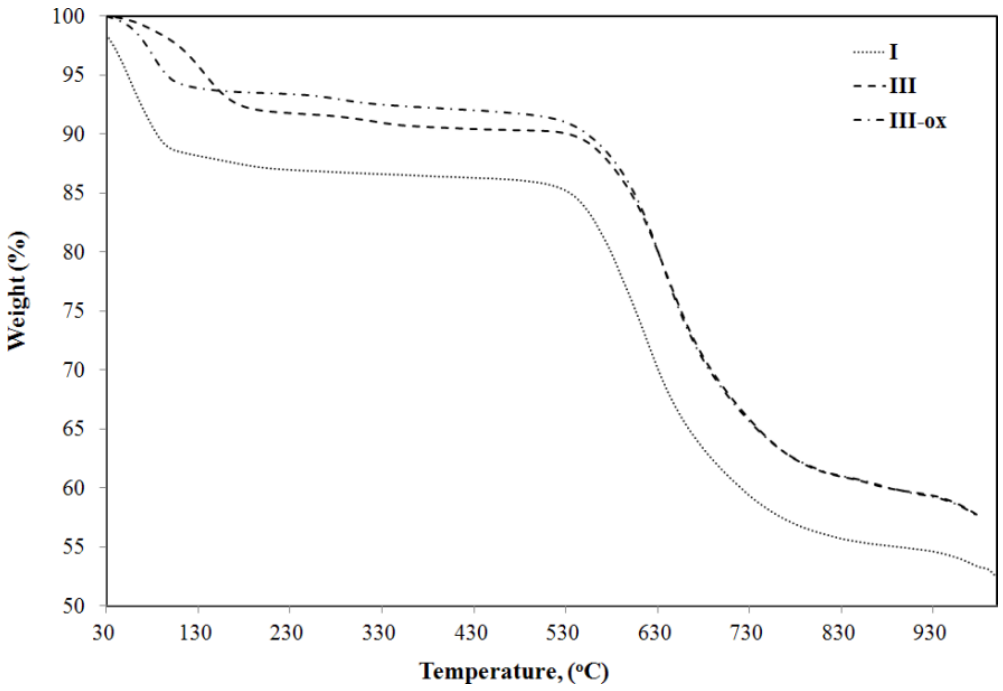

Figure 67. Thermal decompositions for compounds **I**, **III** and **III-ox**

Table 11. Specific weight losses for the thermal decomposition of Al-hybrid materials

	Weight Loss (%)				
Material	30-200	200-500	500-1000	Total	
I	12.70	1.251	33.61	47.56	13.18
III	9.68	2.35	31.88	43.88	12.03
III-ox	11.41	2.37	32.26	46.04	13.78

The solid-state NMR spectra of these materials can be seen in Figure 68. The $^{27}Al\{^{1}H\}$ NMR spectra show a relatively broad resonance at -27.6 ppm which is attributed to aluminum sites with octahedral oxygen environments.[45,46,212] The line shapes are characteristic for quadrupolar splitting interaction.[222] The less broad resonance at 38 ppm is attributed to aluminum sites with tetrahedral oxygen environments.[46,222]

A change in the $^{31}P\{^{1}H\}$ NMR spectra should occur upon oxidation of the phosphite to phosphate. Reported $^{31}P\{^{1}H\}$ resonances for phosphite in aluminum phosphite and phosphonate-phosphite are in the range *ca.* -5 to *ca.* -20 ppm[233,234], while $^{31}P\{^{1}H\}$ resonances for phosphate in layered aluminum phosphate have been observed in the range *ca.* -20 to *ca.* -23 ppm.[235]

The $^{31}P\{^{1}H\}$ NMR spectra for compounds **I**, **III** and **III-ox** reveal the following spectral changes: the resonance at -17.8 ppm disappears while a resonance at -22.0 ppm appears after oxidation. The multiple $^{31}P\{^{1}H\}$ resonances consistent in all phases (-2.5, -8.0 and -13.8 ppm) are attributed to the biphenylenediphosphonates. The $^{31}P\{^{1}H\}$ resonance at -22.0 ppm for compound **III-ox** is similar to the resonances observed for layered aluminum phosphates.[235]

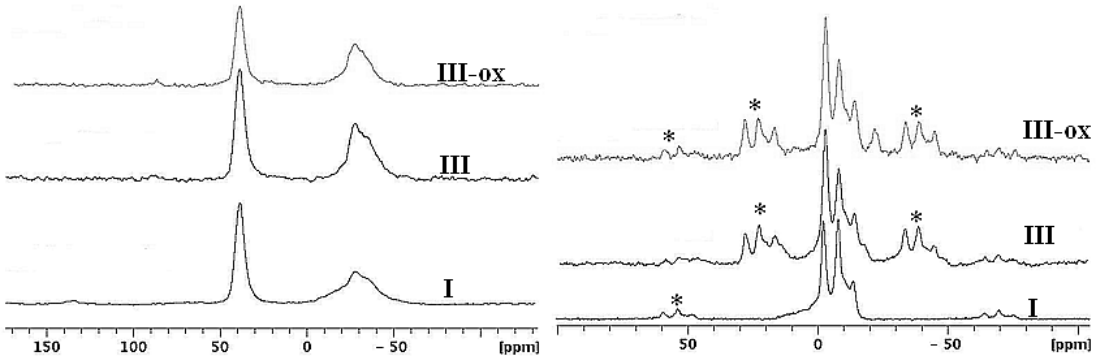

Figure 68. $^{27}Al\{H^1\}$ (left) and $^{31}P\{H^1\}$ (right) solid state NMR spectra of compounds **I**, **III** and **III-ox**. Compound I differs in spinning rate (6 kHz)

The FTIR spectra of compounds I, III and III-ox were studied in the range 800-2650 cm^{-1} (Figure 69 and 70). Although the FTIR spectra are similar, slight differences between spectra are used as evidence for the oxidation of phosphite to phosphate. The difference in the IR spectra occur in three regions: a broad band at 950 cm^{-1} increases, decrease in the band at 1026 cm^{-1} and a loss of the band at 2450 cm^{-1} after oxidation. Phosphites have exhibited P-H stretching in the region 2200-2500 cm^{-1}.[233,234,236]

Considering this, along with the solid state NMR one comes to conclude that a new mixed phosphate-phosphonate phase was successfully synthesized. Comparing the TGA results with elemental analysis, the derived molecular formulas for compound **III**, $Al_4(O_3PC_{12}H_8PO_3)_{2.46}(HPO_3)_{1.08}(H_2O)_7$, and **III-ox**, $Al_4(O_3PC_{12}H_8PO_3)_{2.46}(HOPO_3)_{1.08}(H_2O)_7$, are consistent within experimental error. Not surprisingly, compound **III** was found to have similar properties as the $Al_4(HPO_3)_{0.4\text{-}0.7}(O_3PC_{12}H_8PO_3)_{2.6\text{-}2.8}$ $5.4H_2O$ reported by Brunett and coworkers.[111]

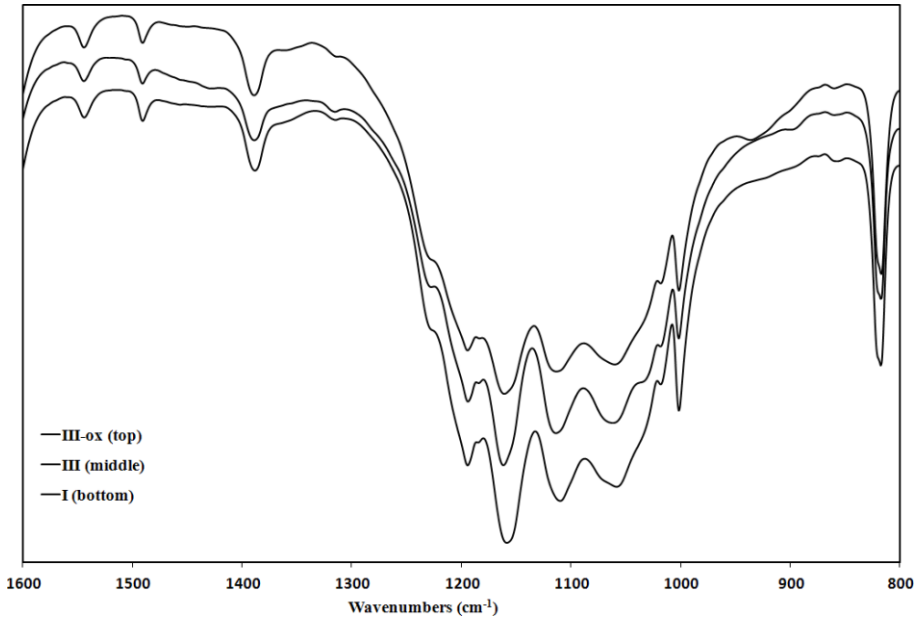

Figure 69. FTIR spectra in the region 800 to 1600 cm^{-1} for compounds **I**, **III**, **III-ox**

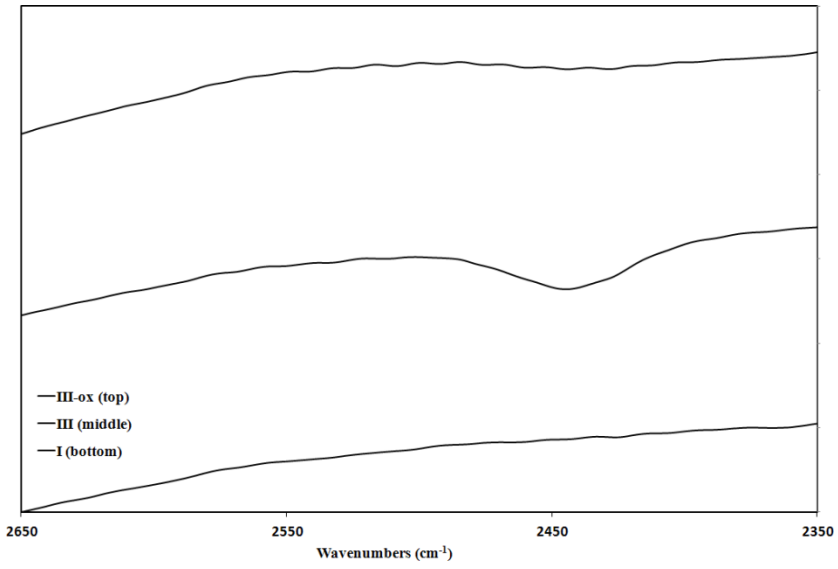

Figure 70. FTIR spectra in the region 2340 to 2650 cm^{-1} for compound **I**, **III**, and **III-ox**. Generally, phosphite P-H stretching band occurs between 2200-2500 cm^{-1}

Textural properties of Al-hybrids

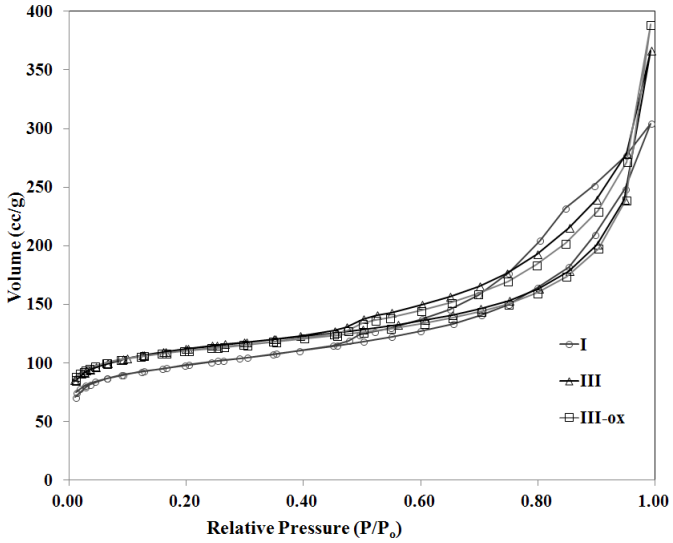

Figure 71. N_2 isotherms for compounds **I**, **III** and **III-ox**

Table 12. The calculated surface area (BET) and percent microporosity (*t*-plot) for indicated materials

Material	2nd ligand	Total Surface Area (m^2/g)	Microporous (%)
I	—	344	46
III	HPO_3	402	69
III-ox	PO_4H	406	70

The N_2 isotherms for the Al-materials are given in Figure 71. Similarly to material **I**, the materials are generally characterized as modified Type II isotherms with small H4 hysteresis loops indicating that a major combination to the total surface area is from slit-like micropores. Mesopores are the other contribution of porosity and are attributed to interparticle mesopores formed by stable aggregates of platelet particles,

"house of cards arrangement".[11] The calculated values of both the total surface area (S_{BET}) and the percent microporosity based on the *t*-plot are given in Table 12. Total surface area and microporosity increase with addition of phosphite to the synthesis.

Ion affinity determination

To rapidly access metal ion affinity for compound **III-ox**, mixed metal solutions were used to calculate K_d coefficients. The distribution coefficient (K_d) is a measure of the fractional uptake of metal ions in solution and gives an idea of metal ion affinity. The cation size, the energy required for dehydration, and the cation charge plays prominent roles in determining selectivity of metal ions. The metal concentrations and evaluated distribution coefficients K_d are given in Table 13. Metal ions Th^{4+} and Yb^{3+} exhibited higher K_d values than other metal ions. Almost all Th^{4+} was removed from the mixed metal solution. The order of ion selectivity for M^{3+} and M^{4+} with respect to the K_d values is $Th^{4+} > Yb^{3+} > Sm^{3+} \cong Nd^{3+}$. The $C_i \sim C_{eq}$, indicating this material has no ion exchange capability for the metal ions M^{1+}, M^{2+}, Sm^{3+} and Nd^{3+}. The order of M^{3+} ion selectivity follows the size of the ionic radii; however, the ionic radius of Th^{4+} has a similar size to the larger lanthanides. The ionic radius for $Zn^{2+} < Th^{4+}$, but the material exhibited no selectivity for this ion. Both the size of the ionic radius and the charge of the metal ion are found to be factors that influence the selectivity. High affinity for Th^{4+} was also found for a zirconium diethylene triamine pentamethylene phosphonate with a separation factor (K_{d1}/K_{d2}) of 1175 for Th^{4+}-Sm^{3+}.[227] The same separation factor was determined to be 1302 for compound **III-ox**, a slight improvement.

Table 13. Selectivity adsorption of metal cations on **III-ox** from a mixed metal solution

	C ppm (mg/L)									
	Na^{+}	Cs^{+}	Ca^{2+}	Sr^{2+}	Co^{2+}	Zn^{2+}	Yb^{3+}	Sm^{3+}	Nd^{3+}	Th^{4+}
C_i	55.1	44.9	44.7	50.5	43.7	46.5	50.9	51.5	52.1	45.0
C_f	59.5	43.6	48.4	50.5	43.8	46.3	35.7	47.7	49.2	< 0.43
K_d(mL/g)	—	—	—	—	—	—	21.3	3.98	—	5183
Ionic Radius, Å	0.99	1.7	1.0	1.2	0.75	0.74	0.87	0.96	0.98	0.94

Ions are assumed to be six-coordinate for ionic radius values[130,237]

Table 14. Selectivity adsorption of metal cations on **I** and **III** from a mixed metal solution

	C ppm (mg/L)							
	I*				**III**			
	Yb^{3+}	Sm^{3+}	Nd^{3+}	Th^{4+}	Yb^{3+}	Sm^{3+}	Nd^{3+}	Th^{4+}
C_i	50.9	51.5	52.1	45.0	50.9	51.5	52.1	45.0
C_f	35.9	46.8	48.9	<0.69	33.5	45.5	47.6	<0.43
K_d(mL/g)	20.3	—	—	3117	26.0	—	—	5183

* 0.0618 g of **I** and 3 mL mixed metal solution was used in the uptake study

To verify that the ion-exchange capability was due to the phosphate group, two additional uptakes studies with compounds **I** and **III** were carried out for the tri/tetravalent mixed metal solution (Table 14) and the results were surprising. Similar to compound **III-ox**, both **I** and **III** exhibited higher selective for Yb^{3+} and Th^{4+} ions than for other metal ions. Similar K_d coefficients were found for both compounds **III** and **III-ox,** while compound **I** had the lowest K_d coefficient for Th^{4+}. The ion-exchange ability is inherent to all three materials; however, incorporation of either phosphite or phosphate similarly increased the metal ion affinity. This brings to question, what exactly is the ion exchange group in the three materials? Initially, the phosphate was considered the ion exchange group; however, K_d coefficients did not improve upon oxidation of phosphite

to phosphate. Additionally, access to the small phosphate group could be blocked by the larger biphenylenediphosphonates (Figure 72). The free phosphonic acids, from the biphenylene groups, are consistent in all three compounds due to the layer growth defects. Increase in free phosphonic acids may occur due to the increase in microporosity with incorporation of a spacer group. This data suggests that the free phosphonic acids may be the ion exchange groups.

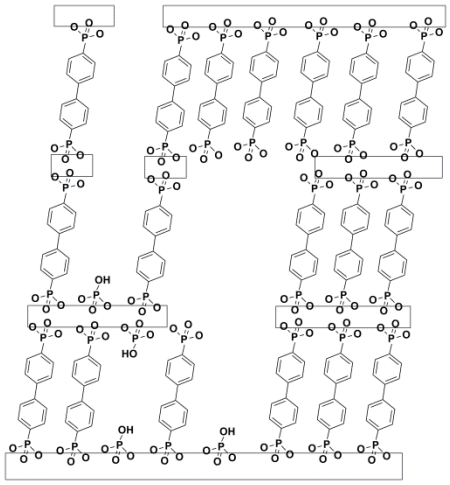

Figure 72. A proposed pore structure for the hybrid aluminum materials

Different ion affinities were found for pillared metal(IV) phenylenediphosphonate-phosphate materials.[64] The pillar is shorter in these materials. The pore structure of the reported materials must be dramatically different than compound **III-ox** due to the change in the metal ion affinities. However, it would be

interesting to examine if the ion-exchange ability is also inherent to the metal (IV) phenylenediphosphonate materials.

Conclusions

Four different aluminum phosphonates $Al_4(O_3PC_{12}H_8PO_3)_3 \cdot 8.75H_2O$ (**I**), $Al_6(O_3PC_{12}H_8PO_3)_3(OH)_6 \cdot 4.5H_2O$ (**II**), $Al_4(O_3PC_{12}H_8PO_3)_{2.46}(HPO_3)_{1.08}(H_2O)_7$ (**III**), and $Al_4(O_3PC_{12}H_8PO_3)_{2.46}(HOPO_3)_{1.08}(H_2O)_7$ (**III-ox**) were synthesized hydrothermally. Compound **II** was determined to nonporous and ion exchange properties were not evaluated. For compound **III-ox** full evaluation of metal ion affinity was carried out. The materials were found to have no ion exchange capacity for M^{1+}, M^{2+}, Sm^{3+} and Nd^{3+} but were selective for both Th^{4+} and Yb^{3+}. The factors influencing selectivity was determined to be both the ionic size and charge of the metal ion. Compounds **I** and **III** were evaluated to determine if they had similar metal affinities. Interestingly, compound **I** and **III** also had high affinity for both Th^{4+} and Yb^{3+}. Addition of the secondary ligands phosphite and phosphate to form hybrid aluminum materials increased the affinity for Th^{4+} ions.

CHAPTER VII

CONCLUSIONS

This dissertation tries to tackle the challenge of developing porous metal arylphosphonates with both high crystallinity and functional porosity by using different synthetic approaches. The use of template molecules and choice of metal ions were used to deviate from the favored pillared structure, which results in nonporous materials. The choice of metal ion is important due to the large influence on crystallinity of the synthesized metal phosphonantes and therefore the method and difficulty in their structure determination. The knowledge of the product structures is very important for better understanding of their properties and the improvement of the materials.

The role of water in solvothermal reactions was found to have a profound influence on the structure of monovalent metal phosphonates (Chapter III). The structures of lithium monophosphonates could be tailored from zero/one-dimensional to two-dimensional structures. Hydrothermal reactions of monovalent metal 4,4'-biphenylenediphosphonates resulted in pillared structures (Chapter II), which could be altered by varying different solvothermal reaction conditions and by using alkyl amines as template molecules (Chapter III).

The conversion of a layered structure (PCMOF-3) to a three-dimensional structure (ZnBP) was assisted by the use of small template molecules in the solvothermal reaction (Chapter IV). The reversible dehydration process exhibited by ZnBP was monitored by both *in situ* powder X-ray diffraction and solid state NMR and revealed a

negative expansion property. The change in the guest molecule positions and structure of the framework were determined throughout the reversible dehydration process.

The variation in structures that can be obtained by the use of aluminum ions in the synthesis were presented in Chapter V and VI. The polycrystalline state of aluminum phosphonates hinders the structure determination; however, by the use of powder X-ray diffraction methods many of their structures were determined. Presented in Chapter V is three different aluminum 4,4'-phenylenediphosphonates that exhibit reversible dehydration behavior. It has a dramatic influence on permanent porosity of the material. The stability of the dehydrated phase was found to be a result of the aluminum atom geometry, which in some cases has coordinatively unsaturated metal sites.

Change in the ligand from 4,4'-phenylenediphosphonic and to 4,4'-biphenylenediphosphonic acid resulted in the aluminum phosphonates presented in Chapter VI. These compounds are described as UMOFs and the pore environment was tailored to favor ion exchange processes. The most important aspect is that these compounds exhibit high selectivity for Th^{4+} ions.

The results of this work were presented at the 2010 American Chemical Society (ACS) annual meeting (Aug. 22- Aug. 25, 2010 Boston, MA) and at the 2011 and 2012 American Crystallographic Association (ACA) annual meetings (May 28-Jun. 2, 2011, New Orleans, LA and Jul. 28-Aug. 1, 2012, Boston, MA). Parts of these results were published in peer reviewed articles.[158,238] The remainder are being prepared for publication.

REFERENCES

(1) Stock, N.; Biswas, S. *Chem. Rev.* **2012**, *112*, 933.

(2) Morozan, A.; Jaouen, F. *Energy Environ. Sci.* **2012**, *5*, 9269.

(3) Kreno, L. E.; Leong, K.; Farha, O. K.; Allendorf, M.; Van, D. R. P.; Hupp, J. T. *Chem. Rev.* **2012**, *112*, 1105.

(4) Gaab, M.; Trukhan, N.; Maurer, S.; Gummaraju, R.; Müller, U. *Microporous Mesoporous Mater.* **2012**, *157*, 131.

(5) Clearfield, A.; Demadis, K.; Editors *Metal Phosphonate Chemistry: From Synthesis To Applications*; Royal Society of Chemistry, 2012.

(6) Almeida Paz, F. A.; Klinowski, J.; Vilela, S. M. F.; Tome, J. P. C.; Cavaleiro, J. A. S.; Rocha, J. *Chem. Soc. Rev.* **2012**, *41*, 1088.

(7) Clearfield, A. *Dalton Trans.* **2008**, 6089.

(8) DiGiacomo, P. M.; Dines, M. B. *Polyhedron* **1982**, *1*, 61.

(9) Clearfield, A.; Wang, Z. *J. Chem. Soc., Dalton Trans.* **2002**, 2937.

(10) Wang, Z.; Heising, J. M.; Clearfield, A. *J. Am. Chem. Soc.* **2003**, *125*, 10375.

(11) Alberti, G.; Marmottini, F.; Vivani, R.; Zappelli, P. *J. Porous Mater.* **1998**, *5*, 221.

(12) Subbiah, A.; Pyle, D.; Rowland, A.; Huang, J.; Narayanan, R. A.; Thiyagarajan, P.; Zoń, J.; Clearfield, A. *J. Am. Chem. Soc.* **2005**, *127*, 10826.

(13) Gabriel Armatas, N.; Burkholder, E.; Zubieta, J. *J. Solid State Chem.* **2005**, *178*, 2430.

(14) Murugavel, R.; Kuppuswamy, S.; Gogoi, N.; Steiner, A. *Inorg. Chem.* **2010**, *49*, 2153.

(15) Murugavel, R.; Shanmugan, S. *Chem. Commun.* **2007**, 1257.

(16) Walawalkar, M. G.; Roesky, H. W.; Murugavel, R. *Acc. Chem. Res.* **1998**, *32*, 117.

(17) Murugavel, R.; Kuppuswamy, S.; Gogoi, N.; Boomishankar, R.; Steiner, A. *Chem. Eur. J.* **2010**, *16*, 994.

(18) Na, K.; Choi, M.; Ryoo, R. *Microporous Mesoporous Mater.* **2013**, *166*, 3.

(19) Valtchev, V.; Majano, G.; Mintova, S.; Perez-Ramirez, J. *Chem. Soc. Rev.* **2013**, *42*, 263.

(20) Murugavel, R.; Kuppuswamy, S.; Gogoi, N.; Steiner, A. *Inorg Chem* **2010**, *49*, 2153.

(21) Murugavel, R.; Gogoi, N. *J. Organomet. Chem.* **2010**, *695*, 916.

(22) Yang, Y.; Walawalkar, M. G.; Pinkas, J.; Roesky, H. W.; Schmidt, H.-G. *Angew. Chem. Int. Ed.* **1998**, *37*, 96.

(23) Murugavel, R.; Kuppuswamy, S.; Gogoi, N.; Boomishankar, R.; Steiner, A. *Chem. Eur. J.* **2010**, *16*, 994.

(24) Murugavel, R.; Shanmugan, S. *Dalton Trans.* **2008**, 5358.

(25) Du, Z.-Y.; Sun, Y.-H.; Liu, Q.-Y.; Xie, Y.-R.; Wen, H.-R. *Inorg. Chem.* **2009**, *48*, 7015.

(26) Murugavel, R.; Kuppuswamy, S.; Maity, A. N.; Singh, M. P. *Inorg. Chem.* **2009**, *48*, 183.

(27) Khan, M. I.; Zubieta, J. *Prog. Inorg. Chem.* **1995**, *43*, 1.

(28) Haushalter, R. C.; Wang, Z.; Thompson, M. E.; Zubieta, J. *Inorg. Chim. Acta* **1995**, *232*, 83.

(29) Soghomonian, V.; Chen, Q.; Haushalter, R. C.; O'Connor, C. J.; Tao, C.; Zubieta, J. *Inorg. Chem.* **1995**, *34*, 3509.

(30) Baskar, V.; Shanmugam, M.; Sanudo, E. C.; Shanmugam, M.; Collison, D.; McInnes, E. J. L.; Wei, Q.; Winpenny, R. E. P. *Chem. Commun.* **2007**, 37.

(31) Chandrasekhar, V.; Nagarajan, L.; Clerac, R.; Ghosh, S.; Verma, S. *Inorg. Chem.* **2008**, *47*, 1067.

(32) Chandrasekhar, V.; Kingsley, S. *Angew. Chem. Int. Ed.* **2000**, *39*, 2320.

(33) Brechin, E. K.; Coxall, R. A.; Parkin, A.; Parsons, S.; Tasker, P. A.; Winpenny, R. E. P. *Angew. Chem. Int. Ed.* **2001**, *40*, 2700.

(34) Tolis, E. I.; Helliwell, M.; Langley, S.; Raftery, J.; Winpenny, R. E. P. *Angew. Chem. Int. Ed.* **2003**, *42*, 3804.

(35) Khanra, S.; Kloth, M.; Mansaray, H.; Muryn, C. A.; Tuna, F.; Sanudo, E. C.; Helliwell, M.; McInnes, E. J. L.; Winpenny, R. E. P. *Angew. Chem. Int. Ed.* **2007**, *46*, 5568.

(36) Murugavel, R., Gogoi, N., Kalita, A.C., Kuppuswamy, S. unpublished work .

(37) Zhang, Z.; Zhao, Y.; Gong, Q.; Li, Z.; Li, J. *Chem. Commun.* **2013**, *49*, 653.

(38) Duren, T.; Bae, Y.-S.; Snurr, R. Q. *Chem. Soc. Rev.* **2009**, *38*, 1237.

(39) Cheetham, A. K.; Rao, C. N. R.; Feller, R. K. *Chem. Commun.* **2006**, 4780.

(40) Sonnauer, A.; Stock, N. *Eur. J. Inorg. Chem.* **2008**, 5038.

(41) Baes, C. F.; Mesmer, R. E. *The Hydrolysis of Cations*; John Wiley and Sons: New York, 1976.

(42) Jorgensen, C. K. *Inorganic Complexes*; Academic Press: London, 1963.

(43) Maeda, K.; Akimoto, J.; Kiyozumi, Y.; Mizukami, F. *Angew. Chem. Int. Ed.* **1995**, *34*, 1199.

(44) Maeda, K.; Akimoto, J.; Kiyozumi, Y.; Mizukami, F. *J. Chem. Soc., Chem. Commun.* **1995**, 1033.

(45) Maeda, K.; Hashiguchi, Y.; Kiyozumi, Y.; Mizukami, F. *Bull. Chem. Soc. Jpn.* **1997**, *70*, 345.

(46) Maeda, K.; Kiyozumi, Y.; Mizukami, F. *Angew. Chem. Int. Ed.* **1994**, *33*, 2335.

(47) Edgar, M.; Carter, V. J.; Grewal, P.; Sawers, L.-J.; Sastre, E.; Tunstall, D. P.; Cox, P. A.; Lightfoot, P.; Wright, P. A. *Chem. Mater.* **2002**, *14*, 3432.

(48) Loiseau, T.; Lecroq, L.; Volkringer, C.; Marrot, J.; Férey, G.; Haouas, M.; Taulelle, F.; Bourrelly, S.; Llewellyn, P. L.; Latroche, M. *J. Am. Chem. Soc.* **2006**, *128*, 10223.

(49) Volkringer, C.; Popov, D.; Loiseau, T.; Férey, G.; Burghammer, M.; Riekel, C.; Haouas, M.; Taulelle, F. *Chem. Mater.* **2009**, *21*, 5695.

(50) Volkringer, C.; Popov, D.; Loiseau, T.; Guillou, N.; Ferey, G.; Haouas, M.; Taulelle, F.; Mellot-Draznieks, C.; Burghammer, M.; Rieke, l. C. *Nat. Mater.* **2007**, *6*, 760.

(51) Haouas, M.; Volkringer, C.; Loiseau, T.; Férey, G.; Taulelle, F. *Chem. Eur. J.* **2009**, *15*, 3139.

(52) Alberti, G.; Costantino, U.; Allulli, S.; Tomassini, N. *J. Inorg. Nucl. Chem.* **1978**, *40*, 1113.

(53) Cunningham, D.; Hennelly, P. J. D.; Deeney, T. *Inorg. Chim. Acta* **1979**, *37*, 95.

(54) Cao, G.; Lee, H.; Lynch, V. M.; Mallouk, T. E. *Inorg. Chem.* **1988**, *27*, 2781.

(55) Cao, G.; Lee, H.; Lynch, V. M.; Mallouk, T. E. *Solid State Ionics* **1988**, *26*, 63.

(56) Martin, K. J.; Squattrito, P. J.; Clearfield, A. *Inorg. Chim. Acta* **1989**, *155*, 7.

(57) Cao, G.; Mallouk, T. E. *Inorg. Chem.* **1991**, *30*, 1434.

(58) Zhang, Y.; Clearfield, A. *Inorg. Chem.* **1992**, *31*, 2821.

(59) Salami, T. O.; Fan, X.; Zavalij, P. Y.; Oliver, S. R. J. *Dalton Trans.* **2006**, *0*, 1574.

(60) Lansky, D. E.; Zavalij, P. Y.; Oliver, S. R. J. *Acta Cryst. C* **2001**, *57*, 1051.

(61) Subbiah, A.; Bhuvanesh, N.; Clearfield, A. *J. Solid State Chem.* **2005**, *178*, 1321.

(62) Kirumakki, S.; Huang, J.; Subbiah, A.; Yao, J.; Rowland, A.; Smith, B.; Mukherjee, A.; Samarajeewa, S.; Clearfield, A. *J. Mater. Chem.* **2009**, *19*, 2593.

(63) Kirumakki, S.; Samarajeewa, S.; Harwell, R.; Mukherjee, A.; Herber, R. H.; Clearfield, A. *Chem. Commun.* **2008**, 5556.

(64) Burns, J. D.; Clearfield, A.; Borkowski, M.; Reed, D. T. *Radiochim. Acta* **2012**, *100*, 381.

(65) Costantino, U. *Advances in Science and Technology* **1999**, *15*, 479.

(66) Alberti, G.; Casciola, M. *Chem. Solid State Mater.* **1992**, *2*, 238.

(67) Thompson, M. E. *Chem. Mater.* **1994**, *6*, 1168.

(68) Rao, K. P.; Vidyasagar, K. *Eur. J. Inorg. Chem.* **2006**, *2006*, 813.

(69) Rao, K. P.; K., V. *Acta Cryst. E* **2005**, *61*, m1794.

(70) Taylor, J. M.; Mah, R. K.; Moudrakovski, I. L.; Ratcliffe, C. I.; Vaidhyanathan, R.; Shimizu, G. K. H. *J. Am. Chem. Soc.* **2010**, *132*, 14055.

(71) Araki, T.; Kondo, A.; Maeda, K. *Chem. Commun.* **2013**, *49*, 552.

(72) Kong, D.; Zoñ, J.; McBee, J.; Clearfield, A. *Inorg. Chem.* **2006**, *45*, 977.

(73) Fu, R.; Hu, S.; Wu, X. *Cryst. Growth Des.* **2007**, *7*, 1134.

(74) Wharmby, M. T.; Mowat, J. P. S.; Thompson, S. P.; Wright, P. A. *J. Am. Chem. Soc.* **2011**, *133*, 1266.

(75) Garczarek, P.; Janczak, J.; Zon, J. *J. Mol. Struct.* **2013**, *1036*, 505.

(76) Taddei, M.; Costantino, F.; Vivani, R. *Inorg. Chem.* **2010**, *49*, 9664.

(77) Byrd, H.; Clearfield, A.; Poojary, D.; Reis, K. P.; Thompson, M. E. *Chem. Mater.* **1996**, *8*, 2239.

(78) Vermeulen, L. A.; Thompson, M. E. *Nature* **1992**, *358*, 656.

(79) Serre, C.; Groves, J. A.; Lightfoot, P.; Slawin, A. M. Z.; Wright, P. A.; Stock, N.; Bein, T.; Haouas, M.; Taulelle, F.; Férey , G. *Chem. Mater.* **2006**, *18*, 1451.

(80) Wharmby, M. T.; Miller, S. R.; Groves, J. A.; Margiolaki, I.; Ashbrook, S. E.; Wright, P. A. *Dalton Trans.* **2010**, *39*, 6389.

(81) Berchel, M.; Hernot, S.; Couthon-Gourves, H.; Haelters, J.-P.; Quentel, F.; Gall, T.; Montier, T.; Lehn, P.; Hix, G. B.; Perez, O.; Rueff, J.-M.; Jaffres, P.-A. *Phosphorus, Sulfur Silicon Relat. Elem.*, Ahead of Print.

(82) Kan, W.-Q.; Ma, J.-F.; Liu, Y.-Y.; Yang, J.; Liu, B. *CrystEngComm* **2012**, *14*, 2268.

(83) Stein, S. E. W.; Clearfield, A.; Subramanian, M. A. *Solid State Ionics* **1996**, *83*, 113.

(84) Groves, J. A.; Miller, S. R.; Warrender, S. J.; Mellot-Draznieks, C.; Lightfoot, P.; Wright, P. A. *Chem. Commun. (Cambridge, U. K.)* **2006**, 3305.

(85) Miller, S. R.; Pearce, G. M.; Wright, P. A.; Bonino, F.; Chavan, S.; Bordiga, S.; Margiolaki, I.; Guillou, N.; Ferey, G.; Bourrelly, S.; Llewellyn, P. L. *J. Am. Chem. Soc.* **2008**, *130*, 15967.

(86) Rueff, J.-M.; Caignaert, V.; Chausson, S.; Leclaire, A.; Simon, C.; Perez, O.; Le, P. L.; Jaffres, P.-A. *Eur. J. Inorg. Chem.* **2008**, 4117.

(87) Grohol, D.; Subramanian, M. A.; Poojary, D. M.; Clearfield, A. *Inorg. Chem.* **1996**, *35*, 5264.

(88) Rao, K. P.; Vidyasagar, K. *Eur. J. Inorg. Chem.* **2005**, 4936.

(89) Iremonger, S. S.; Liang, J.; Vaidhyanathan, R.; Shimizu, G. K. H. *Chem. Commun.* **2011**, *47*, 4430.

(90) Iremonger, S. S.; Liang, J.; Vaidhyanathan, R.; Martens, I.; Shimizu, G. K. H.; Daff, T. D.; Aghaji, M. Z.; Yeganegi, S.; Woo, T. K. *J. Am. Chem. Soc.* **2011**, *133*, 20048.

(91) Poojary, D. M.; Zhang, B.; Bellinghausen, P.; Clearfield, A. *Inorg. Chem.* **1996**, *35*, 5254.

(92) Poojary, D. M.; Vermeulen, L. A.; Vicenzi, E.; Clearfield, A.; Thompson, M. E. *Chem. Mater.* **1994**, *6*, 1845.

(93) Devi, R. N.; Wormald, P.; Cox, P. A.; Wright, P. A. *Chem. Mater.* **2004**, *16*, 2229.

(94) Merrill, C. A.; Cheetham, A. K. *Inorg. Chem.* **2005**, *44*, 5273.

(95) Jones, S.; Vargas, J. M.; Pellizzeri, S.; O'Connor, C. J.; Zubieta, J. *Inorg. Chim. Acta* **2013**, *395*, 44.

(96) Smith, T. M.; Vargas, J.; Symester, D.; Tichenor, M.; O'Connor, C. J.; Zubieta, J. *Inorg. Chim. Acta*. **2013**, *403*, 63.

(97) Kong, D.; Zon, J.; McBee, J.; Clearfield, A. *Inorg. Chem.* **2006**, *45*, 977.

(98) Darling, K.; Zubieta, J. *Inorg. Chim. Acta* **2013**, *394*, 512.

(99) Martinez, C.; Corma, A. *Coord. Chem. Rev.* **2011**, *255*, 1558.

(100) Song, H.-H.; Zheng, L.-M.; Wang, Z.; Yan, C.-H.; Xin, X.-Q. *Inorg. Chem.* **2001**, *40*, 5024.

(101) Sun, Z.-G.; Dong, D.-P.; Li, J.; Cui, L.-Y.; Zhu, Y.-Y.; Zhang, J.; Zhao, Y.; You, W.-S.; Zhu, Z.-M. *J. Coord. Chem.* **2007**, *60*, 2541.

(102) Zheng, L.-M.; Gao, S.; Yin, P.; Xin, X.-Q. *Inorg. Chem.* **2004**, *43*, 2151.

(103) Kimura, T.; Nakashima, D.; Miyamoto, N. *Chem. Lett.* **2009**, *38*, 916.

(104) Zhang, Y.; Clearfield, A.; Haushalter, R. C. *Chem. Mater.* **1995**, *7*, 1221.

(105) Dutta, A.; Patra, A. K.; Bhaumik, A. *Microporous Mesoporous Mater.* **2012**, *155*, 208.

(106) Ma, T.-Y.; Lin, X.-Z.; Yuan, Z.-Y. *Chem. Eur. J.* **2010**, *16*, 8487.

(107) Burns, J. D.; Borkowski, M.; Clearfield, A.; Reed, D. T. *Radiochim. Acta* **2012**, *100*, 901.

(108) Burns, J. D.; Shehee, T. C.; Clearfield, A.; Hobbs, D. T. *Anal. Chem.* **2012**, *84*, 6930.

(109) Saxena, V.; Diaz, A.; Clearfield, A.; Batteas, J. D.; Hussain, M. D. *Nanoscale* **2013**, *5*, 2328.

(110) Kim, S.; Dawson, K. W.; Gelfand, B. S.; Taylor, J. M.; Shimizu, G. K. H. *J. Am. Chem. Soc.* **2013**, *135*, 963.

(111) Brunet, E.; Cerro, C.; Juanes, O.; Rodríguez-Ubis, J.; Clearfield, A. *J. Mater. Sci.* **2008**, *43*, 1155.

(112) Poojary, D. M.; Zhang, B.; Bellinghausen, P.; Clearfield, A. *Inorg. Chem.* **1996**, *35*, 4942.

(113) Ayi, A. A.; Burrows, A. D.; Mahon, M. F.; V.M., P. *J. Chem. Crystallogr.* **2011**, *41*, 1165.

(114) Chui, S. S. Y.; Lo, S. M. F.; Charmant, J. P. H.; Orpen, A. G.; Williams, I. D. *Science* **1999**, *283*, 1148.

(115) Hsieh, P.-Y.; Liu, Y.; Zajdel, P.; Beek, W. V.; Zavalij, P. Y.; Briber, R. M.; Green, M. A. *Prepr. Pap. - Am. Chem. Soc., Div. Fuel Chem.* **2009**, *54*, 614.

(116) Srinivasan, B. R.; Shetgaonkar, S. Y.; Raghavaiah, P. *Indian J. Chem., Sect. A: Inorg., Bio-inorg., Phys., Theor. Anal. Chem.* **2012**, *51A*, 1064.

(117) Xu, L.; Kwon, Y.-U.; de, C. B.; Cunha-Silva, L. *Cryst. Growth Des.* **2013**, *13*, 1260.

(118) Alberti, G.; Costantino, U.; Allulli, S.; Tomassini, N. *J. Inorg. Nucl. Chem.* **1978**, *40*, 1113.

(119) Demadis, K. D.; Nova Science Publishers, Inc.: 2007, p 109.

(120) Shimizu, G. K. H.; Vaidhyanathan, R.; Taylor, J. M. *Chem. Soc. Rev.* **2009**, *38*, 1430.

(121) Clearfield, A. *Dalton Trans.* **2008**, 6089.

(122) Shimizu, G. K. H.; Taylor, J. M.; Vaidhyanathan, R. *Macromol. Containing Met. Met.-Like Elem.* **2009**, *9*, 125.

(123) Gómez-Alcántara, M. d. M.; Cabeza, A.; Moreno-Real, L.; Aranda, M. A. G.; Clearfield, A. *Microporous Mesoporous Mater.* **2006**, *88*, 293.

(124) Caughlan, C. N.; Ulhaque, M. *Inorg. Chem.* **1967**, *6*, 1998.

(125) SAINTP+, B.; Bruker AXS: Madison, Wisconsin, USA, 2005.

(126) Bruker SADABS-2008/1, Bruker AXS Madison, Wisconsin, USA, 2008.

(127) Sheldrick, G. M. In *Structure Determination Software Suite*; SHELXTL 2008/4 ed. Madison, Wisconsin, USA, 2008.

(128) Johnson Carroll K, 1965. "OR TEP: A FORTRAN Thermal-Ellipsoid Plot Program for Crystal Structure Illustrations". ONRL Report #3794. Oak Ridge, Ten., Oak Ridge National Laboratory.

(129) Macrae, C. F.; Edgington, P. R.; McCabe, P.; Pidcock, E.; Shields, G. P.; Taylor, R.; Towler, M.; van de Streek, J. *J. Appl. Crystallogr.* **2006**, *39*, 453.

(130) Shannon, R. D. *Acta Cryst. A* **1976**, *A32*, 751.

(131) Brown, I. D.; Altermatt, D. *Acta Cryst. B* **1985**, *B41*, 244.

(132) TGA: biphenylenediphosphonic acid (250 ^{o}C 0.72 %, 300 ^{o}C 4.24%, 330 ^{o}C 6.61%), lithium biphenylenediphosphonate (300 ^{o}C 0.18%, 330 ^{o}C 1.61%)

(133) Murugavel, R.; Gogoi, N. *Bull. Mater. Sci.* **2009**, *32*, 321.

(134) Rao, C. N. R.; Natarajan, S.; Choudhury, A.; Neeraj, S.; Ayi, A. A. *Acc. Chem. Res.* **2001**, *34*, 80.

(135) Natarajan, S.; K. Cheetham, A. *Chem. Commun.* **1997**, 1089.

(136) Tanaka, D.; Kitagawa, S. *Chem. Mater.* **2008**, *20*, 922.

(137) Vaidhyanathan, R.; Natarajan, S.; Cheetham, A. K.; Rao, C. N. R. *Chem. Mater.* **1999**, *11*, 3636.

(138) Song, H.-H.; Zheng, L.-M.; Wang, Z.; Yan, C.-H.; Xin *Inorg. Chem.* **2001**, *40*, 5024.

(139) Liu, L.; Li, J.; Sun, Z.-G.; Dong, D.-P.; Zhang, N.; Lu, X.; Wang, W.-N.; Tong, F. *Z. Anorg.Allg. Chem.* **2010**, *636*, 247.

(140) Lu, X.; Li, J.; Sun, Z.-G.; Dong, D.-P.; Hua, R.-N.; Zhang, N.; Liu, L.; Tong, F.; Wang, W.-N. *Z. Anorg. Allg. Chem.* **2009**, *635*, 2617.

(141) Li, J.-R.; Kuppler, R. J.; Zhou, H.-C. *Chem. Soc. Rev.* **2009**, *38*, 1477.

(142) Li, J.-R.; Kuppler, R. J.; Zhou, H.-C. *Chem Soc Rev* **2009**, *38*, 1477.

(143) Wilmer, C. E.; Farha, O. K.; Yildirim, T.; Eryazici, I.; Krungleviciute, V.; Sarjeant, A. A.; Snurr, R. Q.; Hupp, J. T. *Energy Environ. Sci.* **2013**, *6*, 1158.

(144) Lee, J. Y.; Farha, O. K.; Roberts, J.; Scheidt, K. A.; Nguyen, S. B. T.; Hupp, J. T. *Chem. Soc. Rev.* **2009**, *38*, 1450.

(145) Allendorf, M. D.; Bauer, C. A.; Bhakta, R. K.; Houk, R. J. T. *Chem. Soc. Rev.* **2009**, *38*, 1330.

(146) Long, J. R.; Yaghi, O. M. *Chem. Soc. Rev.* **2009**, *38*, 1213.

(147) Wang, Z.; Cohen, S. M. *Chem. Soc. Rev.* **2009**, *38*, 1315.

(148) Maeda, K. *Microporous Mesoporous Mater.* **2004**, *73*, 47.

(149) Gagnon, K. J.; Perry, H. P.; Clearfield, A. *Chem. Rev.* **2012**, *112*, 1034.

(150) Ma, T.-Y.; Li, H.; Tang, A.-N.; Yuan, Z.-Y. *Small* **2011**, *7*, 1827.

(151) Ma, T.-Y.; Yuan, Z.-Y. *ChemSusChem* **2011**, *4*, 1407.

(152) Liu, L.; Li, J.; Sun, Z.-G.; Dong, D.-P.; Zhang, N.; Lu, X.; Wang, W.-N.; Tong, F. *Z. Anorg. Allg. Chem.* **2010**, *636*, 247.

(153) Lu, X.; Li, J.; Sun, Z.-G.; Dong, D.-P.; Hua, R.-N.; Zhang, N.; Liu, L.; Tong, F.; Wang, W.-N. *Z. Anorg. Allg. Chem.* **2009**, *635*, 2617.

(154) Plabst, M.; Kohn, R.; Bein, T. *CrystEngComm* **2010**, *12*, 1920.

(155) Reinsch, H.; Stock, N. *Microporous Mesoporous Mater.* **2013**, *171*, 156.

(156) Sarma, D.; Ramanujachary, K. V.; Stock, N.; Natarajan, S. *Cryst. Growth Des.* **2011**, *11*, 1357.

(157) Reinsch, H.; Feyand, M.; Ahnfeldt, T.; Stock, N. *Dalton Trans.* **2012**, *41*, 4164.

(158) Kinnibrugh, T. L.; Garcia, N.; Clearfield, A. *J. Solid State Chem.* **2012**, *187*, 149.

(159) Perry, H. P.; Law, J.; Zon, J.; Clearfield, A. *Microporous Mesoporous Mater.* **2012**, *149*, 172.

(160) TWINABS, B.; Bruker AXS Inc.: Madison, Wisconsin, USA, 2001.

(161) Brandenburg, K.; Berndt, M. **1999** DIAMOND. Crystal Impact GbR Bonn, Germany.

(162) Haky, J. E.; Brady, J. B.; Dando, N.; Weaver, D. *Mater. Res. Bull.* **1997**, *32*, 297.

(163) Poojary, M. D.; Hu, H.-L.; Campbell III, F. L.; Clearfield, A. *Acta Cryst. B* **1993**, *49*, 996.

(164) Cabeza, A.; Aranda, M. A. G.; Bruque, S.; Poojary, D. M.; Clearfield, A.; Sanz, J. *Inorg. Chem.* **1998**, *37*, 4168.

(165) Kimura, T.; Kato, K. *Microporous Mesoporous Mater.* **2007**, *101*, 207.

(166) Subbiah, A.; Bhuvanesh, N.; Clearfield, A. *J. Solid State Chem.* **2005**, *178*, 1321.

(167) Zhang, B.; Poojary, D. M.; Clearfield, A. *Inorg. Chem.* **1998**, *37*, 1844.

(168) Kirumakki, S.; Huang, J.; Subbiah, A.; Yao, J.; Rowland, A.; Smith, B.; Mukherjee, A.; Samarajeewa, S.; Clearfield, A. *J. Mater. Chem.* **2009**, *19*, 2593.

(169) Tan, J. C.; Cheetham, A. K. *Chem. Soc. Rev.* **2011**, *40*, 1059.

(170) Biswas, M. M.; Cagin, T. *Mater. Chem. Phys.* **2011**, *131*, 44.

(171) Reichenbach, C.; Kalies, G.; Lincke, J.; Laessig, D.; Krautscheid, H.; Moellmer, J.; Thommes, M. *Microporous Mesoporous Mater.* **2011**, *142*, 592.

(172) Chapman, K. W.; Sava, D. F.; Halder, G. J.; Chupas, P. J.; Nenoff, T. M. *J. Am. Chem. Soc.* **2011**, *133*, 18583.

(173) Chapman, K. W.; Halder, G. J.; Chupas, P. J. *J. Am. Chem. Soc.* **2008**, *130*, 10524.

(174) Chapman, K. W.; Halder, G. J.; Chupas, P. J. *J. Am. Chem. Soc.* **2009**, *131*, 17546.

(175) Barrera, G. D.; Bruno, J. A. O.; Barron, T. H. K.; Allan, N. L. *J. Phys.: Condens. Matter* **2005**, *17*, R217.

(176) Parise, J. B. *Reviews in Mineralogy and Geochemistry* **2006**, *63*, 205.

(177) Lind, C. *Materials* **2012**, *5*, 1125.

(178) Takenaka, K. *Science and Technology of Advanced Materials* **2012**, *13*, 013001/1.

(179) Lightfoot, P.; Woodcock, D. A.; Maple, M. J.; Villaescusa, L. A.; Wright, P. A. *J. Mater. Chem.* **2001**, *11*, 212.

(180) Miller, W.; Smith, C. W.; Mackenzie, D. S.; Evans, K. E. *J. Mater. Sci.* **2009**, *44*, 5441.

(181) Dubbeldam, D.; Walton, K. S.; Ellis, D. E.; Snurr, R. Q. *Angew. Chem. Int. Ed.* **2007**, *46*, 4496.

(182) Lock, N.; Christensen, M.; Wu, Y.; Peterson, V. K.; Thomsen, M. K.; Piltz, R. O.; Ramirez-Cuesta, A. J.; McIntyre, G. J.; Noren, K.; Kutteh, R.; Kepert, C. J.; Kearley, G. J.; Iversen, B. B. *Dalton Trans.* **2013**, *42*, 1996.

(183) Ogborn, J. M.; Collings, I. E.; Moggach, S. A.; Thompson, A. L.; Goodwin, A. L. *Chem. Sci.* **2012**, *3*, 3011.

(184) Lock, N.; Christensen, M.; Kepert, C. J.; Iversen, B. B. *Chem. Commun.* **2013**, *49*, 789.

(185) Zhao, L.; Yang, Q.; Ma, Q.; Zhong, C.; Mi, J.; Liu, D. *J. Mol. Model.* **2011**, *17*, 227.

(186) Lock, N.; Wu, Y.; Christensen, M.; Cameron, L. J.; Peterson, V. K.; Bridgeman, A. J.; Kepert, C. J.; Iversen, B. B. *J. Phys. Chem. C* **2010**, *114*, 16181.

(187) Mu, B.; Walton, K. S. *J. Phys. Chem. C* **2011**, *115*, 22748.

(188) Zhou, W.; Wu, H.; Yildirim, T.; Simpson, J. R.; Hight, W. A. R. *Phys. Rev. B: Condens. Matter* **2008**, *78*, 054114/1.

(189) Ponomareva, V. G.; Kovalenko, K. A.; Chupakhin, A. P.; Dybtsev, D. N.; Shutova, E. S.; Fedin, V. P. *J. Am. Chem. Soc.* **2012**, *134*, 15640.

(190) Hurd, J. A.; Vaidhyanathan, R.; Thangadurai, V.; Ratcliffe, C. I.; Moudrakovski, I. L.; Shimizu, G. K. H. *Nat. Chem.* **2009**, *1*, 705.

(191) Sen, S.; Nair, N. N.; Yamada, T.; Kitagawa, H.; Bharadwaj, P. K. *J. Am. Chem. Soc.* **2012**, *134*, 19432.

(192) Wei, M.; Wang, X.; Duan, X. *Chem. Eur. J.* **2013**, *19*, 1607.

(193) Maeda, K.; Hatasawa, H.; Kawawa, K.; Nagayoshi, N.; Matsushima, Y. *Chem. Lett.* **2011**, *40*, 215.

(194) Maeda, K.; Takamatsu, R.; Mochizuki, M.; Kawawa, K.; Kondo, A. *Dalton Trans.* **2013**.

(195) Maeda, K.; Kondo, A. *Dalton Trans.* **2013**.

(196) Macrae, C. F.; Edgington, P. R.; McCabe, P.; Pidcock, E.; Shields, G. P.; Taylor, R.; Towler, M.; van de Streek, J. *J. Appl. Crystallogr.* **2006**, *39*, 453.

(197) Chupas, P. J.; Chapman, K. W.; Kurtz, C.; Hanson, J. C.; Lee, P. L.; Grey, C. P. *J. Appl. Crystallogr.* **2008**, *41*, 822.

(198) Coelho, A. A.; Kern, A. *CPD Newsletter* **2005**, *32*, 43.

(199) Bruker; 4.2 ed.; Bruker AXS: Karlsuhe, Germany, 2009.

(200) Le Bail, A.; Duroy, H.; Fourquet, J. L. *Mater. Res. Bull.* **1988**, *23*, 447.

(201) Favre-Nicolin, V.; Cerny, R. *J. Appl. Crystallogr.* **2002**, *35*, 734.

(202) Fox, Free Objects for Crystallography, http://objcryst.sourceforge.net.

(203) Petricek, V., Dusek,M. & Palatinus,L. Jana2006. Institute of Physics, Praha, Czech Republic, 2006.

(204) Bakhmutov, V. I. *Solid-State NMR in Materials Science: Principles and Applications*; CRC Press, Boca Raton, 2011.

(205) Slade, R. C. T.; Forano, C. R. M.; Peraio, A.; Alberti, G. *Solid State Ionics* **1993**, *61*, 23.

(206) Zima, V.; Svoboda, J.; Melanova, K.; Benes, L.; Casciola, M.; Sganappa, M.; Brus, J.; Trchova, M. *Solid State Ionics* **2010**, *181*, 705.

(207) Haase, F.; Sauer, J. *J. Phys. Chem.* **1994**, *98*, 3083.

(208) Ma, D.; Han, X.; Xie, S.; Bao, X.; Hu, H.; Au-Yeung, S. C. F. *Chem. Eur. J.* **2002**, *8*, 162.

(209) Afanassyev, I. S.; Moroz, N. K. *Solid State Ionics* **2003**, *160*, 125.

(210) Morris, W.; Taylor, R. E.; Dybowski, C.; Yaghi, O. M.; Garcia-Garibay, M. A. *J. Mol. Struct.* **2011**, *1004*, 94.

(211) Groves, J. A.; Miller, S. R.; Warrender, S. J.; Mellot-Draznieks, C.; Lightfoot, P.; Wright, P. A. *Chem. Commun.* **2006**, 3305.

(212) Devi, R. N.; Wormald, P.; Cox, P. A.; Wright, P. A. *Chem. Mater.* **2004**, *16*, 2229.

(213) Merrill, C. A.; Cheetham, A. K. *Inorg. Chem.* **2005**, *44*, 5273.

(214) Poeppelmeier, K. R.; Hwu, S. J. *Inorg. Chem.* **1987**, *26*, 3297.

(215) Yamaguchi, G.; Sakamoto, K. *Can. J. Chem.* **1960**, *38*, 1395.

(216) Wang, J.; Toby, B. H.; Lee, P. L.; Ribaud, L.; Antao, S.; Kurtz, C.; Ramanathan, M.; Von Dreele, R. B.; Beno, M. A. *Review of Scientific Instruments* **2008**, *79*, 085105.

(217) Lee, P. L.; Shu, D.; Ramanathan, M.; Preissner, C.; Wang, J.; Beno, M. A.; Von Dreele, R. B.; Lynn Ribaud; Kurtz, C.; Antao, S. M.; Jiao, X.; Toby, B. H. *J.Synchrotron Rad.* **2008**, *15*, 427.

(218) Preissner, C.; Shu, D.; Toby, B. H.; Lee, P.; Wang, J.; Kline, D.; Goetze, K. *Nuclear Instruments and Methods in Physics Research A* **2009**, *in press*.

(219) Oszlanyi, G.; Suto, A. *Acta Cryst. A* **2004**, *60*, 134.

(220) Coelho, A. *Acta Cryst. A* **2007**, *63*, 400.

(221) Stephens, P. W. *J. Appl. Crystallogr.* **1999**, *32*, 281.

(222) Edgar, M.; Carter, V. J.; Tunstall, D. P.; Grewal, P.; Favre-Nicolin, V.; Cox, P. A.; Lightfoot, P.; Wright, P. A. *Chem. Commun.* **2002**, *0*, 808.

(223) Clearfield, A. *Curr. Opin. Solid State Mater. Sci.* **2003**, *6*, 495.

(224) Mincher, B. J.; Martin, L. R.; Schmitt, N. C. *Inorg. Chem.* **2008**, *47*, 6984.

(225) Momcilovic, M.; Kovacevic, J.; Tanic, M.; Dordevic, M.; Bacic, G.; Dragovic, S. *Environ. Monit. Assess.* **2013**, *185*, 1319.

(226) Wang, J.; Liu, J.; Li, H.; Song, G.; Chen, Y.; Xiao, T.; Qi, J.; Zhu, L. *Clean – Soil, Air, Water* **2012**, *40*, 1357.

(227) Patel, P.; Chudasama, U. *Desalination and Water Treatment* **2009**, *12*, 87.

(228) Shah, B.; Chudasam, U. *Desalination and Water Treatment* **2012**, *38*, 276.

(229) Plabst, M.; McCusker, L. B.; Bein, T. *J. Am. Chem. Soc.* **2009**, *131*, 18112.

(230) Patel, P.; Chudasama, U. *J. Sci. Ind. Res.* **2010**, *69*, 756.

(231) Chakrabarty, T.; Shah, B.; Srivastava, N.; Shahi, V. K.; Chudasama, U. *J. Membr. Sci.* **2013**, *428*, 462.

(232) Wu, J.; Hou, H.; Han, H.; Fan, Y. *Inorg. Chem.* **2007**, *46*, 7960.

(233) Hix, G. B.; Carter, V. J.; Wragg, D. S.; Morris, R. E.; Wright, P. A. *J. Mater. Chem.* **1999**, *9*, 179.

(234) Poojary, D. M.; Zhang, Y.; Cox, D. E.; Rudolf, P. R.; Cheng, S.; Clearfield, A. *J. Chem. Crystallogr.* **1994**, *24*, 155.

(235) Nakayama, H.; Eguchi, T.; Nakamura, N.; Yamaguchi, S.; Danjyo, M.; Tsuhako, M. *J. Mater. Chem.* **1997**, *7*, 1063.

(236) Corbridge, D. E. C.; Lowe, E. J. *J. Chem. Soc. (Resumed)* **1954**, *0*, 493.

(237) Shannon, R. D.; Prewitt, C. T. *Acta Cryst. B* **1969**, *25*, 925.

(238) Kinnibrugh, T.; Ayi, A. A.; Bakhmutov, V. I.; Zon, J.; Clearfield, A. *Cryst. Growth Des.* **2013**, *http://dx.doi.org/10.1021/cg400399v*.

APPENDIX A

STRUCTURAL DIFFERENCES OF METAL BIPHENYLENEDIPHOSPHONATES WITH CHANGE IN THE ALKALI METAL

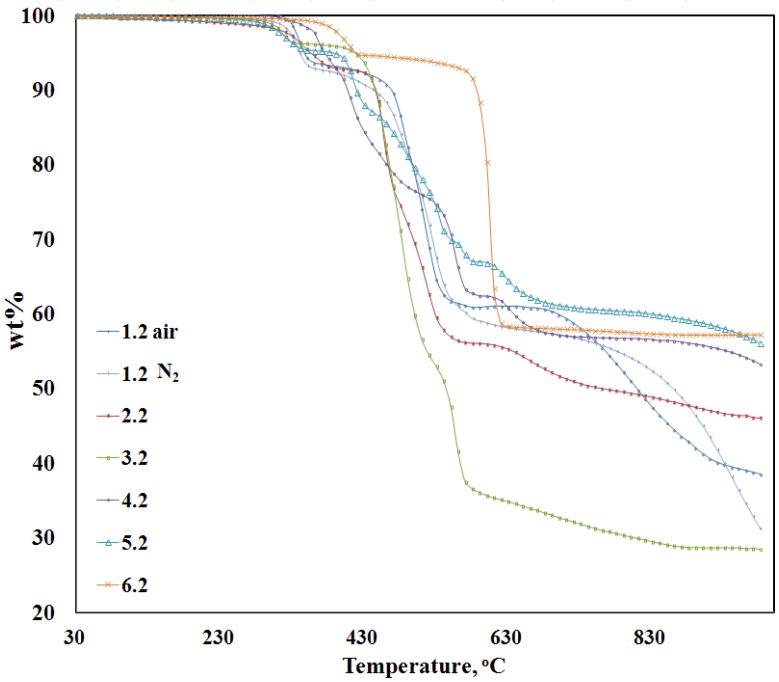

Figure A 1. Presented are the TGA curves of compound **1.2-6.2**, where all compounds show thermal stability up to approximately 300^{o}C

APPENDIX B

SYNTHESIS OF METAL PHOSPHONATES BY CAPITALIZING ON THE SENSITIVITY OF THE STRUCTURE TO SOLVOTHERMAL REACTION CONDITIONS

The synthetic conditions for reactions 1.3-12.3 are given in Table B1-B3.

Table B 1. Synthetic details for lithium based metal phosphonates

	1.3	**2.3**	**3.3**	**4.3**	**5.3**
t-BuPA [mmol]	0.379	0.379	0.379		
t-BuPA [g]	50.1	50.1	50.1		
PPA [mmol]				0.316	0.316
PPA [g]				49.9	49.9
Li_2CO_3 [mmol]	0.365	0.364	0.359	0.340	0.340
Li_2CO_3 [g]	27	26.9	26.5	26.8	26.8
V [mL] toluene	6	6	6	6	6
V [μL] H_2O	30	90	210	30	210
Temperature, ^oC	145	145	145	145	145
Time, d	3	3	3	3	3

Table B 2. Synthetic details for sodium based metal phosphonates

	6.3	**7.3**	**8.3**	**9.3**	**10.3**	**11.3**	**12.3**
PPA [mmol]	1.08	1.08	1.08	1.08			
PPA [g]	106.4	106.4	106.4	106.4			
BPDPA [mmol]					0.036	0.500	0.036
BPDPA [g]					112	157	112
$Na_2CO_3 \cdot H_2O$ [mmol]	0.515	0.515	0.515	0.515	0.105	0.105	0.105
$Na_2CO_3 \cdot H_2O$ [g]	52	52	52	52	11	11	11
V [mL] toluene	4	4	4	4	5	5	5
V [µL] H_2O	60	60	30	0	60	60	60
V [µL] H_3CNH_2		80	80	80			
V [µL] $H_9C_4NH_2$	80				130		
V [µL] $(H_5C_2)_2NH$						81	
V [µL] $H_2NC_2H_4NH_2$							59
Temperature, ^oC	120	120	120	120	120	120	120
Time, d	5	5	5	5	7	7	7

Detailed crystallographic and refinement parameters

Table B 3. Experimental and refinement parameters for compounds **1.3**-**4.3**

Crystal Data	**1.3**	**2.3**	**3.3**	**4.3**	**5.3**
Chemical formula	$Li_9(H_2O)_3(HO_3PC_4H_9)_5(O_3PC_4H_9)_2 \cdot 1.5(H_2O)$	$Li_4(H_2O)(O_3PC_4H_9)_2$	$Li(H_2O)_3(HO_3PC_4H_9)\cdot H_2O$	$Li_2(O_3PC_6H_5)$	$Li(HO_3PC_6H_5)(H_2O_3PC_6H_5)$
M_r	1111.03	315.92	216.09	339.90	322.10
Crystal system, space group	Trigonal, $P\bar{3}$	Orthorhombic, *Pnma*	Triclinic, $P\bar{1}$	Monoclinic, $P2_1/n$	Triclinic, $P\bar{1}$
Temperature (K)	110	110	110	213	110
a, *b*, *c* (Å)	15.799 (6), 12.137 (7)	7.693 (5) 8.953 (8) 21.39 (2)	6.249 (5) 6.575 (5) 15.443 (12)	8.872 (8) 5.161 (5) 30.22 (3)	5.409 (4), 8.613 (7), 15.192 (12)
α, β, γ (°)			80.058 (9) 89.205 (9) 63.423 (8)	90.007 (10)	100.158 (9), 90.856 (9), 89.999 (9)
V (Å^3)	2624 (2)	1473 (2)	557.5 (7)	1384 (2)	696.6 (10)
Z	2	4	2	4	2
Mo *K*α, μ (mm^{-1})	0.32	0.32	0.25	0.34	0.33
Crystal size (mm)	0.19 × 0.15 × 0.03	0.34 × 0.21 × 0.12	0.38 ×0.25 × 0.08	0.52 × 0.30 × 0.03	0.10 × 0.05 × 0.02
T_{min}, T_{max}	0.943, 0.991	0.900, 0.963	0.912, 0.981	0.844, 0.990	0.967, 0.993
No. of measured, independent and observed [$I > 2\sigma(I)$] reflections	14593, 3911, 1305	17184, 2060, 1539	6242, 2441, 1745	19978, 3240, 2438	5626, 2712, 1959
R_{int}	0.185	0.073	0.038	0.045	0.045
$(\sin\theta/\lambda)_{max}$ (Å^{-1})	0.644	0.682	0.642	0.660	0.617
$R[F^2 > 2\sigma(F^2)]$, $wR(F^2)$, *S*	0.136 0.407, 1.03	0.049 0.138, 1.06	0.043 0.112, 1.03	0.042 0.108, 1.04	0.089, 0.243, 1.04
No. of reflections	3911	2060	2441	3240	2712
No. of parameters	199	118	162	257	198
No. of restraints	70	0	0	0	4
$\Delta\rho_{max}$, $\Delta\rho_{min}$ (e Å^{-3})	1.54, −0.88	0.92, −0.56	0.70, −0.38	0.55, −0.43	2.18,−0.73

Table B 4. Experimental and refinement parameters for compounds **7.3-10.3**

Crystal data	**6.3**	**7.3**	**8.3**	**9.3**
Chemical formula	$Na_2(H_2O)_8{\cdot}2(O_3PC_6H_5){\cdot}2(C_4H_9NH_3){\cdot}4(H_2O)$	$Na_3(H_2O)_{13}{\cdot}3(O_3PC_6H_5){\cdot}3(CH_3NH_3){\cdot}2(H_2O)$	$Na_2(H_2O)_{10}(O_3PC_6H_5)_2{\cdot}2(CH_3NH_3)$	$Na_4(H_2O)(O_3PC_6H_5)_2(HO_3PC_6H_5)_2{\cdot}2(CH_3NH_3)$
M_r	360.80	903.62	602.42	800.41
Crystal system, space group	Monoclinic, $P2_1/c$	Triclinic, $P\bar{1}$	Monoclinic, $P2_1/c$	Monoclinic, $P2_1$
Temperature (K)	110	110	110	110
a, b, c (Å)	19.733 (14), 7.215 (5), 12.660 (8)	6.195 (6), 17.470 (17), 20.06 (2)	8.486 (5), 36.123 (19), 9.331 (5)	7.755 (2), 14.638 (4), 14.899 (4)
α, β, γ (°)	92.152 (13)	83.628 (13), 87.581 (14), 82.548 (12)	92.584 (7)	90.068 (3)
V (Å^3)	1801 (2)	2139 (4)	2857 (3)	1691.2 (8)
Z	4	2	4	2
Mo $K\alpha$, μ (mm^{-1})	0.22	0.25	0.25	0.34
Crystal size (mm)	0.22 × 0.20 × 0.03	0.14 × 0.13 × 0.01	0.24 × 0.23 × 0.03	0.42 × 0.23 × 0.18
T_{min}, T_{max}	0.954, 0.994	0.966, 0.998	0.942, 0.993	0.870, 0.941
No. of measured, independent and observed [$I > 2\sigma(I)$] reflections	32504, 3960, 2271	14299,, 7927, 3017	30982, 6213, 4518	7450, 7325, 4993
R_{int}	0.122	0.130	0.094	0.033
$(\sin\theta/\lambda)_{max}$ (Å^{-1})	0.642	0.617	0.639	0.650
$R[F^2>2\sigma(F^2)]$, $wR(F^2)$, S	0.056 0.166, 1.01	0.097 0.268, 1.01	0.070 0.192, 1.05	0.086 0.208, 1.07
No. of reflections	3960	7927	6213	7325
No. of parameters	207	489	330	383
No. of restraints	0	6	0	1
$\Delta\rho_{max}$, $\Delta\rho_{min}$ (e Å^{-3})	0.43, −0.46	0.60, −0.52	0.60, −0.73	1.65, −0.89
Absolute structure				Flack H D (1983), Acta Cryst. A39, 876-881
Flack parameter				0.5 (3)

Table B 5. Experimental and refinement parameters for compounds **11.3-12.3**

Crystal data	**10.3**	**11.3**	**12.3**
Chemical formula	$H_8NaO_4 \cdot 0.5(C_{12}H_8O_6P_2) \cdot C_6H_4O_3P \cdot 0.5(H_{16}Na_2O_8) \cdot 2(HH_9C_4NH_3)$	$Na_4(H_2O)_{12}(O_3PC_{12}H_8PO_3H)(O_3PC_6H_4) \cdot ((C_2H_5)_2NH_2) \cdot H_2O$	$Na_3(H_2O)_3(O_3PC_{12}H_8PO_3) \cdot NH_2C_2H_4NH_3$
M_r	702.57	939.65	494.25
Crystal system	Monoclinic	Triclinic	Triclinic
space group	$P2/n$	$P\bar{1}$	$P\bar{1}$
Temperature (K)	110	110	110
a, b, c (Å)	19.817 (3), 6.5209 (8), 28.457 (5)	9.310 (7), 14.907 (12), 17.752 (14)	6.032 (6), 11.579 (9), 15.422 (12)
α, β, γ (°)	106.235 (6)	113.160 (9), 92.451 (10), 106.844 (9)	97.18 (2), 100.36 (1), 100.95 (2)
V (Å^3)	3530.8 (9)	2133 (3)	1026.0 (15)
Z	4	2	2
Mo $K\alpha$, μ (mm^{-1})	Cu $K\alpha$ 1.97	0.26	0.33
Crystal size (mm)	0.18 × 0.17 × 0.03	0.22 × 0.08 × 0.05	0.10 × 0.08 × 0.02
T_{min}, T_{max}	0.716, 0.943	0.944, 0.988	0.968, 0.994
No. of measured,	25519	16724	7949
independent and	4823	8273	3986
observed [$I > 2\sigma(I)$] reflections	3150	3770	2094
R_{int}	0.089	0.115	0.087
θ_{max} (°)	58.0		
$(\sin\theta/\lambda)_{max}$ (Å^{-1})	0.550	0.617	0.617
$R[F^2 > 2\sigma(F^2)]$,	0.047	0.069	0.082
$wR(F^2)$, S	0.108, 1.03	0.137, 0.91	0.200, 1.08
No. of reflections	4823	8273	3986
No. of parameters	392	530	259
No. of restraints	14	28	3
$\Delta\rho_{max}$, $\Delta\rho_{min}$ (e Å^{-3})	0.41, −0.40	0.43, −0.45	0.91, −0.62

The crystal descriptions of compounds 1.3-12.3

*Crystal structure of **1.3***

The asymmetric unit consists of three independent lithium atoms and two phosphonate moieties (P1 and P2) with full occupancy, a phosphonate moiety positioned on a three-fold axis (P3 with 1/3 occupancy), and a disordered water molecule. The lithium atoms have tetrahedral geometry with each bonding to four different phosphonate moieties. A triangle-shaped cluster with three-fold symmetry is built by six-member rings formed from lithium phosphonate bridges (Figure B 2a). The corners of each cluster overlap, bridging the clusters to form a layered structure with *tert*-butyl phosphonates projected into the interlayer (Figure B 2b). The inorganic layer contains voids occupied by water molecules which are hydrogen bonded to the framework.

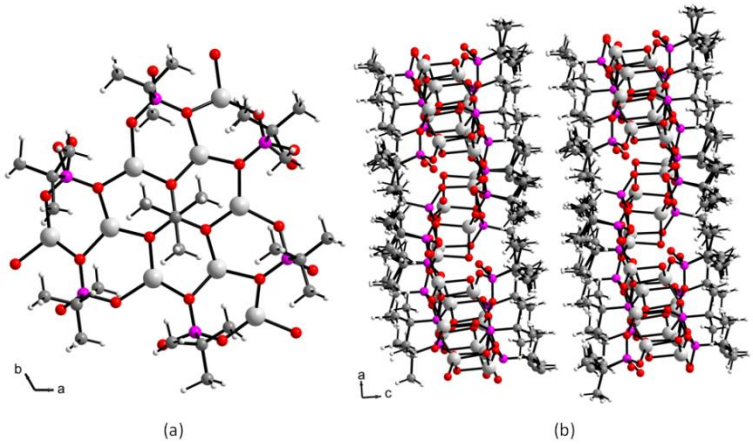

Figure B 2. Crystal structure of compound **1.3**: view of the triangle-shaped cluster (a) and a view down the *b*-axis showing the lithium phosphonate layer (b)

*Crystal structure of **2.3***

The asymmetric unit cell consists of two independent lithium atoms with full occupancy, a water molecule and two phosphonate moieties positioned on mirror planes (P1 and P2 half occupancy). The lithium atoms differ in coordination number even though both bond to three phosphonate moieties. Lithium atom Li2 is three coordinate with a trigonal planar geometry. However, lithium atom Li1 has a tetrahedral geometry and bonds to a water molecule to fulfill the fourth coordination site. A chain built from vertex-shared six-member rings with chair conformation run along the [100] direction. The six-member ring consists of the phosphonate moiety P2 and lithium atoms Li1 and Li1'. The phosphorus atom, P2, and oxygen atom, O4, act as the bridging vertices. The lithium atoms are further connected by a bridging water molecule. Edges of the six-member rings are shared with a second six-member ring along the [010] direction building the inorganic layer (Figure B 3a). The second six-member ring is formed from lithium atom Li2 and phosphonate moiety P1. The inorganic layer is further stabilized by hydrogen bonding between the water molecule and oxygen atom O4 (O…O 2.679 (4) Å, O…H-O 177.9 ^{o}). The *tert*-butyl phosphonates are space far apart, with the shortest distance of 5.894 Å. The steric hindrance of the bulky *tert*-butyl groups forces lithium atom Li2 to have a planar geometry. The possible fourth coordination site is hinder on either side by methyl. Both are too close for any oxygen atom to bond to lithium atom Li2 resulting in the trigonal planar geometry (Figure B 4). The closest possible O…Li interaction (2.702 Å) available would largely distort the tetrahedral geometry.

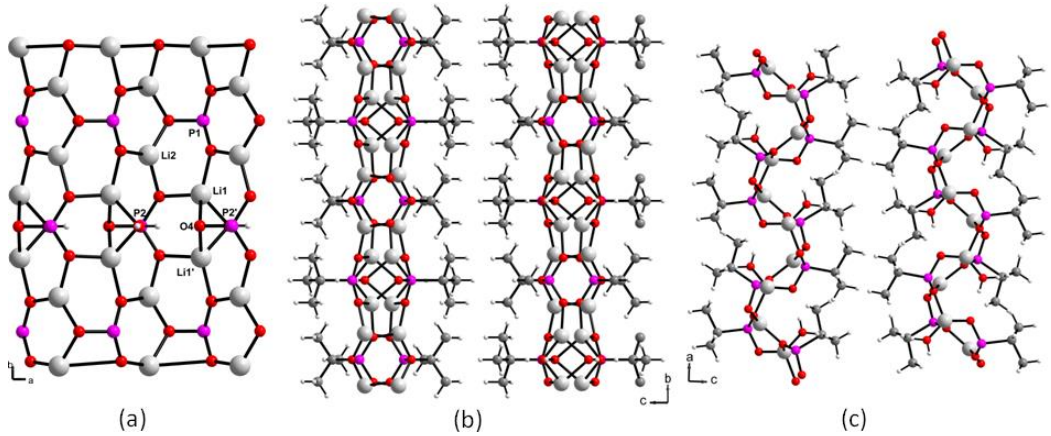

Figure B 3. Crystal structure of compound **2.3**: view of the inorganic layer (a) and two views down the *a*-axis (b) and *b*-axis (c) showing the lithium phosphonate layer

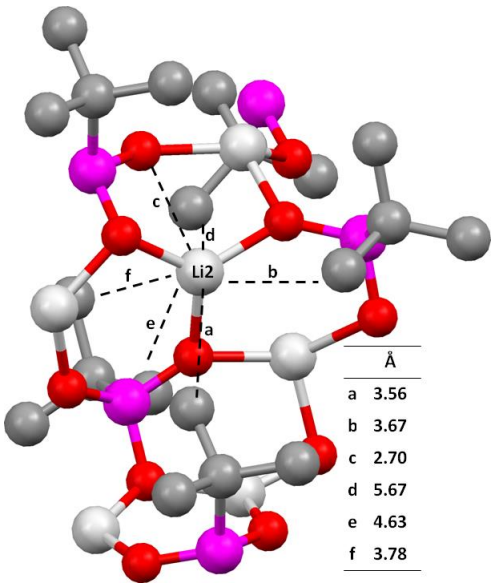

Figure B 4. The geometry of trigonal planar lithium atom Li2 showing the distance to the nearest atoms

*Crystal structure of **3.3***

Four water molecules, a lithium atom and a phosphonate moiety are the asymmetric unit in the unit cell. The lithium atom has a tetrahedral geometry but bonds to only one phosphonate oxygen atom leaving the remaining coordination sites occupied by three water molecules. The lithium phosphonate trihydrate moiety then builds a complex hydrogen bonding network through the remaining free water molecule and symmetry equivalent moieties resulting in a layered structure (Figure B 5). The *tert*-butyl phosphonate groups are directed in to the interlayer. The interlayer distance is 15.443(12) Å which corresponds to the length of the *c*-axis.

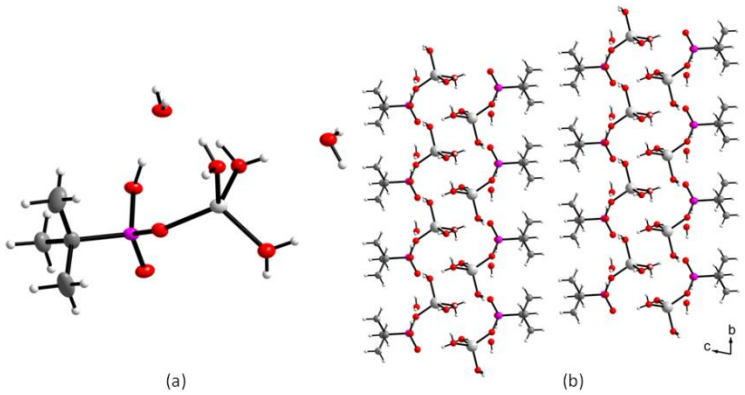

Figure B 5. Crystal structure of compound **3.3**: view of the lithium phosphonate trihydrate moiety (ORTEP 50%) (a) and a view down the *a*-axis showing the hydrogen-bonded lithium phosphonate layer (b)

*Crystal structure of **4.3***

There are four independent lithium atoms in the unit cell each with tetrahedral geometry. The two independent phosphonate moieties are bridged together through six-member rings forming a honeycomb layer in the *ab*-plane, where the lithium atoms are bonded to only three oxygen atoms (Figure B 6). To complete the honeycomb structure, oxygen atoms bond to the lithium atoms in the neighboring honeycomb layer, fulfilling the lithium coordination. Neighboring phenyl groups are rotated ~87^{o} to each other on the surface of the honeycomb structure.

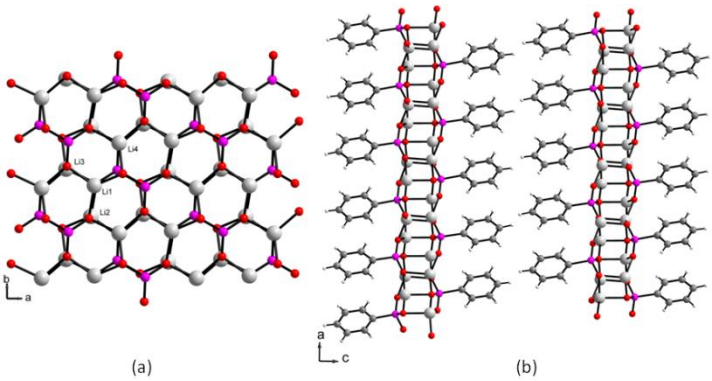

Figure B 6. Crystal structure of compound **4.3**: view of honeycomb inorganic structure (a) and a view down the *b*-axis showing the lithium phosphonate layer (b)

*Crystal structure of **5.3***

The crystal structure was determined to be the same structure as the published compound $Li(HO_3PC_6H_5)(H_2O_3PC_6H_5)$.[88] The tetrahedral lithium atoms form a chain structure.

*Crystal structure of **6.3***

The hydrogen-bonded layered is built from hydrogen bonding between four types of molecules: a edged-shared octahedral chains $(NaO_6)_n$, a phenylphosphonate moiety, a butyl ammonium ion, and two water molecules. The sodium atoms in the $(NaO_6)_n$ moiety have octahedral geometries. The equatorial oxygen atoms bridge neighboring sodium atoms forming corner-shared four member rings along the *b*-axis (Figure B 7a). Non-bridging water molecules occupy the axial positions of the sodium atoms completing the edged-shared octahedral chains. Neighboring chains run along the *c*-axis build the pseudo inorganic layer (Figure B 7b). The phenylphosphonate and the butyl ammonium ion alternate along the neighboring chains forming rows of each compound along the *b*-axis (Figure B 7c). Within each row, water molecules alternate with the respective molecule. A complex hydrogen bonding network builds the hydrogen-bonded layer.

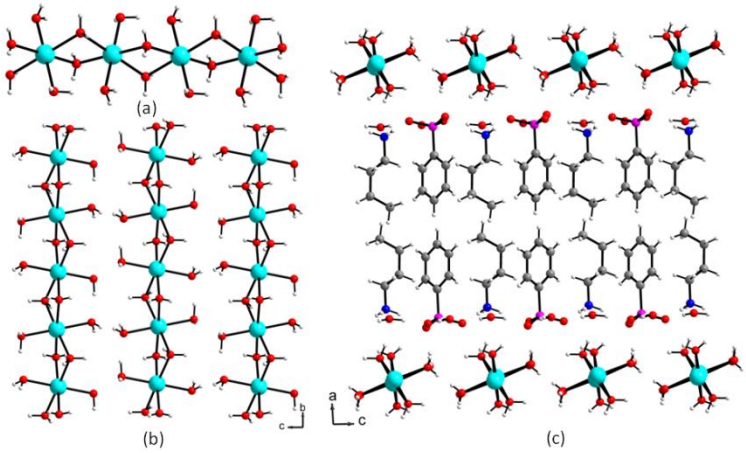

Figure B 7. Crystal structure of compound **6.3**: edged-shared octahedral chains $(NaO_6)_n$ (a), hydrogen bonded inorganic structure (b) and a view down the *b*-axis showing the hydrogen bonded sodium phosphonate structure (c)

*Crystal structure of **7.3***

The hydrogen-bonded layer is built from hydrogen bonding between four types of molecules: a chain built from sodium atoms and water molecules, a methyl ammonium ion, free water molecules and a phenylphosphonate moiety. The chain is built from two edge-shared bioctahedra Na_2O_{10} units bridged by a water molecule in the [001] direction (Figure B 8). In the Na_2O_{10} unit, each sodium atom has an octahedral geometry and is coordinated to six different water molecules. The chains pack along the *a*-axis to form a layer in the *ac*-plane (Figure B 8b). Alternating rows of phenylphosphonates, water molecules and methyl ammonium ions run along the chains in the [001] direction (Figure B 8c). A complex hydrogen bonding network builds the hydrogen-bonded layer.

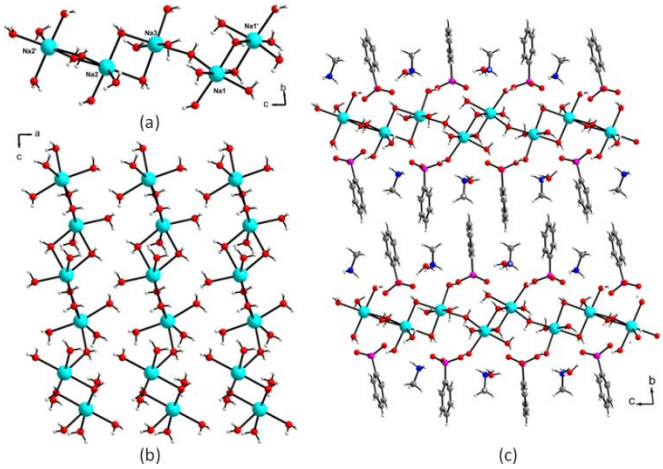

Figure B 8. Crystal structure of compound **7.3**: sodium-water chains (a), the hydrogen-bonded inorganic structure (b) and a view down the *a*-axis showing the hydrogen-bonded sodium phosphonate structure (c)

*Crystal structure of **8.3***

The hydrogen-bonded layered structure is built from hydrogen bonding between three types of molecules: an edged-shared bioctahedral Na_2O_{10} motif, a methyl ammonium ion, and a phenylphosphonate moiety. Each sodium atom in the Na_2O_{10} unit has octahedral geometry and bonded to six different water molecules. The Na_2O_{10} units build the pseudo inorganic layer in the *ab*-plane (Figure B 9a). Alternating rows of phenylphosphonates and methyl ammonium ions run along the *ac*-diagonal and hydrogen bond to each other and the layer built from the Na_2O_{10} unit forming a hydrogen-bonded structure (Figure B 9b).

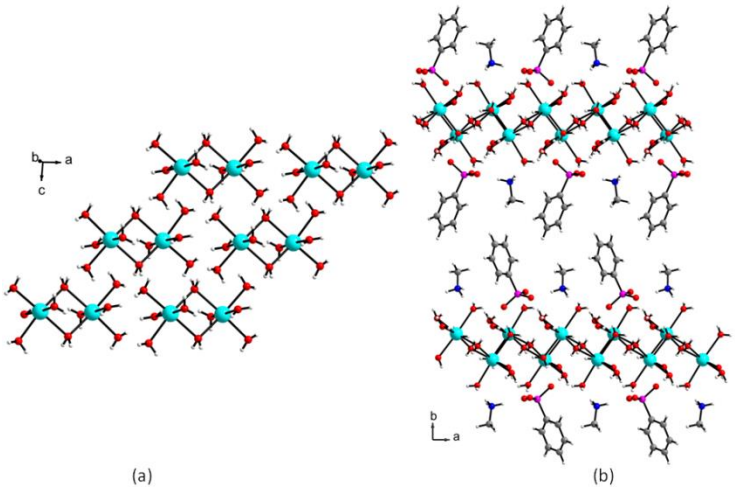

Figure B 9. Crystal structure of compound **8.3**: the inorganic layer built by edged-shared bioctahedral Na_2O_{10} (a) and a view down the *c*-axis showing the hydrogen bonded sodium phosphonate structure (c)

*Crystal structure of **9.3***

Two methyl ammonium ions, a water molecule, four phenyl phosphonates and four sodium atoms make up the asymmetric unit in the unit cell. All sodium atoms have distorted octahedral geometry and are bonded to four different phosphonate moieties. Sodium atoms Na2 and Na3 are also bonded to a water molecule. The inorganic layer lies in the *ab*-plane with phenyl phosphonates and methyl ammonium ions directed into the interlayer. The methyl ammonium ions are surrounded on four sides by phenyl phosphonates forming a pocket (Figure B 10b). The pocket is formed from the four different sodium ions acting as the corners:Na1-Na4 (Figure B 10a). Sodium ions Na2 and Na3 are bridged by oxygen atoms O1 and O11 to form a four-member ring along the [010] direction. Likewise, sodium atoms Na1 and Na4 are bridged by oxygen atoms O2

and O10 to form a four-member ring along the [010] direction. The two four-member rings bridged together along the [100] direction to form the pocket. The remaining phosphonate oxygen atoms and a bridging water molecule link the pockets together to form the inorganic layer.

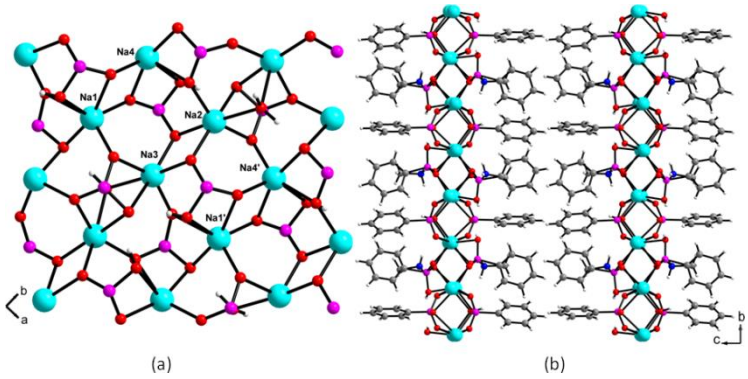

Figure B 10. Crystal structure of compound **9.3**: the inorganic layer (a) and a view down the *a*-axis showing the sodium phosphonate structure (c)

*Crystal structure of **10.3***

The three-dimensional hydrogen bonded network is built from hydrogen bonding between five types of molecules: a butyl ammonium ion, a biphenylenediphosphonate moiety, two water molecules, an edged-shared trigonal bipyramidal Na_2O_8 motif and edged-shared octahedral chain $(Na_2O_{10})_n$. The Na_2O_8 unit is built from two symmetry equivalent sodium atoms and eight water molecules (Figure B 11a). Each sodium atom has trigonal bipyramidal geometry and bonded to five different water molecules. The

inorganic chain $(Na_2O_{10})_n$ is built from two symmetry independent sodium atoms each with half occupancy (Na2 and Na3, Figure B 11a). Each sodium atom has octahedral geometry and bonds to six different water molecules. The oxygen atoms in the equatorial plane bridge the sodium atoms Na2 and Na3 to form four-member rings and extend the chain. The pseudo inorganic layer is built from hydrogen bonding between the Na_2O_8 and the $(Na_2O_{10})_n$ units. The phosphonate moiety, butyl ammonium ion, and second water molecule alternation along the pseudo inorganic background building the three-dimensional hydrogen-bonded structure (Figure B 11b).

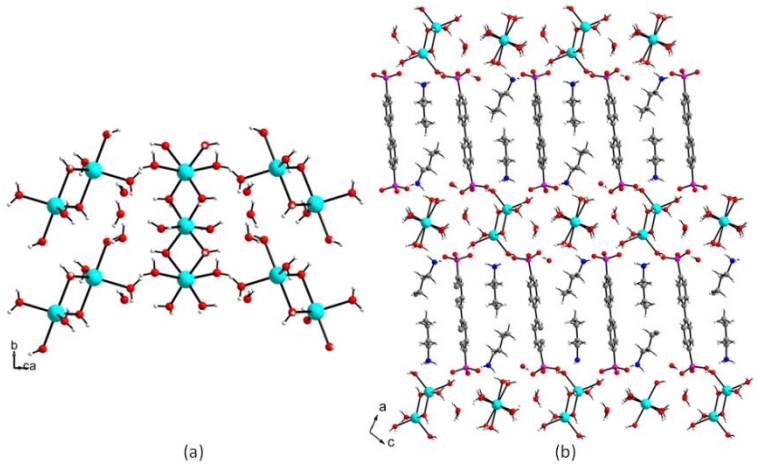

Figure B 11. Crystal structure of compound **10.3**: the hydrogen-bonded inorganic layer (a) and a view down the *b*-axis showing the hydrogen-bonded sodium phosphonate structure (c)

*Crystal structure of **11.3***

Two diethyl ammonium ions, a biphenylenediphosphonate moiety ($O_3PC_{12}H_8PO_3$), a $O_3PC_6H_4$ moiety, water molecules and four sodium atoms make up the asymmetric unit in the unit cell. Sodium atoms Na4 and Na5 have octahedral geometry and bond to only water molecules. Sodium atoms Na3 and Na6 have distorted square pyramidal geometry and bond to water molecules and one phosphonate oxygen atom each (P1 and P3). The phosphonate moiety P2 does not directly bond to a metal atom. The basic unit of the inorganic layer is given in Figure B 12a. The extension of this unit builds the inorganic layer (Figure B 12b). The inorganic layer is cross-linked by the phosphonate moiety P3 to form the templated three-dimensional structure (Figure B 12c).

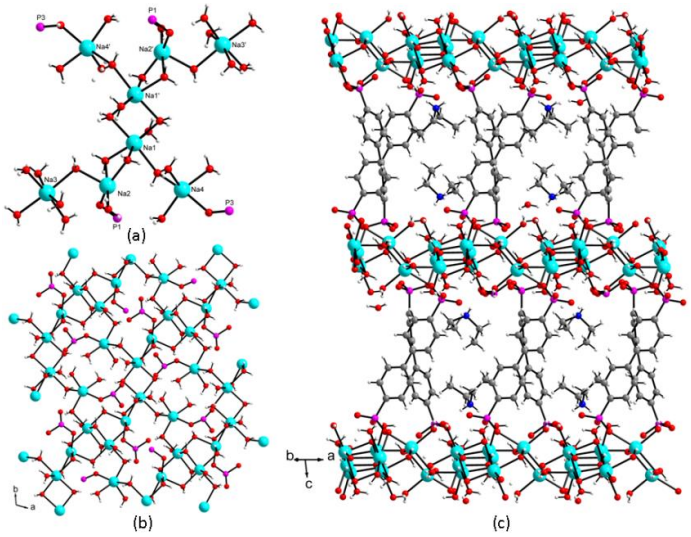

Figure B 12. Crystal structure of compound **11.3**: the basic building unit of the inorganic layer (a), a view of the inorganic layer and a view down the *c*-axis showing the sodium phosphonate structure (c)

*Crystal structure of **12.3***

One ethylene diammonium ion, a biphenylenediphosphonate moiety, water molecules and three sodium atoms make up the asymmetric unit in the unit cell. Sodium atom Na1 has a tetrahedral geometry and bonds to four different phosphonates. Atom Na2 has a distorted square pyramidal geometry and bonds to four different phosphonates. A Na_2O_7 motif is formed between Na1 and Na2 which forms corner-shared four member rings (Figure B 13a). The Na_2O_7 motifs are bridged together along the [100] direction forming a column of Na_2O_7 units. The columns are cross-linked by phosphonate moieties along the [001] direction. This forms a "non-traditional" layered structure. These layers are than bridged together by Na_2O_{10} motifs forming channels (Figure B 13b). The sodium atoms, Na3, in the bioctahedra Na_2O_{10} motif have octahedral geometry and each sodium atom is bonded to two phosphonate atoms and four water molecules. The channels are occupied with ethylene diammonium ions. The templated three-dimensional structure is given in Figure B 13c.

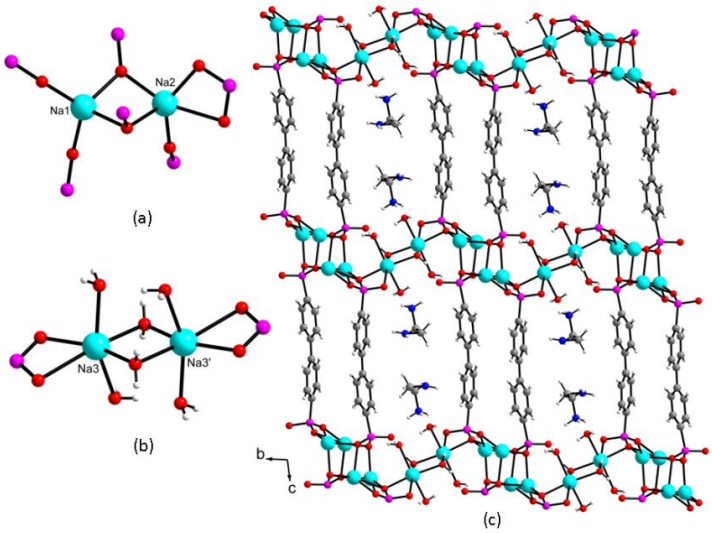

Figure B 13. Crystal structure of compound **12.3**: the Na_2O_7 motif (a), bioctahedra Na_2O_{10} motif (b) and a view down the *a*-axis showing the sodium phosphonate structure (c)

APPENDIX C

PROBING STRUCTURAL CHANGES IN A PHOSPHONATE-BASED MOF EXHIBITING REVERSIBLE DEHYDRATION

Table C 1. Crystallographic parameters and experimental details for the single crystal experiments

Crystal data	ZnBP-NH_4 (Phase Ia)	ZnBP-NH_4 (Phase Ib)	ZnBP-CH_3NH_3
Chemical formula	$Zn_{2.5}(H)_{0.5}(C_6H_3O_9P_3)(H_2O)_2(NH_4)_{0.5}$	$Zn_{2.5}(H)_{0.4}(C_6H_3O_9P_3)(H_2O)_{1.9}(NH_4)_{0.6}$	$Zn_{2.5}(H)_{0.75}(C_6H_3O_9P_3)(H_2O)_2(CH_3NH_3)_{0.25}$
M_r	1036.91	1030.47	1027.85
Crystal system, space group	Orthorhombic, *I bam*	Orthorhombic, *I bam*	Orthorhombic, *I bam*
Temperature (K)	110	110	110
a, *b*, *c* (Å)	8.472 (3), 16.208 (7), 19.816 (8)	8.472 (3), 16.208 (7), 19.816 (8)	8.430 (5), 16.155 (12), 19.840 (11)
V (Å^3)	2721.1 (19)	2721.1 (19)	2702 (3)
Z	4	4	4
μ (mm^{-1})	4.80	4.80	4.83
Crystal size (mm)	0.14 × 0.08 × 0.08	0.14 × 0.08 × 0.08	0.19 × 0.12 × 0.03
T_{min}, T_{max}	0.555, 0.712	0.555, 0.712	0.460, 0.869
No. of measured, independent and observed [$I > 2\sigma(I)$] reflections	18603, 1746, 1330	18603, 1746, 1330	17603, 1550, 974
R_{int}	0.073	0.073	0.204
$(\sin\theta/\lambda)_{max}$ (Å^{-1})	0.671	0.671	0.643
$R[F^2 > 2\sigma(F^2)]$, $wR(F^2)$, *S*	0.034, 0.087, 1.03	0.036, 0.105, 1.02	0.061, 0.187, 1.11
No. of reflections	1746	1746	1550
No. of parameters	115	114	110
No. of restraints	0	0	12
$\Delta\rho_{max}$, $\Delta\rho_{min}$ (e Å^{-3})	1.29, −1.09	1.88, −0.95	1.96, −1.15

Table C 2. Crystallographic parameters and experimental details for the Rietveld refinements

Crystal data	ZnBP-NH_4-2 (Phase II)	ZnBP-NH_4-3 (Phase III)
Chemical formula	$C_{12}H_6O_{18}P_6Zn_5{\cdot}4(O){\cdot}NH_4$	$C_{12}H_6O_{18}P_6Zn_5{\cdot}NH_4$
M_r	1028.9	968.9
Crystal system, space group	Orthorhombic, *Ibam*	Orthorhombic, *Ibam*
Temperature (K)	333	423
a, *b*, *c*(Å)	8.44254 (17),16.2851 (4),19.8132 (4)	8.295735 (18), 16.4162 (4), 19.7053 (5)
V(Å^3)	2724.06 (10)	2683.55 (11))
Z	4	4
Radiation type	Synchrotron,λ=0.6124Å	Synchrotron,λ=0.6124Å
Diffractometer	Diffractometer at APS 1-BM-C	Diffractometer at APS 1-BM-C
Specimen mounting	kapton capillary, 0.9mm diameter	kapton capillary, 0.9mm diameter
Data collection mode	Fixed	Fixed
Scan method	Stationary detector	Stationary detector
2θvalues (°)	$2\theta_{min}$ =3.269 $2\theta_{max}$ =24.994 $2\theta_{step}$=0.013	$2\theta_{min}$=2.969 $2\theta_{max}$=24.994 $2\theta_{step}$=0.013
*R*factors	R_p=0.061,R_{wp}=0.085, R_{exp}=0.048, $R(F)$ =0.034, χ^2= 3.168	R_p=0.050,R_{wp}=0.069, R_{exp}=0.031, $R(F)$ = 0.047, χ^2 = 4.410
No. of data points	1739	1763
No. of parameters	72	75
No. of restraints	11	11

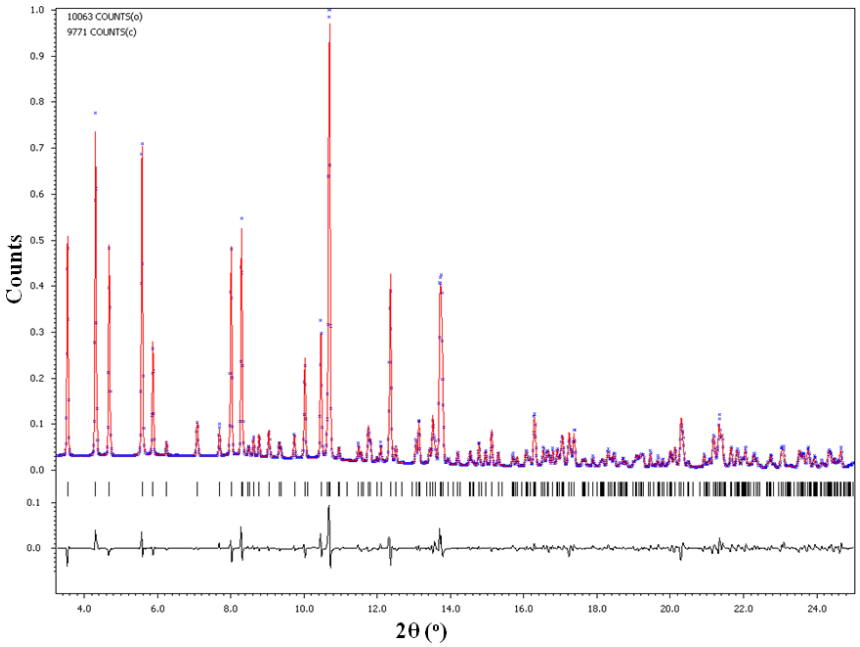

Figure C 1. A plot of the Rietveld refinement for phase II of ZnBP-NH_4

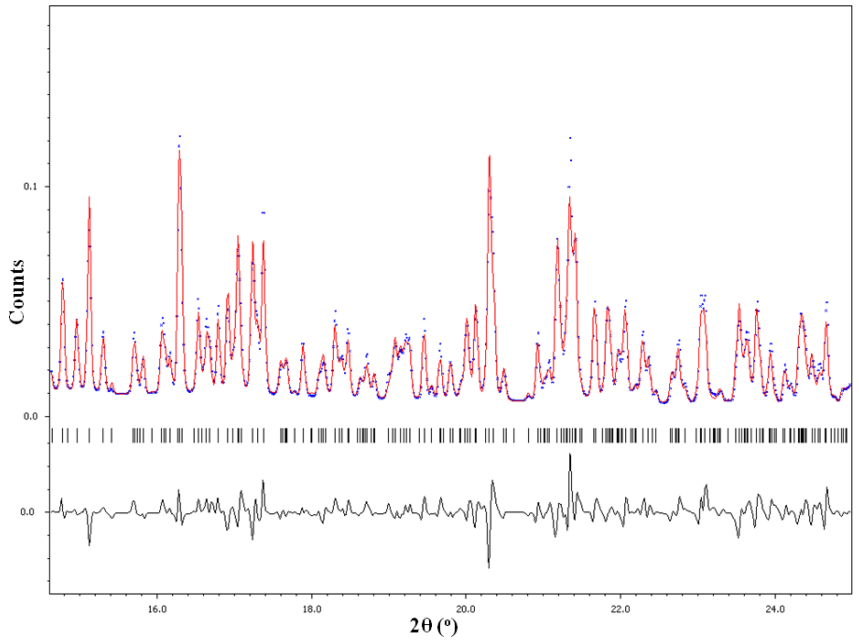

Figure C 2. A view of the high angle plot of the Rietveld refinement for phase II of ZnBP-NH_4

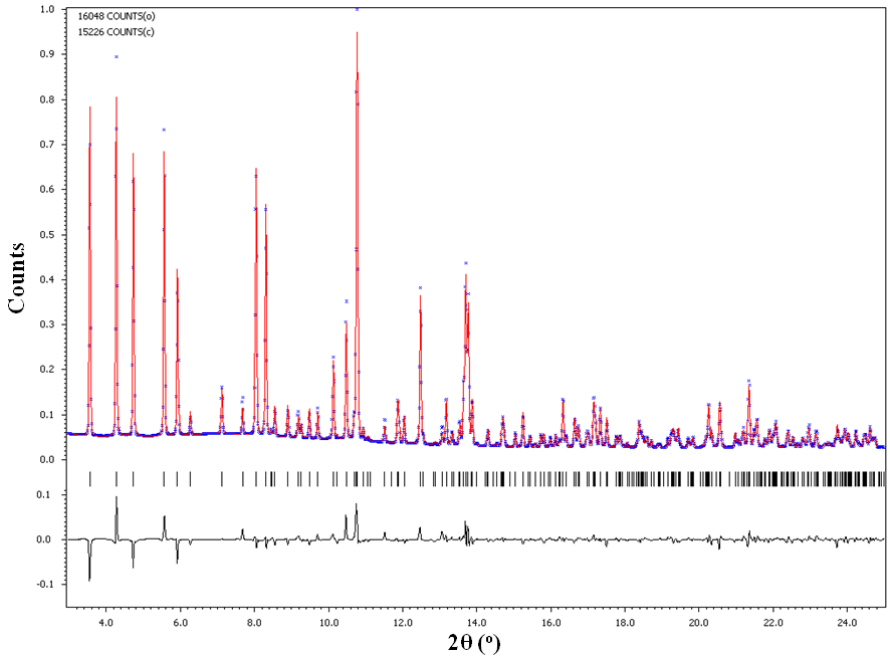

Figure C 3. A plot of the Rietveld refinement for phase III of ZnBP-NH_4

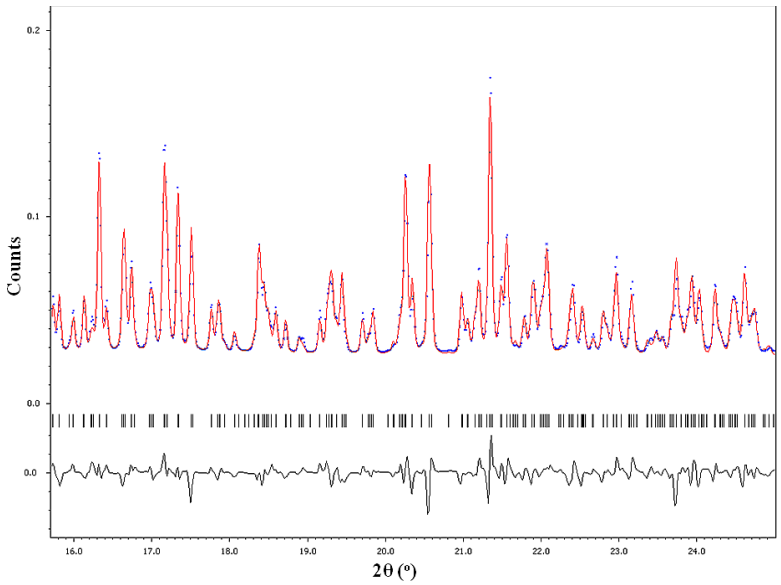

Figure C 4. A view of the high angle plot of the Rietveld refinement for phase III of ZnBP-NH_4

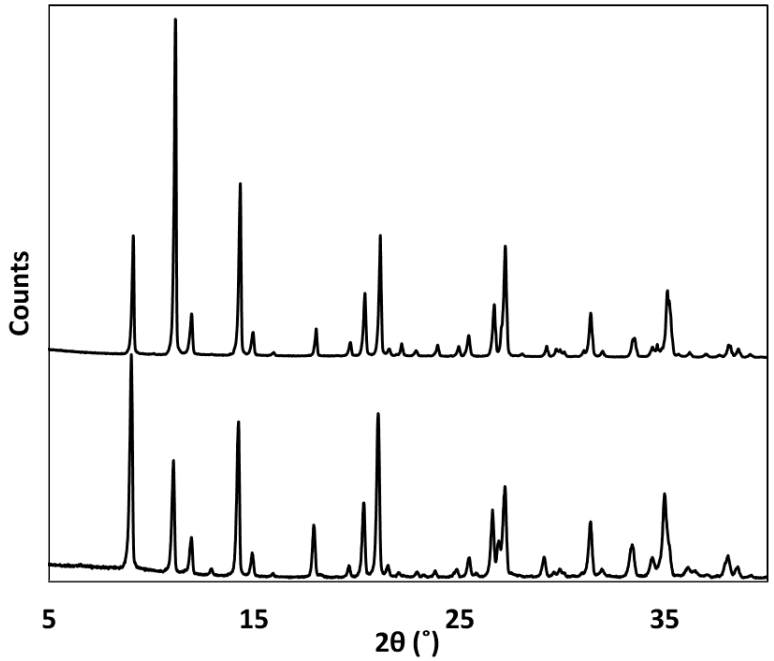

Figure C 5. A comparison showing the similarities in the PXRD of ZnBP-NH_4 (top) and ZnBP-Li (bottom). The PXRD data was collected on a BRUKER D8-Focus Bragg-Brentano X-ray Powder Diffractometer using Cu-Kα radiation (λ = 1.54178 Å). The powder patterns were recorded between 5^o and 40^o (in 2θ)

APPENDIX D

REVERSIBLE DEHYDRATION BEHAVIOR REVEALS COORDINATIVELY UNSATURATED METAL SITES IN MICROPOROUS CRYSTALLINE ALUMINUM PHOSPHONATES

Comparison of PXRD patterns for **2.5** (bottom) and the dehydrated phase **2d.5** (top). Figure D 18

Microprobe BSE images for compound **3.5** (right) and the low temperature phase for compound **2.5** (left), showing homogeneity. Figure D 19

*Synthesis of low temperature phase for compound **2.5**: $Al(O_3PC_6H_4PO_3H)(H_2O)_{2.6}$*

$AlCl_3$ (0.5684 g, 4.26 mmol) and H_4MPDPA (0.1682 g, 0.707 mmol) were placed in a 12 mL Telfon-lined autoclave and filled with H_2O (4 mL) and heated at 120 ^oC for 3 d. . The product was washed with ~200 mL of water and dried in an oven at 70 ^oC giving a white powder. Initial pH: -0.124, Yield: 0.136 g. . Elemental analysis (%) and microprobe Al/P ratio Calc: C23.3, H 3.32 P/Al ratio 2.00. Exp: C 23.2, H 2.85, P/Al ratio 1.91.

Table D 1. $^{27}Al\{^{1}H\}$ and $^{31}P\{^{1}H\}$ NMR chemical shift values for compound 1.5-3.5

	NMR chemical shift values (ppm)	
Samples	$^{27}Al\{^{1}H\}$	$^{31}P\{^{1}H\}$
1.5	-24.3	-0.45, -7.99
1d.5	-0.4to -6.8 (broad)	4.5, 3.3
2.5	38.5, -29.6	-1.0, -7.2, -10.1
3.5	39.8, -25.4	-0.72, -1.6

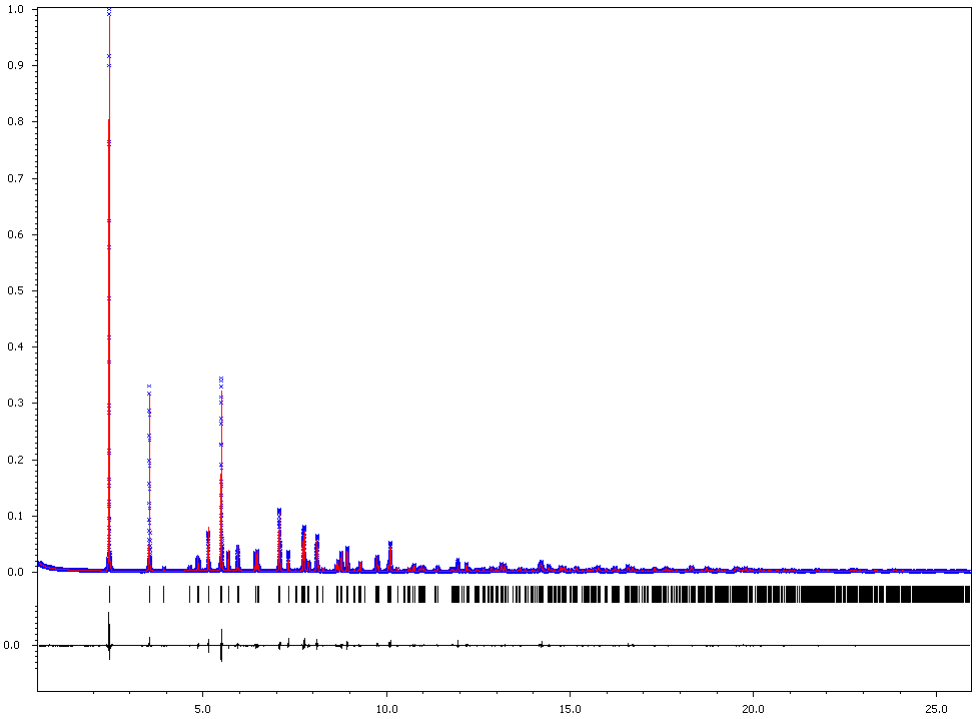

Figure D 1. Rietveld refinement plots for compound **1.5**

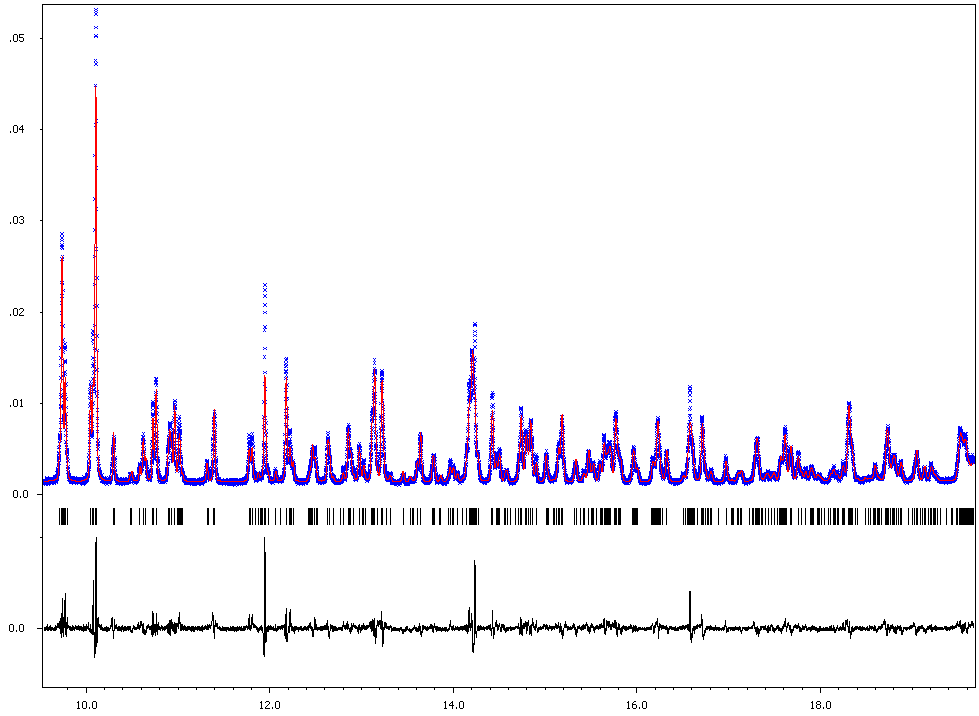

Figure D 2. Rietveld refinement plots for compound **1.5** showing the fit a high 2θ angles

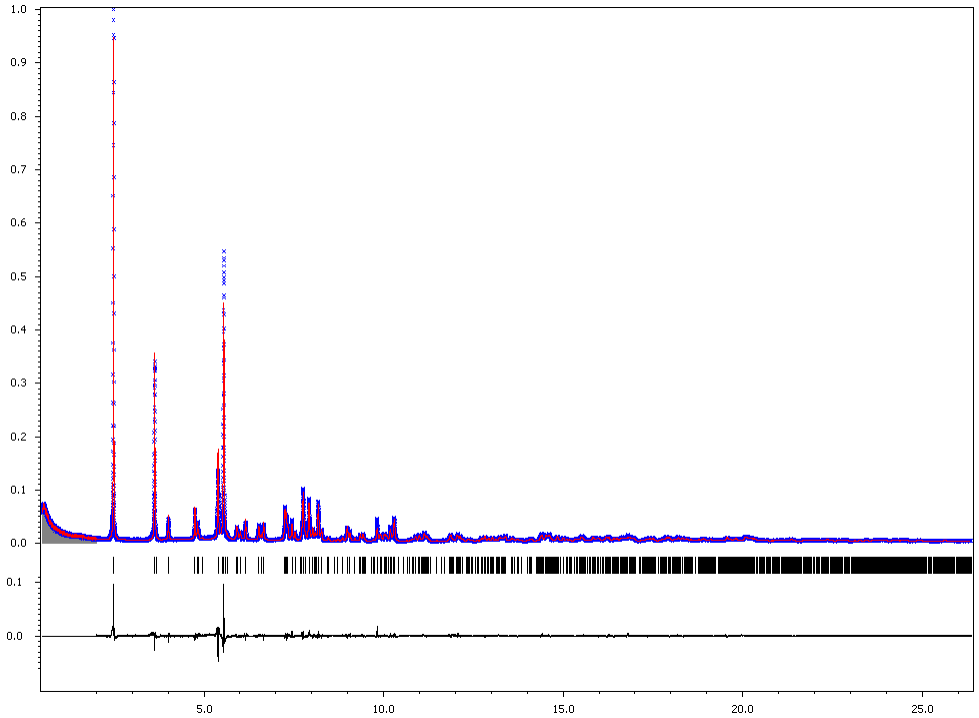

Figure D 3. Rietveld refinement plots for compound **1d.5**

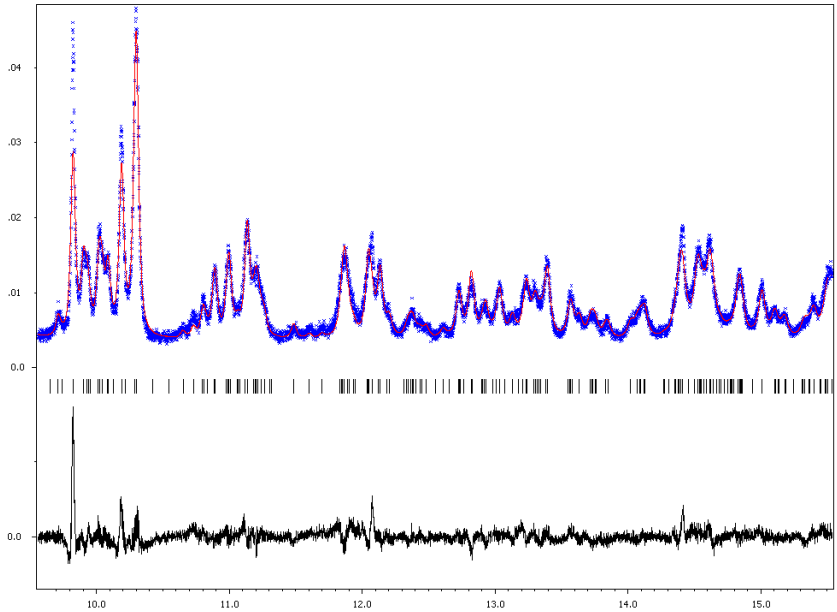

Figure D 4. Rietveld refinement plots for compound **1d.5** showing the fit a high 2θ angles

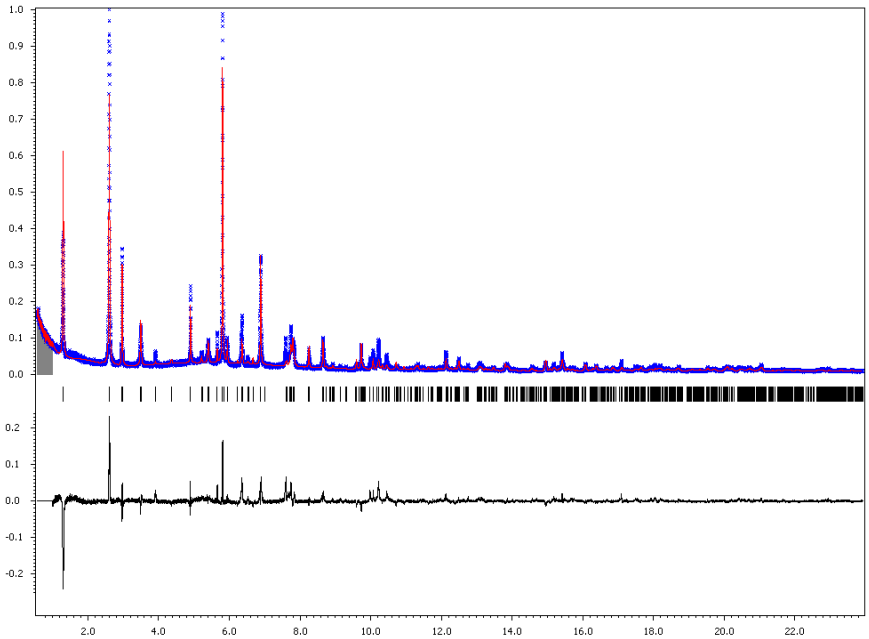

Figure D 5. Rietveld refinement plots for compound **2.5**

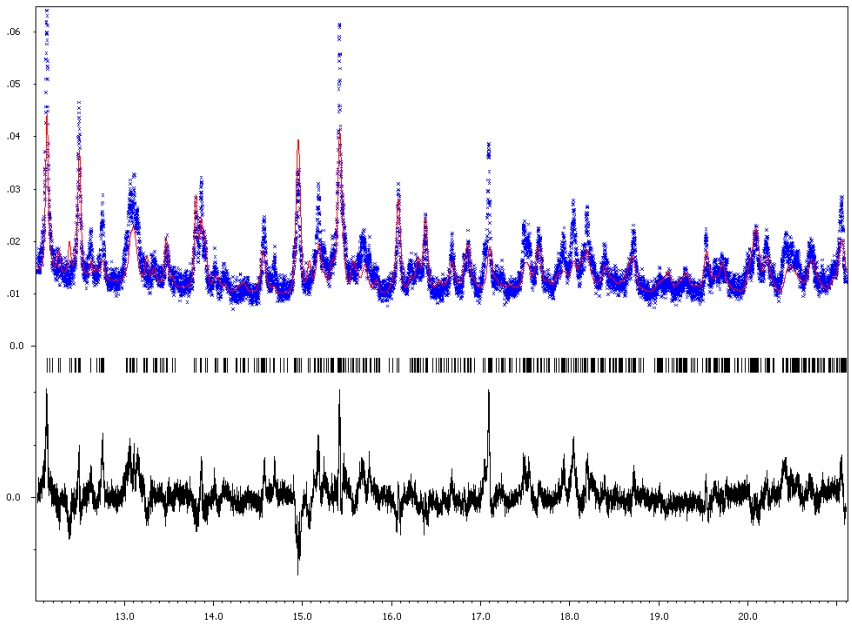

Figure D 6. Rietveld refinement plots for compound **2.5** showing the fit a high 2θ angles

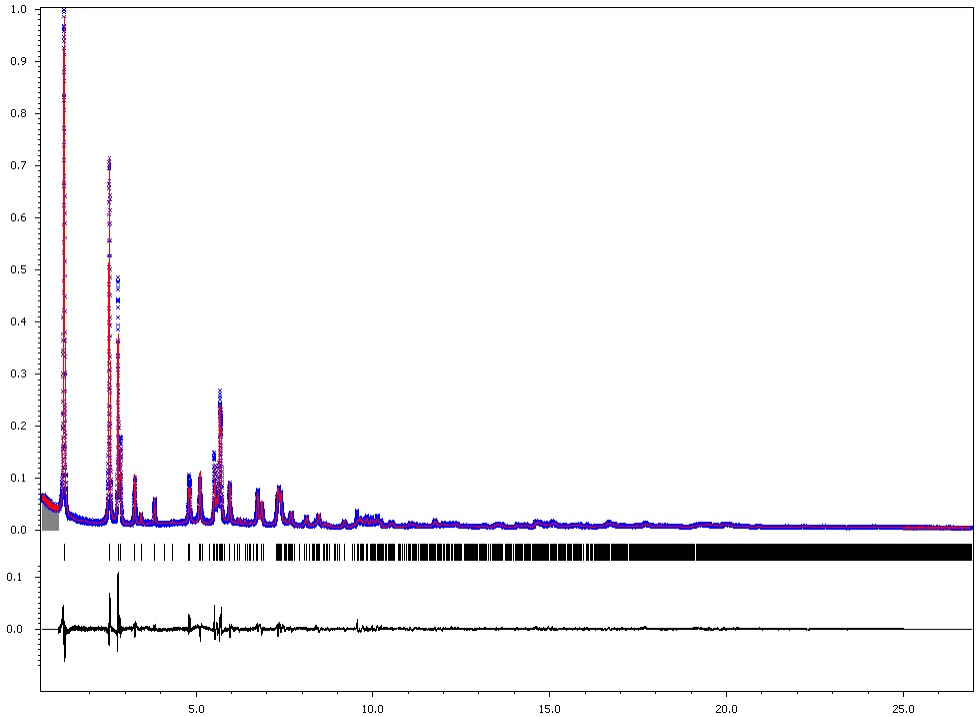

Figure D 7. Rietveld refinement plots for compound **2d.5**

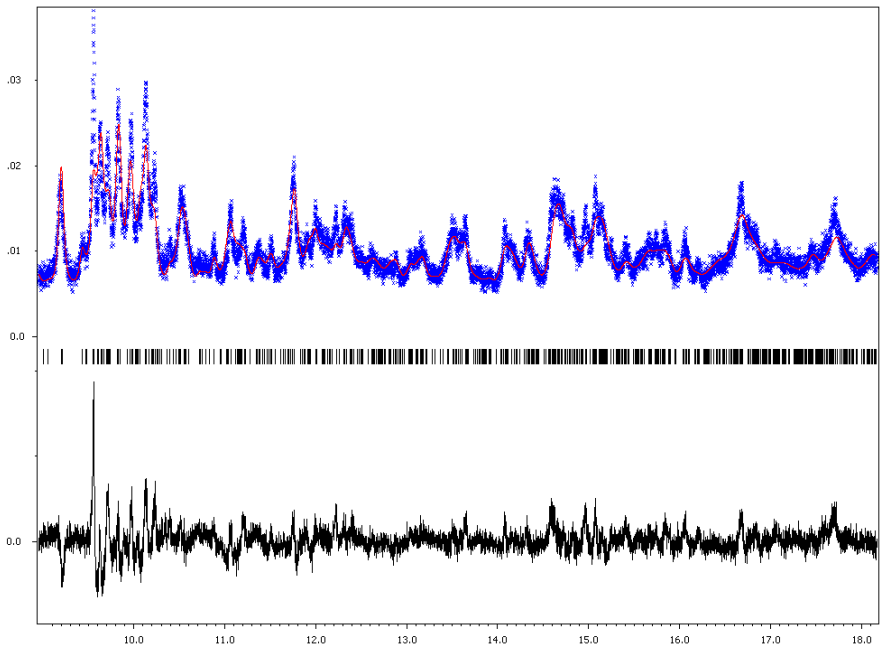

Figure D 8. Rietveld refinement plots for compound **2d.5** showing the fit a high 2θ angles

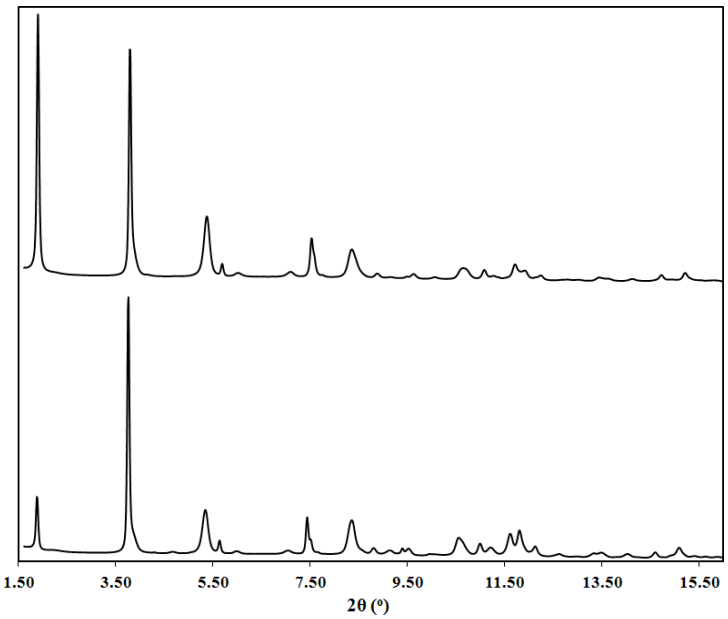

Figure D 9. Comparison of PXRD patterns for **3.5** (bottom) and the dehydrate phase **3d.5** (top)

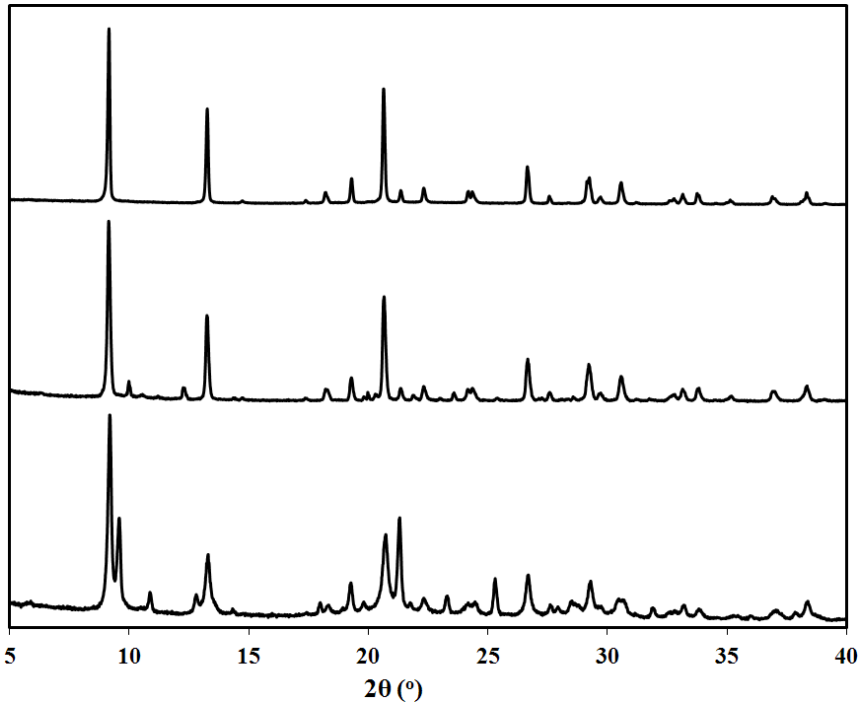

Figure D 10. A series of X-ray diffraction powder patterns where the reaction temperature was varied from 105 ^{o}C (bottom), 120 ^{o}C (middle) to 160 ^{o}C (top, compound **1.5**) showing a phase change with increase in temperature. (Powder pattern was obtained on the Bruker D8-Focus Bragg-Brentano X-ray Powder Diffractometer, Cu (λ = 1.542 Å) radiation)

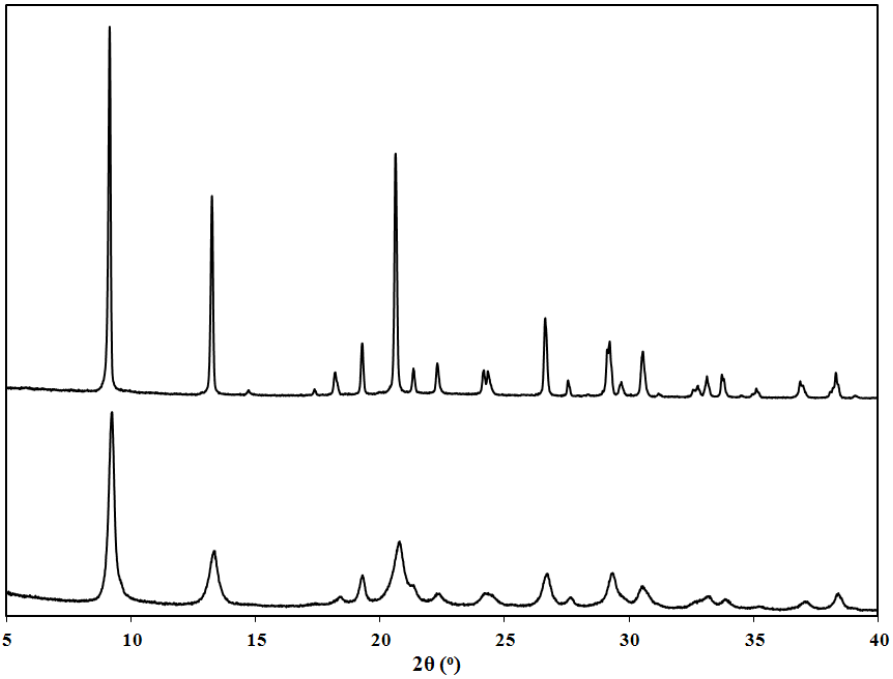

Figure D 11. Comparison of PXRD patterns for compound **1** (top) and the low temperature phase of compound **2.5** (bottom). (Powder pattern was obtained on the Bruker D8-Focus Bragg-Brentano X-ray Powder Diffractometer, Cu (λ = 1.54 Å) radiation)

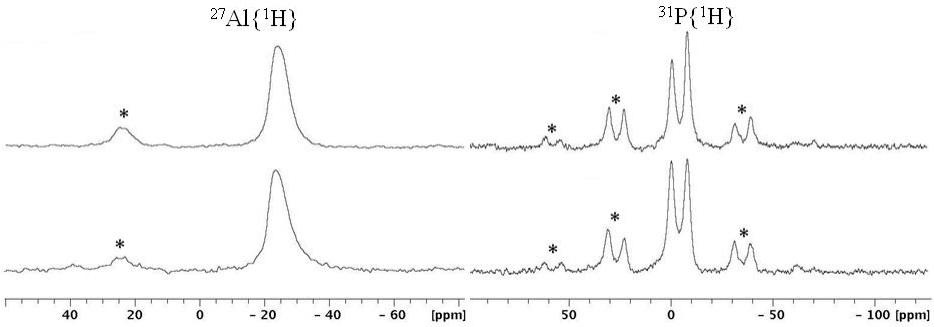

Figure D 12. ^{27}Al{^{1}H} and ^{31}P{^{1}H} NMR spectra from compound **1.5** (top) and the low temperature phase of compound **2.5** (bottom). The symbol * represent side bands

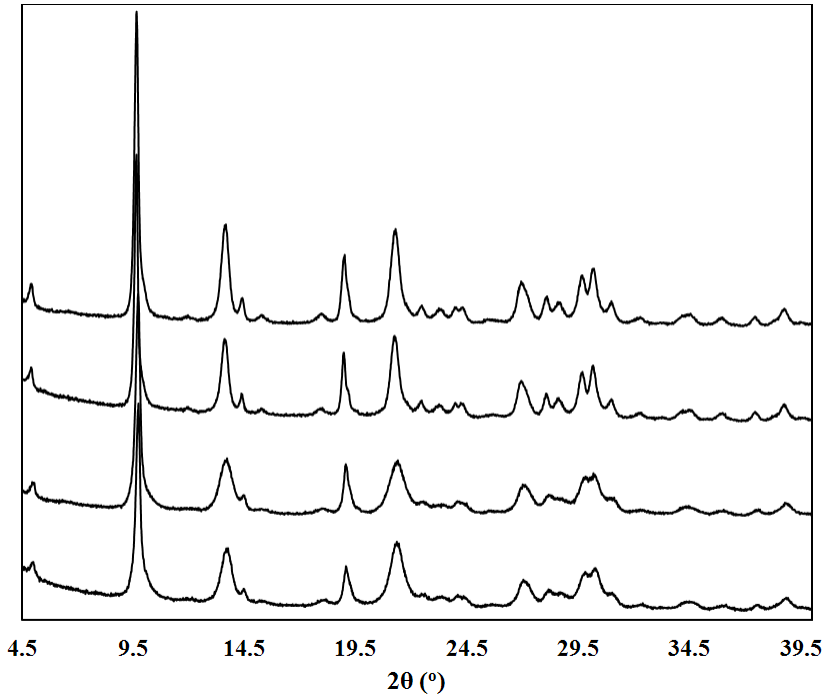

Figure D 13. A series of X-ray diffraction powder patterns where the reaction temperature was varied from 100 °C (bottom) to 210 °C (top, compound **3.5**) showing no phase change with increase in temperature. (Reaction temperatures from bottom to top: 100, 140, 160, 180, 210 °C) (Powder pattern was obtained on the Bruker D8-Focus Bragg-Brentano X-ray Powder Diffractometer, Cu (λ = 1.54 Å) radiation)

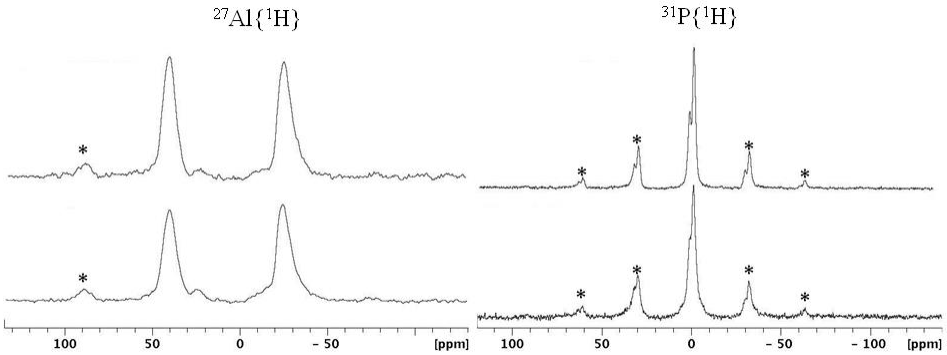

Figure D 14. $^{27}Al\{^{1}H\}$ and $^{31}P\{^{1}H\}$ NMR spectra for compound **3.5** at 100 °C (bottom) and 210 °C (top). The symbol * represent side bands

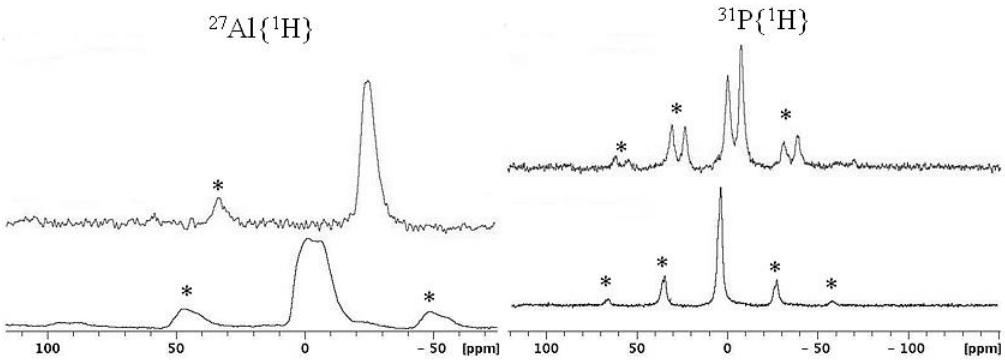

Figure D 15. ^{27}Al{^{1}H} and ^{31}P{^{1}H} NMR spectra for compound **1.5** (top) and **1d.5** (bottom). The symbol * represent side bands

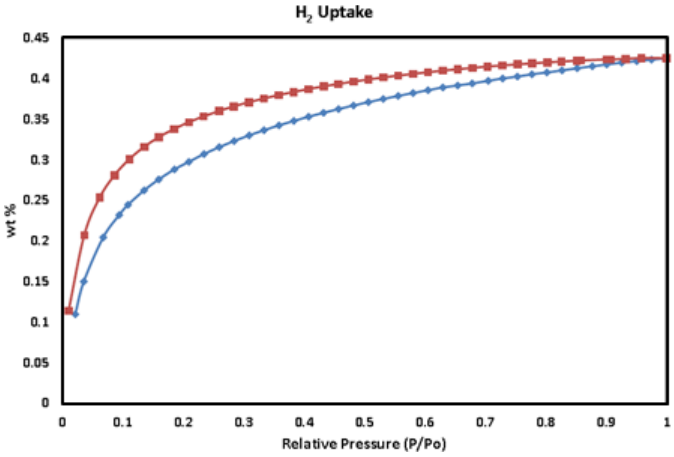

Figure D 16. The isotherm for hydrogen uptake at 77 K for compound **2.5**

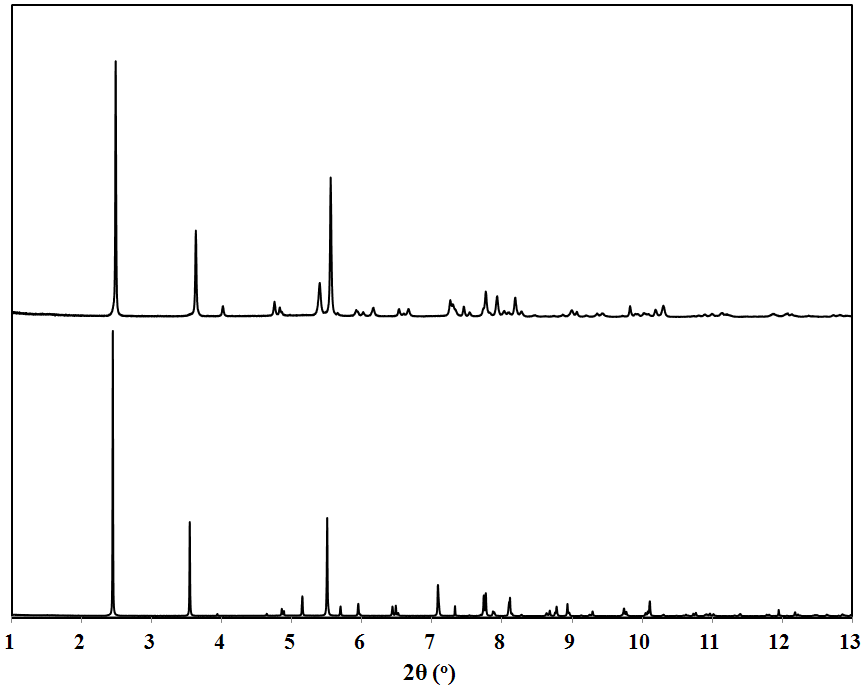

Figure D 17. Comparison of PXRD patterns for **1.5** (bottom) and the dehydrated phase **1d.5** (top)

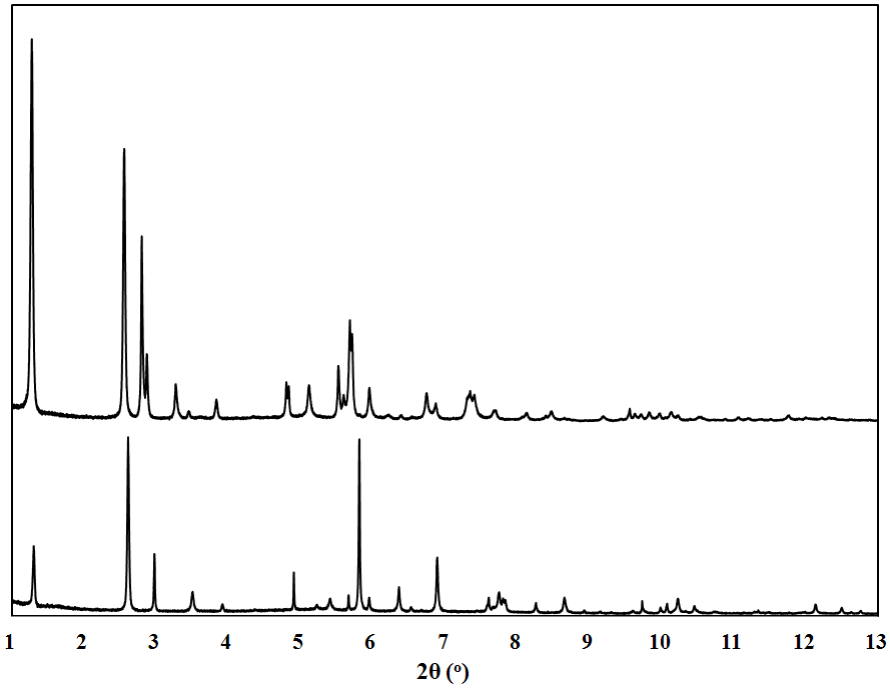

Figure D 18. Comparison of PXRD patterns for **2.5** (bottom) and the dehydrated phase **2d.5** (top)

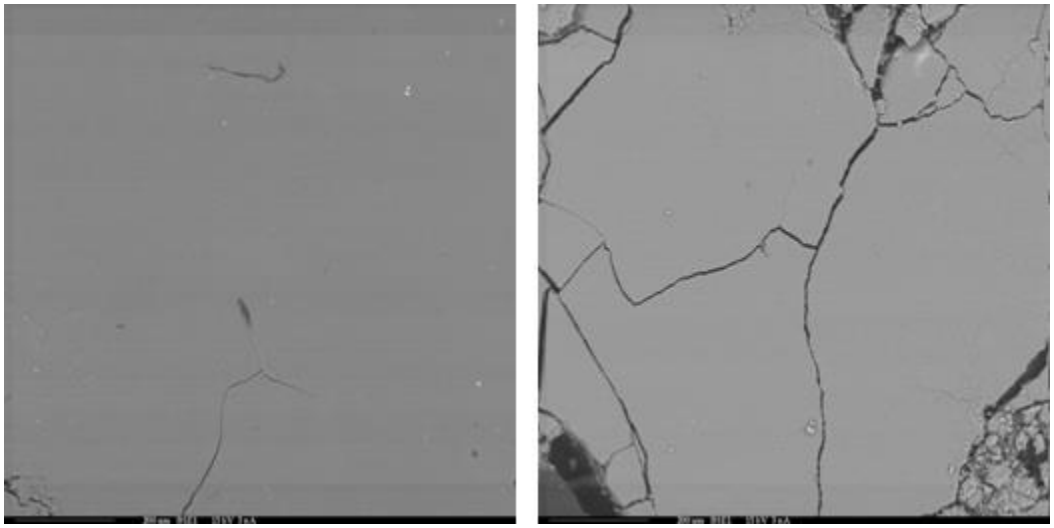

Figure D 19. Microprobe BSE images for compound **3.5** (right) and the low temperature phase for compound **2.5** (left), showing homogeneity

APPENDIX E

DEVELOPMENT OF ALUMINIUM HYBRIDS AS ION EXCHANGERS

Synthesis of $Al_4(O_3PC_{12}H_8PO_3)_3$ $5.4H_2O$

Compound $Al_4(O_3PC_{12}H_8PO_3)_3$ $5.4H_2O$ was synthesized according to the published synthesis at 185 ^oC for 7 d.[111] The reaction temperature and time was increased to 210 ^oC and 10 d to determine if a phase changed occurred for this reaction system.

Microprobe results for compound III-ox: BSE, WSD and ESD

The powder sample exposed to the mixed metal solution containing Yb^{3+}, Sm^{3+}, Nd^{3+} and Th^{4+} was additionally examined with ESD (Figure E 4), BSE (Figure E 3) and WSD to determine homogeneity and composition. ESD showed only elements Al, P, C, O, Th and Yb were present. The BSE images showed no large particles of either Th or

Yb which could have formed from precipitation of the metal ions. The material was confirmed to be homogenous with (ratios P:Al = 1.56 and Th:Al = 0.005).

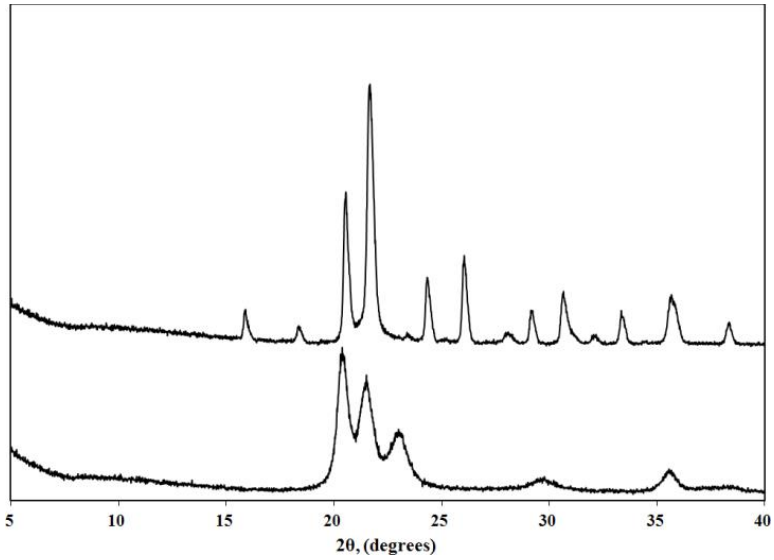

Figure E 1. PXRD patterns for the TGA residue of compound I (top) and II (bottom)

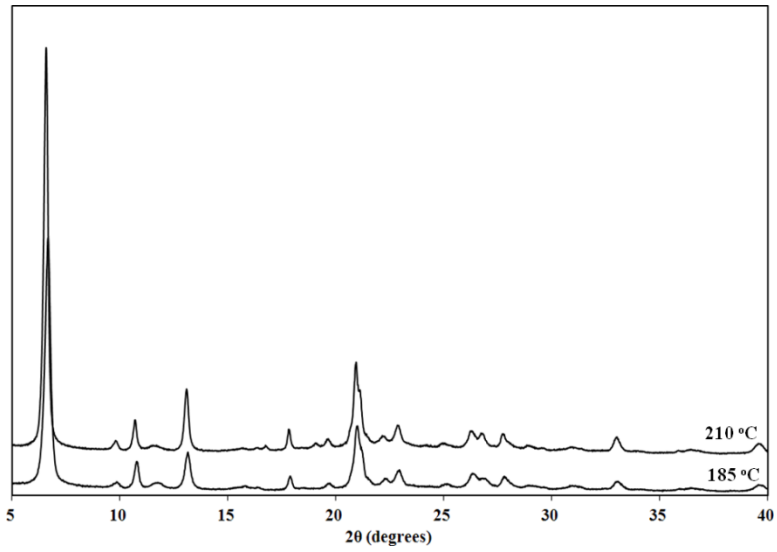

Figure E 2. PXRD patterns for $Al_4(O_3PC_{12}H_8PO_3)_3$ $5.4H_2O$ synthesized at 185 ^oC and 210 ^oC

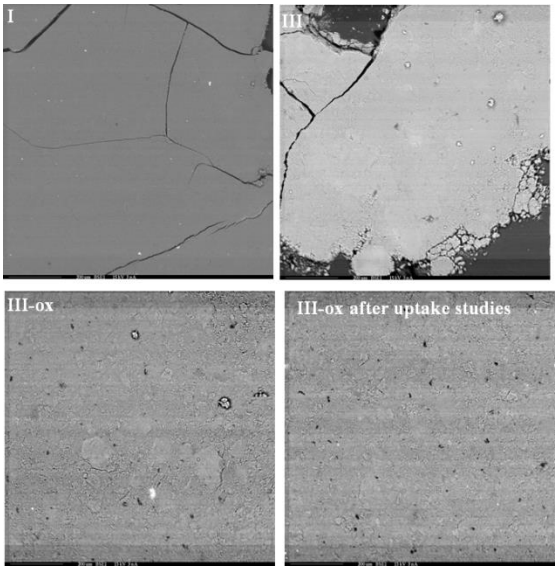

Figure E 3. Electron microprobe images (BSE) for Al-hybrid materials (I, III and III-ox) and III-ox after uptakes with the mixed metal solution (Yb^{3+}, Sm^{3+}, Nd^{3+} and Th^{4+})

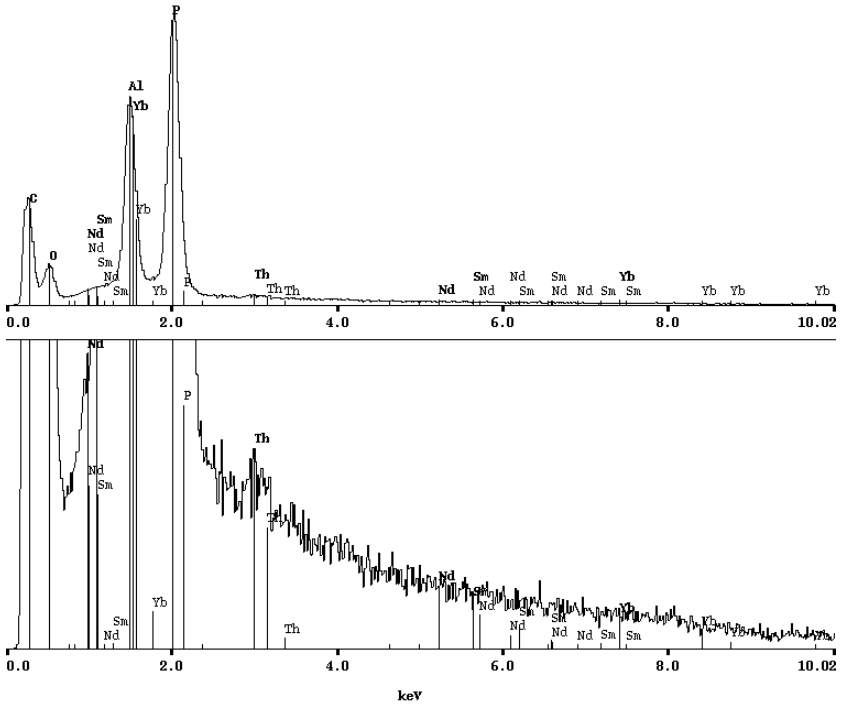

Figure E 4. ESD spectra of compound III-ox after exposure to the mixed metal solution containing Yb^{3+}, Sm^{3+}, Nd^{3+} and Th^{4+}. The labeled lines indicated at what keV elements should appear on the spectra